Aerial Deployment of an Autonomous Remote Sensing Network

Vol. IV: Final Report

Group 06

Marco Xausa	4663535	Victor Morizon	4997948
Jelmer van der Saag	4834259	Šimon ˇCajági	5010454
Hidde Hennecken	4836820	Lukas Uptmoor	5011965
Constantinos Aristodemou	4872576	Tilen Potocnik	5082900
Louis Naets	4992954	Sebastien van den Abeele	5110130

Delft University of Technology

Project duration: April 19, 2022 – June 24, 2022

Under the guidance of: Clemens Dransfeld, Salua Hamaza, Sunyou Hwang and Natalia Gomes de Paula

This page is intentionally left blank.

Executive Overview

The EcoSense EMBER (Environmental Monitoring of Bushfires for Early Response) system is an early-warning forest fire detection system deployed by an aerial vehicle in hard-to-reach areas. The increasing occurrence of wildfires due to climate change that devastates both urban and natural environments is creating a need to detect these fires at an early stage before they are too large to properly fight. This is the use-case that EcoSense EMBER is designed for.

EcoSense EMBER Mission

The EcoSense EMBER was conceptualised by Prof. C.A. Dransfeld and Dr. S. Hamaza, with the aim to create a network of eco-monitoring sensors in hard-to-reach environments. The EcoSense DSE group was tasked with finding an application for this concept, which led to the creation of the following Mission Need Statement:

Mission Need Statement

Gathering spatially- and temporally-dense datasets in hard-to-reach environments for early fire detection.

The EcoSense team analysed comparable solutions, such as satellite imaging, and found that no system existed that could cover a large area (such as can be done with satellites) while maintaining the detection resolution that can be achieved with hand-placed environmental sensors. This led to the development of an aerially-deployed sensor network, which aims to combine the benefits of existing solutions while negating their drawbacks.

The area selected for this mission is the National Park of Wollemi, Yengo, and the Blue Mountains located North-West of Sydney, Australia. This area experiences regular forest fires during the dry season, and its proximity to large urban areas mean that growing wildfires may pose a threat to infrastructure or inhabitants. EcoSense EMBER will monitor a $10\,\mathrm{km}$ x $10\,\mathrm{km}$ area up to $100\,\mathrm{km}$ away from the established ground station where the vehicle is launched. The scalable nature of the design means several missions can be deployed to cover several of these areas, and potentially provide coverage of an entire national park.

The mission is separated into distinct phases, which are shown in Figure 1:

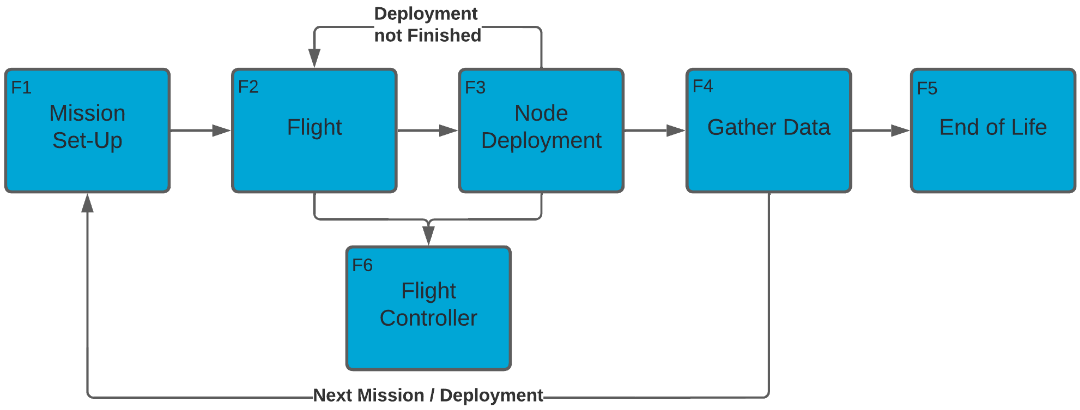

Figure 1: *Top-level functions describing the general phases of the EcoSense EMBER mission.*

A summary of each phase is as follows:

F1 | Mission Set-Up Surveying the area, logistic and operations planning and execution, transporting to mission area.

F2 | Flight Vehicle launch operations, climb and cruise.

F3 | Deploy Sensors Sensor deployment, network set-up and return journey to ground station.

F4 | Gather Data Environmental monitoring, data communication and handling.

F5 | End of Life System dismantling, decomposition and mission conclusion.

Both the vehicle and the deployed sensor network are designed with sustainability as the main focus. Social, economic, and environmental sustainability was incorporated in both the project and mission design. The vehicle is completely solar-powered, emits no greenhouse gases during operation, and uses sustainably-sourced hydrogen as a lifting gas. The majority of the deployed sensor biodegrades after its functional life, minimising the impact upon the environment in which it is deployed.

EMBER Vehicle Overview

Vehicle Performance		
Sensor Capacity	552	
Design Speed	50 km/h	with respect to ground
Range	350 km	at design speed
	100 km	solar panel failure
Endurance	7 h	at design speed
Minimum Turn Radius	24 m	at design speed
Maximum Climb Angle	13.3 deg	at design speed
Lifting Envelope		
Envelope Length	13.58 m	
Envelope Radius	2.26 m	
Envelope Volume	146 m3	
Nominal Envelope Pressure	500 Pa	
Hydrogen Capacity	12.2 kg	at 20 C + nominal pressure
Gondola		
Gondola Length	4.49 m	
Gondola Width	1.15 m	
Gondola Height	0.33 m	(storage height)

Solar Panels	
Cell Type	Maxeon Gen III
Number of Cells	1863
Covering Angle	86.00 deg
Length	10.86 m
Area	35 m2
Buffer Battery Capacity	165 Wh
Nominal Bus Voltage	24 V

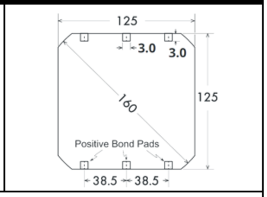

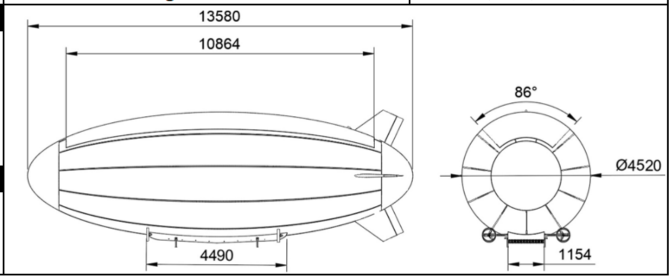

Figure 2: *Datasheet of the EMBER vehicle.*

Structural Subsystem

The structural configuration of the EcoSense EMBER has two main substructures: The envelope and gondola structures.

Envelope The envelope of the airship is a critical structure in the envelope and must fulfil a wide variety of functions. The envelope build-up in the airship consists of an outer weather-ability layer, a middle load-bearing layer, and an inner sealing layer bonded together with an adhesive. The outer layer consists of a Tedlar film, the middle layer is a Vectran woven fabric and the inner layer consists of an ethyl vinyl alcohol film. All layers are connected to a thermoplastic polyurethane film. The fabric weights 200 gsm and is 0.21 mm thick.

Gondola The gondola is structured in a boat-like fashion. It has two main parts. The haul and the deck. It is built from Bcomp material Amplitex[1]. The haul accommodates the propulsion system, landing system, deployment system and provides housing for the majority of the electronic components. The deck is the upper part of the gondola, this part is used to provide protection for the contents of the gondola and provide an attachment area to the envelope.

Propulsion Subsystem

The three main components of the propulsion system are the motor, the propeller, and the thrust vectoring system. The selected motor is the T-motor V505 motor, rewound to 520KV. The motor is capable of producing sufficient thrust for cruise speed at only 20% throttle, enabling redundancy in case of failure. To generate thrust a motor must be combined with a propeller. The designed propeller is a three-bladed design with a diameter of $41\,\mathrm{cm}$. A duct is constructed around the propeller to aid with efficiency and safety of operation. With the setup, the noise at ground level would be equal to 78 dB.

The thrust vectoring is enabled through a mechanism mounted on the end of the mounting rod. The Hitec HS-5805MG servo has been selected, the performance of which has been determined valid through analysis. The final propulsion system weights $1.24\,\mathrm{kg}$ per motor.

Power Subsystem & Electronics

The electronics system was designed to fulfil all needed functions. An overview of distinct electronics groups can be found in the simplified data handling diagram below. The mass of the electronic components adds up to $6.9\,\mathrm{kg}$.

For power generation, a solar array is fitted to the top of the envelope. Due to its complex shape, its power generation capabilities are calculated through a model. To achieve sufficient power generation through the flight, 1863 solar cells are utilised, covering an area of $35.62\,\mathrm{m}^2$ over a coverage angle of $86°$.

In case of solar array failure or a power consumption spike, an auxiliary battery pack is sized for the vehicle.

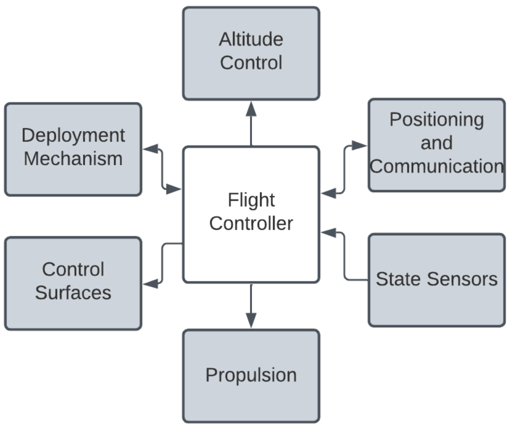

Figure 3: *Simplified data handling diagram.*

With the Li-Ion battery pack, EMBER is capable of returning to the ground base at the maximum range of $100\,\mathrm{km}$. The battery pack is constructed in a 6S18P configuration, made of 108 cells, each with a capacity of 3000mAh.

Vehicle Aerodynamics

The vehicle aerodynamics were evaluated through the sizing of the lifting envelope, the control fins, and the drag estimation.

The lifting envelope was sized to provide storage for a sufficient amount of hydrogen to be neutrally buoyant at a predetermined trim altitude. For a MTOM of $143.4\,\mathrm{kg}$ the required volume is $145.8\,\mathrm{m}^3$, with a surface area of $158.0\,\mathrm{m}^2$.

The control surface design consists of an inflated fin body, with a solid control surface. The fins were sized according to historic data of similar airships. This resulted in a final design with a mass of $1.6\,\mathrm{kg}$, a root chord of $1.4\,\mathrm{m}$ and a span of $1.1\,\mathrm{m}$, per fin.

The drag estimation was performed on the main outer bodies of the vehicle. These include the envelope, fins, gondola, and propulsion system. The estimated volumetric drag coefficient is equal to 0.0278.

Buoyancy Control

The buoyancy control is required to counteract the decrease in mass due to the deployment of sensors. As more than 30% of the mass is dropped during operation, the subsystem is crucial in the success of the mission. The concept used for control consists of ballonets regulating the inside pressure and an exhaust valve, capable of releasing hydrogen to adjust the buoyancy for the loss of mass.

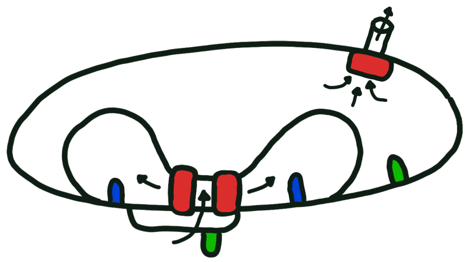

Figure 4: *Sketch of the buoyancy control system.*

Control System

The vehicle possesses two rudders and two elevators at the tail fins, both limited to a deflection of 10 degrees, which can be used to generate a yawing and pitching moment. Making use of aerodynamic envelope lift, the blimp will acquire a vertical velocity upon pitch-up. The vehicle dynamics are modelled as two uncoupled linear time-invariant systems represented in state-space, both having stable eigenvalues. A constant elevator deflection will result in a constant flight path angle, which will in the long run approach zero when the blimp approaches its service ceiling. On the other side, a constant rudder deflection will result in a constant turn rate. Altitude and heading are controlled by a proportional state-feedback controller, making the vehicle easy to operate remotely, but not fully autonomous. There exists a concept for autonomous xy-position control, too, but it is not yet implemented.

Payload Deployment Mechanism

The deployment mechanism uses permanent electromagnets, which lose their magnetic properties, when current is passed through, to hold and deploy the sensor nodes. It consists of two trays, each capable of holding 226 nodes. The assembly of the entire deployment mechanism weights $10.7\,\mathrm{kg}$, with the structure itself being $5.2\,\mathrm{kg}$ and the rest consisting of the magnets themselves and the required supporting hardware.

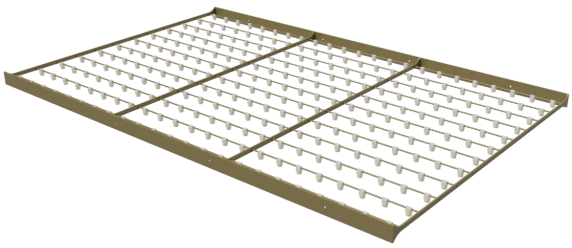

Figure 5: *Render of the payload tray.*

Production Plan

To build up the vehicle, a structured plan is required. The construction starts with the envelope. First, the correct patterns are cut out of the fabric sheets. Then all the valves are installed in the correct places in the sheets with adhesives and extra film. Next the envelope fabrics are joined together, and the fins are attached. Finally, the envelope is closed. Once the envelope is inflated, the solar panels are installed on the top and the aluminium coating is applied. In parallel to manufacturing the envelope, the gondola is constructed. The gondola is built using a Bcomp pre-preg using vacuum infusion on positive/negative foam milled moulds. Once the gondola is finished. the gondola can be attached to the envelope.

Sensor Network Overview

The other main system of the EcoSense EMBER is the sensor network, which is deployed by the vehicle. This network consists of two types of nodes: the sensor node - which detects bushfires - and the relay node - which creates a link between the sensor nodes and the ground station.

Sensor Node

The final sensor node design uses the Bosch BME688 sensor to detect concentrations of carbon monoxide and hydrogen gas, both of which are indicative of smouldering/open fires. They are attached by a deployment string to low-hanging foliage several meters above the ground. A render of the sensor node design can be found in Figure 6:

The mass of this final design is $80\,\mathrm{g}$, costing EUR 45.50 per sensor. The enclosure is made out of cellulose acetate, which naturally biodegrades into non-toxic by-products. As such, every part of the sensor node except the electronics and steel springs/payload attachment plate will disappear after the functional lifetime of the sensor.

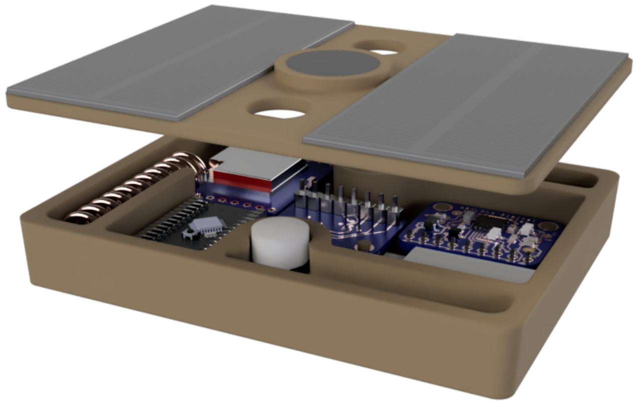

Figure 6: *Exploded view of final sensor node design.*

Network Design

The network design decides the spacing between nodes, as well as the communication infrastructure that is used to relay information to the ground station.

The spacing of sensor nodes is based on a risk distribution map of fire ignition risk. Higher risk results in a higher node density, which optimises the distribution of sensor nodes to achieve the desired reliability. This network configuration will detect a fire anywhere in the park within 10 minutes of ignition with an average reliability of 62%, which is faster than existing solutions. Besides this, 90% of fires of at most $0.2\,\mathrm{km}^2$ are detected, which meets the requirements set for the EcoSense EMBER system.

The network operates upon the LoRa protocol, which allows for long-range communication of small data packets. Sensor nodes do not have the range to directly communicate to the ground station. As such, all sensor nodes operate on decentralised network with relays to link them to the ground station. The network also updates the user on the integrity and health of the network and alerts the user of any failed/compromised nodes.

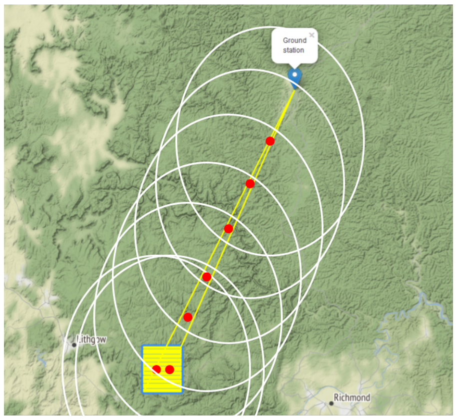

Figure 7: *Relays needed in the worst-case scenario of a $100\,\mathrm{km}^2$ tile located $100\,\mathrm{km}$ from the ground station.*

Relay Node

The relays act as communication hubs for the sensors. Between relays, a distributed network infrastructure is used where each relay communicates with other relays to create a bridge to the ground station. Each relay node has a range of $23\,\mathrm{km}$, which allows a bridge of relays to be constructed between the monitored area and the ground station, creating a complete network such as shown in Figure 8.

Relay nodes have a similar footprint to the sensor nodes, but weigh $156\,\mathrm{g}$ due to additional power requirements. This allows them to be deployed by the same deployment mechanism.

Operations & Logistics

Given the need of the customer for an early fire detection system within a global area of interest, the operations and logistics are the following. At first, all the components of the product need to be transported to the EcoSense HQ which is located strategically between the airport, port, and train station in Sydney. Given the global area of interest, EcoSense shall perform initial mission planning where the entire area is divided up into tiles of $100\,\mathrm{km}^2$ for which the amount of sensors is determined. One EcoSense EMBER product's operations will take approximately $3\,\mathrm{days}$ to monitor an area of $100\,\mathrm{km}^2$. Using smart algorithms the flight planning of the area where the sensors need to be deployed is performed. The flight path minimizes the distance travelled and energy loss due to climb-

Figure 8: *Operations and logistics map (source:Google Maps)*

ing and descending. Furthermore, the hydrogen lifting gas should be ordered and shipped to the ground station which could be done by Coregas. When the initial mission planning is performed, the operations will move forward with the transportation to the ground station. The ground station is located in the centre of the global area of interest which should be sufficient in size and reach all the deployment area's within $100\ \mathrm{km}$. The transportation of the product to the ground station shall happen with a Ford Ranger towing a $20\ \mathrm{ft}$ container in which the product is stored. From the ground station, the product is launched to the deployment area where the sensors and relays are deployed. After the deployment, the product is stored and transported back to the ground station. The sensor data is verified and validated and then sent to a database that contains temperature, humidity, and CO and H_2 concentration data of the area of interest. EcoSense will use this data to deliver the customer an interactive dashboard that contains a wildfire prevention map and a wildfire detection map.

Reliability & Safety

Assessing the reliability and safety of a product design is a crucial aspect of an engineering exercise. Regarding reliability, the EcoSense EMBER deployment vehicle's solar panel and battery over-design means the blimp can operate in almost any weather condition (apart from cloudy and extremely windy days). On the other hand, the sensor network has a total reliability of between $62\ \%$ and $90\ \%$ depending on the detection method (time or size respectively). On the safety side, flying a hydrogen blimp on top of a fire-endangered forest does not sound right. However, after analysis, one can demonstrate that the deployment blimp carries close to 6 times less energy than a Cessna 172 (also used for fire detection in some countries).

Life Cycle Assessment and Sustainability

Employing environmentally, socially, and environmentally sustainable development strategies throughout the organisation and design-led the team to consider sustainability concerning each subsystem and trade-off, as described in each subsystem dedicated sustainability section and generally in the sustainable development strategy. It is also planned for the deployment of the EcoSense EMBER system to have wide-ranging positive impacts on sustainability by reducing the various negative effects of wildfires.

To assess the negative environmental impacts caused by the system production, use, and end-of-life, preliminary assessments were performed and preparations, including scope and goal definition as well as breakdowns of the involved flows and processes, and more, were made for further deeper LCA assessments. With the help of the preliminary assessments, it was already possible to identify key areas for improvement and deeper investigation. The findings include the fact that the sensors have a much higher impact than the airship itself, or that the hydrogen use associated with the use of the airship has a significant impact. These areas shall be reflected upon and further elaborated and improved in further research.

Market Analysis

The total cost of an EcoSense EMBER is estimated to EUR 156k. Most of this is derived from the operations and sensor node costs. The vehicle, which can be reused, only composes a small percentage of the overall cost per mission.

It is estimated that the direct cost of forest fires is EUR $4700\ /\mathrm{km}^2$. Given that fires can be detected within 10 minutes of them starting, and the reliability of the sensor network, it is estimated that EcoSense EMBER can prevent EUR $2900\ /\mathrm{km}^2$ of the area covered.

For an area of $100\ \mathrm{km}^2$, this creates an opportunity cost of EUR 290k. Being sold at a price of EUR225k per mission, this places EcoSense EMBER in a competitive spot where the design is both profitable for the Australian government and the EcoSense company. An overview of how this design compares to its competitors is given in Table 1.

Table 1: *Overview of market solution analysis [2].*

Detection Method	Environmental Sensors	Radiation Sensors	Aircraft Inspection	Satellites	EcoSense EMBER
Cost [EUR/km2/yr]	450	12	7.2	46-115	450
Detection Time [min]	4	10	480	31	10
Fire Size [km2]	0.2	0.004	0.005	0.2	0.002
Accuracy [%]	92	95	93	62	62-90
Applicability	medium-high	low	medium-high	medium	high
Sustainability	medium-high	high	low	medium	high

Contents

List of Variables and Acronyms

AC	Alternating Current
ACS	Altitude Control System
AHP	Analytical Hierarchy Process
AR	Aspect Ratio
AUD	Australian Dollars
BEMT	Blade Element Momentum Theory
CAD	Computer-Aided Design
CO	Carbon Monoxide
CO_2	Carbon Dioxide
CPU	Central Processing Unit
DC	Direct Current
DHI	Diffuse Horizontal Irradiance
DHI	Diffused Horizontal Irradiance
DNI	Direct Normal Irradiance
DOT	Design Option Tree
DSE	Design Synthesis Exercise
EM	Electromagnet
EMBER	Environmental Monitoring of Bushfires for Early Response
EOL	End-of-Life
EPS	Electrical Power System
EUR	Euro
FDM	Fused Deposition Modelling
FFDI	Forest Fire Danger Index
GPS	Global Positioning System
GUI	Graphical User Interface
H_2	Hydrogen
HP	Hazard Probability
HQ	Headquarters
HRI	Hazard-Risk Index
HS	Hazard Severity
ISA	International Standard Atmosphere
ISO	International Organization for Standardization
LCA	Life Cycle Analysis
LCP	Liquid Crystal Polymer
Li-Ion	Lithium Ion
LoRa	”Long Range, Wide Area” Network Protocol
LOS	Line of Sight
MAC	Mean Aerodynamic Chord
MTOM	Maximum Take-off Mass
MTOW	Maximum Take-off Weight
NKY	Not Known Yet
NSW	New South Wales
NTP	Normal Temperature and Pressure
PCB	Printed Circuit Board
PLA	Polylactic Acid
PU	Polyurethane
PVC	Polyvinyl Chloride
PVF	Polyvinyl Fluoride
QFD	Quality Function Deployment
R&D	Research & Development
RAMS	Reliability, Availability, Maintainability & Safety
RFS	Rural Fire Service
RH	Relatively Humidity
RPM	Rotations Per Minute
RTG	Radioisotope Thermoelectric Generator
SATCOM	Satellite Communication
SF	Safety Factor
SNR	Signal-to-Noise Ratio
SPOF	Single Point of Failure
SSL	Standard Sea-Level Conditions
SWOT	Strengths, Weaknesses, Opportunities, Threats
TBD	To Be Determined
TMY	Typical Meteorological Year
UAV	Unmanned Aerial Vehicle
UN	United Nations
USD	United States Dollars
UV	Ultra Violet
VTOL	Vertical Take-Off & Landing
α	Angle of Attack / rad
η	Efficiency / -
γ	Flight Path Angle / rad
Λ	Sweep angle / rad
λ	Taper Ratio / -
ν	Kinematic Viscosity / $\mathrm{m^2/s}$
ω	Angular Velocity / $\mathrm{rad/s}$
ω	Rotational Velocity / $\mathrm{rad/s}$
ρ	Density / $\mathrm{kg/m^3}$
σ	Stress /Pa
σ_t	Tensile Stress / Pa
A	(Aerodynamic Reference) Area / $\mathrm{m^2}$
B	Buoyancy Force / N
B	Number of Blades / -

b	Wing Span / m
c	Chord Length / m
C_d	Coefficient of Drag / -
C_f	Skin Friction Drag Coefficient / -
C_l	Coefficient of Lift / -
C_p	Coefficient of Pressure / -
C_{L_α}	Derivative of C_L w.r.t. α / $/\mathrm{rad}$
D	Diameter / m
E	Energy / J
F	Force / N
f	Frequency /
g	Gravitational Acceleration / $\mathrm{m/s^2}$
G	Gain /
h	Altitude / m
I	Moment of Inertia / $\mathrm{m^4}$
k	Spring Constant / $\mathrm{N/m}$
k_h	Induced-Drag-Parameter of the Tail /–
k_s	Spheroid Ratio / -
L	Path Loss / dB
l	Length / m
M	Molecular Mass / $\mathrm{g/mole}$
M	Moment / Nm
m	Mass / kg
P	Power / W
p	Pressure / Pa
r	Radius / Pa
R	Universal Gas Constant / $\mathrm{J/mole/K}$
r	Radius / m
Re	Reynolds' Number / -
S	Surface Area / $\mathrm{m^2}$
T	Temperature / K
T	Thrust /
T	Torque / Nm
t	Time / s
V	Volume / $\mathrm{m^3}$
v	Velocity / $\mathrm{m/s}$
v_t	Terminal Velocity / $\mathrm{m/s}$
W	Work / J

1 Introduction

”Temperatures are rising across the globe and every year large parts of the Earth’s remaining ecosystems fall victim to wildfires. In 2019 alone, 21% of Australia’s forest area was devastated by flames [3]. Fighting those fires is not only costly, but also puts humans at risk while having little success. Therefore, EcoSense has embarked on the mission to develop an early-detection sensor network, allowing it to fight the outbreak while it can still be restrained. On top of that, the system shall be used to estimate the risk of a fire to meet precautions to prevent outbreaks in the first place. If an outbreak occurs regardless, it shall keep sending data until it gets destroyed by the fire to assist the firefighters. Since most threatened areas are inaccessible to humans, the sensor network is to be deployed by an aerial, unmanned system. Special emphasis is put on minimising the impact on the fragile ecosystems to be monitored, by making large parts of the system biodegradable and emission-free.”[4]

In the baseline report, the requirements for this system were defined and a list of design options was developed. An initial design was then developed in the midterm report along with trade-offs and concept ideation. This report presents a continuation of this design journey, leading to the design of EcoSense EMBER and its operations. The report was divided in three parts.

In Part I, the general overview of EcoSense EMBER is presented. Chapter 2 marks the beginning of the project through the assessment of the mission at hand. Then, an overview of the mission and of the product journey is developed in Chapter 3. Finally, an overview of the final design of the EcoSense EMBER product is presented in Chapter 4.

After having presented EcoSense EMBER and the mission it aims to fulfil, one can dive deeper into the detailed designs of its subsystems, this is done in Part II. Firstly, the detailed airship design is developed through the structures, propulsion, solar & electronics, aerodynamics, buoyancy and payload deployment mechanism subsystems in Chapter 5, Chapter 6, Chapter 7, Chapter 8, Chapter 9 and Chapter 11 respectively, followed by the flight dynamics and control surfaces of the deployment vehicle are developed in Chapter 10. The detailed design part of this report finishes off with the detailed design of the sensor nodes in Chapter 12 coupled with a network reliability optimisation in Chapter 13 and a preliminary design of the network infrastructure and its relay nodes in Chapter 14.

With all the vehicle and sensor network subsystems covered, the report finishes off with mission management, impact and life-cycle of EcoSense EMBER in Part III. It starts with an overview of the production plan in Chapter 15. Then, logistics and operations of a typical mission are assessed in Chapter 16 and Chapter 17, respectively. A RAMS analysis is also performed in Chapter 18 to understand certain vital aspects of the system. Sustainability is also a crucial aspect of the product and is assessed in Chapter 19, through preliminary impact studies and preparations for an LCA. Given the product is meant to be sold and commercialised in the future, a market analysis is performed in Chapter 20 and the future steps to achieving that are presented in Chapter 21, concluding the report and this stage of the investigation and design of the EcoSense EMBER system.

2

Mission Assessment

Australia is a country that has to deal with a lot of bushfires. During the 2021-2022 summer, the New South Wales (NSW) government spent multiple million AU$ on fire protection [5]. The state of NSW has vast amounts of forests that are prone to bushfires such as dry eucalyptus forests north-west of the Sydney region. In this section the mission that EcoSense aims to perform will be assessed in both Section 2.1 and Section 2.2. Stakeholders play a crucial role to EcoSense too and will be identified in Section 2.4. From the assessment performed in this chapter, a list of mission requirements is presented in Section 2.5.

2.1. The EcoSense Project

EcoSense is a Design Synthesis Exercise (DSE) project initiated by Prof. C.A. Dransfeld and Dr. S. Hamaza focusing on the development of a sensor network and its deployment vehicle with the purpose of detecting early wildfires. It will focus its mission on the forests of Blue Mountain National Park, Wollemi National Park and Yengo National Park. These parks cover a total area of around $7708\,\mathrm{km}^2$, making them large and hard-to-reach. The mission of EcoSense is to reduce the impact of bushfires by creating a system that detects these fires at an ultra-early stage.

Mission Need Statement

Gathering spatially- and temporally-dense datasets in hard-to-reach environments for early fire detection.

A renaming of *EcoSense* to *EcoSense EMBER* was performed at the end of the design stage to differentiate between EcoSense, the company deploying sensors, and EMBER, specifically created to detect early fires. The purpose of this renaming is that although the current design was created to detect wildfires, the sensor network could be adapted to fulfil different missions, leading to the distinction. EcoSense EMBER is meant to be designed within 10 weeks by a team of 10 students from the TU Delft Aerospace Bachelor of Science.

2.2. Opportunity for EcoSense

Following an extensive market research performed by the EcoSense team during previous stages of the DSE [2], a set of strengths, weaknesses, opportunities and threats (SWOT) were derived and are presented in Figure 2.1.

In order to understand the current state of the fire detection market and where EcoSense EMBER could fit, an outlook summary of the current market state has been drawn up and is shown in Figure 2.2.

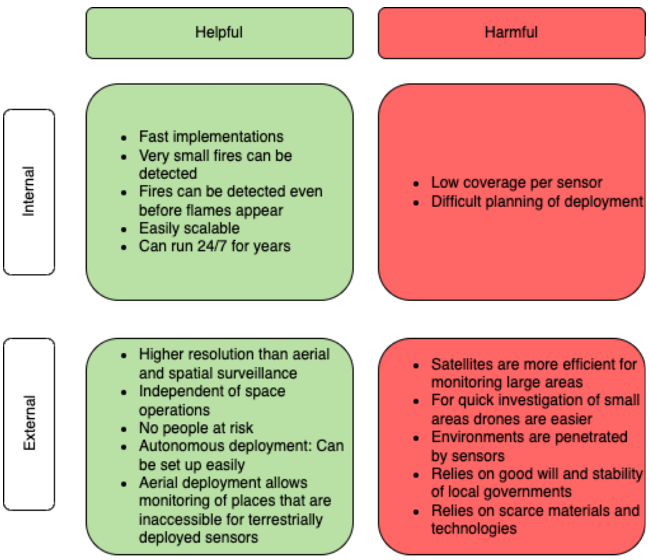

Figure 2.1: *Found Strengths, Weaknesses, Opportunities and Threats to the Proposed Project. [2]*

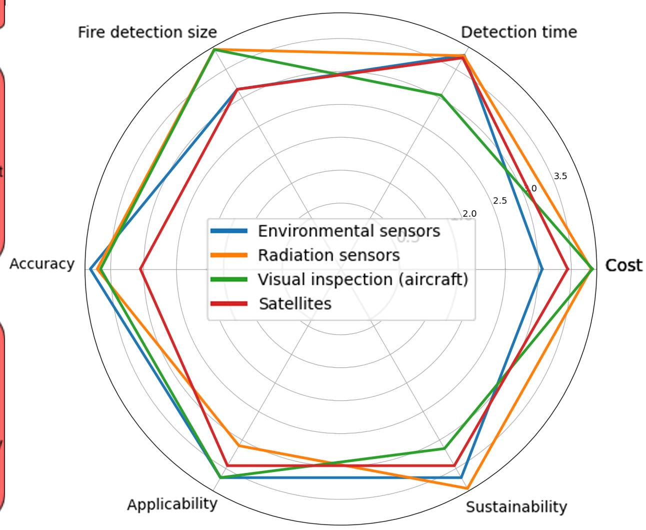

Figure 2.2: *Overview of Current Market Solutions [2].*

One can see from Figure 2.2 that all current fire detection solutions have one or two strong points but also a big weakness. For example, although visual inspection using aircraft is accurate and applicable to large areas and remote locations, sustainability (both ecologically and sociologically through the constant circular flying of detection pilots) and detection time play in its disfavour. On the other hand, current environmental sensors are great in almost all aspects except the applicability, as they currently need to be deployed by hand. This is where EcoSense EMBER can be extremely useful. Designing an early fire detection as applicable (in size and remote locations) as satellites or aircraft and as quick and precise and sustainable as current iterations of environmental sensors.

2.3. Terrain Assessment

As was mentioned in Section 2.1, the EcoSense EMBER mission is initially set to be launched in the North-Western rural areas of Sydney. This includes three National Parks: Wollemi, Yengo and Blue Mountains. It is easiest to understand the terrain and vegetation by looking at pictures. As can be seen in Figure 2.3 and Figure 2.4, important aspects to consider include dense forested areas, ravines, hills or deserted areas covered with rocks. On top of that, lakes, rivers and roads populate the national parks. These are locations where sensors should not be placed. These terrain specifications are very important for the flight planning and attachment mechanism of the sensor and relay nodes. As such, they constitute a large constraint source in Chapter 12, Chapter 14 and Section 17.1.

(a) *Wollemi National Park (Park Granton).*

(b) *Wollemi National Park (NSW National Parks and Wildlife Service).*

Figure 2.3: *Area selection.*

Vegetation is also an important aspect to consider as it directly impacts the fire propagation and sensor node attachment mechanism. According to observations made in the Blue Mountain National Park [6], seven main vegetation groups were identified. An example of a dry sclerophyll forest is also presented in Figure 2.4.

- Dry sclerophyll forests: 85%
- Wet sclerophyll forests: 6%+
- Heathlands: 2%
- Grassy woodlands: 2%+
- Rainforests: 1%+
- Freshwater wetlands: 0.5%
- Forested wetlands: 0.5%.

Figure 2.4: *Blue Mountains Park (Natalie Dang).*

As the names suggest, the area where the sensor network will be deployed are nature reserves containing rare and endangered animal species that should not be bothered. On top of that, it is known that a lot of birds have nests in the trees of the parks, leading to potential dangers regarding the vehicle. A list of obstacles that will need to be considered during the design stages is given below [4]:

- In-air collision between bird and aerial sensor carrier.
- Attachment mechanism of the sensor should not be harmful for the organisms that potential will have an interaction with them.
- Noise of the aerial vehicle that disturbs the fauna.
- Disturbance of birds during breeding season that takes place from late August until November [7].
- Bird attacks from aggressive birds [7].

2.4. Stakeholders

Stakeholders are individuals, groups or organisations having a say or a stake in the EcoSense EMBER project. These will eventually influence EcoSense EMBER and its requirements through specific needs and constraints. All identified stakeholders are described below:

- **State of New South Whales**: Bush and forest fires can cause great economical and sociological damage. Both of these aspects are mostly taken care of by the local government as they have to pay for physical damages and repairs.
- **NSW Rural Fire Service**: The NSW Rural Fire Service will be the prime user of the EcoSense data. They are the organisation responsible for extinguishing bushfires.
- **Employees of EcoSense**: The employees of EcoSense are a direct stakeholder since EcoSense influences their working environment,
- **Citizens of New South Wales**: The citizens of NSW will have less bushfire damage due to the service EcoSense is providing. The citizens pay tax that will potentially be used to facilitate the activities of EcoSense.

2.5. Mission Requirements

A summary of all mission requirements is given in Table 2.1:

Table 2.1: *Mission Requirements.*

Req. ID	Requirement	Section	Compl.
REQ-MIS-1	The EcoSense system shall provide smouldering fire detection capabilities	3.1	✓
REQ-MIS-2	Fire detection capabilities shall be provided by a sensor network	14	✓
REQ-MIS-3	The EcoSense system shall provide sensor deployment capabilities	4	✓
REQ-MIS-4	The EcoSense system shall have a ground shelf-life of a minimum of 10 years	12.3	≈
REQ-MIS-5	The EcoSense system shall reach the designated location by air	3.1	✓
REQ-MIS-6	The EcoSense system shall deploy sensors in a hard-to-reach natural environment	3.1	✓
REQ-MIS-7	The EcoSense system shall be able to deploy a single sensor network for a typical mission in a maximum of two working days	17	✓
REQ-MIS-8	The EcoSense system shall be able to operate autonomously	14	✓
REQ-MIS-9	The design shall be feasible with technology available today	4	✓
REQ-MIS-10	The design shall be finalised in 10 weeks	-	TBD
REQ-MIS-11	The EcoSense system shall be able to monitor environments up to 100 km away from the launch site	4	✓
REQ-MIS-12	The system shall be able to monitor an environment of $100\ \mathrm{km}^2$	4	✓
REQ-MIS-13	The EcoSense product storage mass shall not exceed $3400\ \mathrm{kg}$	17	✓
REQ-MIS-14	The EcoSense product shall have dimensions less than the launch area as described in REQ-VEH-2	4	✓
REQ-MIS-15	The heaviest EcoSense storage component shall not exceed $100\ \mathrm{kg}$	4	✓
REQ-MIS-16	The EcoSense product storage shall have dimensions that fit within a Ford Ranger with towing car : (1.8x1.5x1) car (4.8x2.1x2.2) towing car	17	✓
REQ-MIS-17	The EcoSense product shall have a detecting reliability of at least $62\ \%$	13	✓

All are verified with relative certainty except REQ-MIS-4. This heavily depends on the degradation of the sensor enclosures, which are biodegradable, and as such cannot fully be verified. More information on the shelf life of these enclosures can be found in Section 12.3.

3 Mission Overview

This chapter gives a general overview of the mission. In Section 3.1, an overview of the functional flow and phases of the mission is provided. Section 3.2 gives the functional breakdown of the system. Finally, in Section 3.3 an overview of the product journey of the EcoSense EMBER is given and the sustainable development strategy in Section 3.4.

3.1. Mission Phases and Functional Flow

The EcoSense EMBER mission can be separated into five distinct phases. This section aims to give an overview into these phases and the functions that the system fulfils.

The phases of the mission can be described by top-level functions, which are shown in Figure 3.1.

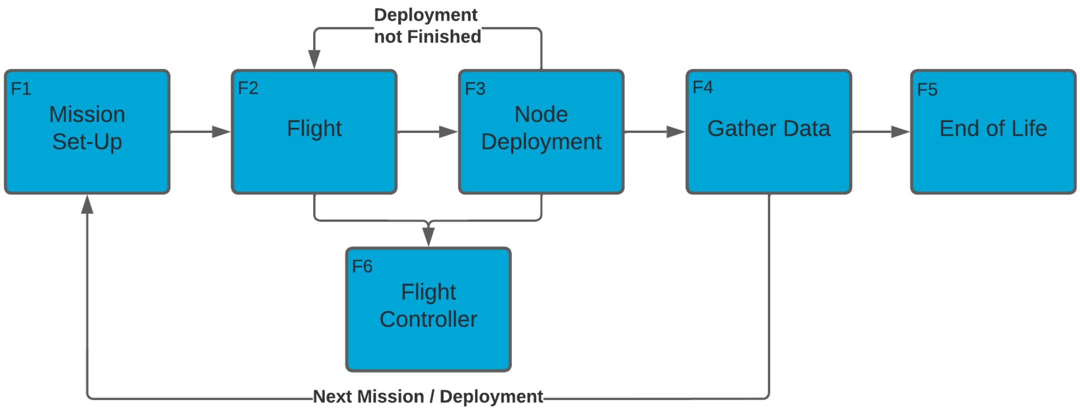

Figure 3.1: *Top-level functions describing the distinct phases of the EcoSense EMBER mission.*

A short summary of each phase is as follows:

F1 | Mission Set-Up Surveying the area, logistic and operations planning and execution, transporting to mission area.

F2 | Flight Vehicle launch operations, climb and cruise.

F3 | Node Deployment Sensor deployment, network set-up and return journey to ground station.

F4 | Gather Data Environmental monitoring, data communication and handling.

F5 | End of Life System dismantling, decomposition and mission conclusion.

F6 is not given as it describes the functioning of the flight controller, and is not inherently a phase of the mission. In Figures B.1-B.3, the phases are split up into lower-level functions, offering a more in-depth overview of each stage of the missions. These stages work to fulfil the main goal of the mission, which is to set up a sensor network to detect forest fires in their earliest stages. This is achieved through the use of a vehicle that emits no harmful emissions during operation to minimally impact the environment that is being monitored. Over the course of this report, the vehicle and sensor network systems will be described, following by an in-depth overview of the operations, logistics and other infrastructure that surrounds the design.

3.2. Functional Breakdown

A functional breakdown diagram organises the functions of the EcoSense EMBER system by similarity instead of ordering them based on the operational order of the system. The functional breakdown can be found in Figure C.1.

3.3. Product Journey

An overview of the product journey is shown in Figure 3.2. This product journey uses the order of operations from the functional flow diagram (Figures B.1-B.3) and the personas that are defined in Chapter 17 to portray the life-cycle and journey that EcoSense EMBER experiences, as well as how its users interact with it. The product journey gives a clear picture of the process that occurs every time a mission is initiated. Many of the phases and steps that are shown in this diagram are explained in more detail in Chapter 17, describing the operations that are required for this mission.

3.4. Sustainable Development Strategy

A sustainable development strategy has been developed [4] and is presented here in full: ”Sustainability is a core value for the EcoSense team. It is striven for in the organisation of the team, as well as in the design itself. The goal for the system being developed is also to have a positive impact on sustainability worldwide. Sustainability has three main aspects - social, economic and environmental sustainability. Each of these shall be discussed separately below in Subsections 3.4.1, 3.4.2 and 3.4.3, respectively. Finally, the tools used for environmental assessment will be discussed in Subsection 3.4.4”[4]

3.4.1. Social Sustainability

”Tackling social sustainability from the organisational point of view, the team is trying to work sustainably by maintaining a work-life balance, taking periodic short breaks as well as lunch breaks. A human resource management structure has also been established to mediate disputes and organise team building events to promote the cohesion of the team.

In designing the EcoSense system, social sustainability will be considered when sourcing components and developing an estimate of the supply chain. The worker quality of life within the supplier companies will be considered and the equality and democracy of the components' countries of origin will be taken into account as well to reflect the United Nations (UN) sustainable development goal 8 by providing decent work for the people involved in our supply chain.

The societal impact that EcoSense aims to achieve is to reduce the societal damage of forest fires. Wildfires have wide-ranging societal impacts ranging from displacement due to property and infrastructure destruction, through evacuation to post-fire mental problems and trauma. As an example, the rate of probable PTSD has been measured in between 24% and 60% of adults three months post fire exposure [8] and forest fires have resulted in the displacement of tens of thousands of people in California between 2017 and 2018 alone [9]. By fighting forest fires, EcoSense also hopes to indirectly combat these societal issues, therefore helping the path towards UN sustainability goals 3 and 11 by aiding disaster prevention and the prevention of mental and physical health issues.”[4]

3.4.2. Economic Sustainability

”The economic sustainability is also considered in the impacts and the design. From the organisational point of view, the team has put rules in place as well as thorough organisational efforts to eliminate time waste. Additionally, lean methods such as the 5S method are being implemented in the team organisation throughout the project.

In the design phase, the economic sustainability is considered by estimating the price of the system and attempting to keep it competitive with other fire prevention systems, keeping in mind the performance benefits of our system and the value of the economic benefits that come with them, such as saving areas of the forest by detecting fires earlier. At this stage of development, a market analysis as well as a cost budget has been performed in the baseline report [2], which helped set metrics and their relevant goals and requirements for tracking and evaluating the economic viability and sustainability of the project as development goes on.

After deployment, EcoSense shall contribute to the economic sustainability worldwide. The cost of a hectare of forest burning is estimated between EUR 3 200 and EUR 16 300 [10] and it is estimated that detecting the fire within the first 30 minutes can decrease these costs by 20% [3]. The wildfire suppression costs in the USA have grown to a 5 year average of USD 2.4 billion [11] and it is expected the fire fighting costs shall also be decreased by EcoSense, allowing for earlier fire detection. The economic viability is further discussed in the market analysis of the baseline report [2]. Furthermore, the prevention of health damage from particulate matter originating from forest fires is another example of EcoSense's contribution to economic sustainability. The healthcare costs associated with the fires over a four-year period between 2008 and 2012 were a total of USD 513 billion, or an average of USD 128 billion per year of fires in the USA alone [12]. Once again, this goal reflects the UN sustainability goal 8, by contributing to worldwide economic sustainability.”[4]

3.4.3. Environmental Sustainability

”Finally, in the environmental sustainability department, the team is keeping the work environment as environmentally friendly as possible by limiting our energy use and the use of single use plastics and packaging. The team also commutes by bicycle or public transport to reduce its environmental footprint.

In designing the EcoSense system, a lot of emphasis will be put on environmental sustainability. To help assess this, multiple tools will be employed to evaluate and improve the environmental sustainability of the product. These tools range from team guidelines to an LCA study and are further described in Subsection 3.4.4. Furthermore, requirements have been established based on regulations, the mission and customer needs which also guide the design towards environmental sustainability. Using these tools and striving for sustainability keeps the project in line with the UN sustainability goal 9 for sustainable industrialisation.

The environmental impact of the EcoSense system will once again be mainly the reduction of the environmental impacts caused by forest fires. First, when forest fires occur naturally, although greenhouse gasses are released, these are usually absorbed again by the new growth in the area eventually, resulting in net neutral impact. However, with the increasing scale and frequency of forest fires, the new growth in the areas may not grow to the same volume before burning again or may restore to a different vegetation structure [13]. Besides, in the short term, the emissions from forest fires have an impact as well. Globally, about two Gigatons of carbon emissions are produced by forest fires yearly [14]. Meanwhile, the environmental impact of the operation, production and development of EcoSense will be minimised using the methods outlined above and should be negligible in comparison to the negative impact of forest fires. Moreover, the team hopes that by implementing a highly biodegradable design, EcoSense will also serve to promote the use of such materials and design principles in other projects. The impacts that the team aims to achieve reflect UN sustainable development goals 13 and 15 by protecting natural land environments and preventing the release of carbon emissions."[4]

3.4.4. Environmental Assessment Tools

"Several layers of tools are employed in the design process to ensure the utmost sustainability of the design, as one of the main concerns of the team. These tools serve to evaluate and improve the design with respect to environmental sustainability.

The most high-level tool is the general mindset of the team. Everyone in the team has to be and is aware that environmental sustainability is a high priority in the design. This leads everyone to strive for sustainability and keep it in mind while coming up with solutions to various problems.

The next level is an educated, purely qualitative analysis. This was employed for example in the vehicle concept trade-off where it was thought prohibitively time consuming to go into more quantitative detail. Still, some sort of environmental assessment of the various concepts was deemed necessary given the great impact on the sustainability that this design stage has."[4]

Going further, a semi-quantitative assessment is used in the detailed design to compare for example material and processing options for a given subsystem. For example, a modified version of the methodology established by Doudrich et al. for Bombardier [15] will be used, with a series of yes or no questions and weighted categories. Alternatively, other methods, such as estimating the CO_2 equivalent of the materials used have been used as a first estimate of environmental sustainability of a component, when this is more practical.

Finally, the deepest planned level of environmental assessment will be provided in a set of LCA studies. The final versions of these will be performed when all of the parameters and components of the design are known. However, preliminary overarching impact assessments of the airship, sensors and mission in total have already been performed and can be seen in Chapter 19. Also covered in Chapter 19 are preparations for the aforementioned LCA studies, including the goals, scope, assumptions, breakdown of flows and procedures per component and system and more. These measures allow the team to evaluate the impact of the mission and identify key areas for improvement, such that development resources can be most efficiently allocated, and recommendations can be made for further research and development.

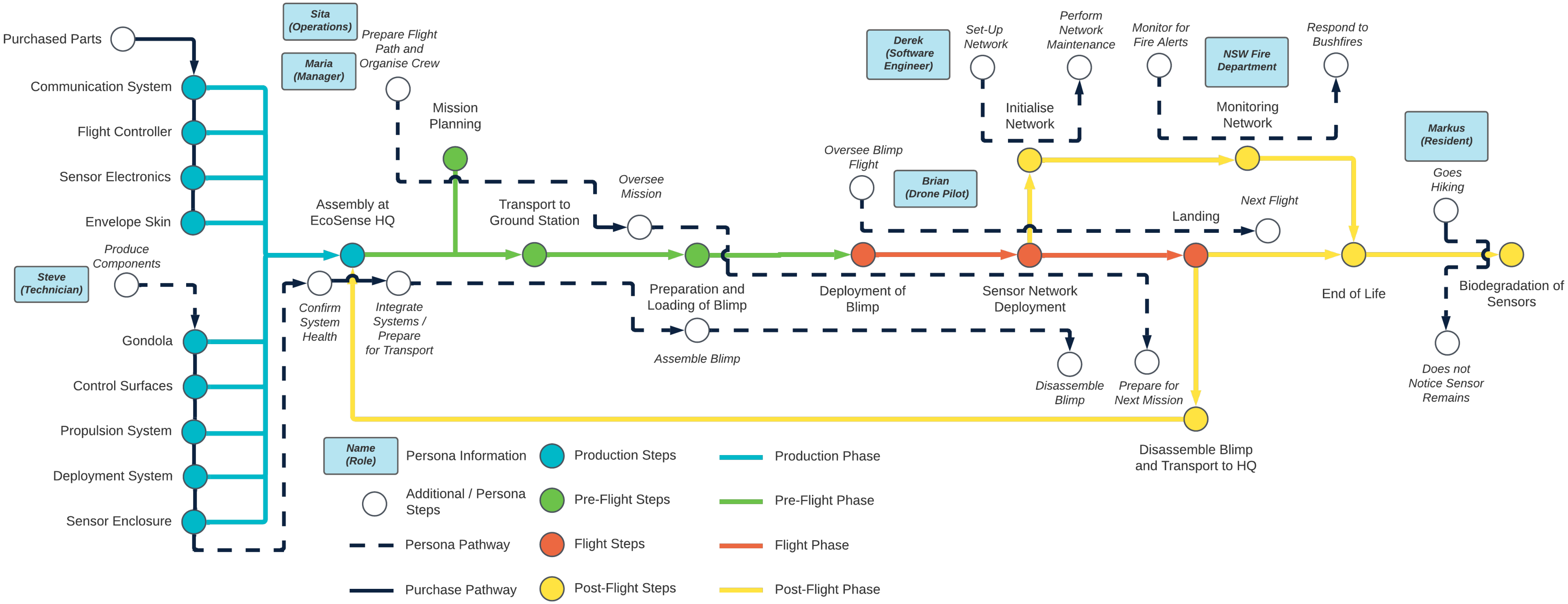

Figure 3.2: *Product journey of EcoSense EMBER.*

4

Design Overview

This chapter provides an overview of the final system design of the EcoSense mission. The overview is provided from the detailed design phase, elaborated upon in Part II. Section 4.1 introduces the repository containing the calculation model. Section 4.2 then provides an overview of the final vehicle and sensor design. Lastly, Section 4.3 goes over the technical performance properties. Section 4.4 provides the power, mass, and cost budgets.

4.1. GitHub Repository

The most important design tool used to obtain the design parameters is a class-based Python script in which the different subsystems can be represented as class instances and assembled to a complete system. This offers high flexibility, since parameters can be changed easily. Even whole subsystem concepts can be swapped to see the consequences on the total system, taking into account the snowball effect. All the code can be found in a central GitHub repository, accessible under the name *"DSE_ecosense"*. The in-house developed tools used to assess operations and sensor network reliability can also be found in this GitHub repository.

4.2. Final Design

The final design of the mission is the EcoSense EMBER (Environmental Monitoring of Bushfires for Early Response), a non-rigid solar-powered airship i.e. a blimp. The main parts of the product can be separated into the envelope, the gondola or undercarriage and the sensors.

Vehicle Performance		
Sensor Capacity	552	
Design Speed	50 km/h	with respect to ground
Range	350 km	at design speed
	100 km	solar panel failure
Endurance	7 h	at design speed
Minimum Turn Radius	24 m	at design speed
Maximum Climb Agle	13.3 deg	at design speed
Lifting Envelope		
Envelope Length	13.58 m	
Envelope Radius	2.26 m	
Envelope Volume	146 m3	
Nominal Envelope Pressure	500 Pa	
Hydrogen Capacity	12.2 kg	at 20 C + nominal pressure
Gondola		
Gondola Length	4.49 m	
Gondola Width	1.15 m	
Gondola Height	0.33 m	(storage height)

Solar Panels	
Cell Type	Maxeon Gen III
Number of Cells	1863
Covering Angle	86.00 deg
Length	10.86 m
Area	35 m2
Buffer Battery Capacity	165 Wh
Nominal Bus Voltage	24 V

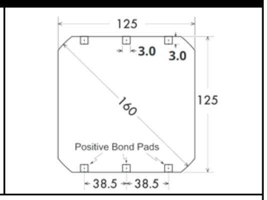

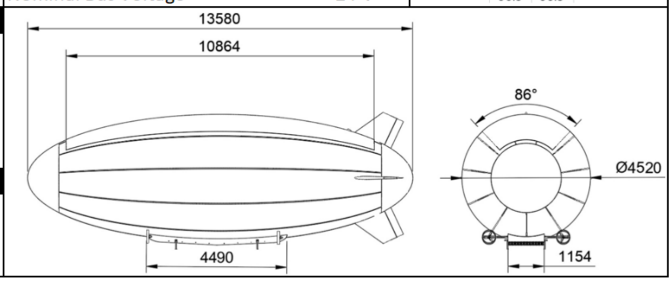

Figure 4.1: *Datasheet of the EMBER vehicle.*

The envelope is the largest part of the vehicle, as it needs to store the required hydrogen to provide sufficient lift to the entire vehicle. The envelope is made of Uretek3216LV, which provides structural strength and a leak tight membrane for the hydrogen, and an aluminium coating, which alleviates static charge and takes care of the thermals due to its high reflectivity. Two more distinct features of the envelope are the solar panels and the control surfaces. The solar panels cover an area of $35.62\ \mathrm{m}^2$ over an angle of $86°$, which is sufficient to provide ample energy to the system in the worst case sun incidence. The control surface subsystem features four fins with actuated control surfaces, capable of providing pitch, roll, and yaw control. The control structure is made of the inflated fins and rigid control surfaces.

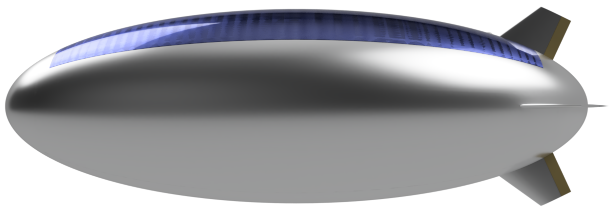

Figure 4.2: *Render of the EMBER envelope.*

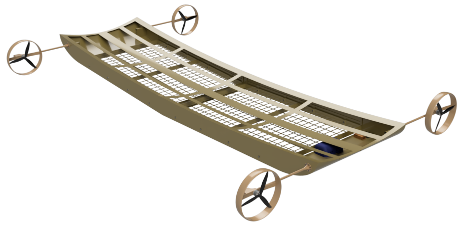

Figure 4.3: *Render of the EcoSense EMBER gondola.*

Furthermore, the second important component, the gondola, is located on the bottom of the envelope. This structure houses a majority of the electronics, the propulsion system and the deployment mechanism. The structure is made of a flax composite from Bcomp. The electronics along with the battery pack are housed in the front compartment of the structure. The propulsion system consists of 4 vectoring electromotors. Combined these motors provide $91.5\ \mathrm{N}$ of thrust with a $41\ \mathrm{cm}$ propeller, consuming nearly $2.2\ \mathrm{kW}$ of power. Each of the engines can independently vector thanks to the servo vectoring system present at each motor. The thrust vectoring enables vertical take-off and landing of the vehicle. The final part of the undercarriage is the sensor deployment system, split over two detachable trays. The system is capable of carrying up to 552 sensors and relays, and deploying each separately at predetermined locations. The deployment is done through permanent electromagnets, which remain magnetised until an electric current is applied to it, causing the node to drop.

Lastly, the sensor and relay nodes will be described. The sensor nodes are responsible for gathering data and detecting fires, while the relay nodes receive that data and enable communication with the ground station. Both systems feature an equal footprint of $65\ \mathrm{mm}$ x $85\ \mathrm{mm}$, with a thickness of $17.5\ \mathrm{mm}$ for the sensor node and $35\ \mathrm{mm}$ for the relay node respectively. The sensor nodes are designed to hang below the canopy, with the help of tangled strings, while the relay node shall sit higher up in the canopy to allow for undisturbed long-range communication.

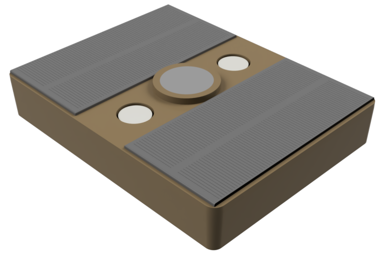

Figure 4.4: *Render of the EMBER sensor node.*

4.3. Technical Performance

This section elaborates on the performance of the vehicle and the sensor network. Firstly, the vehicle performance will be presented, followed by the network.

Vehicle performance can be evaluated based on its carrying performance and its cruise characteristics. The vehicle was designed to carry a sufficient number of sensors to deploy at the designated area which can be up to $100\ \mathrm{km}$ away. This set the vehicle's payload capacity to $45\ \mathrm{kg}$. As the blimp is neutrally buoyant, its endurance is theoretically infinite. However, as it is mainly powered by solar energy, its endurance was limited to 7 hours, to ensure sufficient solar irradiance, from 9:00 to 16:00. In this time the vehicle can travel up to $386.6\ \mathrm{km}$, travelling at a cruise speed of $50\ \mathrm{km/h}$. In case the vehicle needs to travel on battery, it can travel a range of up to $100\ \mathrm{km}$ at a speed of $13.84\ \mathrm{km/h}$ to ensure maximum range.

Performance of the sensor network should be evaluated using their reliability for multiple types of fire detection. For its design, two were considered: time-based and size-based detection. For the former, the sensor network has been designed such that $62\ \%$ of smouldering fires would be detected within the first $10\ \mathrm{min}$ after ignition. Of course this reliability is mediocre at best and was thus couples with a size-based detection reliability. For this one, the sensor network is rated to detect $90\ \%$ of the fires larger than $0.2\ \mathrm{km}^2$. This last reliability is largely underestimated, and it is believed that the sensor network reliability for fire of such size could reach close to $100\ \%$. This would need to be verified by means of experiments in the future.

4.4. Budget Breakdown

This section will present an overview of the budgets for the power, mass, and cost of the EMBER system. Each budget is separated into the vehicle and sensor budget.

Firstly, the vehicle power budget will be presented. The table below presents the budget, from which is can be seen that a vast majority of the power produced is designated to propulsion. As the mission spans over 7 hours, weather may change and solar powers will not be able to provide sufficient power. In that case the auxiliary battery on board can provide power, which is sized for the vehicle to be able to travel $100\ \mathrm{km}$, allowing it to safely return to base in case the power generation system fails.

Furthermore, the sensor and relay node power budgets are presented in Table 4.2 and /Table 4.3. The power is mainly provided by the solar panels, but as the system needs to operate 24/7, the onboard battery provides power during nighttime, when solar panels do not generate power. One can observe that the power consumption's main contributor, in both systems, is the communications subsystem.

Table 4.1: *Power budget breakdown of the EMBER vehicle.*

Component	Constant Power (Momentary Power) [W]
Propulsion	2000 (240)
Flight Control	25 (316)
Communications	44 (-)
Sensor Deployment	- (1)
Total (Max)	2069 (2626)

Table 4.2: *Power budget breakdown of the EMBER sensor node.*

Component	Transmitting Power[mW]	Idle Power [mW]
Computing Unit + Sensor	15	15
Communications Module	396.0	0.019
Accelerometer	0.063	0.063
Total + 5%	**431.6**	**15.84**

Table 4.3: *Power budget breakdown of the EMBER relay node.*

Component	Transmitting Power[mW]	Receiving Power [mW]
Computing Unit	45.6	45.6
Communications Module	396.0	39.6
Total + 10%	**485.8**	**93.72**

The mass budget provides the breakdown of the masses of different components. In the tables below the breakdown of the masses of the vehicle, sensor and relay components can be found. A more detailed version of the vehicle mass breakdown can be found in Appendix E.

Table 4.4: *Mass budget breakdown of the EMBER vehicle.*

Component	Mass [kg]
Propulsion	5
Gondola Structure	21.7
Empennage	6.9
Electronics	1.8
Solar Array	1.3
Envelope	30.3
Deployment System	10.7
Buoyancy Control	6.8
Battery	5.0
Fire Suppression	6
OEM	95.5
Payload	45.00
MTOM	140.5

Table 4.5: *Mass budget breakdown of the EMBER sensor node.*

Component	Mass [g]
Computing Unit + Sensor	0.100
Communications Module	5.000
Accelerometer	0.01
Battery	2.700
Solar Array	17.00
Spring	2.000
String Anchors	0.660
String	2.000
Steel Plate	2.700
Enclosure	43.50
Total + 5%	79.46

Table 4.6: *Mass budget breakdown of the EMBER relay node.*

Component	Mass [g]
Computing Unit	5.00
Communications Module	5.00
Battery	17.0
Solar Array	17.00
Spring	4.00
String Anchors	1.32
String	5.00
Steel Plate	2.700
Enclosure	87.0
Total + 10%	156

Lastly, the cost budget is presented. The tables present the cost per unit. These costs are an estimate for the cost of a single unit, rather than bulk production and can therefore be assumed as the absolute maximum cost per unit.

Table 4.7: *Cost budget breakdown of the EMBER vehicle.*

Component	Cost [€]
Engines + Mount	600
Gondola Structure	5,000
Fins	700
Electronics	7,500
Solar Array	6,000
Envelope	5,000
Lift Gas	100
Deployment System	7,000
Ballonets	500
Battery	800
Total	**33,200**

Table 4.8: *Cost budget breakdown of the EMBER sensor node.*

Component	Cost [€]
Computing Unit + Sensor	22.6
Communications Module	8.00
Accelerometer	3.00
Battery	1.85
Solar Array	1.85
Spring	2.00
String Anchors	0.03
String	2.00
Steel Plate	0.05
Enclosure	1.96
Total + 5%	45.5

Table 4.9: *Cost budget breakdown of the EMBER relay node.*

Component	Cost [€]
Computing Unit	3.71
Communications Module	8.00
Battery	4.10
Solar Array	17.00
Spring	2.00
String Anchors	1.35
String	4.00
Steel Plate	0.10
Enclosure	3.92
Total + 10%	32.0

The top-level requirements and their respective compliance check section can be found in Table 4.10.

Table 4.10: *Vehicle Requirements.*

Req. ID	Requirement	Section	Compl.
REQ-VEH-1	The vehicle shall not exceed $150\,\mathrm{kg}$	4.4	✓
REQ-VEH-2	The vehicle shall have a maximum launch footprint of $80\,\mathrm{m}$ x $200\,\mathrm{m}$	4.2	✓
REQ-VEH-3	The vehicle shall carry at least 100 sensors	4.2	✓
REQ-VEH-4	The vehicle shall be able to operate full time for 10 years	-	TBD
REQ-VEH-5	The potential energy of the hydrogen stored in the vehicle's balloon shall not exceed that of the fuel carried by a Cessna 172	18.4	✓
REQ-VEH-6	The vehicle shall contain a fire suppression system	18.4	✓
REQ-VEH-7	The vehicle shall be able to detect a hydrogen leak in its balloon.	7.4	✓

5

Vehicle Structural Design

An important aspect of the overall vehicle design is its structural build-up. Structure performance is detrimental in attaining mission success. The design process considers many aspects, and it can be difficult to take all of them into account. A proper plan is thus a good starting point and is explained in Section 5.1. Each type of vehicle has its own set of functions which require specific structures. In an airship three major structures are present, namely the envelope, the gondola and the connection between gondola and envelope. These major structures are all discussed in Section 5.2, Section 5.5 and Subsection 5.5.1, respectively.

5.1. Design Approach

A useful guideline in structural design are the requirements. These reflect the important functions a system has to encompass. Next to the functions a system needs to accomplish, the performance with respect to a certain function needs to be defined. In terms of structures, performance is determined by loading. Based on requirements and performance, the material and geometry are selected.

Table 5.1: *Propulsion design requirements.*

Req. ID	Requirement	Section	Compl.
REQ-VEH-STR-1	The structure shall be able to withstand loads experienced in any possible operation defined in the operational envelope	5.2.2	✓
REQ-VEH-STR-7	The structure shall withstand at least 40000 loading cycles before failing	5.4	≈
REQ-VEH-STR-8	The primary structural elements shall have no detrimental deformation under limit loads	5.2.2	✓
REQ-VEH-STR-9	The primary structural elements shall have no rupture under ultimate loads	5.2.2	✓
REQ-VEH-STR-13	The structure shall abide by the safety factors listed in "CS 31GB.25 Factors of safety"	5.2.2	✓
REQ-VEH-STR-15	The structure shall provide mounting to all the required systems in the vehicle	5.5	✓
REQ-VEH-STR-17	Joint peak stresses shall not exceed the material yield stress	5.2.2	✓

The design approach of the envelope is altered slightly because of its complexity in the internal loading. Having no resources for experimental testing and the structure, an overall sheet of which mechanical properties are known, is selected. Only recommendations are given about possible improvements on the material concerning sustainability and cost reduction. In order to close the envelope, a suitable joining methods must be selected. Finally, possible test needed to be performed to assess the mechanical performance are listed.

5.2. Structural Design of the Envelope

In this section the envelope is designed. First, its required functions are listed in Subsection 5.2.1. Next, the internal loading of the structure is determined in Subsection 5.2.2. Then, the general build-up of the envelope is considered in Subsection 5.2.3. With all the information gathered thus far, the material is selected in Subsection 5.2.4. The mechanical performance of the fabric is considered in Subsection 5.2.5. In order to assemble the envelope, the joining methods need to be selected, see Subsection 5.2.6. Furthermore, the risks related to the envelope are assessed and mitigated in Section 5.3. Possible improvements concerning a more sustainable envelope are mentioned in Subsection 5.3.1. Finally, verification and validation is done on the improved sheet with the tests listed in Section 5.4.

5.2.1. Functions of Envelope Sheet

The envelope of the blimp requires numerous properties to fulfil its function. The following properties need to be present in the structure [16]. These properties are explained in more detail below the list.

- High strength
- High strength-to-weight ratio
- Resistance to environmental degradation (temperature, humidity, ultraviolet)
- Low permeability to minimise lifting gas loss
- Joining techniques allowing strong and reliable joints
- Low creep ensuring that the envelope shape is maintained during its operational life
- Fracture toughness

Carrying a large amount of volume of lifting gas implies a large structure and thereby large stresses. As a result the sheet will need to be of high strength and at the same time of low weight. Extra weight amounts to extra required lifting gas and thus extra weight for the envelope, creating a snowball effect. In addition to having high specific strength, the material must also be flexible such that it can be transported compactly.

The blimp operates in an environment that deteriorates the sheet drastically if materials are not selected carefully. UV radiation exposure causes rapid deterioration of polymeric materials with resulting loss of mechanical performance. Similarly, elevated temperature and humidity levels cause accelerated loss of mechanical properties.

The envelope of blimp experiences high stress for a long duration which leads to creep. This phenomenon leads to unwanted plastic deformation even when the stress is lower than yield. Over the envelope's operational life, the shape of the envelope will change which is undesired. Therefore, a material with high creep resistant is needed for the application. Next to being creep resistant, the sheet needs to resist crack propagation. If the envelope were to have a small hole the sheet can not shear open completely immediately.

A blimp flies in the air because of the lift generated by the contained low-density gas. The endurance of the vehicle depends on the rate of lifting gas dissipation. It is desirable to fly for prolonged periods of time and thus a low permeable envelope is essential in proper functioning of the airship.

The sheet width is limited by the machines needing during manufacturing. Therefore, to make one enclosed envelope, the sheets must connect to each other. On top of that, external parts need to be attached to the envelope as well as a connection to the gondola.

5.2.2. Envelope Stress

The biggest part of the structure of the blimp is the envelope which holds the lifting gas. To size and select the material for this envelope, first, the loads inside it must be estimated. This is done according to the initial stress analysis method described in the book Fundamentals of Aircraft and Airship Design Volume 2 [17]. The method uses the pressure inside the envelope as well as the force exerted by the lifting gas on the envelope. It is said that this initial estimate often falls within $10\,\%$ to $20\,\%$ of a highly detailed stress analysis [17]. To determine the load due to the pressure in the envelope, the pressure itself needs to be determined first.

The pressure inside the envelope, also called super pressure, is driven by the stagnation pressure at the nose of the blimp at maximum travelling velocity [17]. The super pressure must be higher than this in order for the nose not to deform when travelling at this speed. The pressure coefficient at the nose of an elliptical body similar to the airship shape proposed by the EcoSense team was found to be 0.827 in the study by Uslu and Bal [18] as can be seen in Figure 5.1.

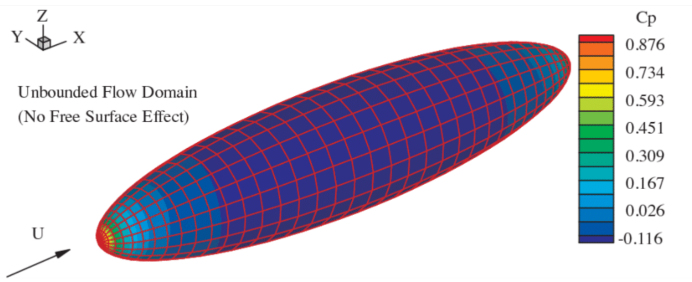

Figure 5.1: *Ellipsoid body pressure coefficient distribution. [18]*

Furthermore, the cruise velocity, which is also the maximum expected velocity of the blimp, was set to be $15.3\,\mathrm{m/s}$ as will be discussed later in the report. Using the pressure coefficient and the velocity, along with the standard sea-level air density into the pressure calculation in Equation 5.1 yields a stagnation pressure of $129.04\,\mathrm{Pa}$ at the nose of the airship. According to the method described in the book which is being followed [17], the super pressure shall be multiplied by 1.2 in early design. However, to account for the fact that the shape described in the CFD study [18] used is not exactly the same as the shape proposed by the EcoSense team, as well as to account for gust loads, a higher multiplication factor shall be used. Furthermore, researching the usual pressures in blimps it was decided that the envelope shall be designed for $500\,\mathrm{Pa}$ of pressure [19] above atmospheric pressure. This is much higher than the calculated required pressure, however it is a low pressure gradient, so it should not increase the weight of the structure significantly, and it will provide ample room for movement in further design e.g. to change the cruise speed. Additionally, using a such a value which is closer to the "industry standard" gives the team further confidence that no unwanted deformations will occur in the operation of the airship.

$$p_{\text{stagnation}} = \frac{1}{2}\rho_{\text{atm}} v_{\text{cruise}}^2 C_p \tag{5.1}$$

With the envelope super pressure determined, the stress due to this pressure can be determined. The hoop stress formula seen in Equation 5.2 can be used for this purpose [17], where r_{max} is the maximum radius of the envelope, p_{sp} the super pressure, and t the thickness of the material. When using this formula with membrane fabrics though, the load per unit length is a more useful unit than stress and so the thickness can be eliminated from the equation, leaving Equation 5.3 in place [17]. Using this equation and with $p_{\text{sp}} = 500\,\mathrm{Pa}$ and r_{max} $2.04\,\mathrm{m}$, the load due to the super pressure can be calculated to be $1020\,\mathrm{N/m}$.

$$\sigma_{\text{hoop}} = (p_{\text{sp}} \cdot r_{\text{max}})/t \quad (5.2)$$

$$\Delta p = (\rho_{\text{atm}} - \rho_{\text{lifting gas}})gh \quad (5.4)$$

$$F_{\text{sp}} = p_{\text{sp}} \cdot r_{\text{max}} \quad (5.3)$$

$$F_{max} = (p_{\text{sp}} + \Delta p) \cdot r_{\text{max}} \cdot SF \quad (5.5)$$

The other load to be considered is the load due to the buoyant force created by the lifting gas in the envelope. This load can be estimated by considering the pressure of the column of gas with the height equal to the maximum height of the envelope, equal to two r_{max}, pushing on the top of the envelope [17]. Therefore, Equation 5.4 [17] can be used, where ρ_{atm} and $\rho_{\text{lifting gas}}$ are the densities of the atmosphere and lifting gas respectively, Δp is the resultant pressure acting on the envelope due to the buoyancy force, g is the gravitational acceleration and h the aforementioned maximum envelope height. The pressure Δp can then be added to the super pressure p_{sp} to be multiplied by r_{max} and a safety factor SF, yielding the maximum skin load F_{max} as seen in Equation 5.5. A factor of safety of 4 is used for manned airship envelopes [17] and shall be used here as well. Plugging all variables in the formula yields a maximum envelope load of $4451.35\ \text{N/m}$. This value can be used to now pick a suitable material for the blimp envelope, in combination with all the other requirements.

5.2.3. Configuration of the Envelope

One single material that meets all the criteria mentioned in Subsection 5.2.1 is not available, therefore envelopes are composed out of different layers. This is to split required functionalities overspecialised materials. In Figure 5.2, the layout can be seen. The outer layer consist of material that has good UV and weather resistance to limit the negative changes of the environment on mechanical properties of the inner layers. The middle layer is a fabric that provides the load-bearing capabilities of the composite. A woven fabric is used as it allows for high strength in two axes and some elongation to load all the yarns. The inner layer contains the lifting gas. Low gas permeability can be achieved by coating the fabric with a polymeric material or by laminating a thin polymeric film. The properties this material should be flexible in the temperatures experienced in operation and good bondability and sealability with the load-bearing layer. All materials used in each layer are listed in Table 5.2.

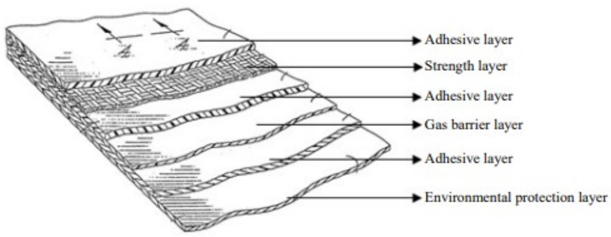

Figure 5.2: *Common build-up of envelope. [20]*

Table 5.2: *List of materials used in each layer.*

Outer Layer	Load Bearing Layer	Gas Barrier Material
Polyurethane (TPU)	Zylon	Neoprene
Polyvinyl chloride (PVC)	Kelvar	Polyurethane (TPU)
Teflon (PTFE)	PIPD	Vinyl chloride copolymers (PVDC)
Tedlar (PVF)	Dyneema	Mylar
Mylar	Spectra	Ethylene vinyl alcohol (EVOH)
Low-density polyethylene (LDPE)	Vectran	-
Vinyl chloride copolymers (PVDC)	Polyester	-

5.2.4. Material Selection

For the material of the envelope, Uretek3216LV is selected. The fabric is typically used in airship envelopes. It consists of 3 different layers: an outer layer made of Tedlar film, a centre layer of Vectra LCP fibres and an inner layer of ethylene vinyl alcohol. Each layer has its own particular function, which is possible due to the envelope being a laminate. The outer layer has good weatherability, which entails degradation of the envelope material caused by elevated temperature, humidity and UV. Additionally, the layer should have low creep and fracture toughness in order to maintain its shape over the operational life of the airship and prevent the lifting gas from leaking, respectively. Underneath a load bearing layer carries most of the loads. The material here should have high specific strength to limit the weight used. The inner layer has the function to seal the envelope. The outer and inner layer should be compatible to be joined together. Underneath, all specific components are investigated in further detail.

For the outer layer the most important properties are concerning weather-ability and fatigue. Weather-ability is the ability of the material to limit degradation of the inner layers of the envelope due to environmental factors. These environmental factors entail UV, humidity and temperature. For the outer layer a Tedlar film was selected. It is more performing than the other because of its excellent weather-ability, flex-fatigue resistance, see Figure 5.3. Additionally, it has low permeability which already helps contain the lifting gas. In the table it is noted that the adhesion of Tedlar film is poor. According to the manufacturer, Dupont, high quality bonds can be achieved [21].

Table 2: Properties comparison of different weathering materials

Materials	Permeability	Heat seal-ability	Weather-ability	Adhesion	Flex-fatigue resistance	Dimensional stability
Polyester	Low	No	Fair	Fair	Fair	Excellent
Polyurethane	Low	Yes	Good	Excellent	Good	Poor
Poly-vinyl chloride	Fair-low	Yes	Good	Excellent	Good	Poor
Poly-vinyl fluoride	Low	Yes (with adhesive)	Excellent	Poor	Excellent	Good
Nylon	Very low	Yes	Poor	Fair	Excellent	Excellent
Poly-tetrafluoroethylene	Fair	Yes (some grades only)	Excellent	Poor	Good	Good
Low density polyethylene	Fair	Yes	Good if pigmented	Poor	Excellent	Poor
Neoprene	Low	No	Good	Excellent	---	---

Figure 5.3: *Property comparison between weathering materials. [20]*

The load-bearing material must have high-strength-to-weight ratio and good fatigue. High strength-to-weight is required to limit the weight of the structure. Fatigue and creep resistance is also an important factor as the blimp needs to function for several years experiencing many load cycles. The strength properties are shown in Figure 5.4. Advantages and drawbacks on other material properties of the fibres are listed on Figure 5.5. In the fabric, Vectran was opted for as on all aspects it is the best suited. It is not the best performing in terms of specific strength, yet it has excellent tear and creep resistance.

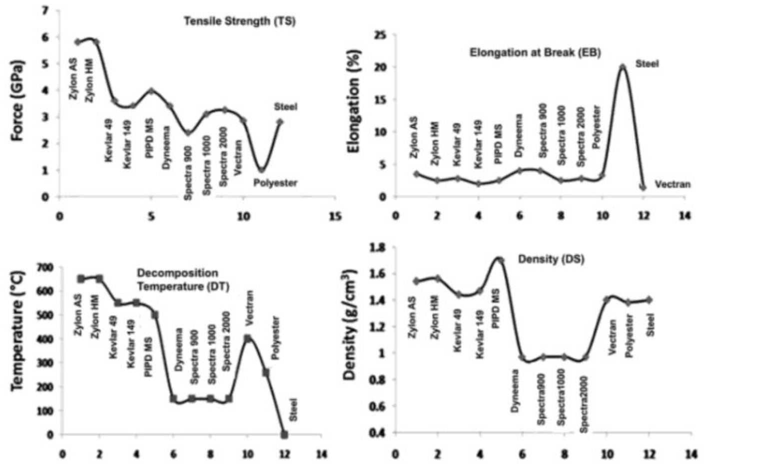

Figure 4.7 Properties of some high-performance fibres for the strength layer of the LTA envelope.

Figure 5.4: *Strength of load-bearing fibres. [20]*

Table 1: Comparison of high performance fibres

Materials	Strength (g/den)[10,19]	Advantages	Drawbacks
M5 (PIPD)	>40	Very high strength to weight ratio, good compressive properties, excellent environmental resistance	Expensive, not commercially available[10]
Zylon (PBO)	42	Excellent modulus, high specific strength[6,19]	Poor abrasion and flexing resistance, poor UV, visible light and moisture resistance, expensive[10,19]
Spectra (PE)	25-40	Light weight, high toughness[19], flexible and good weather-ability[10]	Poor creep resistance, highly hydrophobic reducing its bond-ability with resin and low melting point[19]
Thornel (Cabon)	30	High modulus, good temperature resistance, excellent weather-ability	Stiff and brittle
Vectran (LCP)	23	High strength to weight ratio, excellent tear resistance, excellent resistance to creep and fatigue[10,18]	Not as strong as Spectra or Zylon
E-glass	23	High modulus[19]	High stiffness, damages on folding[19]
Polyester HT	12	Good UV resistance[6]	Poor elastic recovery properties[6]
Kevlar (Aramid)	22	Good strength to weight ratio, high thermal resistance[6]	Susceptible to photo-degradation, poor flex and abrasion resistance, poor stress distribution which may lead to catastrophic failure[6,19]
Nylon	10	Excellent flex resistance, Good elastic recovery[6]	Low modulus, inferior hydrolytic degradation properties[6,19]

PIPD: Polyhydroquinone-diimidazopyridine, PBO: Polybenzoxazole, PE: Polyethylene, LCP: Liquid crystal polymer

Figure 5.5: *Properties load-bearing fibres. [20]*

For the inner layer it is important to have low permeability, as hydrogen is even a smaller molecule than helium. An ethylene vinyl alcohol co-polymer was selected as it has the lowest permeability, see Figure 5.6. Additionally, the material has low density and is heat sealable.

Polymeric Materials		Specific Gravity	Low Temperature Flexibility	Ozone Resistance	Heat Sealable	Permeability[5] (cm^3.mm)/(m^2.day.atm)		
						O_2	N_2	He
polyvinyl fluoride	PVF	1.4	poor	excellent	no	1.2	0.1	59
fluorinated ethylene-propylene copolymer	FEP	2.2	good	excellent	yes	40	125	
polyester	PET	1.4	poor	poor	no	2.4	0.39	67
ethylene vinyl alcohol copolymer	EVOH	1.1-1.2	poor	good	yes	0.02	0.003	9
polyester rubber		1.17-1.25	fair	fair	yes		147	1356
polyurethane rubber	PU	1.05-1.3	fair	good	yes	141-1067	35-297	687-2340
low density polyethylene	LDPE	0.91-0.94	good	good	yes	102-188		
ethylene-propylene rubbers	EPDM	0.96-1.05	good	good	no		553	1410
silicone rubber		1.1-1.16	excellent	excellent	no	19685	17280	19050

Figure 5.6: *Materials used for gas barrier. [22]*

All the layers are connected together via heat sealing at 230 by a thermoplastic adhesive polyurethane film. It was selected as it improves the permeable performance of the envelope material. An aluminium coating is applied on the outer surface of the envelope fabric. A similar coating has already been used in Detroit ZMC-2 airship.

Metallic coatings help to dissipate electrostatic charge such that the hydrogen does not spark when it is vented out of the airship envelope. A metallic coating also decreases heat take-up as it has a high reflectivity coefficient. Only a layer of $800\,\text{Å}$ to $1200\,\text{Å}$ is required to achieve these properties.

5.2.5. Mechanical Properties

The mechanical properties of the fabric are listed in Table 5.3. The envelope fabric weights $200\,\mathrm{g/m^2}$ with a thickness of $0.21\,\mathrm{mm}$. Additionally, a stress strain curve is added to understand the behaviour of the fabric under different applied loading. The curve is based on uni-axial strength test in both warp and weft.

Table 5.3: *Mechanical properties of Uretek3216LV.*

	Max tensile strength [kN/m]	Ultimate strain [%]	Elastic modulus [kN/m]
Warp	85.4	6.6	1,610
Weft	75.9	7.25	1,211

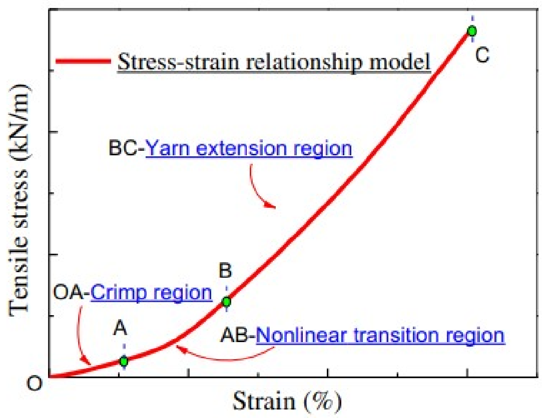

Figure 5.7: *Stress-strain model of a laminated fabric. [23]*

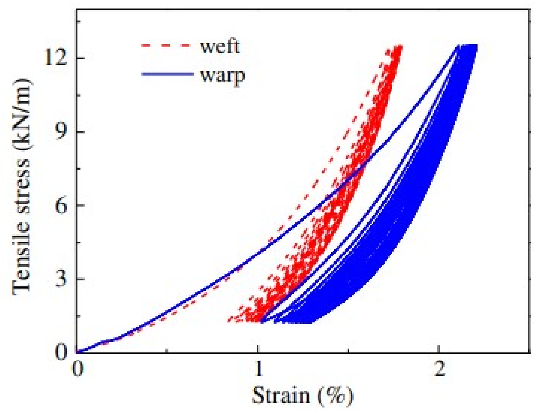

Figure 5.8: *Cyclic loading of Uretek3216LV. [23]*

In Figure 5.7, it can be seen that the laminate has three different regions, namely a crimp region a non-linear transition region and yarn extension region. In the crimp region large strain occurs under low applied loading. This is due to the weaving pattern having some stretch and the yarns straightening. The fabric behaves as a single entity, all layers extend together. If more loading is applied, the non-linear transition region occurs. Here the woven fabric starts bearing all the extra applied loading. After this region, yarn extension happens which at a certain point lead to failure. At the failure the yarns are sheared out of the fabric.

The flex-fatigue properties of the material can be found through cyclic loading tests, the results of which are shown in Figure 5.8. This is a useful property as with it, a prediction of the operational life can be made. Under a cyclic loading ranging from $1.27\,\mathrm{kN/m}$ to $12.7\,\mathrm{kNm}$. A load of $12.7\,\mathrm{kN/m}$ was opted for as it is about 1/6 of the ultimate tensile strength and comes to about $63.5\,\mathrm{MPa}$. This stress is higher than the ultimate hoop stress of $21\,\mathrm{MPa}$ calculated from the maximum stress in the envelope, see Subsection 5.2.2.

5.2.6. Joining Methods for the Envelope Sheets

The assembly of the envelope starts from laminated sheets bought from a supplier. The width of the sheets is limited by the machines used in the process to manufacture the envelope material. Therefore, to put together the whole structure, joining techniques are necessary. For safety reasons, it is desirable that the joint fails after the laminate. The strengths of the joint needs to be higher than the sheet strength to not allow the crack to propagate over the joint. Selecting the correct joining method depends on multiple factors: joint configuration, required strength, level of sealing, processing speed and cost. In literature generally three methods are considered, namely welding, bonding and mechanically stitching.

Welding is a joining method where parts are connected through applying heat and pressure. Welded joints are often butt joint making them smooth. A welded joint is airtight and watertight. Different types of welding exist and can be split in two categories based on how the heat is applied. Heat can be applied via external heat source, mechanical movement and electromagnetism. The options that seem suitable are hot bar welding, hot gas welding, vibration welding, radio frequency welding, laser welding, spin welding and friction stir welding.

Bonding adheres two sheets by a polymeric adhesive. Only a thermoplastic adhesive is suited to be used in an envelope as it is flexible. To join surfaces together the adhesive is heated before it is applied. Bonding does not require holes in the connecting surface area and thus stress concentrations are avoided. As a result the joint has a long lifetime. Additionally, the joint allows for different materials to be connected and is air-and liquid tight. For the adhesive to function properly it must be loaded in shear. Loading the joint by peel or tensile forces creates high stress concentrations and thus should be avoided. In order to attain a high quality bond, pre-treatment of the surfaces is required. Furthermore, the joint can not be disassembled. Possible thermoplastic adhesives include: polyamide, polyester, polyethylene, ethyl-vinyl-acetate, butyl-rubber or polyurethane.

Stitched laminates reduced the mechanical performance by $10\,\%$-$20\,\%$ [24], therefore it is not a desirable way to connect sheets with this method. Decreases in mechanical properties are related to stiffness, strength and fatigue. On top of that, stitching generates holes through the whole envelope increasing the permeability. Another joining method is thus required to seal the envelope.

To keep the assembly of the envelope simple, the sheets are joined by a lap-joint together with a polyurethane cross-linking adhesive. This adhesive was selected as it does not require heat treatment for the seal and allows for a flexible bond. When bonding composite parts together the lap-shear strength is $2.4\,\mathrm{MPa}$ [25]. The number of joints is determined by dividing the largest perimeter of the envelope by the width of the woven fabric, which is $1.2\,\mathrm{m}$. With this 11 sheets are required to cover the envelope's cross-section. The overlap of the joint is assumed to be $3\,\mathrm{cm}$ as it is easy to manually join the sheets. The average stress in the joint is $0.13\,\mathrm{MPa}$ at ultimate loading of $4451\,\mathrm{N}$ per meter of section.

5.2.7. Maintenance of Envelope

In order to guarantee safe operations of the airship, maintenance must be carried out on the envelope. Maintenance consist of two parts, namely inspection and reparation. In order to limit the cost of maintenance, no special equipment should be required to find flaws. As such, flaws having an impact on the performance or structural integrity should be easily seen by the naked eye. A damage tolerance approach is thus required, meaning operation is guaranteed between the cycles of inspection.

Inspection is carried out by qualified personnel every 12 hours of operation or after unsuspected events occurred during operation such as bird collision or lightning. Inspection concerns finding mechanical flaws in the envelope materials. Such flaws could be holes, cracks, bond line flaws. With use of a bright light flaws are more easily spotted. After 50 hours a grab test is performed on a sample of envelope fabric to test the strength. Testing can also be performed on permeability and inter-ply adhesion. Reparation of removed test-samples or weakened envelope material is done by covering the inside and outside of with a patch. These patches consist of the same material as the layer it is connected to.

5.3. Risk Analysis

The envelope is a critical component of the airship. It is thus important to identify the risk coupled to the envelope. To design an operational airship, possible risks should be reduced as much as possible.

Table 5.4: *Hazard severity and hazard probability.*

Category	Consequences	HS	Category	Occurrence frequency	HP
Minor	Slight increase in operative workload and slight reduction in safety margins.	1	Very unlikely	$>10^{-7}$	1
Moderate	Notable increase in operative workload and significant reduction in safety margins with risk of mission failure.	2	Unlikely	$\geq 10^{-7}$ $<10^{-5}$	4
Significant	Drastic increase in operative workload and great risk of fatal mission failure.	6	Likely	$\geq 10^{-5}$ $<10^{-3}$	6
Catastrophic	High chance of fatal mission failure causing a direct threat to the ecosystem health.	10	Very likely	$>10^{-3}$	10

Each risk is assessed with its respective Hazard Severity (HS) and Hazard Probability (HP), the two measure that make up the risk figure. Taking the product of these two values leads to the Hazard Risk Index (HDI), used to assess the total risk value [26]. Table 5.4 shows an overview of the possible values of both HS and HP while building the risk assessment table, one should note that only examples of values are given and any intermediary figure can also be chosen. The levels of risk are calculated according to levels shown in Figure 5.9. This method will be used in all risk assessments throughout the report for consistency's sake. Table 5.5 then shows the risks related to the envelope couples with one or multiple mitigation strategies.

Risk level	HRI	Colour code
Low	1 - 5	
Medium-low	6 - 10	
Medium	11 - 25	
Medium - high	26- 50	
High	51 - 75	
Very high	76 - 100	

Figure 5.9: *Legend risk assessment.*

Table 5.5: *Envelope risk assessment.*

Index	Risk Factor	HS	HP	HRI	Mitigation strategy	HS	HP	HRI
1	System catches fire as result of a critical failure.	10	6	60	Hydrogen venting through tube at exit.	10	2	20
2	System struck by lightning.	10	6	60	Avoidance of storms by meteorological prediction.	10	2	20
3	Leakage in lifting gas envelope.	10	4	40	Use multiple layers of in envelope material.	10	2	20
4	Collision with a bird.	10	6	60	Extra tough material on the nose of the airship	2	6	12
5	System subjected to heavy winds.	6	6	36	Actively monitor envelope pressure by venting/ballonets system to limit stresses.	2	6	12
6	Collision with surrounding during take-off/landing.	6	6	36	Re-evaluate take-off/landing area Require and set safety margins.	5	4	20
7	Material degradation due to exposure to outside conditions.	6	6	36	Regular inspection. Storage in enclosed monitored environment.	6	1	6
8	Structural failure due to landing impact.	6	6	36	Reinforce payload carrying structure.	6	4	24
9	Structural failure due to thermally induced forces.	10	2	20	Reflective aluminium coating protects.	10	3	30
7	System surface subjected to ice formation	10	1	10	Protective coating, monitor weather conditions Pre-flight checks.	6	1	6

5.3.1. Sustainability Analysis

In this section the sustainability of the envelope is analysed. An estimate of the sustainability of the envelope is based on the sustainability of the material out of which the envelope is composed. For each material the greenhouse gas equivalent mass for the material production and recycling is listed in Table 5.6. All the values were found on Granta Edupack 2021 [27].

The previous material selection opted the best performing material for each layer of the envelope fabric. When a material is thus replaced by a more sustainable option, performance will be reduced. From the above table it is clear which materials are pollution the most, namely Polyvinyl Fluoride (PVF) and Vectran. To improve the overall sustainability of the envelope, it is most effective to replace these materials. A possible replacement of PVF is Poly-vinyl chloride. The material provides good weather-ability and bond-ability. Its greenhouse emission is reduced to $1.88\,\mathrm{kg(CO_2)}$/kg. The Vectran layer is not able to replaced, as other high specific strength fibres do not have nice flex-fatigue.

Table 5.6: *Envelope sustainability assessment.*

Materials	CO_2 Production (kg/kg)	CO_2 Recycling (kg/kg)
thermoplastic polyurethane	5.46	1.85
Vectran	17.4	5.72
Poly-vinyl fluoride	23.3	-
EVOH	7.83	2.66
Aluminium	2.49	8

5.4. Verification & Validation

The envelope is a critical structure in the envelope, therefore, in order to apply the envelope material, several tests need to be performed. Determining the laminate's permeability and mechanical properties is of utmost importance. Testing should also be performed with different loading directions and different environmental conditions. On top of that, tests determining the performance of the joint need to be done.

To test the mechanical performance a bi-axial and uni-axial stress test are done. A uni-axial test is done to come up with the stiffness and breaking strength of the envelope material. The test will be performed in two directions as warp and weft mechanical properties can differ. The specimen that is tested will be sized according to ISO standards. The same uni-axial setup will be used to determine the joint strength. Since the envelope material consist of a woven fabric which loaded in operation creates complicated interaction between warp and weft, a bi-axial test also needs to be performed. The test specimen has a cruciform shape with its arms aligned in the war and weft direction of the fabric. The shape is to have orthogonal independent loaded axes and there the interaction between the axes becomes clear.

The envelope will experience cyclic loading during its operational time each time the system is inflated and deflated. In order to have an estimate of the envelope's mechanical performance and deformation over time, fatigue testing needs to be done. This test can be performed on a servo hydraulic test machine. The test specimen is loaded at its limit load until it fails. The limit load is defined as the hoop stress experienced in normal operation times the load factor for the envelope. The elongation of the specimen can be measured using strain gauges.

The envelope material is furthermore tested for crack propagation, since most failures are due to such failure. It is thus interesting what size of crack leads to the envelope to tear. To determine the critical size a uni-axial central crack tear test is used. Additionally, crack propagation leads to holes through which lifting gas easily escapes and can decrease the endurance tremendously. The endurance of the airship also depends on the permeability of the envelope material. It is thus an important property of the envelope and thus must be experimentally tested. To do so a container with on one side hydrogen at similar pressure as in the airship and on the other side a hydrogen detecting device in ambient air. The only separation is a piece of envelope material.

5.5. Gondola Structural Design

The gondola is the structure which carries all the systems needed to be covered or stored away. The main systems contained in the gondola are: battery, electronics, navigation systems, communication and the payload. In addition to having a load-bearing function the structure should be light, durable, aerodynamic and allowing the sensors to be dropped.

The design of the supporting structure starts from the attachment of the sensors to the gondola. Out of a trade-off shown in Chapter 11, an electromagnetic attachment system was chosen. It keeps the sensor attached until it experiences a current. The magnet needs to be fixed to the gondola structure by a cylindrical support. As the vehicle carries 550 sensors, a lot of magnets are required to deploy the complete sensor network. To contain all the magnets in a light manner, two roster-like structure are opted for. The roster is build out of rods placed in the longitudinal direction with two transverse supporting beams. On the rods the cylindrical support structure of the magnet are attached.

All the rods and the two supporting beams are fixed to a rectangular wall structure. This wall structure allows the roster to be mounted on the structure connected to the envelope. The type of mount used are bolts. The structure connected to the blimp is the outer structure of the gondola. It consists of keel structure that follows the shape of the envelope, two long plates on the side and an aerodynamic front and aft container for all the system placed in the gondola. On the side plates four variable-pitch propellers are mounted to provide control.

The whole deployment system contains of two rosters which are placed after one another. All the sensor are positioned close to the centre of gravity of the vehicle. This is because all the sensors are dropped over the duration of the operation. As the sensors take up a large part of the total weight, longitudinal stability changes. In order to limit this change, the sensors are placed central or close to the centre of gravity.

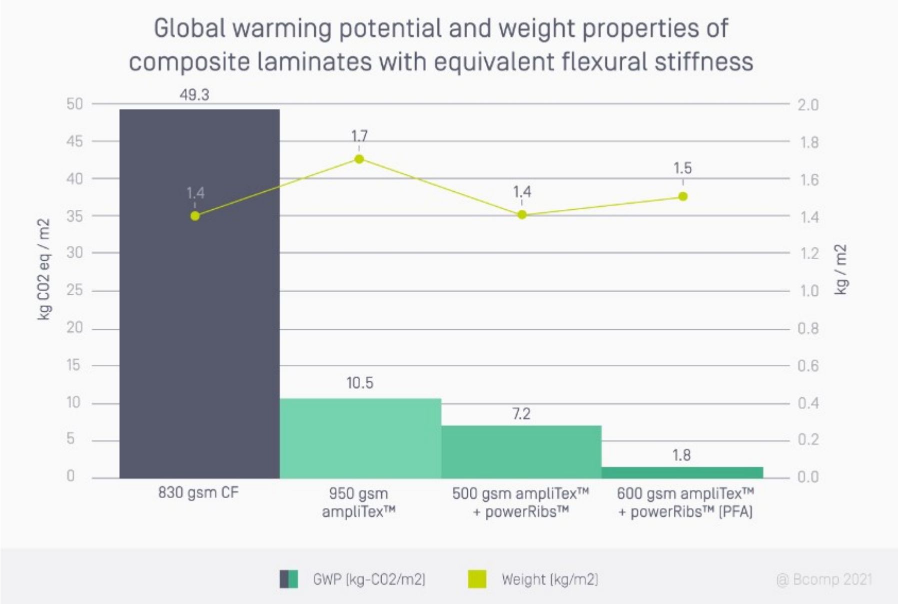

Figure 5.10: *Co2 footprint of Bcomp materials compared to carbon fibre.*

The material used in the gondola structure is composed of Bcomp's Amplitex 5043 sheet and a PA11 resin. For the composite a volume fraction of $50\,\%$ is assumed. Amplitex material was selected over carbon fibre as it the sheet of fibres consists of natural fibres, which increases the sustainability of the gondola. In Figure 5.10, it can be seen that Amplitex has an $80\,\%$ lower footprint than carbon fibre.

The main function of the gondola structure is to carry the sensors. Deformation due to the weight of the hanging sensors should be limited for the overall gondola to be aerodynamic. In Figure 5.11, a finite element analysis was done to check the buckling deformation of the roster. The configuration of the finite element analysis assume that the structure is fixed at it mounting points on the side panel. The only loading on the structure is gravity. Deformation is limited to only $1.7\,\mathrm{mm}$, which is negligible on considering the size of the roster.

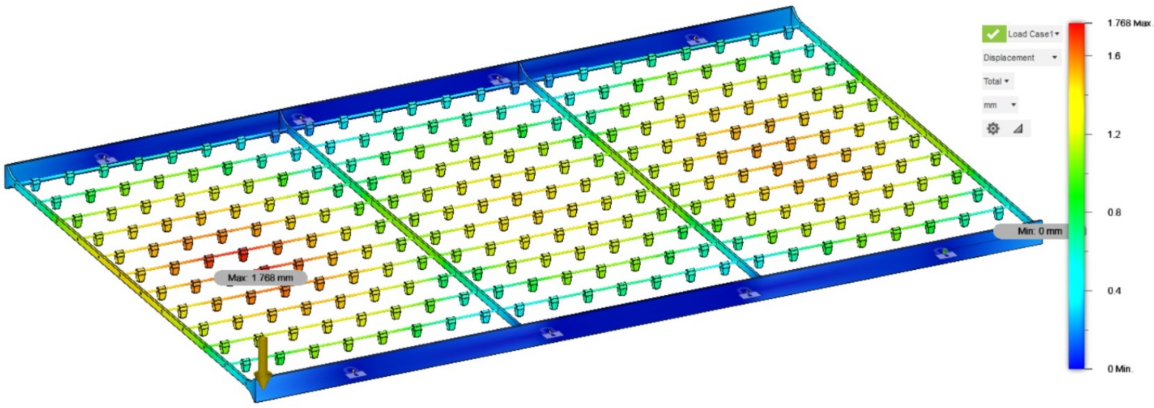

Figure 5.11: *Deployment structure deformation.*

5.5.1. Gondola Attachment Design

Within the airship, the weight of the gondola with its payload constitutes most of the mass to be carried by the lifting gas. Therefore, the attachment of the gondola to the blimp envelope, where the stresses will be transferred, must be carefully considered. However, it is borderline impossible to make preliminary calculations about this complex loading of the envelope membrane and modelling this behaviour numerically is no easy feat either, due to the highly non-linear nature of the loading of a membrane. This is also noted in the book Fundamentals of Aircraft and Airship Design Volume 2 [17] and has been confirmed to the team by Alexander Mijatovic, an expert from the RC-Zeppelin company, who advised the team to simply disperse the weight to as large of an area as possible. Therefore, going further, a conceptual design will be proposed, with the specifics to be determined at a later stage of the development. Furthermore, thorough testing will be required for this attachment for careful validation.

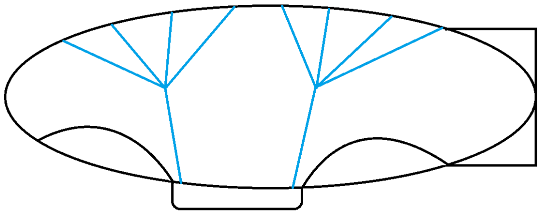

Figure 5.12: *An airship with catenary suspension in blue.*

Figure 5.13: *Gondola attachment of the Trans-Atlantic Solar Airship [28].*

In a non-rigid airship, such as the EcoSense model proposed in this paper, the gondola can either be attached solely to the bottom of the airship envelope, or a catenary suspension system, as seen in Figure 5.12, can be utilised to distribute the loads further into the top half of the envelope as well. A combination of the two is also possible. Looking at similarly sized reference designs such as the Trans-Atlantic Solar Airship from the RC-Zeppelin company [28], the Airship Solutions AS10 [29] and others, it was deducted that an attachment of the gondola solely to the bottom of the envelope shall be sufficient, and should be carried by the envelope without significant deformation. Of course, this is to be verified in further stages of the design. This design allows for simpler manufacturability by reducing the work needed to be done inside the envelope, as well as for easier operations, since there need not be worries about the catenary suspension tangling during transport or inflation.

More specifically, a design similar to the aforementioned Trans-Atlantic Solar Airship shown in Figure 5.13 shall be used, where small, standardised patches can be applied to the envelope, to which the gondola can attach. This design provides easy manufacturability, as the small patches can be produced in series and can be bonded with relative ease thanks to their small area. Furthermore, this design allows for flexibility in operations, as it allows the detachment of the gondola from the blimp, and it provides more possibilities for maintenance, compared for example to a design where the gondola is fully bonded directly to the envelope. An area where this attachment method could struggle is aerodynamics, however this can be optimised in further design.

6 Vehicle Propulsion

The propulsion system is one of the most important systems of the vehicle, responsible for getting the vehicle from A to B. The detailed design of this system is performed in this chapter. Firstly, Sections 6.1, 6.2, and 6.3 present the design approach, design requirements, and the functional analysis respectively. Furthermore, in Section 6.4, a trade-off of the different propulsive methods is performed. Section 6.5 and Section 6.6, describe the sizing of the motor and the propeller, respectively. Section 6.7 delves into the risk assessment of the propulsion system, followed by a sustainability analysis in Section 6.8. Finally, the final propulsion system design is presented in Section 6.9.

6.1. Design Approach

In this section the methods used to develop the final propulsion design are described. A two-level trade-off is performed. First on the top-level propulsion method followed by the detailed sizing of the selected propulsion method. The approach of said method is elaborated in Section 6.6. The driving factors for all trade-offs within this chapter are based on efficiency, weight, sustainability and cost.

6.2. Design Requirements

In this section, the driving requirements for the propulsion of the vehicle are defined as follows:

Table 6.1: *Propulsion design requirements.*

Req. ID	Requirement	Section	Compl.
REQ-VEH-POW-4	The propulsion system shall not interfere with the operation of the deployment system.	6.9.1	✓
REQ-VEH-POW-5	The propulsion system shall provide variable thrust levels	6.4	✓
REQ-VEH-POW-6	The propulsion system shall be able to arm without posing a threat to the operator.	-	≈
REQ-VEH-CO-12	The vehicle shall have a minimum range of 350 km	-	✓
REQ-CG-1	The EcoSense system shall operate with a noise level below 80 dB at ground level	6.8	✓

The first four requirements are related to mission and customer needs, along with safety standards set for the design. The last requirement is related to sustainability. Noise must be below $80\ \mathrm{dB}$ for two main reasons: Firstly, sounds above $85\ \mathrm{dB}$ are considered to be harmful to operators without special hearing protection. Therefore, a hard limit is set at $80\ \mathrm{dB}$ which is comparable to a busy crossroad. Secondly, in communication, noise interferes with the tone, intensity, and structure of signal emissions so that its reception lacks information, producing an acoustic masking effect [30]. In other words, extensive noise reduces the communicating range with the vehicle.

6.3. Functional Analysis

Figure 6.1 presents the functional analysis of the propulsion system. The take-off and landing phase feature the same functions. The most important functions that the propulsion system performs are during the flight phase where it needs to provide thrust, as well as altitude and stability control.

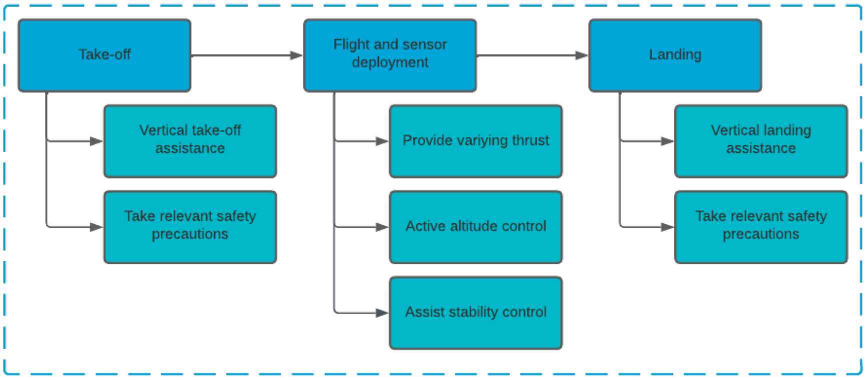

Figure 6.1: *Functional analysis of the propulsion subsystem.*

6.4. Propulsion Type Trade-off

Before starting the detailed propulsion design, a top-level trade-off of four different propulsion methods is performed, this section compares a conventional propeller system with unconventional and novel technologies.

6.4.1. Propulsion Type Design Options

A total of four design options are proposed for the top-level propulsion type trade-off. As depicted in the figures below, an electrically powered propeller (Figure 6.2), fluidic/bladeless propulsion system (Figure 6.3), swimming motion propulsion mechanism (Figure 6.4) and cycloidal rotor (Figure 6.5) are proposed.

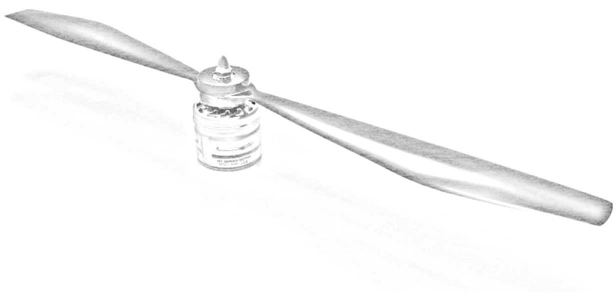

Figure 6.2: *Sketch of an electrically powered propeller.*

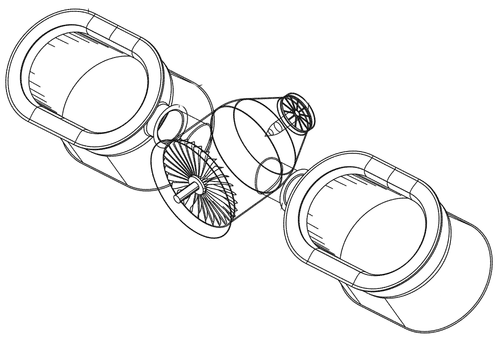

Figure 6.3: *Schematic drawing of a fluidic propulsion system. [31]*

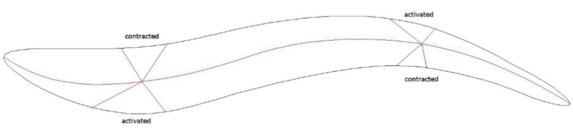

Figure 6.4: *Sketch of swimming motion propulsion mechanism. [32]*

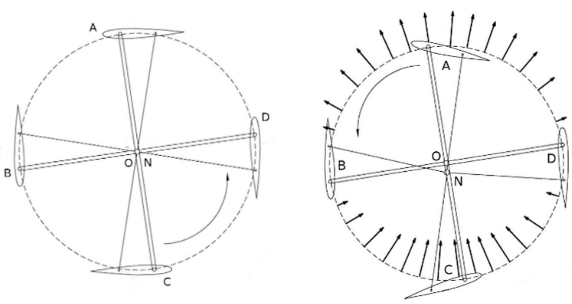

Figure 6.5: *Description of the working principle of a cycloidal rotor. [33]*

Propeller propulsion

A propeller system is the most conventional propulsion system for airships, they present high efficiency at medium to low velocities, and are cheap and lightweight. Additionally, thrust vectoring is possible with this propulsion type either by changing the orientation of the propellers or by applying two or more propellers differentiating in rotation speed, creating a moment around the vehicle's centre of gravity. Another advantage of propellers is their wide application in the drone industry. Hence, lots of research on sizing and configuration is available, and different propeller designs are widely commercially available for many aerospace applications.

Fluidic propulsion

Recently, a new company, Jetoptera, introduced a remarkably different take on aviation propulsion, a new bladeless propulsion system inspired by the British tech manufacturer Dyson. The mechanism is composed of two parts: An electric ducted fan or compressor, and a discharge frame. This device relies on the so-called Coanda effect and the subsequent Coanda ejector. The primary flow is provided by a compressor, which follows the curved contour of the ejector after flowing through the throat. A turbulent mixing zone is developed as a result of expansion/compression waves created due to the pressure at the outlet section which converts to thrust [34].

One of the main benefits of a bladeless propulsion system is its safety for operators and its quiet operation. Additionally, the same thrust vectoring processes as a regular propeller system can be used. However, due to the limited availability of research on this topic, the sizing process is more complicated and ambiguous. For initial sizing, the research paper by Anuta M. et al. [35] is used as a reference to make an initial design, later on, iterations can be made with CAD data and fluid flow simulations. However, according to Sivarman et al. [36], the thrust to weight ratio for small-scale engines at medium to low speeds lie far below that of a conventional electric propeller, mainly due to a closed rigid structure needed for this system to operate.

This propulsion type is brand new and still very experimental. For this reason, test data is too sparse to form a reliable comparison. Therefore, using this propulsion type would require a lot of development and testing which is outside of the scope of this project. For this reason, no further interest will be put in this propulsion type until the technology becomes more publicly available.

Propulsion by Fin Motion

Scientists have been trying to mimic a swimming-like motion for both underwater and aerial applications. This rotorless propulsion type depends on dielectric elastomers. When voltage is applied to the electrodes, the electrostatic forces between them squeeze the dielectric membrane in the thickness direction. Because the dielectric material is nearly incompressible, it expands in the planar direction [32] as depicted in Figure 6.4.

This type of propulsion allows for completely silent low-speed propulsion. However, this method sacrifices control, speed and manoeuvrability compared to the other design options. The concept of a bionic blimp is a multidisciplinary challenge [37]. Aspects like aerodynamics, control, and structural mechanics have to be fulfilled for this solution to be functional.

Although this is a very interesting and innovative design, based on the testing and analysis performed by Jordi C. et al. [32], the velocity reached by this method does not come close to the flight speeds needed to comply with the mission requirements [38] and will therefore be discarded from the trade-off. This is depicted in Figure 6.7. However, this system can still be considered in combination with a different propulsion system for control purposes

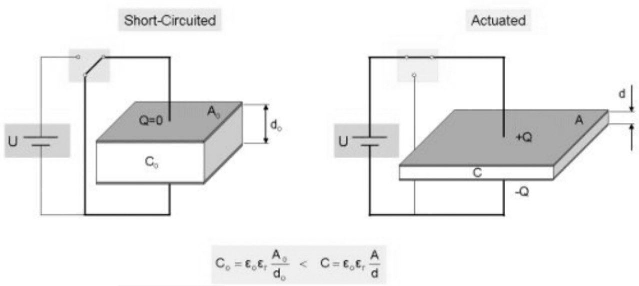

Figure 6.6: *Working principle of electroactive polymers. [32]*

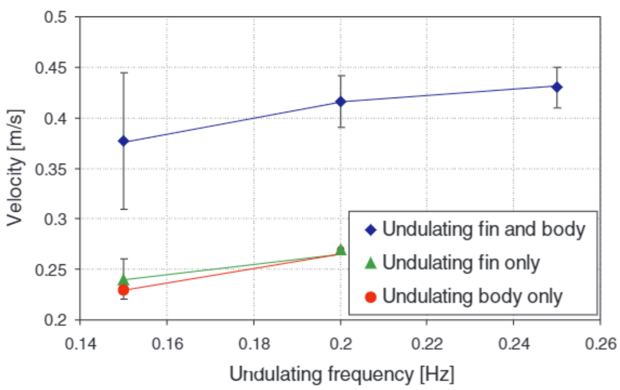

Figure 6.7: *Tested velocity in function of undulating frequency. [32]*

Cycloidal Rotor Propulsion

The last design option is a cycloidal rotor-based propulsion system. The system consists of various pitching blades that turn along the axis around the span of the blades. During rotation, the blades cyclically change in pitch angle to constantly achieve a positive angle of attack. The resulting unsteady motion of each blade results in effective lift and drag forces [33].

A main advantage is that thrust can be varied in magnitude and direction by changing the amplitude and phase of the cyclic blade pitch [33]. This system is also beneficial in terms of noise and ease of installation. However, due to the bigger supporting structure needed to hold the blades in place, the weight is considerably higher than a conventional propeller system.

6.4.2. Trade-off Criteria and Comparison

This section elaborates on the trade-off criteria. The selected criteria are efficiency, sustainability, and cost.

Efficiency

The efficiency of the propulsion system is of utmost importance both to minimise the required power and the weight for maximum amount of thrust. The weight of the propulsion system is to be minimised to allow for sufficient payload mass with minimum needed lifting gas. Therefore, the thrust-to-weight ratio is desired to be as high as possible. The required power strongly influences the weight of the battery and solar cells. To factor this in the equation, the static thrust-to-weight ratio is normalised to its required power so that only the weight of the propulsion system is to be compared while automatically taking into account the weight of power generation for this preliminary estimation.

For the propeller-powered solution, extensive testing databases for different motor-propeller configurations exist. For this estimation, tests from the Tyto Robotics database [39] are used. For safety and efficiency reasons, a ducted propeller design is also proposed. Ducted propellers are known to increase efficiency by decreasing vortex generation at the blade tips and increasing the amount of air that flows through the propeller blades, but heavily increases the system's weight. For this preliminary estimation, only free-tip propellers are considered. If propellers seem the most suitable for the design, duct designs will be proposed and analysed in detail. The reference motor-propeller-system chosen from the data points weighs a total of $537\,\mathrm{g}$, and can produce $33.9\,\mathrm{N}$ of thrust at 5500 RPM, consuming $591\,\mathrm{W}$ of power.

When it comes to the cyclorotor concept, the system can be thought of in the following way: As shown in Figure 6.5, the airfoils are only able to produce maximum lift at their azimuth locations. Every point in between becomes more inefficient reducing to nothing at 90°from azimuth. Still, both structures to support the blades, and to vary the pitch of the airfoil during rotation add weight to the system. As a reference, the quad-cycloidal-rotor UAV, developed by Moble et al. [40], is used. This vehicle acts as a proof of concept, focusing on high efficiency and T/W ratio. The reference UAV's propulsion system weighs a total of $425\,\mathrm{g}$, and can produce a total amount of $8.4\,\mathrm{N}$ of thrust at $1000\,\mathrm{RPM}$, consuming $248\,\mathrm{W}$ of power [40].

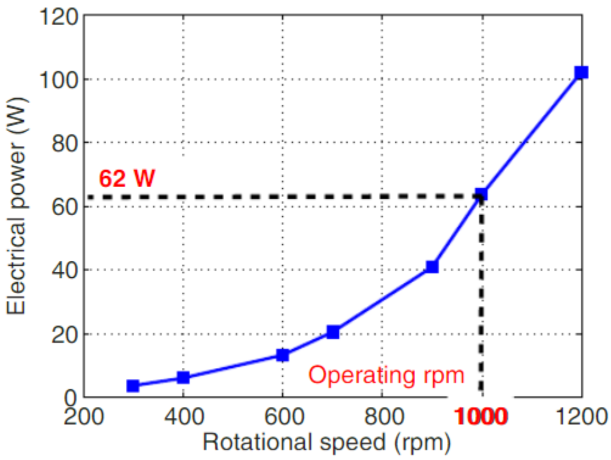

Figure 6.8: *Power consumption test data of the cycloidal rotor [40].*

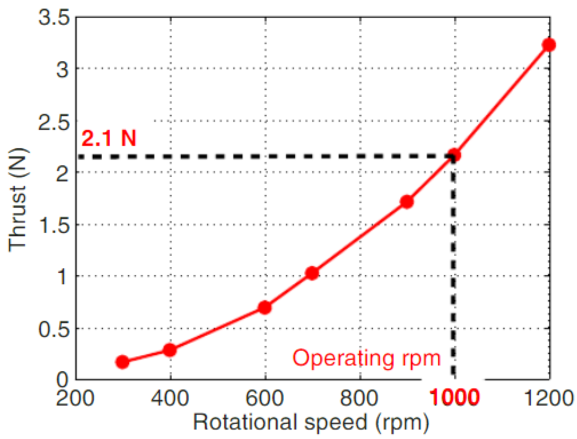

Figure 6.9: *Thrust generation test data of the cycloidal rotor [40].*

In Table 6.2 the thrust-to-weight ratio normalised by power consumption is quantified and compared with each other for both the propeller and cyclorotor design. The propeller system seems to outperform the cyclorotor in terms of efficiency. Based on this comparison, a score from 1 to 5 is given which will be used in the top-level propulsion subsystem trade-off in Subsection 6.4.3.

Table 6.2: *Quantification of efficiency scores.*

	T [N]	m [g]	P [W]	T/(WP) [1/W]	Score
Propeller	33.9	537	591	0.0109	**5**
Cyclorotor	8.40	540	248	0.00639	**3**

Sustainability

EcoSense aims to develop a vehicle with minimal impact on the ecosystem it is operating in. This criterion envelops the amount of noise generated by the propulsion unit and the safety to operators and wildlife.

Noise belongs to the category of aeroacoustics and is caused by unsteady flow field pulsations. Current noise reduction methods include reducing the intensity of the sound source and reducing noise based on the interference of destructive sound waves [41]. Fast spinning blades of a propeller system will strongly disturb the surrounding air, generating powerful sound waves.

During experimental evaluation, cyclorotors produced little aerodynamic noise. This is likely due to the lower blade tip speeds, which produce lower intensity turbulence following the blades [42].

Cost

The trade-off criteria are concluded with a preliminary cost analysis. The cost of every individual part of the same set-ups are estimated and then compared. This cost is expressed in cost per Newton of thrust, since if only half the thrust is produced, double the amount of propulsion systems are to be applied. Only the propulsion system itself will be considered, excluding components like servos and batteries.

Table 6.3: *Preliminary propulsion cost analysis.*

	Motor	Blades	Structure	T [N]	Cost/N	Score
Propeller	EUR 129.17	EUR 21.14	N/A	33.9	EUR 4.43	**5**
Cyclorotor	EUR 42.39	EUR 21.14	EUR 3,50	8.40	EUR 7.97	**3**

6.4.3. Trade-off Results

The final scores between the remaining two propulsion methods are weighed and added up to conclude that the propeller system deems the most fitting design choice. With this system selected, the next steps are to size the motor and propellers.

Table 6.4: *Trade-off on the number of propellers.*

Criterion	Efficiency	Sustainability	Cost	RESULT
Weight	40.00%	40.00%	20.00%	100.00%
Propeller	5.00	3.00	5.00	4.20
Cyclorotor	3.00	4.00	3.00	3.20

6.5. Motor Selection

The motor selection was performed through an iterative process. Firstly, a library of various brushless motors was created to enable selection based on different parameters such as mass and propulsive power. Through iterations on the final design, a motor was selected which could fulfil the following characteristics:

- Provide sufficient thrust with the designed propeller to achieve required cruise velocity.
- Provide sufficient thrust with the designed propeller for vertical take-off.
- Provide sufficient thrust at less than 55% throttle.
- Provide sufficient thrust with the available power.
- Be able to operate at nominal battery voltage.

A requirement that raises interest is the $55\ \%$ thrust limit. This was selected to ensure high efficiency and to extend the lifespan of the motor by not running excessively high currents through it, thus avoiding overheating and wear.

Through the iterations, the T-motor V505 was selected [43]. The motor was designed for VTOL capabilities on UAVs with a high thrust-to-weight ratio, making it a great fit for EMBER. The motor is capable of providing sufficient thrust while operating at $20\ \%$ throttle, thus also enabling redundancy in case one fails. It comes in at $255\ \mathrm{g}$ weight and is designed to operate with a 12S battery [43]. The final specification needs to be mitigated as the on-board battery is a 6S battery. The mitigation is to rewind the motor windings, changing its KV rating from 260 to 520.

6.6. Propeller Sizing

Now that the electrical motor has been selected, the next step of the detailed propulsion design is the sizing of the propeller. The design of the propeller is related to factors like: available power, RPM, mission requirements such as VTOL, cruise speed, and noise requirements.

In this section, the recommended propeller geometry (2-bladed APC 18" x 8") is used as a baseline of the design as an extensive test result database is provided by the motor manufacturer [43]. Then, aspects of the geometry such as the airfoil selection, amount of blades, ducts, and twist distribution are optimised for the specific requirements of the EcoSense mission. Subsection 6.6.1 gives a general overview of the methodology used to calculate basic propeller properties and noise emission. As previously mentioned, the propeller design is highly dependent on the placement, and the amount of thrust that is desired to be produced.

6.6.1. Blade-Element Momentum Theory

Blade-Element Momentum Theory (BEMT) is commonly used in propeller design. This approach is beneficial due to its relative simplicity and computational efficiency, in many cases without a large sacrifice in fidelity [44]. The propeller sizing is done to optimise for maximum efficiency, while also taking into account the aeroacoustics of the design. BEMT relies on breaking down the rotor blade into multiple elements, where each is considered a 2-dimensional wing. Lift and drag calculations are then performed locally using the section's local airfoil parameters, section velocity and chord length. At the tips, a Prandtl tip-loss factor is applied.

With the vector velocities depicted in Figure 6.10 and 2D airfoil section data, C_l and C_d for the airfoil section are calculated. XROTOR is an open source available propeller simulation tool based on this method. The tool is used for performance and aeroacoustic analysis of different propeller designs [45], and will serve as the basis for quantification of the propeller trade-off. XROTOR uses the 2D inviscid potential solver tool XFOIL to provide this airfoil data. Compressibility models for high Mach number operations are implemented in XROTOR. Additionally, transition models are used to estimate the laminar-turbulent transition [46].

The 2D lift and drag coefficients are subsequently used to compute the section lift (L') and section drag (D') of each element, which can be transformed into section thrust (T') and section torque (Q') which are then integrated over the span to obtain a final value for thrust and torque.

$$L' = \frac{\rho}{2} \cdot \mathrm{w}^2 \cdot c_{l_\alpha} \cdot \phi \cdot C_{\text{chord}} \qquad (6.1) \qquad\qquad D' = \frac{\rho}{2} \cdot \mathrm{w}^2 \cdot c_{ld_\alpha} \cdot \phi \cdot C_{\text{chord}} \qquad (6.2)$$

$$T' = L' \cdot \cos(\beta+\phi) - D' \cdot \sin(\beta+\phi) \qquad (6.3) \qquad\qquad Q' = L' \cdot \sin(\beta+\phi) + D' \cdot \cos(\beta+\phi) \qquad (6.4)$$

$$T = N_{\text{Blades}} \cdot \int_{R_{\text{Hub}}}^{R_{Tip}} T'_r dr \qquad (6.5) \qquad\qquad Q = N_{\text{Blades}} \cdot \int_{R_{\text{Hub}}}^{R_{Tip}} Q'_r dr \qquad (6.6)$$

Next, the known torque of the propeller can be used to calculate the power consumption. Using torque, thrust, the angular velocity ω_p, and flight speed v_∞, power consumption (P) and subsequently efficiency (η) is found with the following two equations:

$$P = Q \cdot \omega_{\text{Propeller}} \qquad (6.7) \qquad\qquad \eta = \frac{v_\infty \cdot T}{P} \qquad (6.8)$$

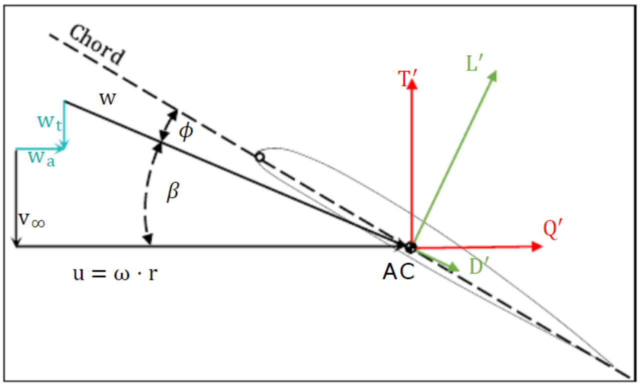

Figure 6.10: *Element forces as described by blade element momentum theory & velocity triangles. [46]*

The equations of BEM are derived assuming that the force from the blades is constant in each element. However, in real life the circulation of the air around the blades must be taken into account. Given a number of blades B and a radius R of the propeller, the Prandtl-Glauert tip correction function is applied by Equation 6.9:

$$F_\lambda(\varphi) := \frac{2}{\pi} \cos^{-1}\left(\exp\left(-\frac{B/2\left(1 - \frac{\lambda U_{-\infty}}{\Omega R}\right)}{\left(\frac{\lambda U_{-\infty}}{\Omega R}\right) \sin\varphi} \right) \right) = \frac{2}{\pi} \cos^{-1}\left(\exp\left(-\frac{B/2(1 - r/R)}{(r/R)\sin\varphi} \right) \right) \qquad (6.9)$$

For the aeroacoustic analysis in XROTOR, the retarded-time concept is used. A sphere collapsing towards the observer at the speed of sound collects acoustic signals from the blade thickness and the blade loading where and when it intersects the blades during its inward travel. The sum of all these signals then results in an instantaneous acoustic pressure p seen by the observer when the sphere collapses on him at some later time t. The total decibel (dB) level at each point of a rectangular grid under the aircraft, thus forming ground noise-level contours.

One contribution to the acoustic pressure is due to the blade airfoil's cross-sectional area and is specified as $\frac{A}{c^2}$. For most airfoils, this is roughly related to the thickness-to-chord ratio:

$$\frac{A}{c^2} \approx 0.7 \frac{t}{c} \qquad (6.10)$$

After the pressure time series is generated, it is Fourier-decomposed and the dB values of the individual components are computed. With ω = blade-passing radial frequency $= B \cdot$ prop shaft speed. The individual dB value for each component is defined relative to 20 μPa, while the total dB level uses the root-mean-square (RMS) pressure:

$$p(t) = Real\left[\sum_{k=1}^{\infty} C_k e^{-ik\omega t} \right] \qquad (6.11) \qquad\qquad p_{rms}^2 = \frac{1}{2\pi} \int_0^{2\pi} p^2 d(\omega t) = \frac{1}{2} \sum_{k=1}^{\infty} |C_k|^2 \qquad (6.12)$$

$$\mathrm{dB(k)} = 20 log_{10}\left(\frac{\sqrt{1/2}|C_k|^2}{20 \cdot 10^{-6}} \right) \qquad (6.13) \qquad\qquad \text{total dB} = 20 log_{10}\left(\frac{p_{rms}}{20 \cdot 10^{-6}} \right) \qquad (6.14)$$

Following this methodology, the overall design procedure is described in figure 6.11

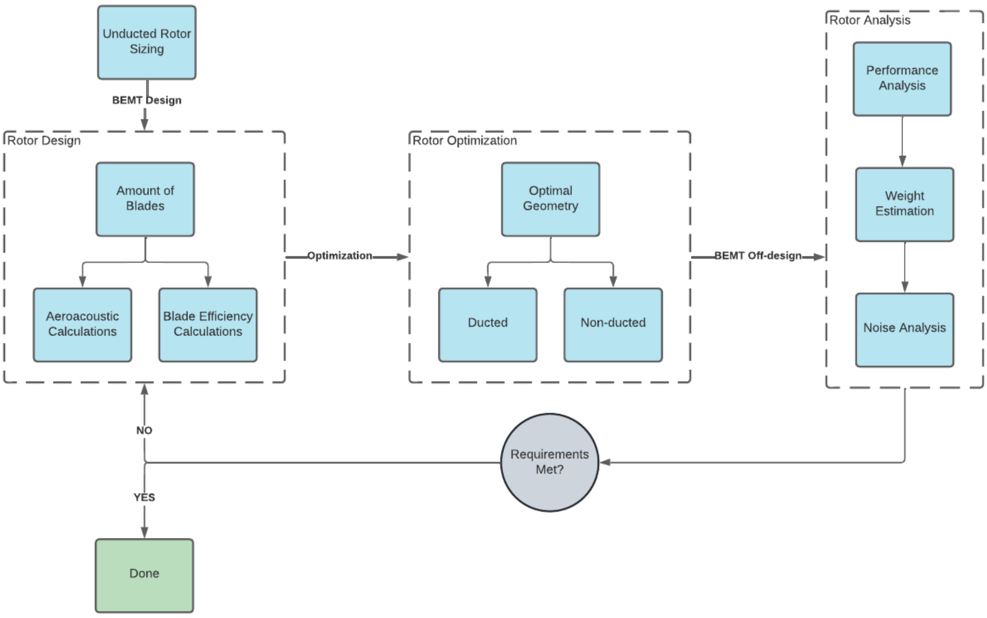

Figure 6.11: *Work flow of the propeller subsystem design.*

6.6.2. Airfoil Selection

The first fundamental step of propeller sizing is the selection of the airfoil. A high lift-to-drag ratio is typically the primary criterion. However, propellers operate in wide-ranging conditions, given the different inflow angles as function of inflow velocity and rotational speed [47].

The dominant basis for the primary airfoil shape used in most APC propellers is similar to the NACA 4415 airfoil. Two other commonly-used airfoils used for rotor design are CLARK-Y and RAF 6. Their Cl - alpha curves are shown in Figures 6.12, 6.13, 6.14, respectively for low Reynolds numbers between $10^4 - 10^5$, propellers usually do not reach higher numbers due to their small sizes compared to rigid wings. The NACA 4415 shows the most fitting stall characteristics at high angle of attack. For the remainder of the design process, an intermediate angle of attack of 7.5°yields a Cl value of 1.2, allowing for some safety before stalling.

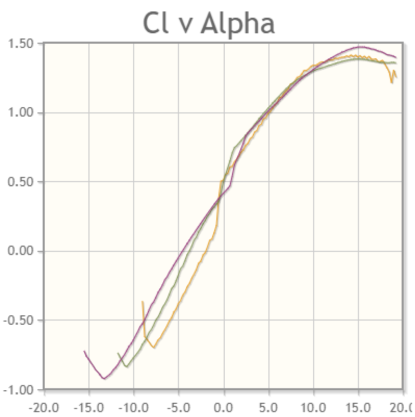

Figure 6.12: *NACA 4415 Cl - α, Re $10^4 - 10^5$.*

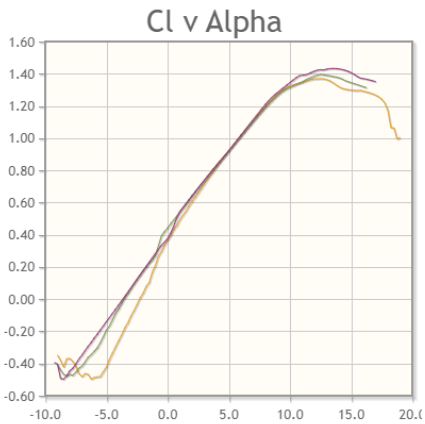

Figure 6.13: *CLARK-Y Cl - α, Re $10^4 - 10^5$.*

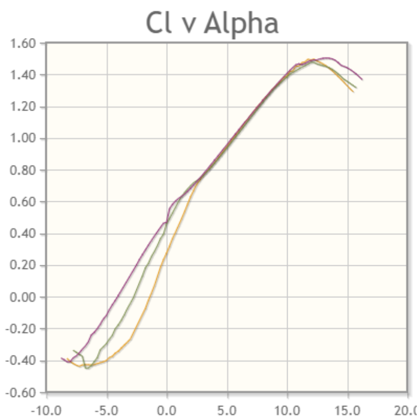

Figure 6.14: *RAF 6 Cl - α, Re $10^4 - 10^5$.*

6.6.3. Number of Blades

Propeller-powered UAVs typically use two, three or four propeller blades. This number can be increased to some applications where up to eight propeller blades are used. More blades produce more thrust at a given RPM due to extra lifting surfaces, but it will also be heavier and most importantly, less efficient than a propeller with fewer blades. For this analysis; two-, three- and four-bladed propellers with the same power consumption of 0.5 kW will be considered.

Again, for the two-bladed propeller now with the new selected airfoil, the 18” x 8” geometry will be used as a baseline. Changing the number of blades, while keeping the same shape, diameter, and pitch, from B_1 to B_2 linearly increases the power consumption.

Scaling the propeller to change the diameter from D_1 to D_2 changes the power needed to achieve the same RPM like:

$$P_2 = P_1 \cdot \left(\frac{D_2}{D_1}\right)^5 \tag{6.15}$$

Putting both trends together to achieve the same power consumption, and solving for the new propeller diameter D_2 finally leads to the formula:

$$D_2 = D_1 \cdot \left(\frac{B_1}{B_2}\right)^{1/4} \tag{6.16}$$

So for the next steps of this analysis, D_1, D_2 and D_3 are sized to have the same power consumption, and are run through the BEMT software. The resulting efficiency, delivered power and thrust are shown in Table 6.5. The data shows that an increase in blades decrease the efficiency and hence the produced thrust for given power consumption. In other words, two-bladed propellers give maximum endurance.

Table 6.5: *Change in propulsive power and generated thrust for 2-, 3-, and 4-bladed propellers with 0.5 kW of power delivered by the motor.*

B	D (m)	P_m (W)	η	P_p (W)	T (N)
2	0.46	500	0.7843	392.15	20.2
3	0.41	500	0.7692	384.6	19.8
4	0.38	500	0.7581	379.1	19.5

Another factor to be considered in this design is the noise production of the propulsion system. It is expected that a propeller with more blades vibrates less, making less noise. To verify this statement, XROTOR has the function to plot the acoustic signature of propeller designs for a certain altitude and climb angle. A detailed noise analysis is performed in Section 6.8

6.6.4. Ducts or Free-Spinning

Next, the design choice of adding ducts around the propeller or not will be discussed. There are two main reasons why ducts increase the efficiency of the propeller:

Since a propeller is essentially a spinning wing, thrust is generated by the pressure difference between the front and back surface. At the wing tips, strong vortices are generated from air travelling from the high pressure area at the back to the low pressure area at the front. This reduces the efficiency of the rotor. A duct that is tightly fitted to the tip of the propeller significantly reduces these vortices.

One more advantage to ducted propellers is the safety it provides. Ducts act as a protection to operators against the quickly spinning blades, but also as a mitigation of the risk of puncturing the blimp's envelope, or damaging other components if a blade comes off. A fully detailed risk assessment is performed in Section 6.7.

Due to the very small gap between the blade and the duct necessary, it is very important to choose a stiff, non-crimping material for these ducts. If the wall of the duct touches the rotating blade, substantial damage to the propeller may occur. AmpliTex™350 from Bcomp is a non-crimp biaxial flax fabric with fibres oriented at +45° and -45°, suitable for manufacturing fibre-reinforced composite products with a high performance and a low environmental impact, and is a perfect fit for the design of the duct. The density of this material is $1350\,\mathrm{kg/m^3}$. An extensive sustainability analysis for this material is done in Section 6.8.

Duct Design

A poorly designed duct will have no use, or even a negative impact on the performance of the propeller, therefore, it is most important to generate a preliminary duct design in order to estimate its increase in performance. CFD modelling is one way to do it, but real measurements stay the most reliable way to estimate increase in efficiency.

First, an airfoil for the duct is selected based on test data by Yilmaz et al. [48]. A very similar propeller is tested with different duct designs, a suitable duct design for cruise conditions of 70 km/h will be made based on this testing setup. Note that data has to be extrapolated to T = $36.4\,\mathrm{N}$. Figure 6.15 shows the power to thrust ratio, which is inversely proportional with ideal efficiency. Figure 6.16 shows the P_m/T % reduction, which directly translates to the percentage increase in ideal efficiency. Based on both these graphs, the NACA 4312 airfoil is chosen.

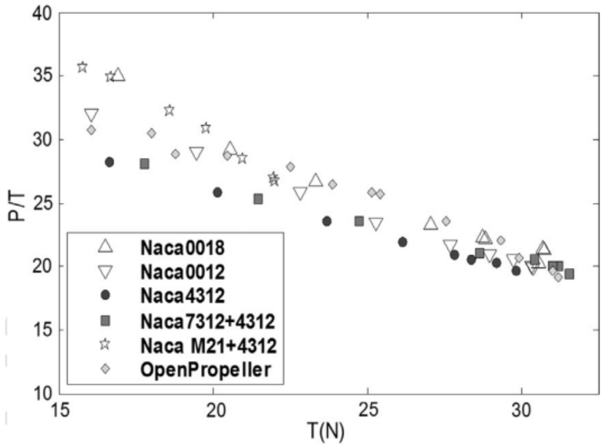

Figure 6.15: *Power/thrust ratio of ducted propellers versus thrust. [48]*

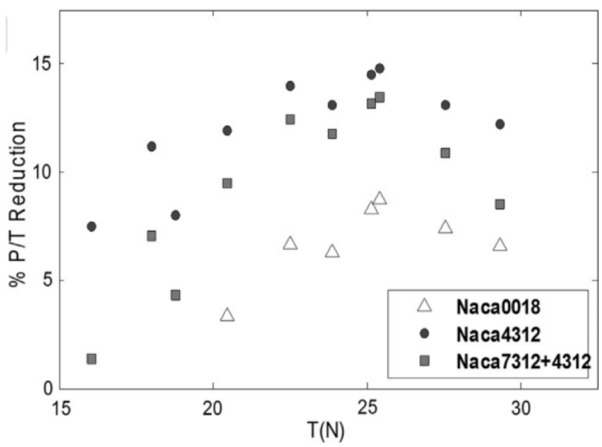

Figure 6.16: *P/T reduction obtained for each duct. [48]*

For this analysis, a NACA 4312 shaped duct with inner diameter of 410 mm, 1 mm thick sheets and length of 70 mm is used. A simple support structure is designed and included in the weight estimation. The following design, made out of previously mentioned AmpliTex™350 from Bcomp yields a mass of 285 g.

With a free-tip propulsion weight of 537 g, the ducted propeller weight becomes 822 g, which is a 53 % increase in weight. Based on tests by Li et al. [49] and Yilmaz et al. [48], a projected increase in power efficiency of 9 % compared to the free-tip propeller is measured for the cruise conditions of this mission.

6.6.5. Pitch Angle

To conclude the detailed propeller design, the most efficient pitch angle and geometry of the propeller blades are computed. The angle of pitch is the angle between the main body axis and the horizon. Low pitch causes less turbulence and more torque in the air, while high pitch causes less torque and more turbulence in the air. XROTOR has the function to optimise this angle by iteration for the designed 6500 RPM and P_m of 500 W. It will re-twist the rotor (the beta distribution) to achieve a MIL circulation while holding the current chord distribution fixed. The optimised twist distribution and geometry is then found for the free-tip propeller. Due to the duct structure, the airflow changes and the geometry is updated. The final optimised geometries for both designs are shown in Figures 6.17 and 6.18. The most notable changes are the increased twist at all angles and the flat wing tip at the ducted propeller. The latter is designed this way to reduce the gap between the blades and the duct.

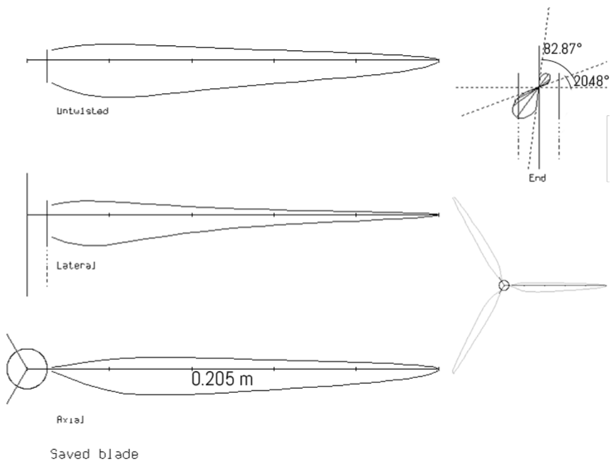

Figure 6.17: *Optimized geometry of free-tip propeller.*

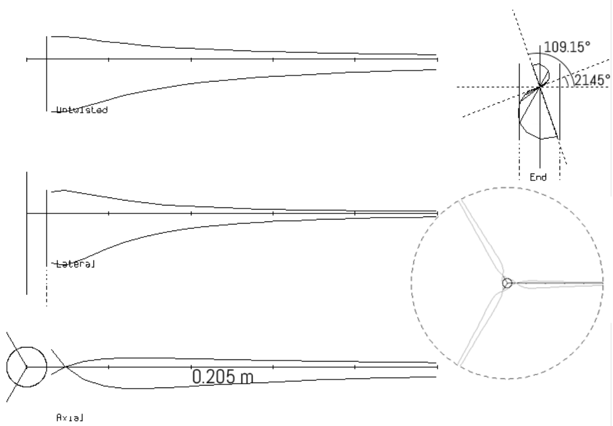

Figure 6.18: *Optimized geometry of ducted propeller.*

6.7. Risk Assessment

This section revises the propulsion-related risk assessment. Each risk influences the design of the final propulsion system done in Section 6.9. One existing risk is analysed, and three new risks are added along with new mitigation strategies. One strategy that often comes back is the use of a duct around the propeller for safety reasons, reducing the hazard probability.

Table 6.6: *Propulsion system risk assessment.*

Index	Risk factor	HS	HP	HRI	Mitigation strategy	HS	HP	HRI
Detailed propulsion subsystem design risk assessment								
38	Loss of control due to failure of propulsion system	6	6	36	Redundant propulsion system	2	6	12
x	Damage to structure due to failure of propulsion system	6	10	60	Protective shield in the direction of the structure Use of materials resistant to cutting	2	6	12
x	Failure of propulsion system due to collision	6	4	24	Protective duct all around Redundant propulsion system	2	4	8
x	Spinning blades injure operator	6	6	36	Protective duct all around Clear safety instructions	6	4	24

6.8. Sustainability Analysis

The main component of developing a sustainable propulsion system are noise emissions and the use of sustainable materials. As previously mentioned, AmpliTex™350 from Bcomp is a material suitable for manufacturing fibre reinforced composite products with a high performance and a low environmental impact. The flax fibres are CO_2 neutral over their life cycle, the high mechanical performance reduces the amount of material needed, and the thermal energy recovery within municipal waste allows for good conversion into usable heat, electricity or fuel at its end-of-life. Free tips are straightforwardly the most sustainable option as no coping material at all is used.

The double-, triple-, and quadruple-bladed propeller designs are analysed for level flight at ground level and an altitude of 150 m. For ground level, requirement REQ-CG-1 must be satisfied. As a reference, sounds above 85 dB are considered to be harmful.

Comparing the acoustic signatures in Figures 6.19, 6.20, and 6.21, the noise production decreases with increasing blade number. It should be noted that XROTOR calculates the noise map for a single propeller. Adding sources increase the sound pressure in the following relation:

$$\Delta L_{\Sigma} = 10\left(\log_{10}\left(\frac{2\ \mathrm{Pa}^2 + 2\ \mathrm{Pa}^2}{2\mu\mathrm{Pa}^2}\right) - \log_{10}\left(\frac{2\ \mathrm{Pa}^2}{2\mu\mathrm{Pa}}\right)\right) \qquad (6.17)$$
$$\Delta L_{\Sigma} = 3\ \mathrm{dB}$$

Hence, assuming a maximum of four propellers, 6 dB extra is considered to satisfy REQ-CG-1. This requirement is not satisfied with the two-bladed propeller when using more than one propulsion system. The three-bladed propeller produces a maximum noise of $72\ \mathrm{dB}$ at ground level, so a maximum of four propellers may be used to comply with the previous requirement. A single four-bladed propeller produces the least noise, at $64\ \mathrm{dB}$.

At an altitude of $150\ \mathrm{m}$, the maximum noise received at the ground by the double-bladed system is $35\ \mathrm{dB}$. This is equivalent to the noise of an average refrigerator, so at this altitude and higher, noise is negligible.

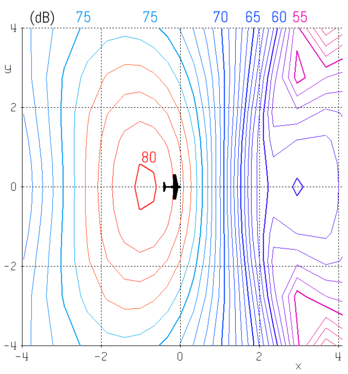

Figure 6.19: *Double-bladed acoustic signature at ground level.*

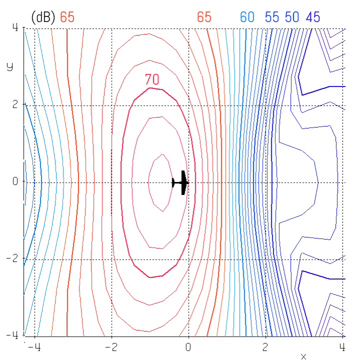

Figure 6.20: *Triple-bladed acoustic signature at ground level.*

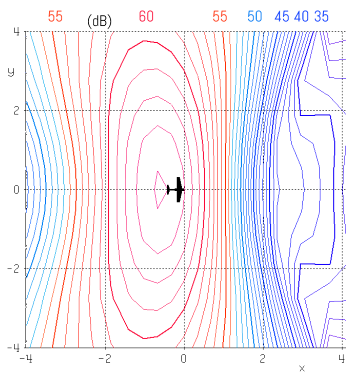

Figure 6.21: *Quadruple-bladed acoustic signature at ground level.*

6.9. Final Propulsion System Design

As demonstrated in Table 6.9, the triple-bladed propeller shows the best balance between efficiency and aeroacoustics. As the double-bladed system is far off the noise requirements, intensive noise reduction methods will have to be applied that may negatively influence the performance of the blades.

For the design choice of adding ducts or not, it can be noted that the increase in efficiency is outweighed by the extra mass of the duct. However, as discussed in the risk assessment the use of a duct as a protection mechanism both serve as a HS and HP mitigation strategy, creating an overall safer and more reliable design.

Table 6.7: *Detailed trade-offs of the propeller number.*

Criterion	Efficiency	Weight	Sustainability	RESULT
Weight	50.00%	20.00%	30.00%	100.00%
Double-bladed	5.00	5.00	1.00	3.80
Triple-bladed	4.00	4.50	4.00	4.10
Quad-bladed	3.00	4.00	5.00	3.80

Table 6.8: *Detailed trade-offs of the propeller design.*

Criterion	Efficiency	Weight	Risk	RESULT
Weight	40.00%	30.00%	30.00%	100.00%
Free tip	4.60	5.00	2.00	3.94
Ducted	5.00	3.30	4.00	4.19
Protection Cap	4.60	4.42	3.00	4.07

The final detailed propulsion design is chosen by means of two trade-off tables. As depicted in table 6.9, the airship will be propelled by four T-motor V505 motors, with ducted triple-bladed propeller blades with the optimized geometry shown in figure 6.18. An overview of the technical specs of the final design is given in table 6.9.

Table 6.9: *Final propulsion subsystem specifications per unit.*

N	D (m)	RPM	V (m/s)	P in (W)	η	P out (W)	T (N)	β (°)	Cp	Ct
3	0.41	6500	19.44	500	0.84	491.21	13.9	61.58	0.028	0.049

6.9.1. Vectoring Motor Mount

To enable the vertical take-off capability of the blimp, vertical thrust is required. This can be achieved through means such as positive buoyancy, vertical motors or thrust vectoring. The first is rejected due to buoyancy control requirements and dropping of payload, the second is rejected due to the additional weight and drag which hinder cruise flight, therefore only thrust vectoring is a viable choice.

As thrust needs to only be vectored around one axis, to enable vertical thrust, a simply vectoring system can be designed to allow for engine vectoring. Three concepts were thought of, presented in the following paragraphs.

Continuous Rod Concept

This concept consists of a rod onto which motors are mounted. The rod runs through the entire undercarriage and has motors on either side. The vectoring is done through a servo and gear mechanism on the inside of the undercarriage. The positive aspects of this system come from the decrease in components as one servo is needed to actuate two sides of motors, but comes at the downside of high internal volume and added weight due to the long rod required, as well as a decrease in portability due to the difficulty to remove such a system.

Strut Mounted Concept

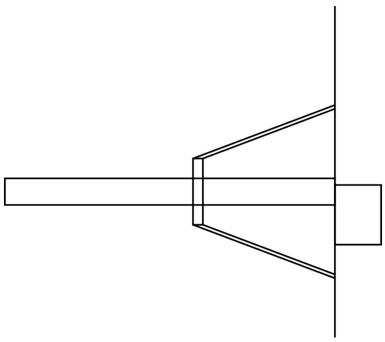

Figure 6.22: *Sketch of the strut mounted concept.*

Integrated Concept

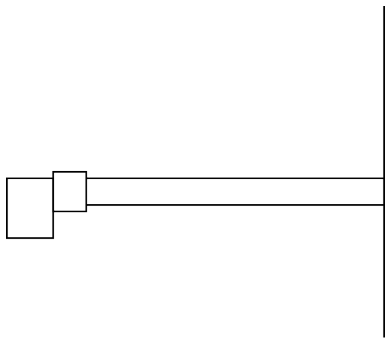

Figure 6.23: *Sketch of the integrated concept.*

Another option is the strut-mounted concept. This concept eliminates the full length rod and replaces it with a rod leading from the payload bay wall to the motor. The struts, with a bearing around the rod, are introduced to alleviate the bending moment on the servo due to the thrust. Compared to the previous concept, this one reduces the structural weight needed, as well as the internal volume required. It improves on the storing capabilities of the previous concept but introduces two separate structures which are part of the concept (rod and struts).

The final considered concept features a vectoring system incorporated within the motor mount at the end of the strut. This can alleviate all bending moments from the servo, features very little added structure and can be easily disassembled due to one attachment point to the undercarriage. Due to the concept improving on all faults of the previous two, it was selected for further analysis.

6.9.2. Servo Sizing

The servo selected is the Hitec HS-5805MG servo. To check if the servo is a good fit for the purpose, the torque it needs to overcome is calculated. The torque modes which need to be overcome are the holding torque, the acceleration torque, as well as the gyroscopic torque generated by the rotating propeller.

The masses the servo needs to move are the servo itself, the enclosure, the duct, the motor, and the propeller. To simplify the calculations, the components of the assembly are assumed as a stick with the mass of the components equally distributed, spanning from the servo axis to the end of the duct. This results in a stick of $1172.3\,\mathrm{g}$, $100.75\,\mathrm{mm}$ long.

Firstly, the holding torque is evaluated. The worst case scenario is the holding torque, when the motor is in the cruise orientation. The holding torque is calculated using the force induced by the stick mass and the arm, which is the distance to the centre of the stick. Using the equation $T = F \cdot r$, gives the holding torque of $0.575\,\mathrm{Nm}$.

Furthermore, the acceleration torque is calculated. For the calculation, the angular acceleration is required. The servo shall be able to rotate $90°$ in $2\,\mathrm{s}$. The servo is assumed to be capable of accelerating to its rotational velocity in $0.2\,\mathrm{s}$ [50]. Through the acceleration profile [50], the required travel angular velocity is calculated as $0.873\,\mathrm{rad/s}$, with a required angular acceleration of $4.35\,\mathrm{rad/s^2}$. The moment of inertia of the stick is defined as $\frac{1}{3}m \cdot l^2$, which results in an inertia of $0.00397\,\mathrm{kgm^2}$. This results in the acceleration torque equal to $0.0173\,\mathrm{Nm}$.

Lastly, the calculations for the gyroscopic torque are performed. From the motor datasheet [43], the propeller can be assumed to rotate at $6500\,\mathrm{rpm}$. The moment of inertia, resulting from Fusion360, equals to $0.0009\,\mathrm{kgm^2}$. To calculate the required torque, the following equation is used, where I is the moment of inertia, ω_s the servo rotational velocity, and ω_p the rotational velocity of the propeller.

$$T = I \cdot \omega_s \cdot \omega_p \tag{6.18}$$

The equation results in the required torque of $0.535\,\mathrm{Nm}$. The total required torque is the sum of the calculated torque, equalling to $1.13\,\mathrm{Nm}$. As the servo can deliver $2.42\,\mathrm{Nm}$ of torque, it is deemed fit for the purpose.

6.9.3. Rod Sizing

The main load that the rod needs to withstand is the bending moment due to the thrust produced by the motor. The length of the exposed rod was selected to be equal to $60\,\mathrm{cm}$, to provide sufficient clearance for the propeller to not collide with any other components, and a $15\,\mathrm{cm}$ rod protruding inside the gondola, for additional moment support. This leads to the following moment equilibrium equation.

$$\sum M : 0 = T \cdot d_{prop} + M_{react} \tag{6.19}$$

The thrust produced by each motor is equal to the required thrust of $89.45\,\mathrm{N}$, equally distributed between every motor rod. From the moment the ultimate stress in the rod is calculated as shown in Equation 6.20, here y is the distance from the centre, and I is the moment of inertia of the ring section. Rearranging the equation yields Equation 6.21, used to calculate the minimum thickness needed to withstand the induced moment with a hollow circular rod, where r is the outer radius of the rod, selected as $10\,\mathrm{mm}$.

$$\delta = \frac{M \cdot y}{I} \tag{6.20}$$

$$t = r - \left(r^4 - \frac{M \cdot r}{\frac{\pi}{4} \cdot \delta}\right)^{1/4} \tag{6.21}$$

The material selected to be used for the rod is the Bcomp AmpliTex™ 200 composite, a composite reinforced with flax fibres. Its ultimate tensile strength is taken as $200\,\mathrm{MPa}$ [51], verified by Bcomp. Lastly, the calculated moment is equal to $13.4\,\mathrm{Nm}$. This results in the minimal thickness of the rod of $0.22\,\mathrm{mm}$. According to data from Bcomp, a $50\,\%$ volume fraction composite ply thickness is $0.27\,\mathrm{mm}$, therefore a 2 ply composite is taken for the rod, to ensure a safety factor, resulting in a wall thickness of $0.54\,\mathrm{mm}$.

6.9.4. Final Design

To finalise the design, a CAD design was made to aid with the integration of all components as well as the mass estimation of the components themselves. The final product a rod with a reinforced end and screw holes to allow for attachment to the undercarriage, seen in Figure 10.10. To alleviate the stresses imposed due to moments, the rod is extended into the undercarriage and inserted into a slot, to distribute loads. At the connection point an electrical connector will be present to allow for connection of the motor and servo to the flight controller. Furthermore, at the end of the rod an enclosure enclosing the servo and load carrying bearings is located, as presented in Figure 10.11. The motor and the duct screw onto the enclosure, to finalise the assembly, which can be seen in Figure 6.26. The mass of the final assembly can be seen in Table 6.10.

Figure 6.24: *Render of the motor mount rod.*

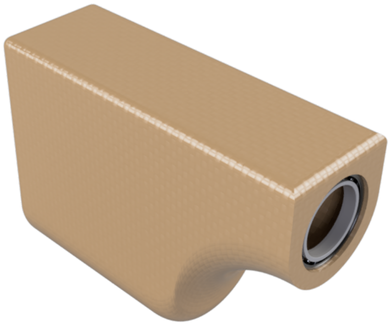

Figure 6.25: *Render of the vectoring system enclosure.*

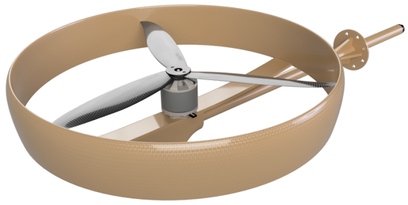

Figure 6.26: *Render of the complete motor mount assembly.*

Table 6.10: *Mass per component of the final propulsion assembly.*

Component	Rod	Enclosure	Duct	Motor	Servo	Bearings	Propeller	Fasteners	Total
Mass [g]	166.8	153.4	284.9	255.0	197.0	10.0	129.0	46.4	1239.5

6.9.5. Verification & Validation

To verify the results from XROTOR, performance test data of the APC 9” x 4.5” blade is compared to the replicated geometry in the BEM software. A total of 10 combinations of RPM, V_∞, and power shown in Table 6.11 are compared with each other.

Table 6.11: *Data point characteristics.*

RPM	1000	2000	3000	4000	5000	6000	7000	8000	9000	10000
V (m/s)	3.58	7.60	11.62	15.65	19.67	23.70	27.72	31.74	35.77	39.79
P (W)	2.24	17.9	58.91	132.73	258.52	397.46	632.35	952.26	1398.93	2012.64

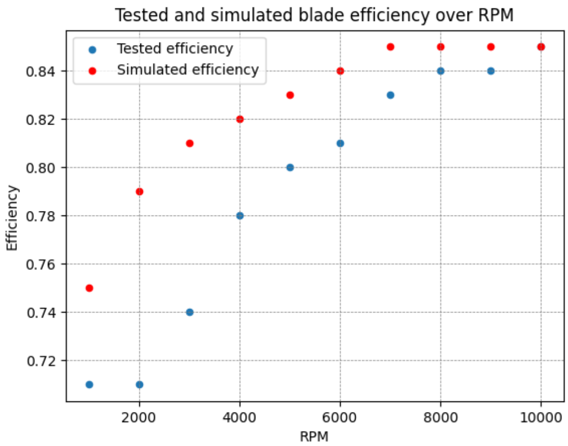

Figure 6.27: *Verification of computed and tested blade efficiency.*

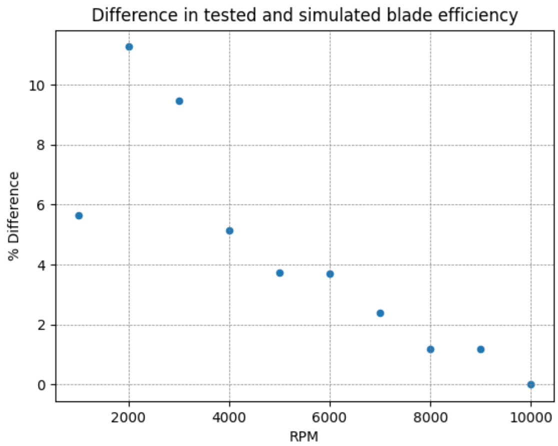

Figure 6.28: *Percent difference of Figure 6.28.*

The blade efficiency seems to be overestimated using BEMT. These inaccuracies are related to simplifications that are not easily corrected. Basically, these errors begin with the assumption of uniform inflow over each annulus of the rotor disc and no interaction between annuli. Also, the tip loss model accounts for blade number effects but not effects due to differences in blade planform [52].

7

Vehicle Solar Power & Electronics

Part of the design is the electronic analysis and configuration of the UAV. The blimp will have to operate mostly autonomously while communicating with the base to inform the operators of various useful information. The vehicle will have to determine its state and perform the necessary actions to follow a predetermined path given by the flight path software. Firstly, the design requirements are given in Section 7.1, followed by the data handling and electronic block diagrams in Section 7.2 and Section 7.3 respectively. The electronic components are listed in Section 7.4. Section 7.5 delves into the design and sizing of the electronic power system. Lastly, Section 7.6 provides the verification and validation of the chapter.

7.1. Design Requirements

This section presents the requirements, driving the design of the power and electronics systems. The requirements and the compliance of the design are presented below.

Table 7.1: *Propulsion design requirements.*

Req. ID	Requirement	Section	Compl.
REQ-VEH-POW-1	The energy storage system shall be able to provide energy required throughout the whole mission.	7.5.2	✓
REQ-VEH-POW-2	An energy generation system shall be used.	7.5.1	✓
REQ-VEH-POW-3	The energy storage system shall have a capacity to travel $100\,\mathrm{km}$ without solar energy input.	7.5.2	✓
REQ-VEH-CO-1	The vehicle communications system shall be able to receive telecommands from the ground station.	7.2	✓
REQ-VEH-CO-2	The vehicle communications system shall transmit telemetry data to the ground station.	7.2	✓
REQ-VEH-CO-3	The vehicle communications system shall have an up-time of more than 99% throughout its mission.	-	✓
REQ-VEH-CO-4	The vehicle communications system shall communicate with the OBC/FC.	7.2	✓
REQ-VEH-CO-5	The antenna shall be mounted in a way that the vehicle structure does not interfere with the communication path to the ground station.	-	✓
REQ-VEH-CO-8	The vehicle communications system shall have a peak power consumption of 60W.	7.4	✓
REQ-VEH-CO-9	The vehicle communications system shall transmit at a minimum bitrate of 100 bit/s.	7.4	✓
REQ-VEH-CO-10	The vehicle communications system shall have a minimum SNR with the ground station of 20 dB.	7.4	✓
REQ-VEH-CO-11	The vehicle shall be controllable from the ground station via telecommands.	7.2	✓
REQ-VEH-CO-19	The vehicle shall be able to monitor its power reserves.	7.4	✓
REQ-VEH-CO-21	The vehicle shall be able to monitor communications link strength.	7.4	✓
REQ-VEH-CO-22	The vehicle shall be able to monitor its attitude.	7.4	✓
REQ-VEH-CO-23	The vehicle shall be able to monitor control surface positions	7.4	✓
REQ-VEH-CO-24	The vehicle shall be able to monitor its position	7.4	✓

7.2. Data Handling Diagram

The data handling diagram gives a clear overview of the flow of information through the systems. The critical component of this diagram is the flight controller. It gathers all the necessary information from the sensors around the craft and determines the necessary commands for the propulsion and control surfaces to get the craft to the correct flight path. The craft also needs to communicate useful data back to the base. This will be done with a satellite communication system, which can also be used to control the vehicle manually. Worth noting is that the flight controller contains an accelerometer and that the power generation and storage system is not present in Figure 7.1 simply because no information flows through that system.

The various components are grouped by their system for better visualization. All the systems will be explained in their respective chapters. The blimp will have capabilities of detecting hydrogen leakage with hydrogen sensors.

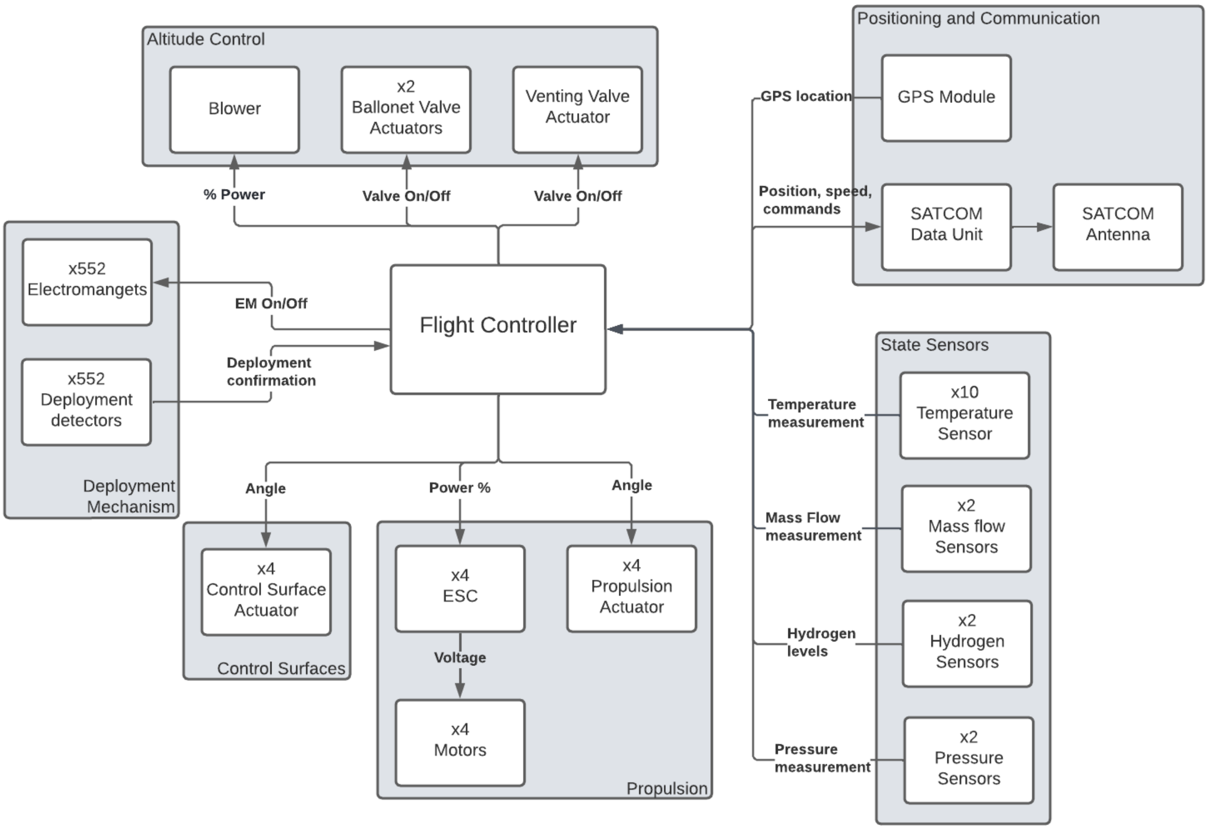

Figure 7.1: *Data handling diagram.*

They will be placed close to the batteries and inside the ballonets. Moreover, the temperature will be monitored in case of a fire on the craft. The craft will be recording its location through a GPS module.

7.3. Electronic Block Diagram

The electronic block diagram demonstrates the flow of power within the system. It showcases how the circuit is connected and its operating voltages. As can be seen in Figure 7.2, the battery pack is the central component of the system. Solar cells generate power from the sun and then transfer that energy to the battery. A solar charge controller is placed in-between the battery pack and the solar cells to stabilise the voltage before transferring the power to the battery. This will increase the life of the battery. All the power first passes through the battery pack and is then distributed around the system. This ensures that the batteries will always be charged in case of an emergency. The battery pack provides power at a voltage of $24\,\mathrm{V}$. Electronic components require power provided to them at a specific voltage. Thus, three DC voltage buses were created (they can be seen in yellow in Figure 7.2) to provide the required voltages for the components. One bus at $24\,\mathrm{V}$, one at $12\,\mathrm{V}$ and one at $5\,\mathrm{V}$. The decrease in voltage was made with a DC/DC step-down converter.

The colour scheme can be seen in the Figure 7.2. Different components were coloured with different colours, depending on their power requirements. Green background refers to the components that need power constantly for the whole duration of the mission. The red background refers to the components that need power only some time during the mission, and white refers to components that do not require power to work.

7.4. Electronic Components

A list of the electronic components used for the functionalities presented in the previous sections along with their power consumption and operating voltage can be found in Table 7.2. The components were selected based on their fit for their purpose or through investigation in prior chapters or reports [4]. The mounting locations of these components can be seen in Figure 7.3.

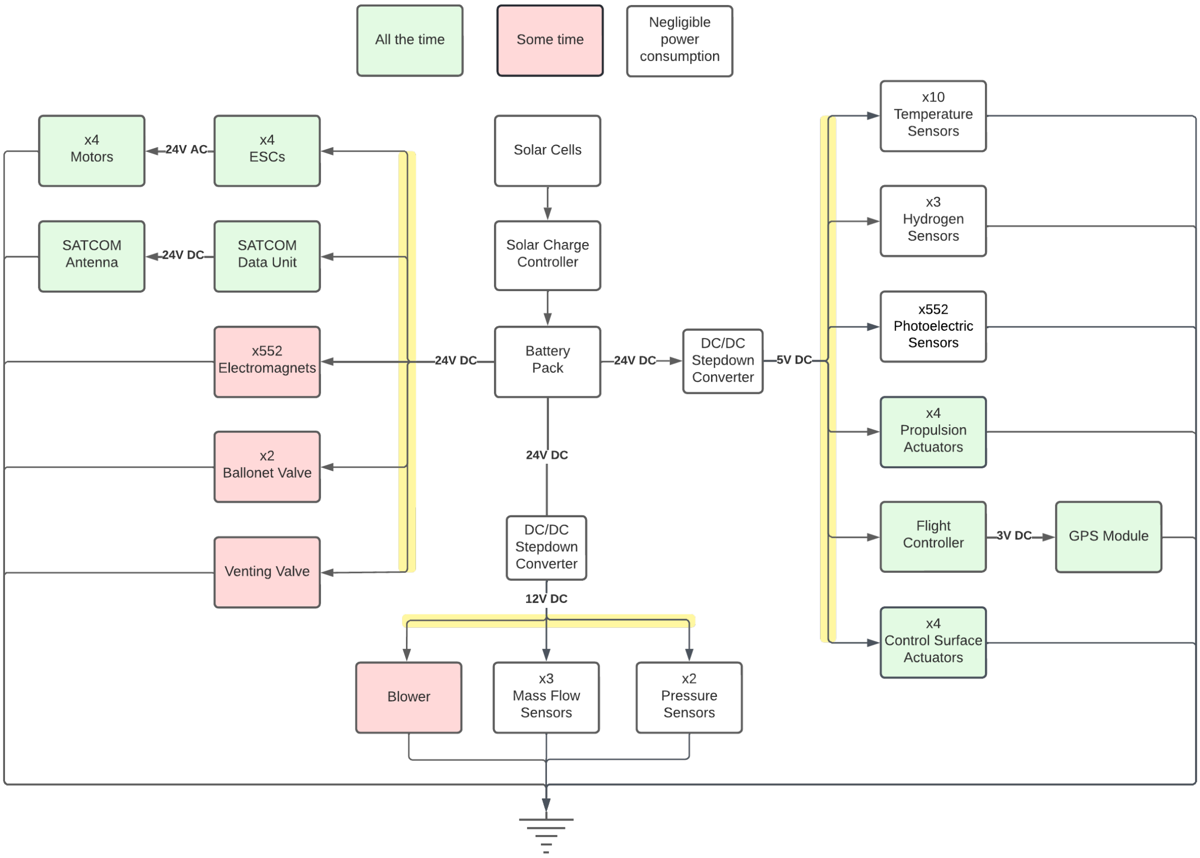

Figure 7.2: *Electronic Block Diagram.*

Table 7.2: *Overview of electronic components.*

Function	Name	Quantity	Constant (Momentary) Power [W]	Operating Voltage [V]	Mass [g]	Cost [€]
Flight controller	Auterion Skynode[53]	1	25	5	188	1490.00
Communications	Honeywell SATCOM Data Unit & Antenna [54]	1	44	24	994	2800.00
GPS module	ZED F9P [55]	1	0.204	3	5	189.99
Propulsion actuators	HS-5805MG Mega [56]	4	0.012(60)	5	197	77.00
Control surface actuators	HS-5805MG Mega Equivalent [Section 8.2]	4	0.012(60)	5	136	77.00
Electromagnet	PEM1213A [57]	552	0(1)	24	10	7.00
Photoelectric sensor	GL5516 LDR Photosensitive resistor [58]	552	-	5	0.25	0.05
Blower	Sanyo Denki 9CRA0412P4K03 [59]	1	(19.2)	12	80	26.90
Ballonet valve	RS PRO Solenoid Valve [60]	2	(19)	24	235	364.67
Venting valve	RS PRO Solenoid Valve [60]	1	(19)	24	235	364.67
Motor	T-motor V505 KV260 [61]	4	477.5	24	255	115.18
Electronic Speed Controller	T-Motor FLAME 80A [62]	4	-	24	109	115.18
Hydrogen sensor	H2-7HYE [63]	3	-	5	40	30.00
Pressure sensor	MPX 2200DP [64]	2	-	12	50	17.54
Temperature sensor	TMP36GT9Z [65]	10	-	5	0.2	1.2
Mass flow sensors	BOSCH 0281002980 [66]	3	-	12	450	75.00
Battery	Sony US18650VTC6 3000mAh[67]	108	-	-	46.6	7.50
DC/DC Stepdown converter	LM2596 3A [68]	2	-	-	30	3.00
Solar charge controller	SmartSolar Laadcontroller MPPT 250/70 [69]	1	-	-	3	907.00
Solar cell	Maxeon Gen III [70]	1863	-	-	6.5	3.33

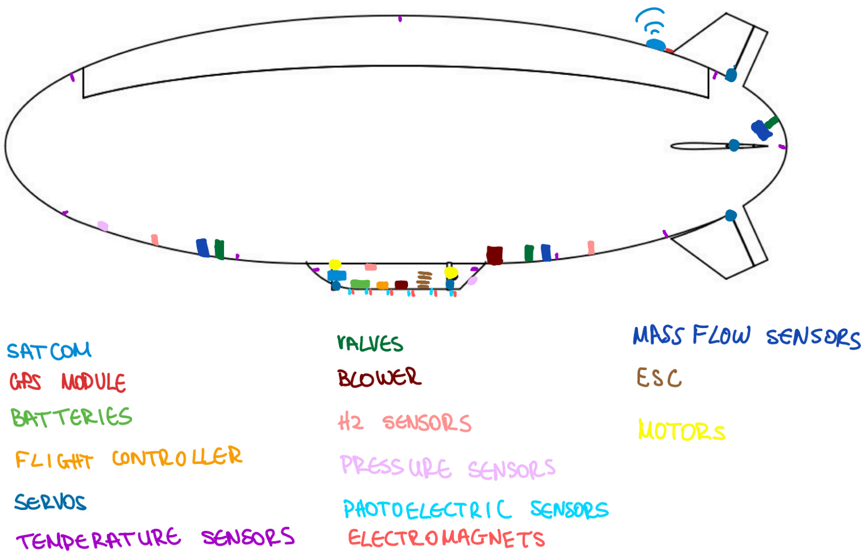

Figure 7.3: *Electronic component placement.*

7.5. Electronic Power System

The electronic power system consists of a power generation and a power storage system. The former is a solar array, while the latter is a battery pack. The design approach for the two systems is described in the following sections.

7.5.1. Solar System Design

The solar array needs to be designed to be sufficient for the power consumption of the electronics components. Due to its double-curved shape and non-constant sun incidence angle, a model has been developed to aid with the design. This section delves into the methodology and final design of the solar array.

Solar Irradiance

The solar irradiance must be evaluated first to be able to calculate the power output of solar panels. The evaluation of the incoming irradiance was performed through the use of Typical Meteorological Year (TMY) data. Such a data sheet provides the typical weather conditions at a location for hourly samples throughout the year. The two values which are of use for this case are the Direct Normal Irradiance (DNI) and Diffuse Horizontal Irradiance (DHI). DNI represents the incoming radiation directly from the sun, while DHI is the incoming radiation from scattering through the atmosphere. The former is dependent on the incoming angle and the latter is equal at any direction, not subject to any shade [71].

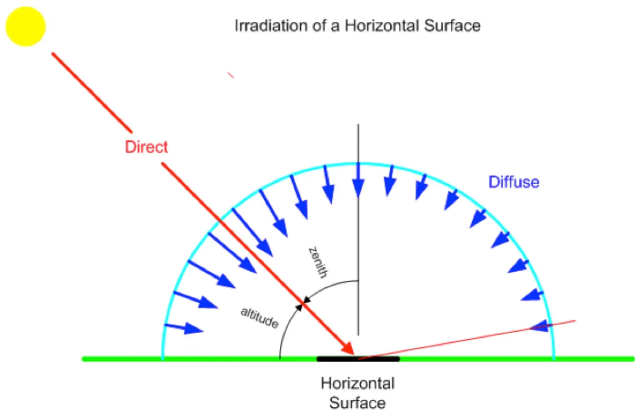

Figure 7.4: *Comparison of the irradiance modes. [72]*

Table 7.3: *Calculated DNI and DHI values.*

	DNI	DHI
Irradiance [W/m2]	404	160

The DNI and DHI values were taken as mean values of the irradiance over the year for the selected flight time slot. These values can be found in Table 7.3.

Solar Panel Area Projection

Due to the nature of the blimp, the solar array is of a complex shape, featuring a double-curved surface. This means simple angle calculations do not suffice for solar power calculation. To calculate the generated power, a model was created which generates the projected solar panel area based on the solar incidence.

Firstly, a model was created to generate 3D points of the solar array. To form the array, x, y and z coordinates of an ellipsoid were generated using Equation 7.1[73].

$$
\begin{aligned}
x &= a \cdot cos u \cdot sin v \\
y &= b \cdot sin u \cdot sin v \\
z &= c \cdot cos v
\end{aligned}
\tag{7.1}
$$

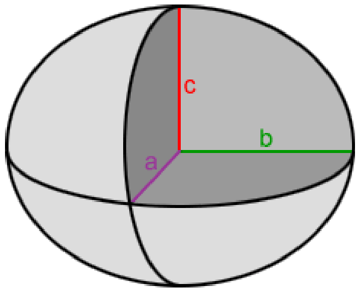

Figure 7.5: *Representation of the ellipsoid semi-axis. [https://www.math.net/ellipsoid]*

In the equation, a, b, and c represent the semi-axes of the ellipsoid, as seen in Figure 7.5. The u and v are distributed arrays of radians, the former spanning the solar panel coverage angle and the latter spanning 180°. The aforementioned solar panel angle is the main driver in the iterative calculation of the array area, as it defines the span of the solar panels over the blimp envelope. The final parameter used in the generation of the array mesh is the length factor, which defines the lengthwise coverage of the solar panel array compared to the total length of the envelope. To achieve the sizing from the length factor, points on the x axis, which fall out of the length factor were removed. The result of the process is seen in Figure 7.6.

Furthermore, with the generated geometry, a projection algorithm was created to generate the actual area exposed to DNI. This is done assuming the sun shines in from the front, which results in the minimum shone area, so it will be a lower bound. The first consideration in the projection is the cut-off angle. This occurs in case the sun incidence is at such an angle that some panels are located at more than 90° from the incident rays, as presented in Figure 7.7. To account for this, the angle is checked and in case of the cut-off, the u or v is adjusted accordingly.

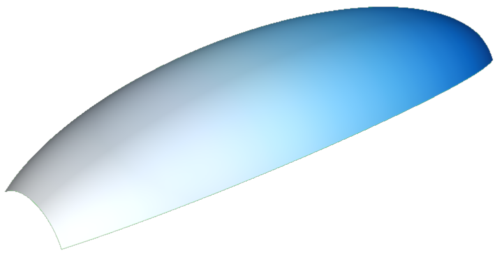

Figure 7.6: *Solar panel geometry generated from the developed model (Panel angle = 100°, Length factor = 0.9).*

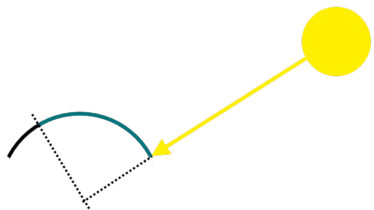

Figure 7.7: *Representation of the cut-off angle.*

The second step in the panel projection is the projection of points onto a plane orthogonal to the incoming sun rays. To create the projection, a vector is defined, pointing from the origin in the direction of the sun rays. Then, each point of the previously defined array mesh is orthogonally projected to a plane, with the aforementioned vector representing its normal vector. The projection is accomplished using Equation 7.2 and the result can be seen in Figure 7.8. P represents the 3D point to be projected, $\vec{v}$ the solar ray vector, and $\vec{N}$ the normal vector of the plane being projected to.

$$P_{proj} = P - \vec{N}((P - \vec{v}) \cdot \vec{N}) \tag{7.2}$$

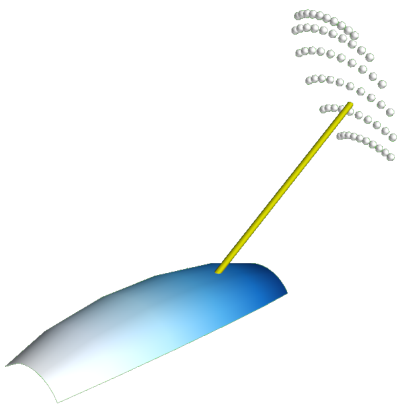

Figure 7.8: *Example of the projected solar array points.*

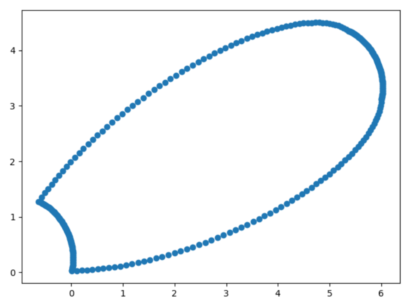

Figure 7.9: *2D polygon of the projected area.*

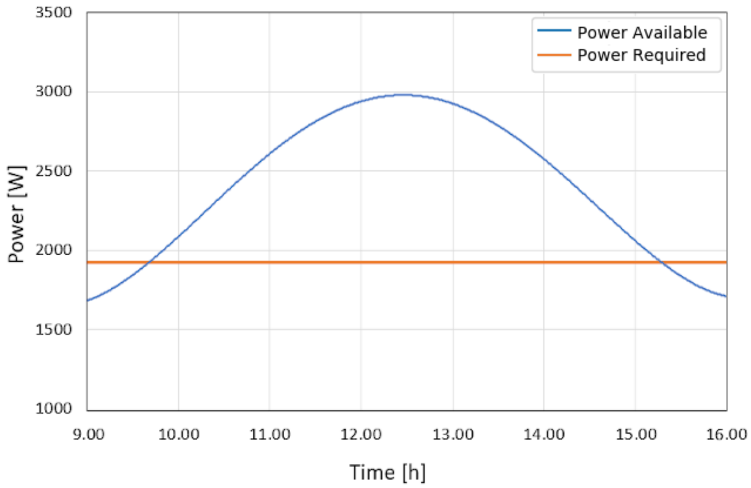

Figure 7.10: *Electrical power required and minimum power available from solar panels versus daytime on an average 21/03 in Sydney, Australia, predicted by the model described in this section.*

Lastly, the projected points are converted into 2D and the area they encompass is calculated. The point coordinates are generated through polar coordinates relative to the origin point (0,0) and the vector from the origin to the second point. The inside points are eliminated so only the points encompassing the polygon remain, as shown in Figure 7.9. Lastly, the area of the polygon is calculated, resulting in the final projected area of the solar array.

Generated Solar Power

Finally, the power generated by the solar array can be calculated. The maximum generated power is calculated using the following equation.

$$P_{solar_{net}} = (A_{projected} \cdot DNI + A_{total} \cdot DHI) \cdot FF \cdot \eta \tag{7.3}$$

Here $A_{projected}$ is the projected area of the solar array calculated in the developed model, A_{total} the total physical surface area of the array, FF the fill factor, η the efficiency and DNI as well as DHI are the previously mentioned irradiance values. The selected fill factor is the typical fill factor of silicon panels, at 80%. The chosen solar cells are the Maxeon Gen III Ultra High Performance cells[70], with an efficiency of 23.1%.

Solar Panel Sizing

This model can be used to size the solar area. The design condition is that the average net available solar power equals the power required for propulsion plus the onboard electronic power. The gross electrical power needed for propulsion is calculated as follows.

$$P_{prop_{el}} = \frac{\rho V^3 S C_D}{2\eta_{eng}\eta_{prop}} \tag{7.4}$$

Where eng stands for the engine efficiency in converting electrical power to mechanical shaft power and prop stands for the propeller efficiency in converting to propulsive power. Utilising iterative means in Python, the solar panel covering angle could be increased until the aforementioned solar model predicted enough power to fly at the target speed. This iteration also took into account that more solar panels will result in more weight, which needs to be born by more lifting gas, and therefore also needs a larger envelope which causes more drag and so forth (snowball effect).

For reliability concerns, the design tool only allows using 80 % of the generated power to be used for propulsion, since the solar model uses average radiation power. However, in reality, the blimp will fly for seven hours and therefore the available power will change, as seen in Figure 7.10. For this reason, the blimp is equipped with a $165\,\mathrm{Wh}$ battery on top of the reserve battery that provides power during the late and early hours and is charged during midday. The slightly larger solar panels also ensure that the vehicle is able to maintain a constant ground speed and can therefore even fly against the wind. Due to sensor placement accuracy concerns, it is not recommended to fly at high wind speeds, though.

For the final design, the solar panel coverage angle was calculated to be 86°, resulting in a total area of $35.62\,\mathrm{m}^2$, or approximately 1863 solar cells. The mass thus results in $1.33\,\mathrm{kg}$, according to provided data[70].

7.5.2. Reserve Battery

The energy storage present on the blimp consists of a battery pack. Its sizing is mainly driven by REQ-VEH-POW-3.

Prior to calculations, the battery type was selected. For this purpose, Li-Ion cells were selected, as they offer better longevity and safer operation, compared to the other candidate, the Li-Po battery cells. Li-Ion cells have a nominal voltage of $3.7\,\mathrm{V}$, with a typical depth of discharge of 90%. The battery pack was sized for travel at optimal velocity, where the least amount of energy would be consumed. This is found to be at the point where the onboard electronics power is twice the propulsive power. This relation was found by differentiating the equation for total stored energy, Equation 7.5, with respect to travel time. Finally, the equation used to calculate the optimal travel velocity is presented below in Equation 7.6.

$$E = P_{el.}t + \frac{1}{2}\rho V^3 S C_D t \tag{7.5}$$

$$V = \left(\frac{\eta_{prop}\cdot\eta_{engine}\cdot P_{electronics}}{\rho\cdot A_{ref}\cdot C_D}\right)^{\frac{1}{3}} \tag{7.6}$$

This resulted in the optimal travel speed of $12.97\,\mathrm{km/h}$ and a travel time of $7.6\,\mathrm{h}$ for $100\,\mathrm{km}$. Furthermore, the reserve battery capacity needs to be $1080\,\mathrm{Wh}$. With the depth of discharge, the final battery pack can be designed. The design is a 6S18P battery pack, consisting of 108 cells Sony VTC6 cells.

7.6. Verification & Validation

The verification and validation is to be performed on the solar system model. The equations used were verified through manual calculation. The main parts to be verified are the body and projection generation. These aspects were verified through visual inspection and measurement of the given visuals. The body generation is verified by plotting the raw body. The panel size is defined through the length factor and panel angle. Verification of the panel size definition is verified in Table 7.4. Deviation from ideal values was found, but is within expected due to the limited number of points used in the generation of the body.

Table 7.4: *Comparison of the model generated values.*

Input Parameter	Input Value	Generated Value	Deviation
Length Factor	0.8	0.79	1%
Panel Angle	133°	133.3°	0.2%

Furthermore, the projection aspect is verified, with the help of Figure 7.8. Through visual inspection, the projection was verified. The projected area was larger than should be, which was adjusted as it was larger by the same factor no matter the configuration. Lastly, the polygon generation for the area calculation was verified by plotting the points in Figure 7.9.

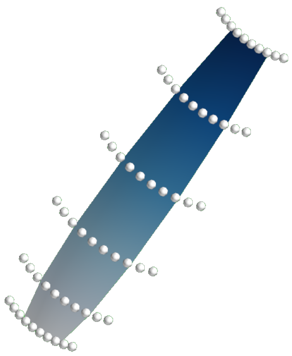

Figure 7.11: *Verification of the body generation.*

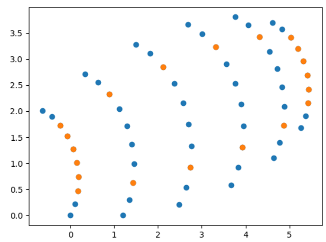

Figure 7.12: *Verification of the panel angle.*

8

Vehicle Aerodynamics and Aerostatics

This chapter delves into the aerodynamic and aerostatic design and behaviour of the vehicle. Firstly, Section 8.1 provides the information on the sizing of the lifting envelope. In Section 8.2 the control and stability surfaces are designed, followed by Section 8.3, which delves into the estimation of the drag coefficient. Finally, the stability and control derivatives are elaborated upon in Section 8.4.

8.1. Lifting Envelope Sizing

All the vehicle weight needs to be borne by the lifting envelope. Since the envelope is filled with hydrogen, it is lighter than air, meaning that the surrounding air will exert a net force B on the envelope, which can be used to lift the payload, equal to the result of equation Equation 8.1.

$$B = g \cdot V_{envelope} \cdot (\rho_{atm} - \rho_{H_2}) \tag{8.1}$$

This equation shows that the envelope volume is proportional to the weight it needs to carry. However, since a larger envelope also requires a heavier hull, which in turn requires more lifting gas, the envelope must be sized iteratively. These calculations are the heart of the design tool, created in Python.

8.1.1. Altitude Effects

As seen in Equation 8.1, the density of the lifting gas, hydrogen, as well as the density of the surrounding air are important factors for buoyancy. The density of the hydrogen can be determined by the state equation

$$\rho = \frac{pM}{RT}, \tag{8.2}$$

where p is the absolute internal pressure, $M = 0.002\mathrm{kgmol}^{-1}$ the molar mass of hydrogen, $R = 8.314\mathrm{kg/J/K}$ and T the temperature in Kelvin. Ergo, the density mostly depends on the atmospheric conditions and therefore altitude, as well as the chosen internal pressure of the envelope. For structural considerations discussed in Subsection 5.2.2, the internal pressure difference was chosen to be $500\,\mathrm{Pa}$ over the air pressure.

Making use of the International Standard Atmosphere, it is possible to size the envelope such that the vehicle is neutrally buoyant for the maximum take-off weight (MTOW) at a certain altitude, called trim altitude. This trim altitude can be reduced by filling the envelope with less hydrogen and instead fill a bit of air into the ballonets at the start of the mission, by the processes described in Chapter 9. However, for a set envelope size, the trim altitude cannot be increased without releasing sensors. Looking at typical mission profiles, the envelope is sized such that the maximum trim altitude at MTOW is $1500\,\mathrm{m}$. This does not mean that the blimp cannot fly higher than $1500\,\mathrm{m}$. Using the active altitude control system, explained in Section 10.2, the blimp can still fly about a kilometre above trim altitude. Moreover, after dropping sensors, the trim altitude can be increased if necessary. This is done by venting less hydrogen than needed to keep equilibrium. For the final design, a hydrogen volume of 146m^3 or $12.2\,\mathrm{kg}$ was calculated.

8.1.2. Mass Estimation

Having determined the required envelope volume, its weight can be obtained by multiplying the ellipsoid surface area by the area density of the chosen material. The surface area of a prolate ellipsoid can be estimated by Equation 8.3.

$$S = 4\pi \left(\frac{2(ab)^p + a^{2p}}{3} \right)^{1/p}, \tag{8.3}$$

Where a is the radius of the envelope, $p = 1.6$ is an ellipsoid constant, and b half the length. For a chosen spheroid ratio of 3, $b = 3a$, the optimal ratio according to [74]. The radius a is determined as follows in Equation 8.4.

$$a = \left(\frac{V}{4\pi} \right)^{1/3} \tag{8.4}$$

For a MTOM of $143.4\,\mathrm{kg}$, the required volume is equal to $145.8\,\mathrm{m}^3$, resulting in an envelope of radius $2.22\,\mathrm{m}$, length $13.58\,\mathrm{m}$ and surface area $158\,\mathrm{m}^2$. For the material chosen in Chapter 5, this results in an envelope mass of $30.3\,\mathrm{kg}$

8.1.3. Envelope Aerodynamic Lift

Every body at an angle of attack will generate a drag and a lift force when exposed to airflow. For ellipsoids, the relation following in Equation 8.5 about its aerodynamic lift force can be made.

$$C_{L_\alpha} = \frac{2}{k_s}, \tag{8.5}$$

where k_s is the fineness or spheroid ratio of a prolate ellipsoid, chosen to be three for the final design[74]. Furthermore, the aerodynamic centre of the envelope was estimated to lie at 37% of its length, based on a similar blimp design [17].

8.2. Control Fin Design

The blimp features tail fins at the rear end of the envelope, which act the same as a tail in airplanes, to provide stability and control. This section will explore the sizing process and the final design of the aforementioned fins.

8.2.1. Sizing Methodology

The sizing of the control fins was performed by using historical data on existing airships and extrapolating the data to the blimp in question. The fin surface area was calculated through the surface to volume ratio of 0.0327[17].

From the surface area the remaining geometric properties were calculated, assuming an aspect ratio of 0.5 and the span assumed as the average of the root and tip chord[17]. The equations utilised are found below[17].

$$c_{root} = \sqrt{\frac{2 \cdot S(1+\lambda)}{1+\lambda+\lambda^2}} \tag{8.6}$$

$$c_{tip} = c_{root} \cdot \lambda \tag{8.7}$$

$$b_{exposed} = 0.5 \cdot c_{root}(1+\lambda) \tag{8.8}$$

$$MAC = \frac{2}{3} \cdot c_{root}\left(\frac{1+\lambda+\lambda^2}{1+\lambda}\right) \tag{8.9}$$

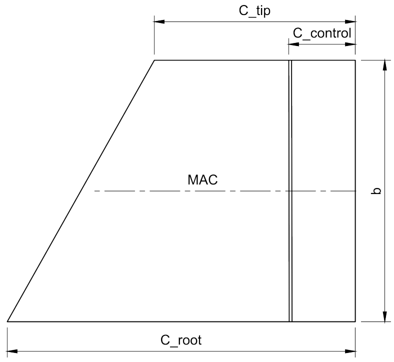

Figure 8.1: *Tail fin geometry.*

Furthermore, the control surface of the fins is sized according to a paper on the design of a small airship[75]. The control surface is decided to have an equal root and tip chord. To allow for parametric scaling of the control surface, it is defined as a ratio of the root chord. This ratio is calculated as 19.78% of the total root chord. The geometry of the control fin is presented in Figure 8.1.

Lastly, the mass of the fins is estimated. The fin itself is an inflatable structure, as presented in Figure 8.2, with a solid control surface. The estimations for the mass of the fin are found below [17]. ρ is the surface density of the material used, S denotes the total surface of the object, and F denotes various coefficients. The 4.88 present in Equation 8.11 and Equation 8.12 represents the conversion factor from $\frac{lb}{ft^2}$ to $\frac{kg}{m^2}$, as F_{PSQ} and $F_{actuator}$ correlate to units in $\frac{lb}{ft^2}$.

$$W_{fin} = \rho_{surface}(S_{total} - S_{control}) \cdot F_{AF} \cdot F_T \tag{8.10}$$

$$W_{control} = F_{PSQ} \cdot S_{control} \cdot [4.88] \tag{8.11}$$

$$W_{actuator} = F_{actuator} \cdot S_{control} \cdot F_{instal} \cdot [4.88] \tag{8.12}$$

$$F_{AF} = 1.26 \qquad F_T = 2.36 \qquad F_{PSQ} = 0.3$$
$$F_{actuator} = 0.08 \qquad F_{instal} = 1.15$$

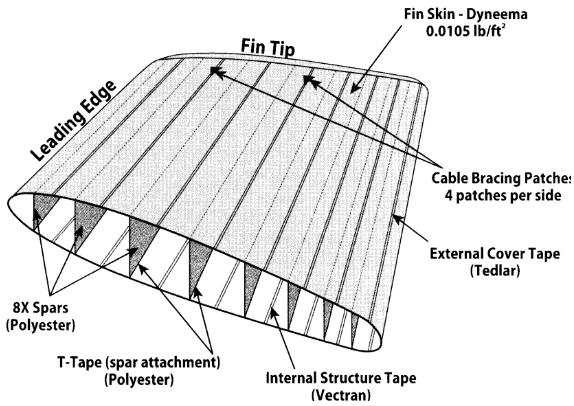

Figure 8.2: *Sketch of the fin structure[17].*

8.2.2. Final Design

The final design properties were calculated iteratively, through the iterative Python model, and resulted in the values presented in Table 8.1. The values are for each of the four fins present on the blimp in a "+" configuration at the tail.

Table 8.1: *Final properties of a control fin.*

Property	Value
Airfoil	NACA 0008
Planform Surface Area	$1.18\,\mathrm{m}^2$
Root Chord	$1.43\,\mathrm{m}$
Tip Chord	$0.72\,\mathrm{m}$
Exposed Span	$1.07\,\mathrm{m}$
MAC	$1.11\,\mathrm{m}$
Taper Ratio	0.5
Mass	$1.59\,\mathrm{kg}$

With the final properties, the control performance of the fins will be evaluated. The main property in question is the lift coefficient of the fins. The lift coefficient slope is calculated according to the following equation[17], where AR is the aspect ratio, and Λ_{LE} is the leading edge sweep.

$$C_{L_\alpha} = \frac{2 \cdot \pi \cdot AR}{2 + \sqrt{4 + AR^2(1 + tan\Lambda_{LE}^2)}} \tag{8.13}$$

The leading edge sweep was evaluated from the geometry, and is equal to $29.4°$. The aspect ratio was calculated equal to 4.17. By definition[17] the span and surface area used in the aspect ratio calculation is the total span and surface area, including the area obstructed by the envelope, as can be seen in Figure 8.3.

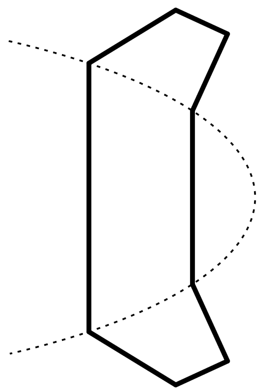

Figure 8.3: *Representation of the total planform used in the aspect ratio calculation.*

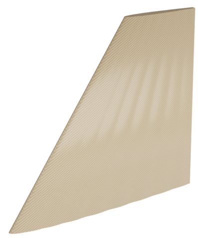

Figure 8.4: *Final render of the control fin.*

With the values, the lift coefficient curve is calculated, to be used in the flight dynamics analysis. The curve was calculated as $C_{L_\alpha} = 0.3636$. The render of the final design of the inflatable fin can be found in Figure 8.4.

8.3. Drag Estimation

An important aspect of the vehicle design is the drag generated. It drives the required thrust and consequentially influences nearly every system. To calculate the drag, the final geometry previously generated is required, along with the drag coefficient. In this case, the volumetric drag coefficient is used, as is common for bodies of rotation and airships [74]. The blimp is separated into sections for which the drag is estimated. These sections are the envelope, the control fins, the gondola, and the engines.

8.3.1. Envelope Drag Coefficient

The drag of the envelope is predicted as a bare smooth hull, based on the spheroid ratio and the turbulent skin friction drag coefficient C_f. The C_f is dependent on the flow Reynolds number, calculated with the equation following in Equation 8.14[74], where V is the cruise velocity, l is the envelope length and ν is the kinematic viscosity of air, equal to $15.06 \times 10^{-6}\,\mathrm{m}^2/\mathrm{s}$[74]:

$$Re = \frac{V \cdot l}{\nu} \tag{8.14}$$

With the Reynolds number, the skin friction coefficient can be calculated. For the skin friction, two relations are used: the Blasius skin friction in Equation 8.15 [74] and the Schoenherr skin friction equation in Equation 8.16 [76]. The first equation is valid up to $Re = 10^6$ and the latter is valid from the limit of the previous one up to $Re = 10^{10}$.

$$C_f = \frac{1.328}{Re} \tag{8.15}$$

$$C_f = \frac{0.075}{(\log_{10} Re - 2)^2} \tag{8.16}$$

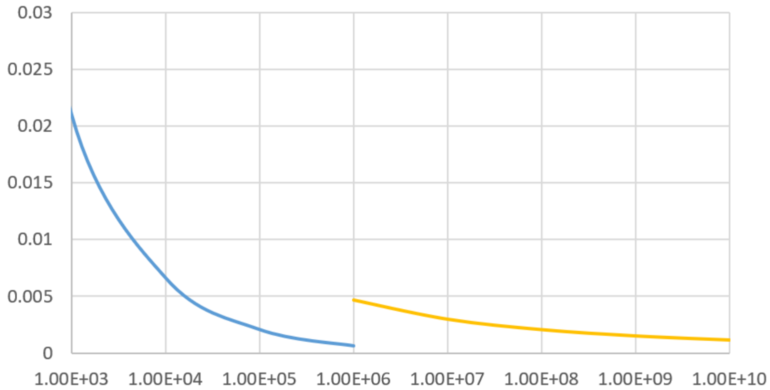

Figure 8.5: *Friction coefficient plotted versus the Reynolds number.*

Lastly, to calculate the envelope drag coefficient, the ratio between the drag coefficient and the skin friction needs to be set up. The ratio is calculated using Equation 8.17[74], where l is the length and d the diameter of the envelope.

$$\frac{C_d}{C_f} = 4(l/d)^{1/3} + 6(d/l)^{1.2} + 24(d/l)^{2.7} \tag{8.17}$$

8.3.2. Control Fin Drag

As previously mentioned, the airfoil used on the control surface uses the NACA0008 airfoil. The C_d curve of the airfoil is presented in Figure 8.6 [77]. From the data, the C_d at $\alpha = 0°$ is equal to 0.00392. However, this is the surface drag coefficient, which needs to be converted to the volumetric drag coefficient, relative to the envelope volume. This is achieved by multiplying the drag coefficient with its reference dimension, in this case, the fin surface area, and dividing it by $V^{2/3}$, an approach which will be utilised for further drag coefficients.

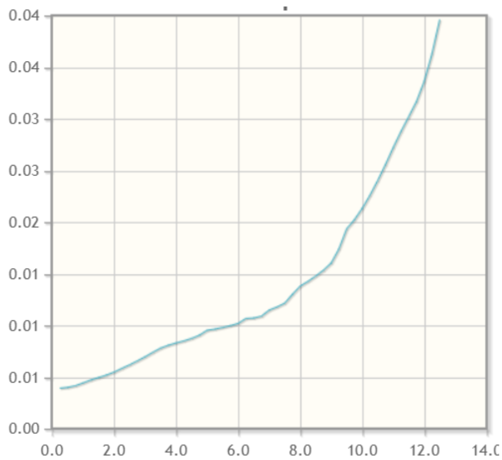

Figure 8.6: *Drag coefficient curve plotted against the angle of attack, of the NACA0008 airfoil. [77]*

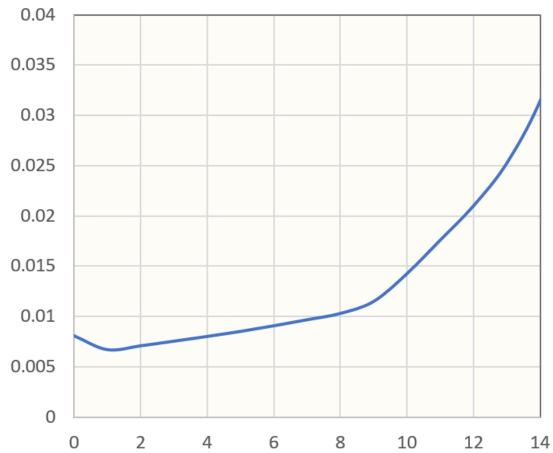

Figure 8.7: *Drag coefficient curve plotted against the angle of attack, of the NACA4312 airfoil. [77]*

Furthermore, as the fins are attached to the envelope, there is an interference drag induced. This drag coefficient is calculated based on Equation 8.18 [74] and converted using the previously mentioned approach. In the equation, t/c is the thickness ratio of the airfoil, which is equal to 8 % for the NACA0008 airfoil.

$$C_{d_{interference}} = 0.75(t/c) - 0.0003/(t/c)^2 \tag{8.18}$$

8.3.3. Gondola Drag

The gondola and payload bay of the blimp is an added protrusion to the streamline shape of the envelope. Hoerner presents drag coefficients of several appendages, similar to the gondola, in Figure 8.8 [74]. From the presented examples a C_d of 0.11 is chosen, due to the aerodynamic shape of the gondola. The second consideration is the interference drag between the payload bay and the envelope. This is calculated through Equation 8.19, which depends on the ratio between the length and height dimensions of the gondola [74]. Both of the drag coefficients are later converted to volumetric drag coefficients.

$$C_{d_{interference}} = 0.002 \cdot (l/h) \tag{8.19}$$

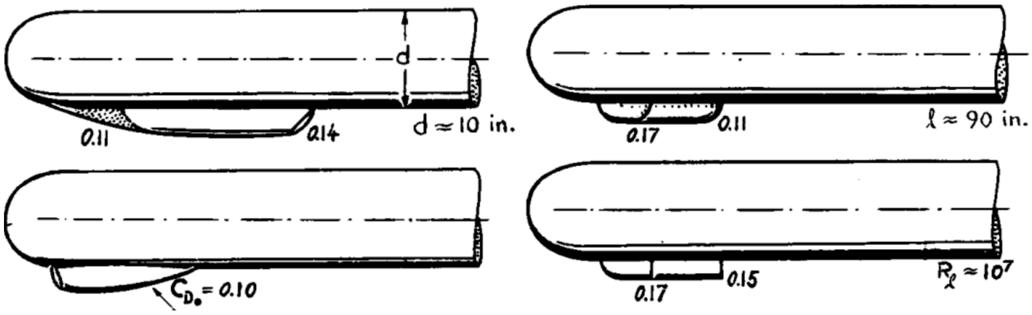

Figure 8.8: *Drag of several appendages [74].*

8.3.4. Propulsion Drag

The final component of the drag coefficients is the drag induced by the propulsion and its mounts. The equation of the drag coefficient of the engines is equal to $0.5 \cdot 1.2$[74], with the reference dimension being its projected frontal area. The 0.5 indicates a relatively rough shape, including the drag of the mounting rod, and the 1.2 accounts for the interference drag induced between the mount and the gondola[74]. This does however not account for the drag induced by the duct. The duct is constructed from a ring with the shape of a NACA 4312 airfoil. The drag coefficient was generated through XFOIL and equals to 0.00807 at $\alpha = 0°$, which is the nominal angle through cruise, presented in Figure 8.7.

Finally, in the table below, the summarised coefficients of drag are presented. The table presents the drag coefficient in the original reference dimension, the converted volumetric drag as well as the total drag coefficient of the blimp. These values are then used in the drag force calculation, in the iterative Python design tool.

Table 8.2: *Summary of the blimp drag coefficients.*

Component	Original Cd	Volumetric Cd	Nr	Total Cd
Envelope	0.0248	0.0248	1	0.0248
Control Fins	0.0170	0.000175	4	0.000696
Gondola	0.142	0.00103	1	0.00103
Propulsion	0.608	0.000317	4	0.00127
Total				0.0278

8.4. Control and Stability Derivatives

The forces the tail fins exert on the vehicle are generated due to lift if the fins are at an angle of attack or the control surfaces are deflected. Stability and control derivatives are therefore directly proportional to the C_{L_α} of the fins. The equations used to obtain the derivatives can be found on page 283 of [17]. A list of all derivatives can be found in Appendix D.

9

Vehicle Buoyancy Control

At the start of the journey, the blimp requires some level of buoyancy, or aerostatic lift, to be able to fly. However, as sensors are deployed, the amount of lift required to maintain the same altitude decreases. To counteract this, the blimp will have a buoyancy control subsystem, the design of which is discussed in this chapter. Firstly, Section 9.1 presents the design approach, followed by Section 9.2 listing the design requirements, and Section 9.3 with the functional analysis. Section 9.5 writes up on the trade-off of concepts presented in Section 9.4. Section 9.6 gives the detailed design of the buoyancy system. Lastly, Sections 9.7, 9.8, and 9.9 provide the sensitivity, risk, and sustainability analyses.

9.1. Design Approach

In this section the way the altitude control system design was approached will be discussed. All the design options will be evaluated with respect to the criteria introduced below, selected after looking at the various possible options and taking into account the differences between them and their impact on the mission and vehicle designs. The weights assigned to each criterion are discussed below as well.

Risk
First, the risk is especially important for this part of the vehicle designs, since there are different considerable risks associated with each of the identified design options. The risk assessment will be performed qualitatively by discussing the risks associated with each option after preliminary sizing and journey creation for each option. Although the risk is a key differentiator between the options, it is expected that all of these risks will be able to be mitigated and the magnitude of them will be similar. Therefore, a weight of two out of four was assigned to this criterion.

Ease of Operation
Ease of operation is also of great importance to the EcoSense mission and the operation of each of the design options here varies quite widely. Once more, this criterion will be evaluated qualitatively after deliberating the user journeys associated with each design option. Since user centred design is at the core of EcoSense's methodology and the buoyancy control subsystem has a sizeable impact on the user journey, this criterion was given the highest possible weight.

Sustainability
Sustainability is an essential part of the design of all subsystems, however, it was found difficult to estimate the relative sustainability performance of each subsystem option. Therefore, a separate sustainability scoring system was devised and will be introduced later. This was done to reduce the ambiguity of the sustainability rating. Given the importance of sustainability in the EcoSense project, this criterion was given a weight of three out of four.

Manufacturability
The ease with which the given design can be finalised and brought to production is also important for the decision at hand. There is an opportunity cost, as well as an actual cost of choosing a design which is harder to design and manufacture while providing the same performance. This waste of resource is to be avoided, and therefore this criterion is given a weight of three out of four.

Weight
The final criterion is the weight which was selected as an indicator of the efficiency of each design option. Added weight in the subsystem will result in a snowball effect of the weight of the whole vehicle. This causes operations to be more challenging and costs to grow. This criterion, though considerable, was not taken as the most important in this decision, and so a weight of two out of four was assigned to it.

9.2. Design Requirements

Among the requirements defined for the vehicle, there is only a single one which calls for the altitude control system directly.

Table 9.1: *Buoyancy control requirements.*

Req. ID	Requirement	Section	Compl.
REQ-VEH-CO-14	The vehicle shall deploy the sensors from an altitude of less than 500 metres above ground.	-	✓

9.3. Functional Analysis

The functional flow below in Figure 9.1 describes all the functions that need to be performed by, and in relation to the buoyancy control system. This provides a framework for idea creation as well as idea evaluation, through looking at the functions in relation to especially the risk and ease of use criteria.

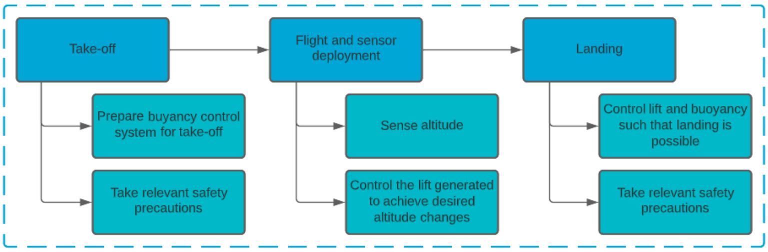

Figure 9.1: *Functional flow and breakdown of the buoyancy control subsystem.*

9.4. Design Options

To generate design options, first, an ideation was conducted, resulting in a swarm of ideas. After elimination of the clearly impractical and infeasible ones, these concepts can be compressed and organized into the design option tree presented below in Figure 9.2.

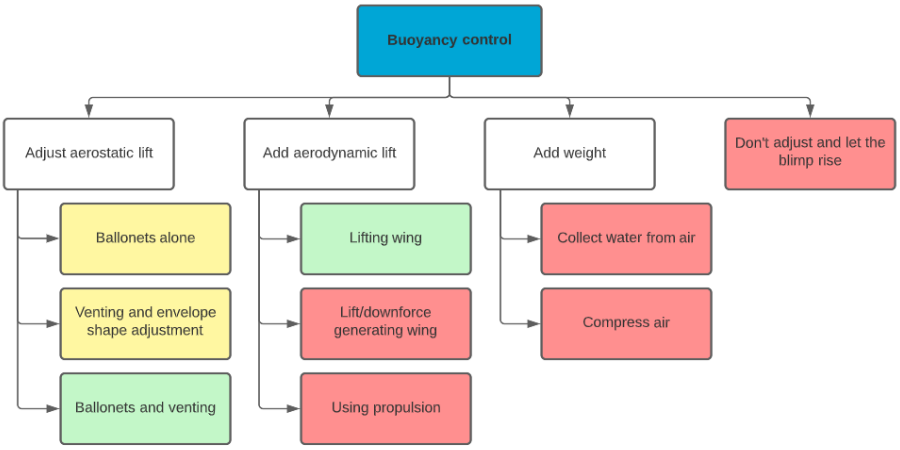

Figure 9.2: *Buoyancy control design option tree.*

Preliminary sizing was performed on all the options in the design option tree to investigate their feasibility. This led to the elimination of the options which add weight to the blimp over time, to make up for the weight lost by dropping the sensors. The equipment needed to extract enough water fast enough from the potentially very dry air would be too big, heavy and power-hungry. The same goes for the air compression, but even the air itself would require either very high compression with a very heavy pressure tank, or the air would take up too much volume.

The option to let the blimp rise was also deemed infeasible, as it would rise to altitudes in the order of kilometres and would thus not only break requirement REQ-VEH-CO-14 which stipulates that sensors shall be released at an altitude of up to only 500 meters above the ground. It would also make it excessively hard to fulfil the deployment accuracy requirement. Furthermore, landing with this design option would require additional measures, such as venting or thrust downwards.

The concept where a wing is used to generate lift for the first half of the mission and downforce for the other half had the same issue. At the end of the mission, it would be positively buoyant, only held down by the downforce generated by the wing, and it would therefore require venting or downwards propulsion to land, too. This was not deemed a safe option, as the blimp would start rising in case of propulsion, control or communications failure.

Finally, using propulsion to provide the additional force required to lift the payload until it is dropped would drastically increase the power budget and the power requirements would no longer be able to be fulfilled by the solar panels on the blimp. Therefore, this option was eliminated as well.

This leaves four design options on the table to be investigated more deeply, of which two seem more promising. The aspects of these solutions will be discussed below and illustrations of all of them can be seen in Figure 9.3.

9.4.1. Ballonets

The traditional way to control buoyancy is to use ballonets. These are sacks inside the envelope which can be filled with air pumped in from the atmosphere as needed. This compresses the lifting gas and results in an increase of the average density of the gas in the envelope, thus decreasing the lifting force magnitude. However, the main problem with this solution is the amount of mass that needs to be dropped during flight. All the sensors make up for a significant fraction of the overall mass of the blimp, so dropping them and remaining neutrally buoyant results in a big increase of pressure in the envelope, in the order of tens of kilo-pascals. This then increases the mass of the envelope. Additionally, to create such pressures, quite a heavy air compressor is required. The manufacturing of these will also have an impact on the sustainability of this solution. Furthermore, carrying hydrogen in a highly pressurised envelope comes with additional risks. On the other hand, one big advantage of this solution would be the ease of operation. The take-off and landing would be safer, since the blimp would have static lift stability at all times and no hydrogen refilling would be required unlike some other solutions presented below. Manufacturing would also not be made more difficult by employing this option.

9.4.2. Ballonets with Venting

To avoid the issues associated with high envelope pressures described above, it is possible to vent the lifting gas to retain the same pressure, while decreasing the aerostatic lift. Then, the envelope as well as the air compressor can be much lighter, however, more problems are introduced with the venting of hydrogen. From a risk standpoint, allowing hydrogen to mix with air in the vicinity of the blimp is a dangerous process which will need to be carefully handled. From an operations point of view, the gas will need to be refilled after each flight (once a day) making operation more complicated for the user. This also means a lot more hydrogen would have to be used during the operation. While hydrogen itself has no environmental impact when released freely, it is the production and even more so the transport of the hydrogen which cause some penalty to the sustainability of this design option. From a performance point of view, once the lifting gas is vented, the buoyancy cannot be increased back again, which could be a problem in some instances of change of environment, but can easily be compensated with the active altitude control system. Moreover, the weight and manufacturability would both be great with this option.

9.4.3. Venting with Adapting Shape

The next concept pairs venting of the lifting gas with a different compensation method. Instead of blowing up air ballonets inside the envelope to fill the space, the volume of the envelope is adjusted. This comes with the same venting associated issues as the previous solution, but without the need to create the ballonet system, instead replaced with the challenges of changing the shape of the envelope in flight. This would likely be done with an arrangement of strings being pulled in by winches, to change the shape of the blimp to a more slender one throughout the flight. The problem is, this would be hard to perform while retaining optimal aerodynamics, with the solar panels on the envelope further increasing the difficulty of this problem. The manufacturability and difficulty of the design are therefore big downsides of this solution. There would also likely be a lot of reliability issues with so many new attachments inside the envelope, leading to increased risk of failure. On the sustainability front, this meets the same problems as venting with ballonets, and it performs somewhat worse than that solution in the weight aspect, due to the weight of the internal suspension system with winches being expected to be higher than that of a low pressure ballonet system.

9.4.4. Lift-generating Wings

Lastly, an aerodynamic lift generation idea: Within this concept, the blimp only provides enough lift to support the structure, envelope and everything else except for the payload (about $45\ \mathrm{kg}$). This weight would then be lifted first by propellers during the vertical take-off, and then by a set of lift generating wings during cruise. As the sensors are deployed, the lift generated by the wings would be adjusted and at the end of the mission, when landing, the blimp would be neutrally buoyant. Taking off with negative buoyancy and using a lot of propulsion power, increases the risk of something going wrong during take-off, as well as during the operation, as the blimp can no longer hover for most of its journey. Additional safety procedures would be required to address this, making operations somewhat more difficult, especially during take-off, but still easier than when having to refill the hydrogen after every flight. On the weight side, a bit of weight is added by the wing itself, but much more weight is taken up by the additional propulsion system weight and battery weight required to provide enough power and energy for the power-hungry take-off procedure. On the other hand, since the envelope would no longer have to lift the payload, it could be made smaller, thus also decreasing drag and via a positive snowball effect, ending up at a weight very comparable to the solution with the venting and ballonets combination. The sustainability of this solution comes with the problem of using much more batteries, but without the problems associated with venting hydrogen. Finally, in terms of manufacturability, this option is the winner out of the pack, as it allows for a very simple envelope without any ballonets, only adding a wing which, at the required size, could be produced quite simply.

9.5. Trade-off

With all the options introduced, in this section it will be attempted to put relative numbers on all the up and downsides of each option, in a trade-off. Before the overall trade-off however, the sustainability comparison was elaborated as shown in Table 9.2 to allow a deeper level of understanding of the differences between the options regarding sustainability. As can be seen in the table, the impacts were sorted into the three life phases: manufacturing, use and end of life. The importance of the impacts of each of these phases was rated from zero to three. Then, sustainability questions were devised relevant to each of these phases, and rated once again from zero

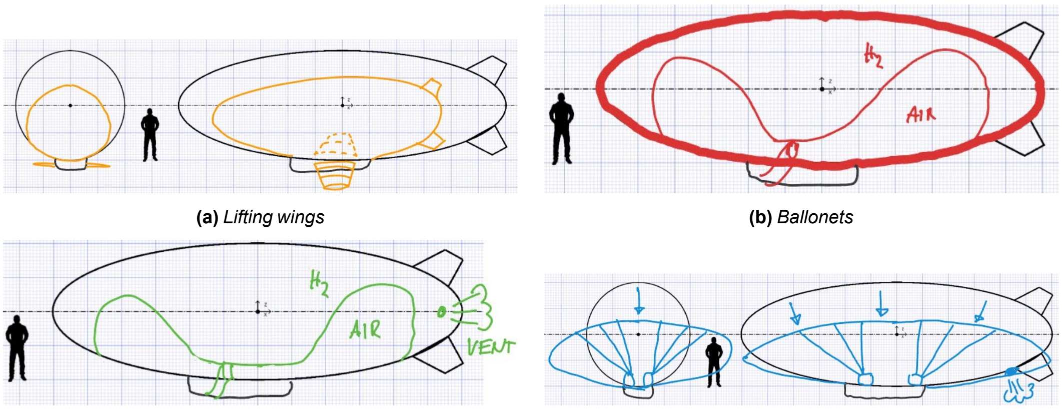

(a) *Lifting wings* **(b)** *Ballonets*

(c) *Ballonets with venting* **(d)** *Venting with deflation*

Figure 9.3: *Buoyancy control concepts*

Table 9.2: *Sustainability comparison*

Sustainability	Weight	High score is	Wings	Ballonets	Ball + vent	Vent
Manufacturing	3		1.25	1.00	2.00	3.00
Can sustainable materials be used?	1	Sustainable	2	1	2	3
How much material is used?	3	Little	1	1	2	3
Use	2		2.11	1.56	2.56	2.56
Does it increase energy use?	3	Low energy	2	1	3	3
Are expendables used in the operation?	1	No expend.	3	3	1	1
Does it make transportation harder?	0.5	Easy trans.	1	2	3	3
End Of Life	3		2.17	1.33	1.67	1.67
Can materials used be recyclable?	2	Recyclable	2.5	2	2	2
Is a mix of materials necessary?	2	No mixing	2	1	2	2
Is disassembly of parts easy?	2	Easy	2	1	1	1
Rated from 0 to 3		Total score:	**1.81**	**1.26**	**2.01**	**2.39**

Table 9.3: *Trade-off of buoyancy concepts*

Criteria	Risk	Ease of Ops	Sustainability	Manufactur.	Weight	
Weight	2	4	3	3	2	Result
Wing	1.5	2.25	1.81	3	3	32.43
Ballonet	3	3	1.26	2.5	0	29.29
Ball, vent	2	2	2.01	3	3	33.04
Deflation	2	2	2.39	0	1.5	22.17

to three, depending on how important they are to the impact in that life phase. Finally, each concept was scored from zero to three with respect to each question. Then, by way of weighted averages, the final sustainability scores for each solution were reached.

With the sustainability sorted, let us now look at the final trade-off table in Table 9.3 below. Here, it can be seen that the lifting wing and ballonet venting systems performed the best in the trade-off, followed by the ballonets without venting and the deflation in last place. However, the decision was not entirely concrete after performing this trade-off, as the results are very sensitive to any changes. Therefore, both the wing and ballonets with venting options were explored in-depth. In the end, the decision was made to go with the ballonets with venting solution. Even though both solutions came with their own challenges, the team felt that the challenges of this solution were more known, and that more unexpected challenges would await with the wing solution, especially in relation to control and more elaborate risk mitigation strategies. Therefore, the ballonet with venting solution will be further discussed in detail in the next section.

9.6. Detailed Design

With the concept selected, the details of the design and exact components can be investigated. As part of this, the subsystems examined will be the ballonets and their size and material selection, the ballonet inflation and deflation system, the hydrogen venting system and the control of the whole buoyancy control subsystem.

9.6.1. Ballonet Design

First, the ballonets will be investigated. These are not a readily available part and will therefore be designed and manufactured by the EcoSense team. The first parameter of interest for the ballonets is the size that they are required to have. This is determined by the amount of hydrogen that shall be vented to accommodate the release of all sensors. A volume of air equal to that volume of hydrogen will need to be pumped into the envelope and thus into the ballonets to maintain the same envelope pressure, while decreasing the buoyancy. This is expressed in Equation 9.1, with m_{MTOM} the maximum take-off mass, $m_{payload}$ the mass of all the sensors to be dropped during the mission, $V_{envelope}$ the volume of the entire balloon envelope and finally, $V_{ballonets}$ the maximum inflated volume of the ballonets.

$$V_{ballonets} = \frac{V_{envelope}}{m_{MTOM}} \cdot m_{payload} \tag{9.1}$$

This volume will be divided into two separate ballonets, a front and a rear one, to provide the possibility to control the distribution of the aerostatic lift and correct for any unfavourable change in centre of gravity position. For this purpose, the volume of each ballonet will be equal to $\frac{V_{ballonets} \cdot 1.2}{2}$, with the 20 percent margin to allow for the aforementioned lift distribution control even when the ballonets are required to be fully inflated. This results in a volume of $23.7\,\mathrm{m}^3$ for each of the two ballonets.

The next question for the ballonets is the one of material choice. The ballonet envelopes are not under any pressure, since there is naturally no pressure difference between the ballonets and the hydrogen in the envelope. Therefore, stress is not a factor in the design of the ballonets. The main requirements are therefore for the material to be impermeable to gas, such that the hydrogen and air do not mix, and to be durable, such that it is able to withstand the inflation and packing cycles. Although quite a low mass of this material will be used, it should be sustainable if possible. Keeping this in mind, preliminarily, PU film was selected as the material, which is the same as the layer ensuring low permeability in the envelope.

That concludes the top level design of the ballonets. For the ballonets to be useful, a mechanism is needed which will fill them and this is the topic of the next section.

9.6.2. Inflation System Design

The inflation system operates the ballonets by filling them with air gradually. First the architecture of the system will be discussed, followed by the sizing of each component.

Architecture

The inflation system will consist of a blower, which will provide the airflow, connected through a junction to two solenoid air valves. The valves are required to enable the closing of the ballonets, which is required, for example, on the way back to the launch site after the deployment of all the sensors. A single blower is used to save power and weight, with the valves controlling the distribution of the air. The blower sucks air in through a manifold to protect it from potential water spray or other debris. The architecture can be seen in Figure 9.4, with the blower in blue and valves in red, with the arrows indicating airflow. The tubing continues from the valves into the ballonets inside the envelope. The rest of the system is located in the gondola, outside the envelope, to limit the contact of components with hydrogen. With the architecture established, individual components can be investigated and sized.

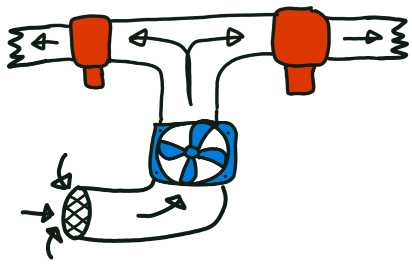

Figure 9.4: *Architecture of the ballonet inflation system*

Blower

There is a wide range of air fans available on the market, and therefore it makes sense to select one that is already available. To select a suitable fan (as well as a valve, later on), one must consider the airflow and pressure requirements posed on the system. On the airflow front, enough airflow must be provided to fully fill the combined volume of the ballonets in the time window in which all sensors are dropped. Equation 9.2 describes this in terms of volumetric airflow $\dot{V}$ and the total time of sensor deployment $t_{deployment}$ in hours. This results in a required airflow of $13.9\,\mathrm{m}^3/\mathrm{h}$.

$$\dot{V} = \frac{V_{ballonets}}{t_{deployment}} \tag{9.2}$$

On the pressure side, the pressure inside the envelope will be $500\,\mathrm{Pa}$ over the atmospheric pressure, and so the inflation system must be able to create a $500\,\mathrm{Pa}$ pressure as well, to be able to fill the ballonets and maintain the same pressure. Both the pressure and airflow requirements need to be fulfilled at the same time, so a suitable blower must be able to provide $13.9\,\mathrm{m^3/h}$ of air while overcoming a $500\,\mathrm{Pa}$ back-pressure. It should also be powered by direct current.

An example of such a blower with minimal weight and power draw is the Sanyo Denki 9CRA0412P4K03 which provides a flow of $27\,\mathrm{m^3/h}$ at the required $500\,\mathrm{Pa}$ pressure, while drawing $19.2\,\mathrm{W}$ of power and weighing in at $80\,\mathrm{g}$, powered by $12\,\mathrm{VDC}$ [78].

Valve
The same pressure and airflow requirements hold for the solenoid valves as well. The valve needs to be able to hold the envelope pressure of $500\,\mathrm{Pa}$ when closed, and it shall be able to allow an airflow of $13.9\,\mathrm{m^3/h}$ when open, to be able to send all the air pumped by the blower into only one of the ballonets. Additionally, a decision needs to be made between a normally open and a normally closed solenoid valve, as these valves either consume power when open or when closed respectively, while not consuming power in their other state. For the designated application, the valve needs to be closed for a longer part of the journey than it needs to be open for, and so a normally closed valve has been selected, which consumes no power when closed.

A valve that fulfils all of these requirements is the RS Pro 144-0803, with a maximum flow rate of $17\,\mathrm{m^3/h}$ while being able to hold a pressure of $1.2\,\mathrm{MPa}$ and being normally closed [79]. The flow requirement was the limiting one for this component.

With these specifications, the inflation system shall be able to replace all the volume of hydrogen vented by the hydrogen venting system, which is described below.

9.6.3. Hydrogen Venting System

The most important factor driving the design of the hydrogen venting system is the safety. Since a flammable gas is being dispersed into the atmosphere, it is important how this is handled. Other than this, there is also a requirement for how much hydrogen needs to be vented, equal to the rate of inflation of the ballonets, so $13.9\,\mathrm{m^3/h}$.

The hydrogen shall be vented through a solenoid valve and an exhaust. The solenoid valve can be the same one as the one used for the ballonets, that is the RS Pro 144-0803, as it is required to hold the same pressure and flow the same amount of volume. The diameter of the vent needs to be such that the hydrogen is vented at a rate slightly above the desired rate naturally due to the internal envelope pressure. To calculate this, the Bernoulli equation can be used as seen in Equation 9.3, rearranged to solve for velocity and simplified for a case where the gas starts with a pressure and no velocity and ends with a velocity and no pressure, such as is the case for the hydrogen being vented. With a $p_{envelope} = 500\,\mathrm{Pa}$ and a hydrogen density of $\rho_{H_2} = 0.08375\,\mathrm{kg/m^3}$, the velocity at which the hydrogen escapes can be solved to be $v_{vent} = 109.3\,\mathrm{m/s}$. Knowing this, the natural rate of hydrogen escape through a hole in the envelope with radius r can be calculated using Equation 9.4, which can be rearranged to solve for the radius r. Solving this with the required volumetric flow rate of $13.9\,\mathrm{m^3/h}$ converted to SI units of $3.889\times10^{-3}\,\mathrm{m^3/s}$, results in a hole radius of $r = 3.37\,\mathrm{mm}$.

$$v_{vent} = \sqrt{\frac{2 \cdot p_{envelope}}{\rho_{H_2}}} \tag{9.3}$$

$$\dot{V} = \pi \cdot r^2 \cdot v_{vent} \tag{9.4}$$

To ensure the safety of the hydrogen release, the airflow over the vent must be such that the concentration of hydrogen in the airflow is less than four percent, the limit above which the hydrogen-air mixture becomes flammable, taking the lowest hydrogen flammability criterion from the paper *Flammability of methane, propane, and hydrogen gases* [80]. To ensure that this is the case, consider Figure 9.5. The cross-section of the column of gas being released per second creates a plane. The cruise speed of the blimp, perpendicular to the venting speed, adds the third dimension, creating a volume. The volume is maximised when these two speeds are perpendicular, so the vent shall be placed such that this is the case.

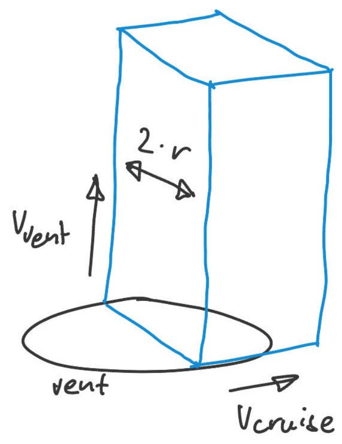

Figure 9.5: *Volume of the mixture of hydrogen and air.*

It is known that this volume contains $3.889 \times 10^{-3}\,\mathrm{m^3}$ of hydrogen and the rest of it is air. Calculating the volume to be $11.24\,\mathrm{m^3}$, the concentration of hydrogen in the volume can be calculated to be 0.02 percent, which is way under the maximum required concentration of 4 percent, and thus will be safe. To further promote the dispersion of hydrogen, vortex generators will be placed upstream from the vent to ensure a turbulent flow above it.

Another safety measure to be taken for the vent is to offset it from the envelope, so that even in the highly unlikely case that the gases being vented ignite, they are not in immediate vicinity of the rest of the hydrogen, stored in the blimp envelope. For now, a $20\,\mathrm{cm}$ distance from the envelope was chosen. The impact of this distance shall be explored more deeply in further research. Moreover, the vent is to be placed somewhere along the top half of the envelope, such that the rising hydrogen does not travel back closer to the envelope. The reflective coating of the envelope also helps to repel the thermal flux in case of ignition.

9.6.4. Control

Finally, the whole system needs to be controlled to be useful. To do this, the electronic devices which constitute the buoyancy control system will be controlled by the flight computer. For the flight computer to decide on how to operate these devices, sensors will provide data on the relevant metrics. These sensors can be seen in the diagram below in Figure 9.6, followed by an explanation of each of theirs function.

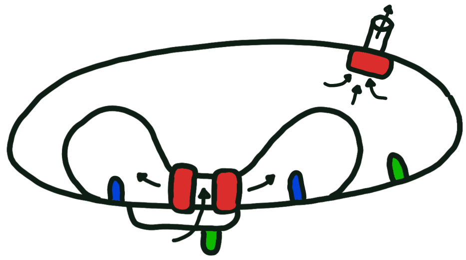

Figure 9.6: *Sensors of the buoyancy control system (airflow sensors in red and pressure sensors in green and blue).*

Two pressure sensors will be used, shown in blue in Figure 9.6. One will be placed in the envelope and one outside of it, to take atmospheric pressure measurement. These will keep track of the pressure differential between the inside and outside the envelope. Additionally, three mass airflow sensors will be used, shown in red in the figure above. Two of these sensors allow the team to keep track of the amount of air that is in each ballonet. This could not be done with pressure sensors, as the pressure in both ballonets is the same as the pressure in the envelope. The final mass airflow sensor at the vent serves to monitor more exactly the amount of hydrogen being vented from the envelope, as a more precise supplement to the envelope pressure measurement.

9.7. Sensitivity Analysis

Subsection 10.3.1 describes how the net buoyancy force results in a lift force. Temperature changes have an effect on the density and volume of the balloon. For this analysis we assume that the internal pressure is always $500\,\mathrm{Pa}$ larger than the ambient pressure. This is in line with Chapter 5. Another assumption is the validity of the ideal gas law. The total lift force created by the lifting gas is given by Equation 10.2. As can be seen, the lift force is dependent on the difference in density of the external air and internal hydrogen of the balloon. The densities can be derived via the ideal gas law leading to Equation 9.5

$$\rho = \frac{Mp}{RT} \tag{9.5}$$

M and R are constant, and the ambient and internal temperature T are assumed to be equal. Due to the elastic characteristic of the envelope, the gas in the envelope can expand. According to Charles's law, the volume will expand proportional to the temperature increase [81]. A 5% increase in temperature will cause a 5% increase in volume under the condition that the pressure stays constant. An extreme temperature change between morning and afternoon in New South Wales could be from $5°C$ to $25°C$. In terms of Kelvin, this is a temperature increase of 7.2%. Assuming a 7.2% volume increase, increases the pressure with 3% and an atmospheric density of the air of $1.225\,\mathrm{kg/m^3}$. The density of hydrogen will increase with 3% due to the linear relation of Equation 9.5. The decrease in total lift will be 0.22%. These calculations have a low accuracy, but even if the lift reduction would be five times higher, the vehicle would still be able to operate.

9.8. Risk Analysis

Table 9.4: *Buoyancy system risk assessment*

Index	Risk factor	HS	HP	HRI	Mitigation strategy	HS	HP	HRI
Detailed buoyancy subsystem design risk assessment								
1	Possibility for hydrogen ignition due to mixing with air	10	4	40	Detect mixing of hydrogen and air, return to base immediately	10	1	10
2	Possibility for hydrogen ignition when venting	10	4	40	Offset vent from the envelope, ensure good mixing with air, ensure non-flammable concentrations, ground the vent	6	1	6
3	Incorrect trade-off result due to team bias	6	6	36	Effective communication strategy and critical discussions	6	4	24
4	Electronics failure in buoyancy control system causes crash	2	6	12	Sensor redundancy, failure detection	2	1	2

The risk associated with the buoyancy control system are of utmost importance in its design. A summary of the risks and mitigations can be seen in Table 9.4. Due to the fact that venting of a flammable gas, hydrogen, occurs in the operation of the buoyancy control system, many considerations have been made to ensure this venting happens safely. These measures are more closely described in the section dedicated to the design of the venting subsystem, Subsection 9.6.3. In summary, they include ensuring that the hydrogen gets diluted in sufficient amounts of air for it not to be flammable any longer, supporting the dispersion of the hydrogen by adding vortex generators upstream of the vent, ensuring that the vent is spaced away from the envelope and ensuring that it is placed such that the rising hydrogen does not get closer to the envelope in its path.

Another risk to be mitigated is the risk of rupture of the ballonets, which would result in the mixing of hydrogen and air, making a flammable mixture. There is little reason for this to happen since the ballonets are at the same pressure as the helium and therefore there should be little to no stress in the envelope of the ballonets. Furthermore, simply the fact that the hydrogen gets mixed with air is not a disaster in itself, as it would still need additional energy for a fire to start. Keeping that in mind, it is still important to know when this has happened, to cancel the mission. For this reason, hydrogen detection sensors will be installed in each of the ballonets.

The failure of any other part of the buoyancy control system, that is the failure of the sensors, valves or blower, should not result in the inability of the airship to return home. The failure of these components should be detectable by other sensors and this should be able to be accounted for in the return to home mission planning. While this is expected, more research into this matter, and exact planning for the case of the failure of each component are required before the airship would go into production.

9.9. Sustainability Analysis

Sustainability was kept in mind during the development of the buoyancy control system, mainly from the environmental point of view. To select the most environmentally sustainable concept, a set of question was devised in relation to each life phase, and these were answered in relation to each concept. This gave a deeper look into the sustainability of the various systems at the conceptual design stage. The results of this investigation can be seen in Table 9.2.

Further, in the detailed design, many of the shelf components, including sensors, valves and a blower, were chosen for this subsystem. This contributes to economic sustainability by employing economies of scale. Moreover, this contributes to environmental sustainability too, by avoiding the need to set up more production facilities and increasing the efficiency of the production. For the rest of the buoyancy control design, very little mixing of materials shall be required, leading to easy disassembly, the ability to maintain the subsystem for a long time, and the ability to recycle parts of it, such as the tubing required or the envelopes of the ballonets, at the end of its life.

However, during the impact assessment study described in Chapter 19, it was found that the impact related to the buoyancy control eclipsing all other is the venting of hydrogen associated with it. These new findings need to be considered in further research and the amount of hydrogen vented shall be attempted to be reduced, possibly by aiming for some level of compression of the hydrogen in the envelope, or even selecting a different concept.

10

Flight Dynamics and Control

Once the vehicle design is set, the forces and moments occurring during its operation need to be considered. This chapter aims to develop at model of the flight mechanics and the atmospheric forces. Section 10.1 starts with the forces that constitute cruise equilibrium. Thereafter, the hardware design of the control system is explained in Section 10.2. Next, Section 10.3 gives a model for the atmospheric forces. Concerning the flight dynamics, model assumptions are given in Section 10.4. The longitudinal dynamics model and altitude control are explained in Section 10.5 and Section 10.6, respectively. Moving on, the lateral dynamics and heading control are respectively documented in Section 10.7 and Section 10.8. At last, the verification and validation conclusion can be found in Section 10.9.

10.1. Cruise Equilibrium

Cruise is the condition the vehicle spends most of its time in and what it is designed for. Before the manoeuvrability can be assessed, the blimp needs to be in equilibrium. A free body diagram for this scenario can be found in Figure 10.1.

The datum feature for all following vehicle FBDs is the centre of buoyancy (c.b.), which is also the point about which all moments will be considered. Although while airborne the blimp will rotate about its centre of gravity, static and dynamic analyses can be carried out about any chosen point, as confirmed by prof. S.G.P. Castro, who was consulted for verification.

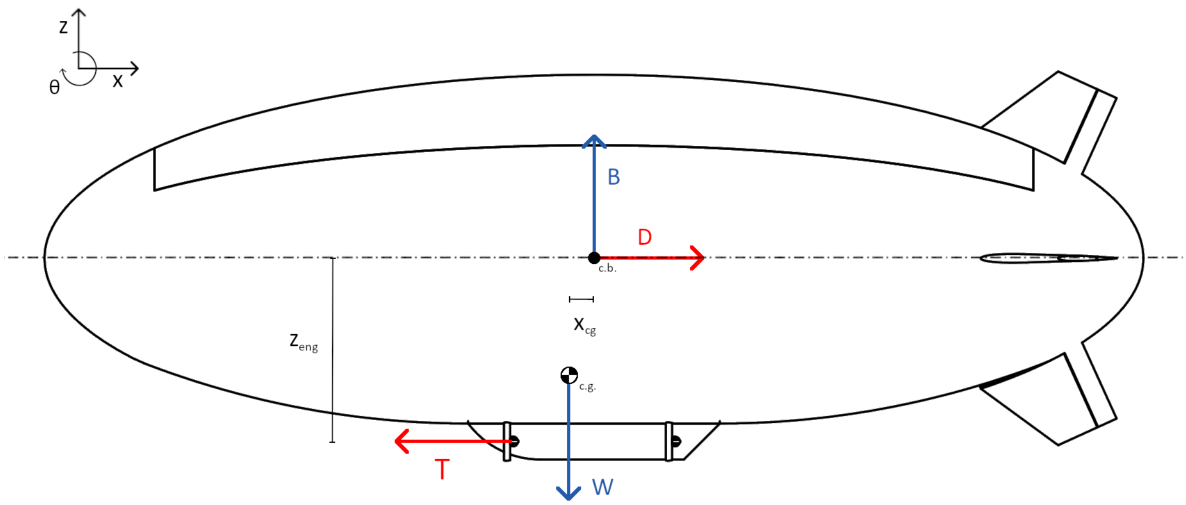

Figure 10.1: *Free body diagram of blimp in side view. Thrust (T), drag (D), buoyancy (B) and weight (W) need to be arranged such that the resulting force and moment are zero.*

In order to have static equilibrium, the buoyancy force needs to bear the weight and the thrust force needs to overcome the drag. Moreover, it can be observed that the engine thrust is offset from the centre of buoyancy and will hence produce an upward pitching moment. From an aerodynamic point of view, however, it is desirable to fly horizontally, so a simple method to counteract this moment is shifting the gondola and consequently also the c.g. forward, such that the weight force will cause a neutralising downward pitching moment. Mathematically, the following condition must hold:

$$T z_{eng} = W x_{cg} \tag{10.1}$$

During take-off and landing, there will be no horizontal thrust force, so, the offset centre of gravity will cause the blimp to hang down at an angle of 5°, which is negligible since take-off and landing take place at low speeds.

Abiding by the principle of superposition, it is possible to impose a second set of forces on this equilibrium state without having to deal with the static considerations again. This is done for altitude and heading control in the following two subsections, respectively.

10.2. Control Actuator Design

The blimp is designed to be neutrally buoyant. However, the buoyancy force strongly depends on the atmospheric conditions. In Chapter 9, the passive altitude control system is explained, which ensures that the blimp remains neutrally buoyant for a certain atmospheric condition. This condition is called trim condition, and making use of the International Standard Atmosphere (ISA), it can be reduced to a trim altitude. During its operation the vehicle will need to deviate from the trim altitude, such that there will be a net buoyancy force pulling the blimp down if above trim altitude or pushing it up if below trim altitude. The same happens if air temperature or air pressure change. In order to make sure that the vehicle still follows the planned path, there will be an active Attitude Control System (ACS) that creates temporary vertical forces.

Travelling upwards means that the airflow will come at a negative angle of attack. If the lifting body is not aligned with the airflow, this will push the blimp down. Therefore, while moving up the vehicle also needs to pitch up, such that it can ideally attain a positive angle of attack, which even produces additional lift and thus helps with the ascent.

Creating such a pitching moment can be done in several ways. During earlier stages of the design the idea was to use thrust vectoring of the engines, since thrust can be used both as upforce and to pitch the vehicle up. Unfortunately, due to the limited available moment arm of the motors, it was found that the pitching moment was not enough and the procedure became inefficient.

Another means to control the pitch is using elevators, which create a downforce at the aft. Although it was at first suspected that this downforce would be larger than the resulting lift force, since the envelope has a lift coefficient about ten times smaller than that of a wing, this method was found to be the most efficient. Even better would be using canards, since they achieve the same effect with a beneficial upforce, but due to the resulting instability, the elevator solution was finally selected.

For heading control, rudders are used, which are physically not to be distinguished from the elevators, except for their vertical orientation.

10.3. Atmospheric Forces Model

In the previous section was explained, why there will be a net buoyancy force if the blimp deviates from trim condition. This section aims to develop a model to quantify those forces.

10.3.1. Net Buoyancy Force

At trim altitude there is vertical equilibrium, so the following holds:

$$W = B = gV_{env}(\rho_{h_{trim}} - \rho_{gas}) \tag{10.2}$$

So the net force is zero. At other altitudes however, assuming the ideal gas law:

$$\begin{aligned} F_{net} = B - W &= gV_{env}(\rho_h) - \rho_{gas}) - gV_{env}(\rho_{h_{trim}} - \rho_{gas}) \\ &= gV_{env}(\rho_h - \rho_{h_{trim}}) \\ &= gV_{env}\Delta\rho_{\Delta h} \end{aligned} \tag{10.3}$$

From this can be seen that the net force is proportional to the density deviation from trim condition. With the help of ISA, this density difference can be linked to an altitude difference. Despite the relationship being rather complicated, it can be linearised very well, such that the net force is modelled as a linear spring:

$$F_{net} = gV_{env}\frac{d\rho}{dh}|_{h_{trim}}\Delta h = k\Delta h \tag{10.4}$$

Indeed, Figure 10.2 shows, that this is a good approximation even for deviations of more than a kilometre.

10.3.2. Vertical Drag Force

Next to the buoyancy force there is also aerodynamic drag due to the upwards motion. If there is a horizontal velocity V_x (cruise speed) and a vertical one V_y, the magnitude of the velocity will be:

$$V = \sqrt{V_x^2 + V_y^2} \tag{10.5}$$

This velocity will cause a drag force opposing the motion. The vertical component is then equal to:

$$D_{vert} = \frac{1}{2} = \rho V^2 SC_D \sin\gamma = \frac{1}{2}\rho V^2 SC_D \frac{V_y}{V} \tag{10.6}$$

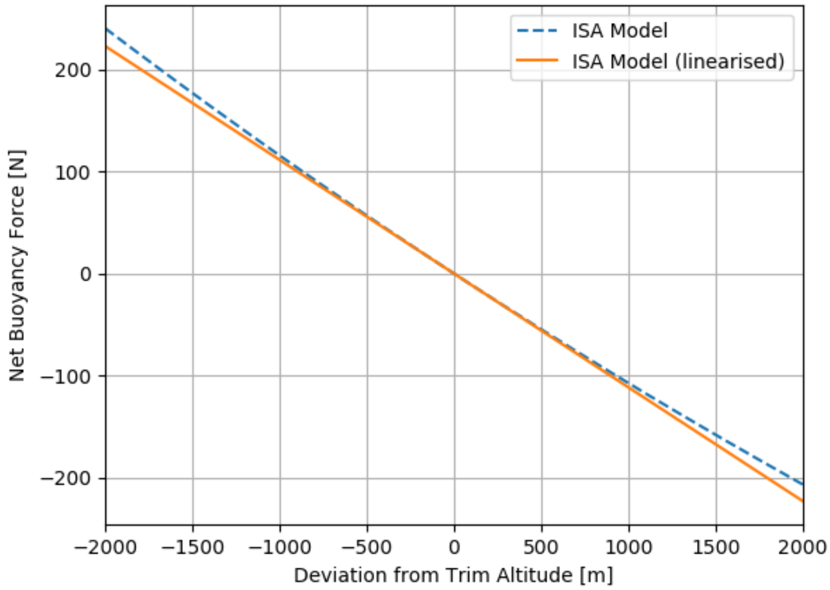

Figure 10.2: *Net buoyancy force versus deviation from trim altitude. Shown are calculated forces based on ISA model and the linearisation used for this model.*

Simplifying and substituting Equation 10.5:

$$D_{vert} = \frac{1}{2}\rho\sqrt{V_x^2 + V_y^2}V_y S C_D \tag{10.7}$$

Since $V_x >> V_y$, this expression can be linearised (small angle approximation):

$$D_{vert} = \frac{1}{2}\rho V_x V_y S C_D = c V_y \tag{10.8}$$

And therefore, the vertical drag can be modelled as a linear dashpot, proportional to the vertical velocity, see Figure 10.3.

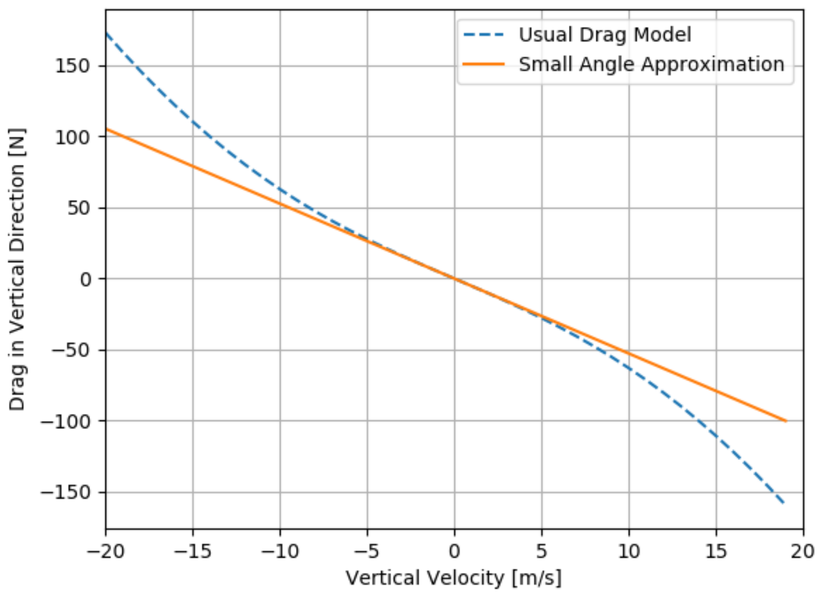

Figure 10.3: *Vertical drag versus vertical speed and linearisation with small angle approximation.*

10.4. Flight Model Assumptions

The following assumptions were made during the analysis of the blimp mechanics:

- Drag acts directly through the centroid of the envelope
- Aerodynamic forces grow linearly with angle of attack
- Both envelope and control fins are symmetric, so do not cause an aerodynamic moment
- Angles are very small, so $\sin\theta \approx \theta$
- Since the envelope creates little aerodynamic lift, there is no downwash, so angle of attack is the same everywhere
- There are no gusts
- The air density stays constant throughout the mission and is assumed to be at trim altitude
- The vehicle is a rigid body and does not deform under loads
- Longitudinal and lateral dynamics are not coupled

10.5. Longitudinal Dynamics

Understanding the longitudinal dynamics is paramount for designing the active altitude control system (ACS). As a first step, again a free body diagram is drawn.

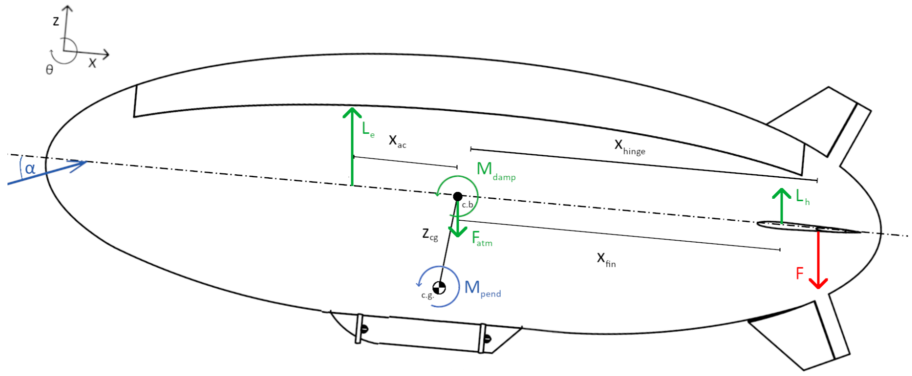

Figure 10.4: *Side view of blimp at an angle of attack (α). Forces and moments acting in the longitudinal direction comprise aerodynamic lift of the envelope (L_e) and tail (L_h), the atmospheric forces explained earlier (F_{atm}), an aerodynamic damping moment (M_{damp}), the control force (F) as well as a pendulum restoring moment (M_{pend}) due to the weight being offset from its initial position at an angle θ.*

Transitioning from statics to dynamics, the sum of forces will no longer be zero and cancel out, but will cause a change in velocity, according to Newton's second law. This motion is dictated by the following equations:

$$\Sigma F_z: \quad L_e + L_h - F - F_{atm} = m\ddot{z} \tag{10.9}$$

$$\Sigma M_y^{cb}: \quad F x_{hinge} + L_e x_{ac} - L_h x_{fin} - M_{damp} - M_{pend} = I_{yy}^{cb}\ddot{\theta} \tag{10.10}$$

The moment of inertia about either axis was first estimated by calculating it for the envelope and adding equipment such as fins, electronics and engines as point masses. For the final simulation, values were determined from the CAD drawing, which were found to agree sufficiently with the hand-calculated estimations.

Knowing all the design characteristics, this system of linear differential equations can be first linearised and subsequently represented in state-space, facilitating the development of a state-feedback controller. For a full derivation of the state-space representation, as well as stability and control derivatives, please refer to Appendix D.

From the model the eigenvalues can be easily determined using the *"matlab.control"* library in Python. An important check is to see whether they all have a negative real part. This is the case for the designed system, so the longitudinal motion is dynamically stable and as a corollary also statically stable.

10.6. Altitude Controller Design

The reason why the longitudinal model was created in the first place is to make predictions of the vehicle's behaviour upon elevator control inputs with the ultimate target to actively control the altitude. For that matter the longitudinal dynamics state-space representation can be loaded in MATLAB and incorporated in a Simulink Model. Around this a proportional controller with saturated outputs is designed that decides what the elevator deflection should be for a given control error, as seen in Figure 10.5. Due to structural limitations, the elevator deflection is limited to 10° in each direction. A useful controller gain was found to be 0.03, making use of Matlab Sisotool. Moreover, in order to maintain horizontal equilibrium, the additional drag needs to be countered by throttling up the motors. This power is calculated with the following equation:

$$P = \alpha^2 \left(C_{L_{\alpha_e}}^2 k_e + \left(\frac{V_v}{V}\right)^2 C_{L_{\alpha_h}}^2 k_h \right) \frac{1}{2}\rho V^3 S, \tag{10.11}$$

where k_h is the induced-drag-parameter of the tail surfaces.

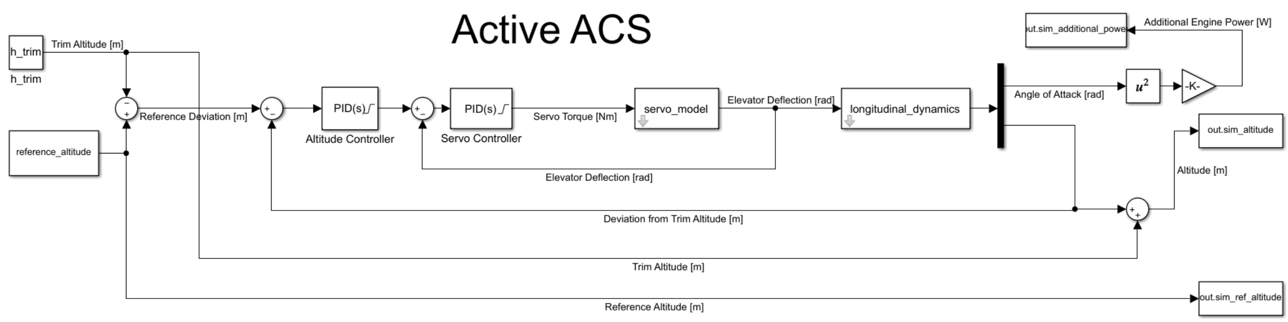

Figure 10.5: *Block diagram of active altitude control system and elevator servo model.*

The elevator control servo was sized as a second order system that acts as a low-pass filter with break frequency around $1.6\,\mathrm{Hz}$. This has the effect that the elevator deflection is modelled realistically and to prevent oscillations.

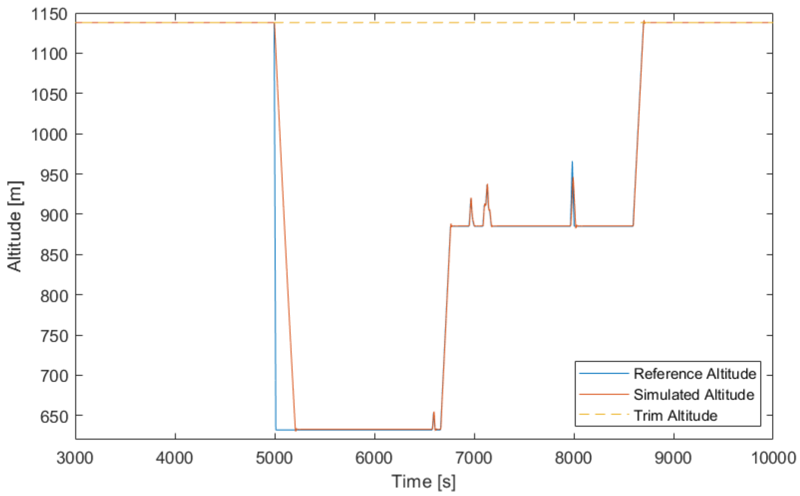

Figure 10.6: *Simulated altitude path of vehicle with control system described above. Trim altitude was set to* $1138\,\mathrm{m}$.

Figure 10.6 shows the simulated performance of the system for a certain mission profile. A clear weakness that can be observed is the steep descent into a ravine at $5000\,\mathrm{s}$. Due to the capped elevator deflection, the blimp is not able to descend that steep, which should be accounted for in the next flight path optimisation iteration. Another thing to consider in the future is having a variable trim altitude, that could for instance linearly increase from about $5000\,\mathrm{s}$ to $9000\,\mathrm{s}$.

10.7. Lateral-Directional Dynamics

Next to controlling the flight altitude, the vehicle moreover needs to be able to change its flight direction for successful sensor deployment. Again starting from the cruise equilibrium, it is possible to draw an FBD of the forces involved in the lateral dynamics, as seen in Figure 10.7.

Once more it is possible to set up the equations of motion. Looking from the top, the c.g. and c.b. almost coincide. Since weight does not play a role here, only the c.b. is drawn.

$$\Sigma F_y: \quad F + Y_r - Y_e - Y_v = m\ddot{y} + mV_\infty\dot{\psi} \tag{10.12}$$

$$\Sigma M_z^{cb}: \quad F x_{hinge} + Y_e x_{ac} - Y_v x_{fin} - N_{damp} = I_{zz}^{cb}\ddot{\psi} \tag{10.13}$$

Next to the linear inertia term in the sum of forces equation, there is also a Coriolis term due to the body being at significant yaw rates [17], which is neglected for the longitudinal dynamics.

Unlike in airplanes, yaw and rolling motion are less coupled. While the control force F will induce a roll angle proportional to the yaw rate, similar to lorries taking steep turns, this roll angle has no effect on the other dynamics and is therefore typically not controlled in blimps [17].

Like for the longitudinal dynamics, this system is also linearised and represented in state-space. For the full derivation as well as the stability and control derivatives, please refer to Appendix D. Eigenvalues were found to lie altogether in the left half plane and therefore, the system is yaw- and roll stable.

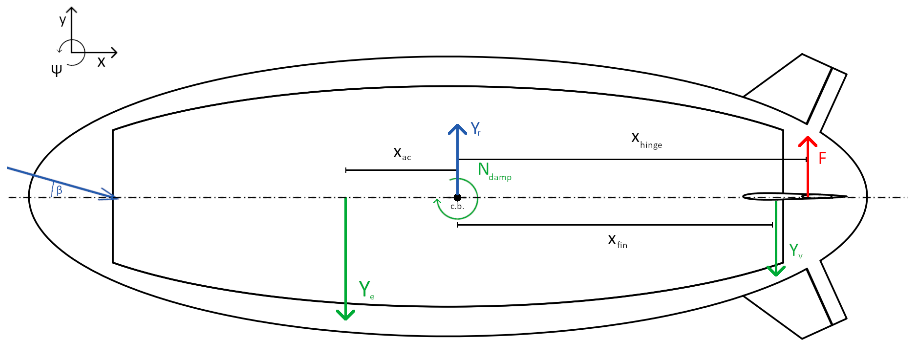

Figure 10.7: *Top view of the blimp and the lateral forces. Visible are the aerodynamic sideforce at the envelope (Y_e), aerodynamic sideforce at the vertical tail (Y_v), aerodynamic sideforce due to yaw rate (Y_r), tail force (F) due to rudder deflection, and an aerodynamic damping moment (N_{damp}).*

10.8. Heading Control System Design

For a specified reference heading a proportional controller with gain 5 inserts a rudder deflection between -10° and 10° to a servo, which is modelled the same way as for the longitudinal system. A constant rudder deflection will lead to a constant yaw rate, which can be integrated to obtain the heading angle. Since heading, however, only gives the direction of travel, it is no measure of position. To obtain the actual positions, the following equations can be used to simulate the position in the xy-plane. The North-South direction corresponds to the y-axis and the East-West direction to the x-axis.

$$x(t) = \int_0^t V \sin\chi dt\,, \quad y(t) = \int_0^t V \cos\chi dt \tag{10.14}$$

The simulated position can then be compared to the scheduled position of the flight path. The general idea for lateral control was to calculate the distance from the target position by

$$d = \sqrt{\Delta x^2 + \Delta y^2} \tag{10.15}$$

The desired elevator deflection should then be proportional to the distance, which can be facilitated by a proportional controller. What remains to be solved is the direction of deflection. If the target point is left of the vehicle's flight direction, a positive rudder deflection will be needed, if it is to the right, a negative rudder deflection needs to be fed in.

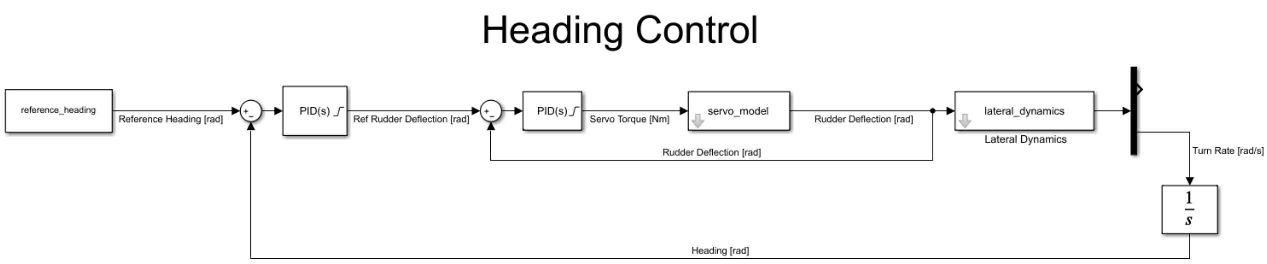

Figure 10.8: *Control block diagram of heading control system and actuator model.*

Due to time constraints, the controller demonstrated here purely regulates the heading angle and makes sure the direction of flight is controlled. In consequence, this means that the vehicle will be remote-controlled by a heading and altitude input of an operator. Since most of the flight path on the xy-plane is linear and the altitude regulates itself, remote control is rather simple, and a single operator might be able to monitor multiple vehicles. This is subject to further research of course.

10.9. Verification and Validation

The model was created based on Newton's second law, i.e. summing the forces or moments and letting them equal the change in linear or angular momentum. Most forces are due to aerodynamics and vary linearly with coefficients determined with the help of [17], so they are trusted to be reasonable. Moreover, this approach is also the one used in the flight dynamics course of the B.Sc. curriculum. The system is then completed by adding definitions of angles such as angle of attack or sideslip angle, which are conventional. The built model is therefore

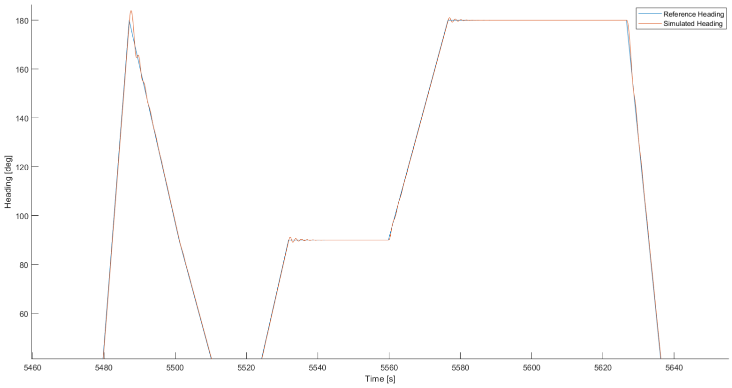

Figure 10.9: *Simulated vehicle behaviour for a reference heading as likely to be used for the sensor deployment.*

funded on theory that has been agreed on for decades. Of course, a better confidence could be established by extensive real-world testing, e.g. in wind tunnels. Unfortunately, we were not given this opportunity yet.

All coefficients in the Python code were printed and verified by hand to a precision of 4 significant figures. Moreover, the linear algebra operations were conducted both in Matlab and in Python and came to the same result.

The coordinate system used was checked multiple times and step responses were plotted for different inputs. A positive rudder deflection e.g. resulted in a constant steady-state turn rate to the left and a positive elevator deflection resulted in a constant upwards flight path angle, which in the very long run decreases due to the decrease in buoyancy at higher altitudes. Moreover, simulation results were tested on convergence for decreasing time steps. As the model makes use of small angle approximation, control deflections are limited to 10° in both directions. The resulting attitude angles stay below 15°, validating this assumption.

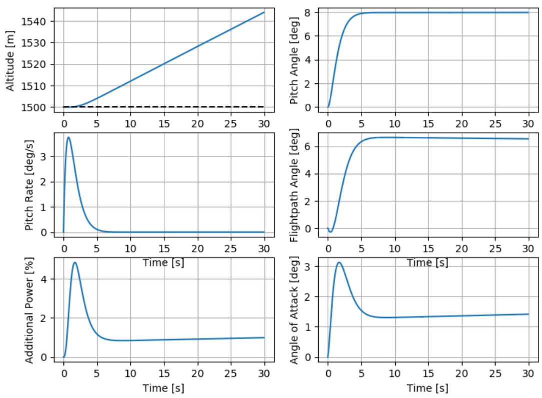

Figure 10.10: *Longitudinal system response at an elevator step input of 5° at* $t = 0$.

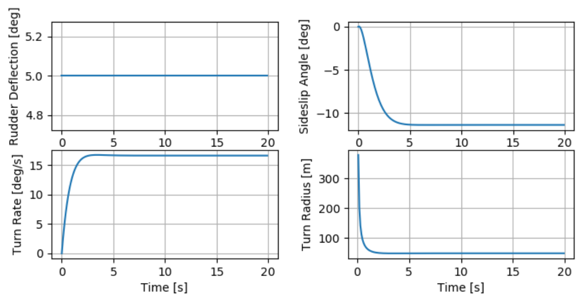

Figure 10.11: *Lateral system response at a rudder step input of 5° at* $t = 0$.

Table 10.1: *Flight mechanics requirements.*

Req. ID	Requirement	Section	Compl.
REQ-VEH-CO-22	The vehicle shall be able to monitor its attitude	7.4	✓
REQ-VEH-CO-23	The vehicle shall be able to monitor control surface positions	10.6	✓
REQ-VEH-CO-24	The vehicle shall be able to monitor its position	7.4	✓
REQ-VEH-CO-25	The vehicle shall have a maximum turn radius of 140 metres	4.2	✓
REQ-VEH-CO-26	The vehicle shall be able to sustain a minimum pitch rate of 0.6 deg/s	10.9	✓
REQ-VEH-CO-27	The vehicle should be roll-stable	10.7	✓
REQ-VEH-CO-28	The vehicle shall be yaw-stable	10.7	✓
REQ-VEH-CO-29	The vehicle shall be pitch-stable	10.5	✓
REQ-VEH-CO-30	The vehicle shall be able to provide a minimum yaw rate of 4.5 deg/s	10.9	✓

11

Payload Deployment Mechanism

Dropping sensors is an essential requirement for the EcoSense mission. The sensors will be stored in a payload bay attached at the bottom of the blimp. The vehicle can hold up to 552 sensors, and a mechanism is needed to load the sensors, hold them and deploy the sensors efficiently and safely. This section will discuss in detail these aspects of the design. The chapter starts by discussing the design Approach. The design requirements are discussed in Section 11.2. The functional analysis that goes over all the functions of the design is discussed in Section 11.3. The trade-off where four design options are compared is done in Figure 11.7. The chosen design is discussed in more detail in Section 11.6. The chapter ends with a risk analysis and a sustainability analysis in Table 11.2 and Section 11.10.

11.1. Design Approach

In this section, the methods used to reach the final design are discussed. The design of the payload bay and mechanisms went through a thorough trade-off where different design options were analysed. The design processes started with an ideation phase, and from there a detailed investigation of each design was performed. The trade-off criteria will be discussed in the section below. First, the design criteria and their importance will be discussed. After that, the design options are introduced along with their relation to each of these criteria.

Weight

Weight is contributing to a snowball effect on other subsystems in total design. A heavier payload system will increase the total size needed of the blimp envelope to lift the vehicle.

Reliability

Each flight is tasked with dropping more than 500 sensors. The reliability of the payload bay and the deployment mechanism therefore needs to be of high order. Reliability of the system is the leading criteria for choosing the design. In each of the designs to be discussed later in the report, a team of engineers brainstormed about all possible ways the design would potentially malfunction.

Cost

While cost of the design is being taken into consideration, it is not of top priority. The EcoSense vehicle will be used for multiple missions, so the costs per flight will decrease with the amount of fights that will be performed. Manufacturability of the design is also included under this criterion. A more difficult system to manufacture is directly related to increasing costs.

Operations

To decrease the resources needed in man-hours, difficulty of operations and reliability of the operation method, the operations criteria is of importance. During design phase the team looked at questions like:

- How easy is it to fill up the payload bay?
- How long does it take to refill the payload bay?
- Can it be operated by one person?

Energy Consumption

The energy consumption of the deployment system are ideally minimised. Three of the deployment options make use of a motor that is rotating. To calculate the energy consumed by the system the total amount of work is calculated by integrating the torque over the rotation, as shown in Equation 11.1 [82].

$$W_{torque} = \int \vec{\tau} \cdot \mathrm{d}\vec{\theta} \tag{11.1}$$

11.2. Design Requirements

The payload bay needs to fulfil a set of requirements. The capacity of the payload bay is depended on the operations of EcoSense. Mainly we have to look at how large the payload bay needs to be to fulfil the deployment time requirement. For the trade-off an amount of 650 sensors is used for the calculation.

Besides the operational requirements. Requirements related to structural strength have to fulfil as well. In Table 11.1 below the deployment system requirements are given.

Table 11.1: *Deployment requirements.*

Req. ID	Requirement	Section	Compl.
REQ-VEH-DEP-1	The deployment mechanism shall be able to deploy nodes with a 99% reliability.	14.2	TBD
REQ-VEH-DEP-2	The deployment mechanism shall be able to deploy 3.5 nodes per minute.	11.6.5	✓
REQ-VEH-DEP-3	The deployment mechanism shall verify successful deployment.	14.1	✓
REQ-VEH-DEP-4	The deployment mechanism shall load sensor nodes from the payload storage bay.	14.2	✓
REQ-VEH-DEP-5	The deployment mechanism shall be able to receive a signal to initiate the deployment.	11.6.5	✓
REQ-VEH-DEP-6	The deployment mechanism shall be able to deploy sensors after an unsuccessful deployment.	11.6.5	✓
REQ-VEH-DEP-7	The sensors and relay nodes will stay connected within the loading requirements the total structure is designed for.	11.6.2	✓
REQ-VEH-DEP-8	The payload bay shall be able to with show no signs of permanent deformations or cracks within the loading requirements the total structure is designed for.	11.6.2	TBD

Besides the aforementioned design requirements [4], there are extra requirements that need to be taken into account when designing the payload deployment mechanism. These requirements came up after thinking better about the construction of the payload mechanism. The detailed design will go in-depth to fulfil these requirements, so that successful functionality of the design can be achieved. The added requirements are REQ-VEH-DEP-5 until REQ-VEH-DEP-8.

11.3. Functional Analysis

The function that the deployment system will go through are described here in detail. From here the design can be created. The functional breakdown structure of the deployment system is given in Figure 11.1. Each of these functions should be satisfied in the design.

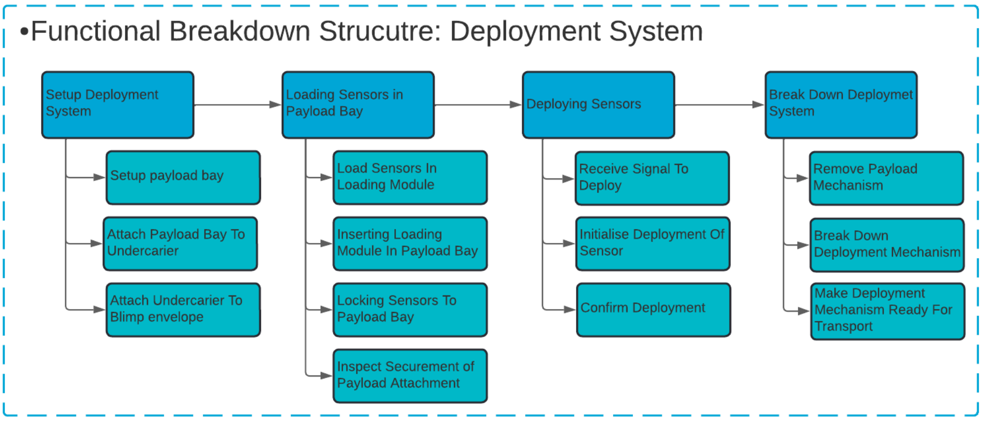

Figure 11.1: *Functional analysis of the deployment system.*

11.4. Design Options

Four design options were created. In the following sections, each of these options will be discussed. We will go over each of the above-mentioned criteria and reflect on how the design is performing in these aspects. In the end, a summary in a trade-off table will be given that resulted in the final design.

11.4.1. Electromagnetic Attachment

First, an option utilizing magnets is proposed. Here, sensors are held onto the blimp with a magnet each. They can then be deployed after a current is applied to the magnet, cancelling out its magnetism. Such electromagnets are called electro-permanent magnets, and they are suited to this application since they do not consume power to keep the sensors attached, leading to less power consumption and reduced risk. The holding magnet used for the analysis is the PEM1213A produced by Kendrion [83].

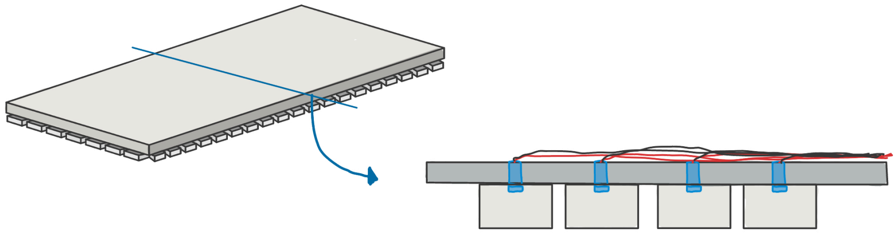

Figure 11.2: *Sketch of the electromagnetic deployment system concept.*

Weight
For this system, each sensor will have an individual electromagnetic locking mechanism. Each of the electromagnetic connectors has a weight of $0.01\,\mathrm{kg}$ [83]. Solely the locking mechanism for the 650 sensors will weight $6.5\,\mathrm{kg}$. For the system to work, the sensors will need to have a ferromagnetic part that provides the option to magnetically connect to the payload bay. This piece will be a round disk that can have a diameter of $15\,\mathrm{mm}$ and a $2\,\mathrm{mm}$ thickness. The volume of this part will be $3.534 \times 10^{-7}\,\mathrm{m}^3$. Using the density of iron, the total weight for connector parts of 650 sensors will be $1.79\,\mathrm{kg}$. The total weight for only the connection mechanism will come down to $8.3\,\mathrm{kg}$.

Reliability & Risk
The reliability and risk of this method are qualitatively scored as high. Each electromagnet can be connected in parallel. If one of the elector magnets will not work, the system can still deploy the sensors and the mission won't be impeded further. The electromagnets also have a relatively high reliability, as there are no moving parts.

Cost
The cost of an electromagnet similar to the PEM1213A was found to be EUR 6.36 [84]. The electromagnet is not the same as the model that is being used for the estimations [85]. The electromagnet that is used for the price estimation has a strength of $10\,\mathrm{N}$. The PEM1213A has a strength of $8\,\mathrm{N}$. Because the PEM1213A is manufactured by a more respectable manufacturer, which will potentially increase the price, but the bulk purchase of the magnets could give a discount, the cost per electromagnet is estimated to be EUR 7 per electromagnet. With 650 electromagnets needed, the cost will come down to around EUR 4550. Manufacturing of this system will not have significant difficulties and will not induce exceptional costs.

Operations
Loading sensors into the payload bay is simple for this deployment mechanism. A special grid could be created where the sensors would be placed in. When loading the system, the vehicle could easily be pressed on the grid where the electromagnets are located and the sensors will attach to the payload bay. This would be an effective and low-effort method to load the sensors. Operations are given a score: very good.

Energy Consumption
The electromagnet uses 1 Watt to deploy the sensor. Because we are dealing with a permanent electromagnet, there is no energy used for holding the sensor. Each of the sensors would only need to be active for a split second. Assuming each sensor has a nominal activity and power respectively $0.5\,\mathrm{s}$ and $1\,\mathrm{W}$. The total estimated power consumption of the system would be $325\,\mathrm{J}$. The energy use for this method is rated as very low.

11.4.2. String-Based Mechanism

A string-based mechanism was another proposal. Here, a string is taught through a channel running throughout the payload bay. This channel has holes where the string is exposed, and the sensors can be attached. To deploy the sensors, the string is reeled in. When the end of the string reaches a sensor, the sensor simply falls.

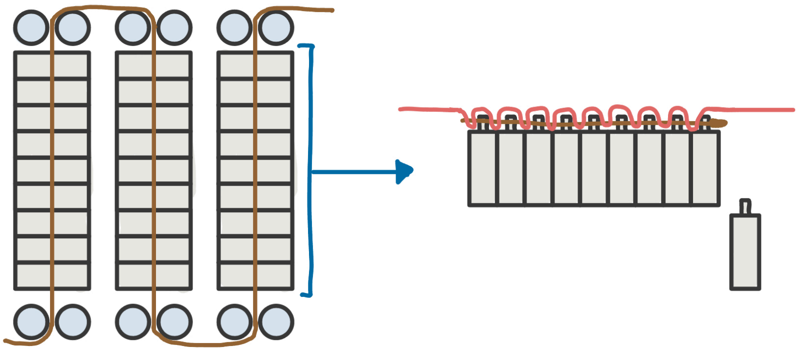

Figure 11.3: *Sketch of a string based system concept.*

Weight
For the estimations, a sensor layout of 25 x 26 and a sensor size of 65mm by 65mm is used. The weight of this system will be mainly related to the wire and the guidance system for the wire. The total length of wire between the sensors is 44m and an additional 2m is added, bringing the total length to 46m.

Using a paracord that can withstand a weight of $250\,\mathrm{kg}$ and has a weight of $6.6\,\mathrm{g}$ per meter [86]. This means the total weight of the wire will be $303.6\,\mathrm{g}$ The supporting mechanism will contain two guidance rollers per row and a supporting mechanism for the cable within the rows. The rollers are estimated to be $15\,\mathrm{g}$ each and the guidance in each row is estimated to be 100g for each row. This will come down to a total weight of $3350\,\mathrm{gm}$ To reduce tension in the wire, the wire can be split up into three segments. This means three rolling engines will be needed. The weight of these planetary gearbox stepper motors is estimated to be $391\,\mathrm{g}$ [87]. The total weight of the motor will be $1173\,\mathrm{g}$. The total estimated weight for the components is $4.8\,\mathrm{kg}$.

Reliability & Risk
The reliability of this system is expected to not be optimal. There are multiple scenarios where the system could fail. For example, the wire could derail from its guiding system, a sensor hole is too tight, and the motor can not pull the cable through it or a wire could break. All of these scenarios are critical to the deployment system. Pulling a wire through numerous sensors could also introduce extensive tension which inducing create a design risk. The reliability and risk of this system scored: low.

Cost
The costs of this system consist of the wire, wire guiding system, and the motor to pull the wire. The motor will cost around 50 euro each [87] and the wire has a cost of around 30 euro [88]. The guiding system consisting of 60 rollers, where one roller cost is estimated at EUR 5, will cost EUR 300. The total cost is estimated to be around EUR 480. The cost calculation is not very accurate, for that reason we rate this system as low cost.

Operations
The loading of the sensors in this system is expected to laborious task. The wire needs to go through each of the 650 sensor connection points. This is a labour-intensive job compared to the systems that could be created for the vending mechanism or electromagnetic mechanism, this design scored a low on this criterion.

Energy Consumption
The energy consumption of this system is due to the motor that will pull the cable. The motor has an efficiency of 94% [87]. To calculate the energy consumption, the total amount of work needs to be calculated. With an average arm of $3\,\mathrm{cm}$ of the rolling engine and an average pulling force of $60\,\mathrm{N}$, the torque induced on the engine is estimated to be $1.2\,\mathrm{N}{*}\mathrm{m}$. Taking a wire length of $44\,\mathrm{m}$, the total work performed on the system will be 1760 joule [82].

11.4.3. Vending machine design
The vending machine-based design is inspired by how a vending machine disposes of its items. By a rotating shaft, the items are being pushed forward until the item will fall. The sensors will be stacked up on each other. The spiral at the bottom will dispense the sensors one by one. The sensors will be deployed per column.

There will be 4 rows where 23 sensors will be in line that are stacked up with 7 sensors.

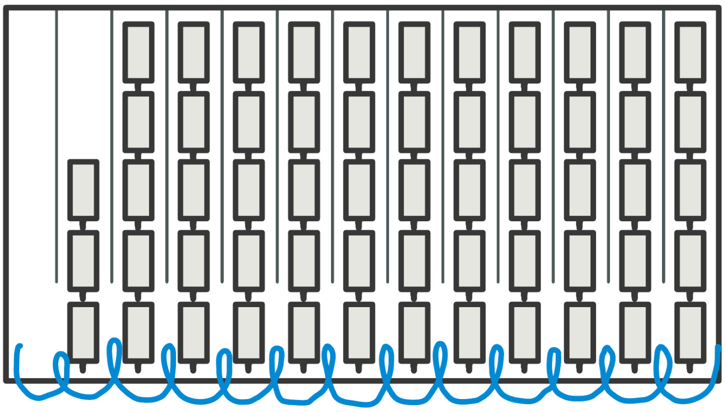

Figure 11.4: *Vending machine concept*

Weight
The main contribution of the weight will be in the metal shafts and the motor to rotate the shaft. There will be four metal shafts that will push the sensors forward. The length of these shafts will be around $6.6\,\mathrm{m}$ when taking a pitch angle of the spiral shaft of 70°and a length covering the length of $1.5\,\mathrm{m}$. With a diameter of the shaft of $4\,\mathrm{mm}$, each shaft will have a mass of $0.875\,\mathrm{kg}$. This gives a total mass for the shafts of $3.5\,\mathrm{kg}$ For the rotation of the shafts, the same mass as for the motor if the rope method is being used. This leads to a total mass for the motors of $1564\,\mathrm{g}$. The total mass of all components will come down to $1.56\,\mathrm{kg}$.

Reliability & Risk
The reliability of this method is decided to be low. The sensors will be sliding over each other and there are a lot of points in which one of the sensors could get blocked. Sensors could also get stuck in when being released and dropped. The result of one of these failures will be catastrophic for the system. A sensor that is blocking the exit of the deployment system will result in a loss of the deployment system. There is also a risk that one of the sensor's wire attachments will deploy unexpectedly. This will entangle the whole deployment system and causes a loss of the deployment system. The reliability & risk aspects of this method are scored very low.

Cost
The cost of this method is deduced from the four motors that would be needed and the metal wire that needs to produce. The four motors will have a cost of around EUR 50 per engine. The same motor of previous estimations is used. The wire is estimated to be 30% material costs and 70% production costs. A shaft of aluminium alloy 7075 costs 23.61 euro for $1.5\,\mathrm{m}$ and has a diameter of $20\,\mathrm{mm}$ [89]. Because the diameter of the product is larger we multiply the cost by 0.8. This will result in an estimated cost of EUR 1108. Combining this with the cost of the engines. The estimated cost will be EUR 1308.

Operations
Loading of this system can be done easily. The sensors can be dropped into the payload bay from the top. This would make it quick and easy for the person who operates the system to reload it. The score given for this aspect is "good".

Energy consumption
By taking a pitch angle of the metal shaft of 70°. A total of 140 winding is estimated to be in each shaft. An average torque required is estimated to be twice the force of the wire mechanism, coming down to $120\,\mathrm{N}$ on the arm of the shaft. The shaft will have a radius of $0.75\,\mathrm{cm}$. This will result in 791.7 Joule per shaft. In total and taking the motor efficiency [87] into account. The total power consumption will be $3368\,\mathrm{Joule}$.

11.4.4. Tape method

The tape method refers to a spool mechanism that stores the sensors rolled around it in a deployment belt. This deployment belt attaches to a pushing and rolling mechanism that rolls the belt to the correct position and then pushes the sensor out for deployment.

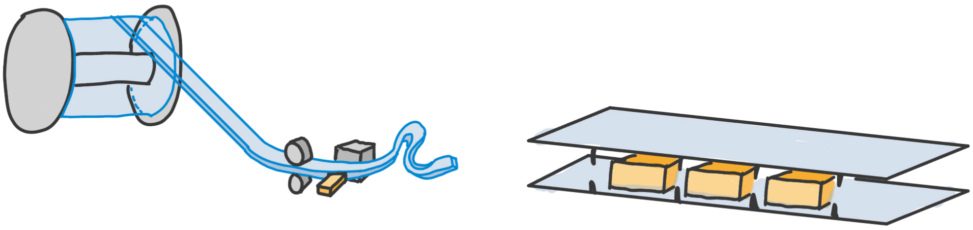

Figure 11.5: *Sketch of a tape method system concept.*

Weight

The weight of this design depends on its main components (neglecting the attachment structure to the blimp structure). The spool, motor, piston, and belt. With some preliminary sizing, the size of the spool turns out to be around $31\,\mathrm{cm}$ for its outer diameter, $6\,\mathrm{cm}$ for its inner diameter and $44.5\,\mathrm{cm}$ for its length. Considering a hollow PLA 3D printed spool with density $1.25\,\mathrm{g/cm^3}$ and wall thickness of $4\,\mathrm{mm}$, the spool weight is $0.937\,\mathrm{kg}$ [90]. A spool can be bought online with different material but for the sake of this trade-off, PLA will be considered. The motor and the linear actuator is estimated at $0.34\,\mathrm{kg}$. For the belt, two rubber strips of $1\,\mathrm{mm}$ thickness, at the required length($42\,\mathrm{m}$x$0.085\,\mathrm{m}$) were taken into consideration for the weight estimation. The belt weighs $7.57\,\mathrm{kg}$. For a thickness of $2\,\mathrm{mm}$ the weight of the belt will be $15\,\mathrm{kg}$ Therefore, the whole tape system (with $1\,\mathrm{mm}$ rubber strip thickness) weighs $8.84\,\mathrm{kg}$.

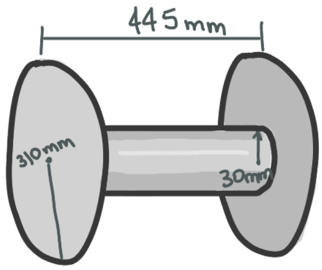

Figure 11.6: *Spool sizing*

Reliability & Risk

Regarding the reliability and risk, the system has the benefit of securing the sensors in a belt and thus decreases the risk of falling sensors or sensors getting stuck. The moving part is the belt that if it remains stretched no big risks are presented. However, this system has a lot of moving parts that need tuning to work with each other. Considering that the blimp will have to be transported regularly, a bigger risk is posed to the reliability of the system since the spool system is fragile to movement and vibrations. Another risk would be that the tape would break. This would be fatal for the system. The system is given the score "low" on this criterion.

Cost

The cost of the main components of the system consists of the motor, piston, spool, and belt cost. The motor and linear actuator can be bought EUR 25 and EUR 23 respectively [91] [92]. The spool will be estimated with the cost of PLA. The mass of the spool is $0.937\,\mathrm{kg}$ and the PLA cost per kilogram is around $20\,€/\mathrm{kg}$. Thus, the spool will cost $18.74\,€$. The belt can be bought and manufactured by EcoSense at a cost of $51\,€$. The price was calculated linearly with the price of a rubber strip found online [93]. The total cost of the system is $117.74\,€$.

Operations

Operationally the tape method consists of two main phases. The flight phase and transporting phase. During the flight, the working operations of the tape method will be as follows. The motor rolls the belt by the appropriate amount to locate the next sensor right in front of the piston. Then, the piston pushes the sensor out of the belt and deploys it. This procedure repeats until all the sensors are deployed. During the transportation phase, the system will have to be disassembled and assembled with every mission. This makes the operations quite complicated and time-consuming. This also introduces risks as discussed in the previous subsection. Replacing the system and getting the sensors in the tape and on the spool could induce some difficulties. Because of this, the operations is given a score 'low'.

Energy Consumption

By considering an average pulling force of $15\,\mathrm{kg}$ over an average arm of $0.3\,\mathrm{m}$ we get an average torque of $44\,\mathrm{Nm}$. The tape length is $42\,\mathrm{m}$. Over an average radius of $0.3\,\mathrm{m}$ the total number of windings needed to deploy all the sensors is 22. Using Equation 11.1, the total amount of energy equals $6082\,\mathrm{J}$. Worth noting is that this is a slight overestimation due to the assumed length of the average arm and radius.

11.5. Deployment Mechanism Design Trade-off

the aforementioned characteristics of each design option are summarised in one trade-off table 11.7. The estimations in previous sections are rough but can be used to respectively rate each of the systems to each other. A method is being used to rate each system by qualitatively and analytically comparing them to the other system. A percentage for each category is given per design and must sum up to 100%. The most important criteria are given the large weights. Reliability and risk are leading criteria for this design. Cost is less of importance due to the fact that the vehicle will be reusable, and the costs will be spread out over all the missions that it will perform.

option \ criterion	weight kg	R&R	cost	operations	energy
electro magnet	8,3 [blue]	good [green]	4550 [orange]	very good [green]	325 [green]
wire design	4,8 [blue]	low [red]	480 [blue]	low [orange]	1760 [blue]
vending machine	1,56 [green]	low [red]	1308 [blue]	good [green]	3368 [blue]
tape method	8,67 [blue]	low [red]	260 [blue]	low [orange]	6082 [orange]

legenda
Excellent, exceeds requirements
good, meets requirements
Not optimal, but don't violate requirements
unacceptable

Figure 11.7: *Deployment trade-off*

From the trade-off, the electromagnetic design is chosen. It performs excellently on reliability and energy consumption which outweigh is relatively high weight and cost.

11.6. Electromagnetic System

The requirements listed in Table 11.1 are driving the design of the payload mechanism. The design is chosen to be an electromagnetic deployment system. In this section, a more detailed look will be given at this subsystem. The design will focus to fulfil these requirements. The trade-off of the design is made with the design of 650 sensors. After an iteration of the total design, an amount of 555 sensors is needed to be housed in the payload bay. This includes also the relay nodes that need to be deployed by the system. The layout will be a matrix with 37 sensors in the longitudinal direction and 15 in the lateral. The decrease in sensors will not change the outcome of the trade-off. The weight and energy consumption are generally to be in a linear relation related to the number of sensors. So the relative score on each of these criteria will stay constant.

11.6.1. Electromagnet Selection

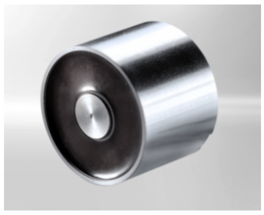

Figure 11.8: *Real photo of the electromagnet*

The electromagnet that is suitable for the connection between the sensor and payload bay is the PEM1213A from Kendrion [85]. The Sensor can hold $8\,\mathrm{N}$ of force and weights $100\,\mathrm{g}$. The sensor itself has a mass of $77.306\,\mathrm{g}$. Gravity will induce $0.75837\,\mathrm{N}$ of force downwards. This means the connection is over-designed. The electromagnet was the smallest size available we could find. By creating a linear regression of the available electromagnets, the weight of weaker electromagnets could be estimated. The four family sensors of the chosen model are used for the regression and had a R^2 value of 0.997%. It is estimated that the weight of an electromagnet with a holding force of $4\,\mathrm{N}$ will weight $7.789\,\mathrm{g}$. This could reduce the estimated weight by around $1.25\,\mathrm{kg}$. Because a smaller electromagnet is not available and contacting manufacturers to request a custom electromagnet that would be more suitable for EcoSense is out of the scope of the design synthesis, the PEM1213A will be used for the payload deployment mechanism. Regarding the relay node that will have a weight of $156\,\mathrm{g}$ and will have the same footprint as the sensor nodes. This means that no adjustments to the payload bay need to be made because both can be attached to the same electromagnet.

In Figure 11.8 the electromagnet is shown. The height of the sensor is $13\,\mathrm{mm}$ and diameter is $12\,\mathrm{mm}$. Further dimensions are found in the product manual [85].

11.6.2. Attachment to Gondola

The electromagnets will be connected to the gondola with the use of separate connection parts. The connection part that can be seen in Figure 11.9. The electromagnet has a pin that will be glued to the connection part. The connection part will then be connected to the payload bay. This will be held in place by glue and a pin locking mechanism. The payload bay needs to be able to hold a distributed weight of around $45\,\mathrm{kg}$. The payload bay is a major part of the gondola. The loading of this is discussed in Chapter 5.

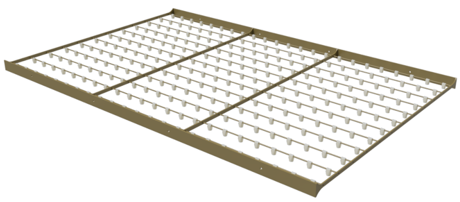

(a) *Render of the payload tray.*

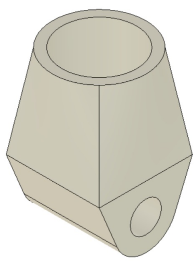

(b) *Connection part for electromagnet*

Figure 11.9: *Electromagnet attachment.*

11.6.3. Energy Consumption

The energy consumption was already calculated inSubsection 11.4.1. For 650 magnets the energy consumption is 325 J. Due to the linear relation between energy consumption and the number of magnets, the energy consumption is now 275 J.

11.6.4. Loading Sensors in the Payload Bay

By creating a grid where the sensors can be in aligned on the ground, the sensors can be easily connected to the payload bay. When all sensors and relays are aligned in the grid, the blimp can be lowered onto the sensors. The sensors will automatically attach to the electromagnet Because the payload bay will be open from the bottom, the sensors will automatically be attached to the electromagnets.

11.6.5. Sensor Deployment

The sensors can be rapidly deployed. The Deployment system will receive a signal from the flight computer when to deploy. Successful deployment will be confirmed with photo conductive cells. The detachment of a sensor or relay node will expose the Photo Conductive cell to light. This will make it possible to verify the deployment. An unsuccessful deployment can be detected within one second. Due to the speed, the deployment system can operate, a new sensor can almost instantly be deployed to avoid and gap in the distributed network of sensors.

11.7. Sensitivity Analysis

A sensitivity analysis will be performed to determine if the payload mechanism and payload bay can function disregarding small deviations of influencing aspects. Each of the critical aspects of the design on which a sensitivity analysis is performed is to be found in this section.

Deviation in sensor and relay size

The footprint for a relay node and sensor node are equal. They have a dimension of 65 mm by 85 mm. The payload bay will have spacing between each of the sensors of 10mm on each side. This gives a margin of 5 mm per sensor on each side. In the longitudinal direction of the payload bay, the sensors have a margin of 15.3% and in the lateral direction a margin of 11.8% in dimensions.

Deviation in sensor and relay weight

The PEM1213A electromagnet can hold 8 N. This is equal to a holding weight of 815 g. When taking a safety factor of three into account, the sensors will weight 7946g, giving it a margin of 342%. The relay node's weight is 156 g. This gives the weight of the relay node a margin of 174%. The margins for both the sensor node and relay node disregard the tolerable maximum payload mass of the vehicle.

Deviation in electromagnet holding force

The sensitivity analysis for a variation in holding for of the electromagnet can be directly related to the sensitivity analysis of the deviation in weight of the sensor and relay nodes. However, the maximum deviation that the electromagnet could have is solely related to the heaviest component and this is the relay node. This results that the electromagnet holding force can maximum decrease with 42.6% before becoming too weak.

11.8. Risk Analysis

The risks and risk mitigation of the payload deployment mechanism are given in Table 11.2. It needs to be mentioned that it is near impossible to identify all possible risks that are imposed on the payload deployment mechanism, but by performing this analysis on the known risks, the total risk is significantly reduced.

Table 11.2: *Risk assessment of deployment mechanism and payload bay.*

Index	Risk Factor	HS	HP	HRI	Mitigation strategy	HS	HP	HRI
1	Deployment mechanism gives false positive on successful deployment, resulting in a gap in sensor network.	8	4	32	Using reliable photo-conductive sensors.	7	1	7
2	Deployment mechanism breaks due to hard landing.	10	3	30	Adding safety margins for the structural design.	6	1	6
3	Electromagnet unable to deactivate for deployment.	7	4	28	Add extra capacity to payload bay to cover broken electromagnets. Perform health check on electromagnets before flight. Capability of system to detect failed deployment and can rapidly deploy new sensors.	2	2	4
4	Deployment mechanism is not able to receive signal to deploy sensors.	10	2	20	Perform system check before flight of the mission.	6	1	6
5	Sensor deploys its strings before separated from vehicle and damages other sensors.	5	3	15	Placing deployment strings on top of sensor so that strings will be launched against bottom of payload bay and not against other sensors.	1	3	3
6	Sensor and relay footprint are larger than than expected.	7	2	14	Design a margin between sensors in payload bay.	2	2	4
7	Payload bay has insufficient capacity.	4	3	12	Add extra capacity to payload bay.	2	1	2
8	Sensors and relay nodes having a larger mass than expected.	6	2	12	Adding safety margin to the holding force of electromagnet.	1	2	2
9	Deployment mechanism gives false negative on successful deployment. (system deploys a sensor too many).	4	3	12	Increasing capacity of payload bay.	2	3	6

11.9. Verification and Validation

The design of the deployment system is chosen by quantitative and qualitatively comparing four different design options. For the qualitative part, commercially available parts and components were used. The components selected are chosen to be over-designed. By doing this and in combination with engineering experience, it can be validated with reasonable certainty that the comparisons are valid.

Requirements REQ-VEH-DEP-1 and REQ-VEH-DEP-8 are yet to be determined. In the current design phase it is not possible to validate these requirements. These requirements should be verified through testing, which falls outside the scope of the DSE

11.10. Sustainability Analysis

The payload deployment mechanism will contain mainly its electromagnet, wiring, and photo conductive sensors. Each of the components is essential for the functioning of the deployment mechanism. Regarding sustainability, these components can't be replaced with a more sustainable variant. To reduce the impact of the components on the environment, economy, and society the following has been thought of. To reduce environmental impact, the components should be of high quality and have a long lifespan. This will reduce the need for maintenance and in place reduce the carbon footprint. Simultaneously this will also reduce the economic impact due to the costs that are spared that come with maintenance. To ensure this, high-quality electromagnets are selected for the deployment mechanism. Regarding impact on society, this deployment system will only have an impact on the workforce that has to load the payload bay. The electromagnet system can be loaded very efficiently without a lot of effort. This will have a positive impact on the person who has to operate the vehicle. More on the sustainability aspect of the total design can be found in Chapter 19.

12 Sensor Nodes

During its mission, the vehicle deploys a large amount of devices that, when arranged into a network, detect fires much earlier than comparable methods, such as satellite detection. These devices, from now on referred to as 'nodes', act as detectors of gases produced by fires in their early stages, such as carbon monoxide and hydrogen.

The design of this network incorporates two types of nodes: the sensor nodes, which monitor gas concentrations, temperature and humidity levels and the relaying nodes, which communicate the measurements taken by the sensor node back to the ground station and user. This chapter describes the sensor node design process and its outcome in Section 12.1, after which its functions are described in Section 12.2. Following this, a sustainability analysis is performed in Section 12.3. Finally, the risk of the design is considered in Section 12.4 and the design is verified and validated in Section 12.5.

12.1. Sensor Node Design

The sensor node must fulfil several functions, which are all driven by the requirement to detect fires. The requirements that are placed upon the sensor nodes are as follows in Table 12.1.

Table 12.1: *Sensor Node Requirements.*

Req. ID	Requirement	Section	Compl.
REQ-SENS-3	The sensor node shall have a functional lifetime of 5 years.	12.3	✓
REQ-SENS-DG-1	The sensor node shall be able to detect smouldering fire gases (H□, CO, CO□).	12.1.2	✓
REQ-SENS-DG-2	The sensor node shall contain a temperature sensor.	12.1.2	✓
REQ-SENS-DG-3	The sensor node shall contain an atmospheric pressure sensor.	12.1.2	✓
REQ-SENS-STR-1	The sensor node shall be made of at least 50% biodegradable materials.	6.8	✓
REQ-SENS-STR-2	The sensor node structure shall prevent failure of internal hardware after the deployment impact.	12.1.2	≈
REQ-SENS-STR-3	The sensor node shall be at least IP55 rated for the duration of its lifetime.	12.1.2	TBD
REQ-SENS-STR-4	The sensor node shall withstand a UV index of 15 for the duration of its lifetime.	12.3	TBD
REQ-SENS-STR-5	The sensor node structure shall not contain any materials which could lead to the contamination of the area of deployment.	12.3	×
REQ-SENS-STR-6	The structure shall enable mounting of sensor node hardware.	12.1.2	✓
REQ-SENS-STR-7	The sensor node shall be manufacturable.	15.3	✓
REQ-SENS-POW-1	The energy storage system shall enough capacity for the sensor node to have 7 minute of transaction time per day.	12.2	✓
REQ-SENS-POW-2	The power subsystem shall produce energy.	12.1.2	✓

Explanation regarding the (non-)compliance of these requirements is given in Section 12.5. All the requirements guide the design process. The main demands that the design must fulfil in order to meet the requirements, and its corresponding requirement identifier, are given below in no particular order:

Water and Dust Resistance (*Requirement ID*: REQ-SENS-STR-2)
Leading directly from REQ-SENS-STR-2, the sensor must be resistant against rain, dust or other environmental factors. Given this, it was decided that the sensor must be rated at IP55, which states that the sensor must continue to function when exposed to a low-pressure jet of water or dust.

Although this requirement is usually verified through testing, this falls outside the scope of the DSE. As such, inspection of the final design will be used to verify its water and dust resistance by ensuring that all electronics or critical parts are protected.

Sensor Performance (*Requirement ID*: REQ-SENS-DG-1 to REQ-SENS-DG-4)
The ability to detect fires is imperative to the design. As such, the sensing node must be designed in such a way that the gas, temperature and humidity sensor is not hindered. This requires wind from any direction to reach the sensor so that the presence of gases such as CO or H^2 can be detected.

This requirement conflicts with the requirement to be water and dust resistant, as the gas sensor must be exposed, which provides an entryway for water or dust. As such, the design will have to find a way to fulfil both these requirements concurrently.

Biodegradability (*Requirement ID*: REQ-SENS-STR-1, REQ-SENS-STR-5)
As the sensor is left in the environment permanently, care has to be taken to not cause excessive pollution. This includes limiting the use of materials that directly harm flora or fauna, but also the inclusion of biodegradable materials in the design to limit its ecological impact.

This requirement materialises itself in the material selection of the enclosure and subsystems, where biodegradability becomes one of the most important selection criteria.

Attachment Strategy (*Requirement ID*: REQ-SENS-STR-6)
The attachment strategy of the node to the environment has a great impact on the geometry of the design. It can affect the impact it has to resist, or make space for additional mechanisms that are required.

Power Generation (*Requirement ID*: REQ-SENS-POW-1, REQ-SENS-POW-2)
If a solar panel is present, the design must accommodate it. Room also must be made for any energy storage systems.

Manufacturability (*Requirement ID*: REQ-SENS-STR-7)
Depending on the material, different manufacturing techniques are available. These may impose restrictions on the geometry of the material. As such, care must be taken to ensure that the final design is manufacturable.

12.1.1. Iterative Process

The design of the sensor node was done through CAD prototyping. Iterative designs were made, each aiming to fulfil the demands listed above, with limitations being identified in each design and ratified in future iterations. In the figure below, a few iterations of the sensor node design can be found:

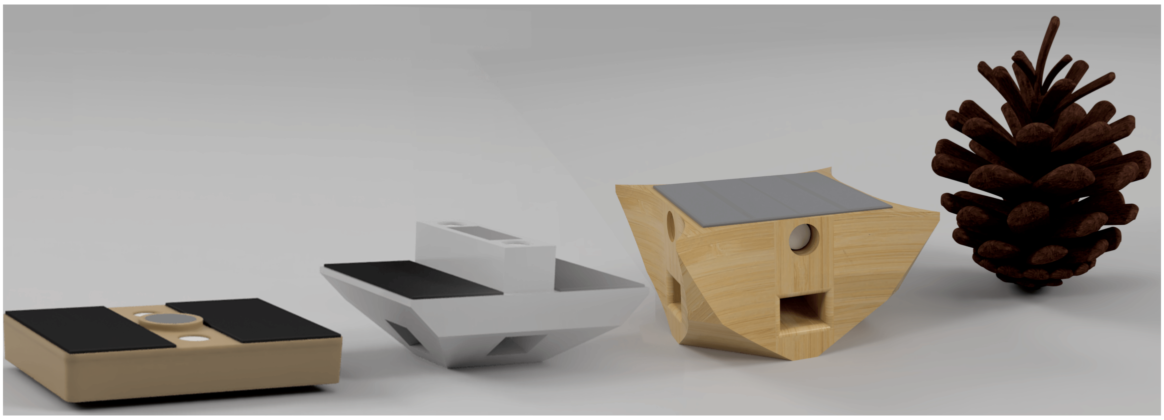

Figure 12.1: *Three iterations of the sensor node, first to last from right to left. Pine cone is shown for scale.*

For the sake of brevity, not every iteration will be shown in depth. Instead, it will be shown how each iteration improves upon fulfilling the demands listed in the previous subsection, and the design decisions taken along the way.

Water and Dust Resistance
This demand is mostly met through material choice and geometry. The gas sensor must be exposed to air, which means that there will always be a gap in the enclosure which provides a chance for water or dust to enter. It is therefore imperative that the geometry aims to prevent jets of water and dust from getting to the rest of the electronics.

Initially, the sensor was placed on the bottom of the node. Due to gravity, most rainwater cannot get to the sensor like this. Water being sprayed at an angle or from below is prevented through channels that shield the sensor and allow for the ejection of any standing water. An example of these channels in the initial iteration can be seen here:

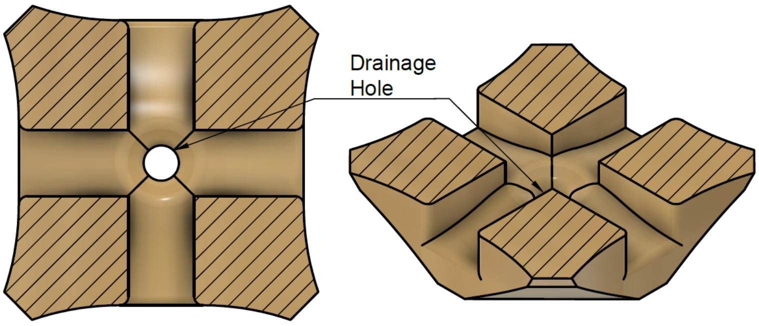

Figure 12.2: *Cross-sectional view of the first iteration of the design, and an example of channels to eject water from the sensor node.*

Adding these channels prevents line-of-sight from outside to the gas sensor, reducing the chance of a jet of water getting to the sensor. Drainage holes can remove any water that does happen to settle in the channel.

Over the iterations these channels became smaller to reduce the overall mass of the enclosure. In the last iteration, a very small cover is placed over the gas sensor to protect it from direct sprays, and a thin film of a material named TEMISH® is placed over the sensor. This allows air and gases to pass through, but is impermeable to water [94].

Sensor Performance
The sensor performance, as said beforehand, may significantly affect the water and dust resistance. The more resistant to water and dust entry, the harder it is for gas to reach the sensor. In early iterations, the channels were large allowing for significant airflow, but this made the intrusion of water more likely. Over the iterations, these channels became smaller in order to reduce the mass of the enclosure, but this might have an impact on the performance of the sensor. The final iteration includes the TEMISH® film, which allows for the channels to be made much smaller. This allows gaseous molecules, including carbon monoxide and hydrogen, to pass through but blocks water from entering[94]. The effect this film has on the performance of the gas sensor is impossible to quantify without actual testing. However, given that it significantly reduces the size and mass of the sensor, and in theory does not impede airflow [94], the decision was made to include this in the final iteration with the assumption that it does not meaningfully hinder sensor performance.

Biodegradability and Manufacturability
These two demands have been combined as they both are heavily governed by the material choice. Given the demands that most of the enclosure must be biodegradable, and that it must be manufacturable in large batches, a material that allows for these demands to be met is required. The material does not have to carry significant load except for the weight of the components, and as such the only requirement is that it is stiff enough to not significantly deform when deployed. It is important that the material is as light as possible, so lower densities are preferred. The materials selected are all biodegradable or compostable to some extent:

Table 12.2: *Overview of potential materials and their properties. [95] [96] [97] [98]*

Material	Manufacturing Method	Water Resistance	Biodegradability in Soil	Density [g/cm^3]
PBT	Additive manufacturing or injection molding	Low water absorption	Slow if not composted	1.31
Cellulose Acetate	Additive manufacturing or injection molding	Impermeable	3-5 years	1.31
PLA	Additive manufacturing or injection molding	Impermeable	Extremely slow if not composted	1.25
Bamboo Laminate	Milling or additive manufacturing with PLA	High water absorption	Without PLA, 5-10 years	0.79

To fulfil the functional lifetime, the enclosure must not biodegrade significantly before 5 years. After these 5 years, it is desired that the enclosure biodegrades relatively quickly. This means that materials that must be composted, such as PBT or PLA, are not viable alternatives.

Besides this, the manufacturability plays an important role. Bamboo, while much less dense, is not easy to manufacture for larger batches with complex geometry. Additive manufacturing can be used, but this process often uses PLA as a resin which does not biodegrade unless composted.

This leaves cellulose acetate as the material selected. Over the iterations, it can be seen how the material changes from bamboo to PBT to cellulose acetate, which is indicative of the discovery of new material during iterations. Eventually, cellulose acetate was settled on for the aforementioned reasoning.

Attachment Strategy
The chosen attachment method for the sensor was to use deployable strings that entangle themselves in foliage, thereby attaching the sensor node above the forest floor. The sensor's performance is optimal when placed several meters above the ground [4] [99], and as such an elevated attachment is ideal.

For redundancy, several strings were included on the node, starting with 4 on the first iteration as shown in Figure 12.1. These fired outwards with the idea that it would hang from multiple strings causing the solar panel to face upwards. However, it was realised that if only one string attached, the sensor would hang sideways limiting the solar panels' effectiveness.

From the second iteration, the string deployment mechanism was moved to the top. Now, two strings are deployed, with only one being required for successful attachment. Having it on the top means the solar panel will face upwards regardless of whether one or two strings are attached. In the final iteration this mechanism was also moved into the main housing of the sensor node, as will be shown in more detail in Subsection 12.1.2.

Power Generation
A solar panel is included in all iterations that was sized to provide enough power for the operation of the sensor node [4]. As described earlier, the string attachment method ensures proper orientation. The inclusion of curved solar film was explored to allow for more options in the sensor's geometry, but commercially available solar films have an efficiency that was 50% worse than the poly-crystalline panels used in the final design [100]. This meant they were not feasible in the inclusion of this design.

12.1.2. Final Design
Having implemented design concepts discovered during the iterative prototyping, the final design was created:

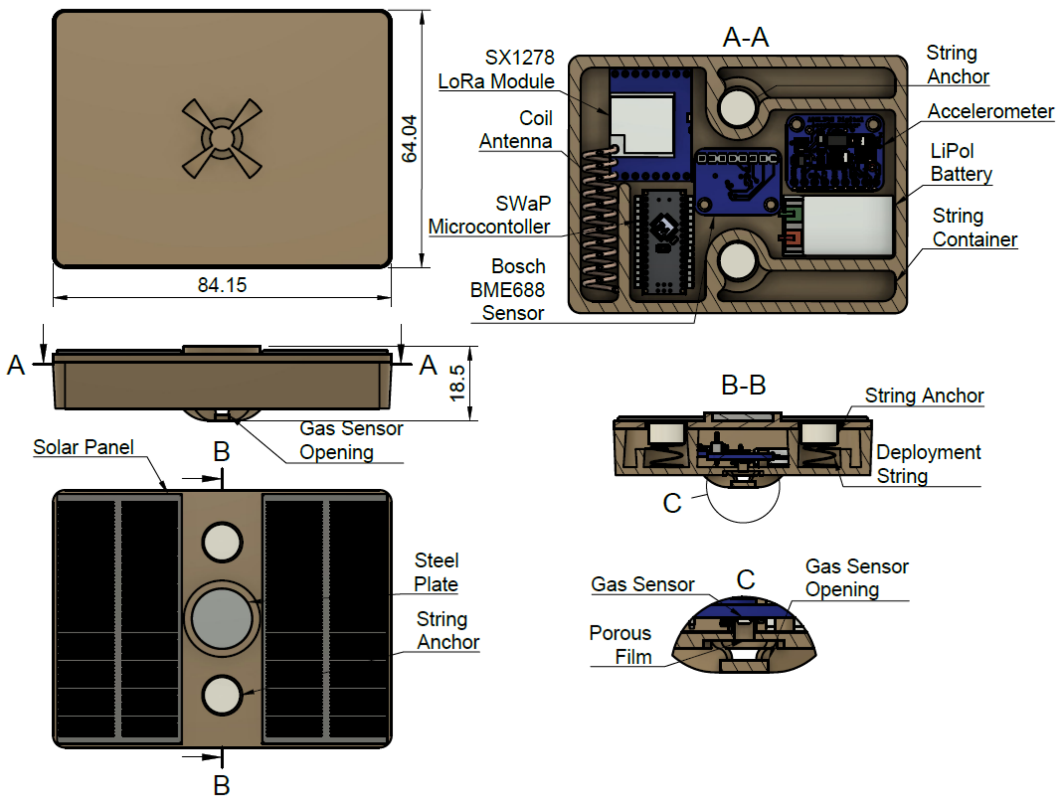

Figure 12.3: *Drawings of the final sensor design, all measurements in* mm.

Table 12.3: *Mass estimation of sensor node. [4] [101]*

Component	Contribution [g]
Bosch BME688 + SWaP microcontroller	0.100
SX1278 + Antenna	5.000
Accelerometer	0.018
Battery	2.700
Solar Array	17.00
Spring	2.000
String Anchors	0.660
String	2.000
Steel Plate	2.700
Enclosure	43.50
Subtotal	75.678
Total (+5% margin)	79.462

Table 12.4: *Cost estimation of sensor node. [4] [101] [102]*

Component	Contribution [€]
Bosch BME688 + SWaP microcontroller	22.60
SX1278 + Antenna	8.00
Accelerometer	3.00
Battery	1.85
Solar Array	1.85
Spring	2.00
String Anchors	0.03
String	2.00
Steel Plate	0.05
Enclosure	1.96
Subtotal	43.34
Total (+5% margin)	45.50

Table 12.5: *Power consumption of sensor node. [4]*

Component	Contribution [mW]	
	Transmitting	*Idle*
Bosch BME688 + SWaP	15.00	15.00
SX1278 + Antenna	396.0	0.019
Accelerometer	0.063	0.063
Subtotal	411.1	15.08
Total (+5% margin)	431.6	15.84

Most cost, mass and power estimations are derived from commercially available alternatives [4]. Other mass and cost estimations, such as the string anchors, steel plate and enclosure are derived from the CAD model using the corresponding densities or price for the chosen material [102] [101]. As such, most estimations are relatively accurate, and the total contains a 5% margin instead of a 20% margin as used previously [4]. Manufacturing cost is not yet included.

The design features several subsystems, which are the power subsystem, the deployment subsystem, the communication subsystem, and the sensor subsystem. The performance of these subsystems is elaborated upon in Section 12.2.

The enclosure is made out of cellulose acetate. The sensor features a steel plate, which is so that it can attach to the electromagnetic payload deployment system of the vehicle. The enclosure is also given a brown colour, to stand out less from the environment in which it is deployed. The string is made out of lyocell.

The system transmits for seven minutes over $24\,\mathrm{h}$, two of which are dedicated to a status check, where once during the day and once during the night the sensor sends out an update saying it is still operational for one minute each. The remaining five minutes are in case of a fire detection. In that case, the sensor will continuously transmit an alert to the ground station for five minutes to prompt a firefighting response. Given this transmitting time, it is determined that the sensor needs an average of $17.86\,\mathrm{mW}$ for two minutes of status check and five minutes of fire alert transmission. At night, the sensor also needs to transmit for five minutes in case of a fire, while needing one minute of a status check transmission. This means that on average $18.81\,\mathrm{mW}$ is needed during the night to fulfil this requirement. During the day, the solar panel should therefore produce the sum of these values, equal to $36.66\,\mathrm{mW}$.

The sensor must be attached to foliage via strings, but must not attach to the top of the canopy as this severely hinders sensor performance [4]. As such, the deployment subsystem deploys two strings when the sensor has passed through the forest canopy, to ensure the sensor attaches to low branches or shrubbery, both of which are widely distributed in the national park that this mission is aimed at [4]. A description of how this deployment is timed is given in Subsection 12.2.2. The strings are deployed upwards using springs, and the strings tangle into nearby foliage in order to attach the sensor to the environment. Once the sensor hangs off one or two of these strings, the sensor is oriented with the solar panel facing upwards. A description of the sizing of the deployment mechanism is given in Subsection 12.2.2.

The sensor is made out of cellulose acetate, a material that is biodegradable in soil in 3-5 years [96]. All subsystems operate on $3.3\,\mathrm{V}$, with the input voltage from the solar panel being stepped down using a charge controller. A detailed overview of the electronics is given in the electrical block diagram in Subsection 12.2.1.

Finally, the sensor contains two types of sensors: the BME688 sensor - which measures temperature, CO and H^2 concentration and humidity [103] - and an accelerometer. The accelerometer detects disturbances to the sensor, which can indicate whether the sensor has dropped from its attachment method, or moved by an animal. If this happens, the predetermined deployment location is no longer accurate. It is also used to determine the string deployment timing as shown in Subsection 12.2.2. These sensors are controlled by a microcontroller, which is a controller designed to be dropped from insects[104]. Its small mass and low power consumption are ideal for the application of a low-power sensor node.

12.2. Functional and Performance Analysis

This section describes the functions and performance of each subsystem. It is subdivided into the power, string deployment communications and sensor subsystems.

12.2.1. Power Subsystem

The sensor node features a solar panel with an area of $3850\,\mathrm{mm}^2$. Under a dense canopy, the solar irradiance is estimated to be $74.5\,\mathrm{W/m}^2$ [105]. Given that the used poly-crystalline panel has an efficiency of 20%, this means the solar panel can generate $14.9\,\mathrm{W/m}^2$ [4]. As such, the area of this solar panel is enough to provide $0.057\,\mathrm{W}$ of power, which is more than the $0.036\,\mathrm{W}$ needed for operation. This additional margin can compensate for cloudy days with reduced solar irradiance.

The battery has a capacity of $0.55\,\mathrm{Wh}$. Given the average power consumption of $18.81\,\mathrm{mW}$ during the night, and assuming a maximum night length of 14 hours, [106], the capacity of the battery must be $0.26\,\mathrm{Wh}$. As such the battery provides roughly twice the capacity needed to fulfil this requirement, compensating for the loss of capacity over the lifetime of the battery [107]. The power required to charge this battery is included in the power required from the solar panel.

An electrical block diagram of the system is given below:

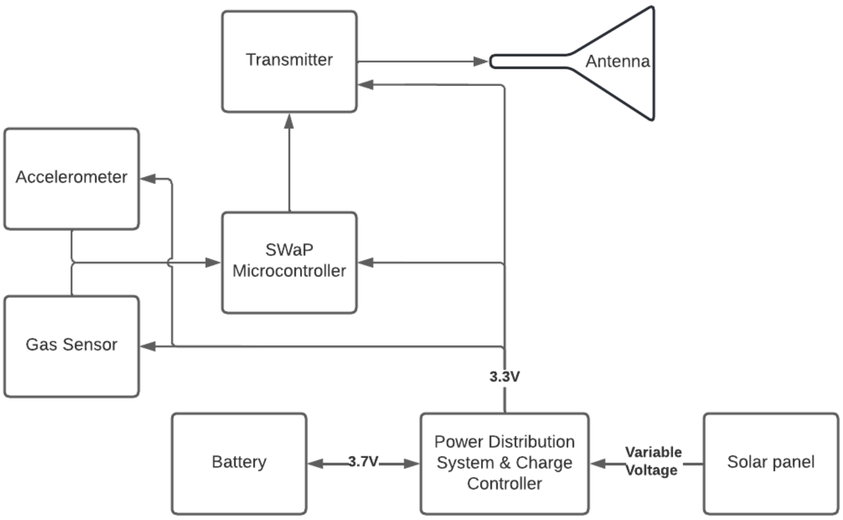

Figure 12.4: *Electrical block and hardware diagram of the sensor node.*

12.2.2. String Deployment Subsystem

When deployed, the sensor node contains an accelerometer that determines when to release the string. The goal is to entangle the sensor node in low foliage such as shrubs or low-hanging branches, and avoid it entangling in the high canopy of the trees, which are common in the Wollemi National Park. During free-fall, the accelerometer measures only acceleration due to wind and drag. When it collides with leaves or branches in the canopy, a peak in acceleration will be detected as shown in Figure 12.5.

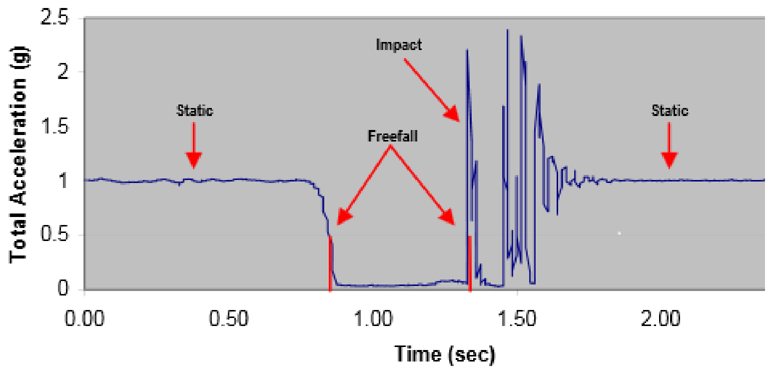

Figure 12.5: *Accelerometer readings of object during free-fall until impact. [108]*

After this peak has occurred, the strings can be deployed, which ensures that they do not entangle themselves in the canopy. The exact timing of this deployment after passing through the canopy is difficult to estimate, and must be determined through testing which falls outside the scope of this DSE.

The strings that are deployed must be strong enough to withstand deployment. The weight of the sensor node is approximately $0.8\,\mathrm{N}$. During impact, when the string gets tangled and slows down the sensor node, additional tension is applied to the string. To estimate the actual value of this additional force, the deformation of both strings have to be estimated. A suitable material for the string is lyocell, a cellulose-derived fibre that has a tensile strength, when wet, of $430\,\mathrm{MPa}$, can stretch 18% of its length before rupture, and can be derived from plant-based sources [101].

Given that the string is $1\,\mathrm{m}$ long, the maximum deformed length is $1.18\,\mathrm{m}$ when the string gets tangled. Using the terminal velocity, the force the string experiences during deployment can be calculated. Firstly, terminal velocity is given by the following equation:

$$v_t = \sqrt{\frac{2m \cdot g}{\rho \cdot A \cdot C_d}} \tag{12.1}$$

Where m is the mass of the node (approximately $80\,\mathrm{g}$), A the worst-case wetted surface area ($65\,\mathrm{mm}$ x $18.5\,\mathrm{mm}$) and C_d the drag coefficient - assumed to be 0.9 for a rectangular box [109]. Assuming sea level density, this leads to a terminal velocity of approximately $34\,\mathrm{m/s}$. Using this, the force on the string can be determined assuming that the force is applied parallel to the string:

$$F = \frac{W}{s} = \frac{\frac{1}{2} m \cdot v^2}{s_{\text{string}}} = 260\mathrm{N} \tag{12.2}$$

Where W is the work done or the string, the kinetic energy of the sensor node at terminal velocity and s_{string} is the deformation of the string, which is $0.18\,\mathrm{m}$ before breaking. Given this force and using the following formula, it can be determined that a string of $1\,\mathrm{mm}$ in diameter experiences a tensile stress of approximately $330\,\mathrm{MPa}$:

$$\sigma_t = \frac{F}{A} = \frac{F}{\pi r^2} \tag{12.3}$$

Where r is the radius of the string, equal to $0.5\,\mathrm{mm}$. This tensile stress is below the tensile strength of lyocell, and as such the string is estimated to not break during impact. As one string is strong enough to not break during impact, two strings introduce additional redundancy to prevent failure of the attachment system.

Finally, the spring used is rated to produce enough energy to propel the string anchor with a desired velocity of $5\,\mathrm{m/s}$, ensuring the entire length of the string is fully deployed in under a second before the sensor collides with the ground [110].

12.2.3. Communication Subsystem

The design features a coil antenna that amplifies the signal produced by the SX1278 LoRa module [111]. In the forest. More detail regarding the link budget, range and network design is given in Chapter 14.

12.2.4. Sensor Subsystem

The sensor performance depends heavily on its placement. An alert can only be triggered when an adequate temperature or gas concentration has been reached at the location of the sensor node. To estimate how the sensor placement and spacing affects the sensor performance, a simulation is carried out in Section 13.2, determining the sensor spacing required to complete the requirements of sensor performance.

12.3. Sustainability Analysis

Biodegradability and sustainability are an important part of the design. The enclosure, which composes 56% of the mass of the entire sensor node, is fully biodegradable. This section discusses the sourcing of materials, and whether these processes can be considered sustainable.

12.3.1. Enclosure and String

Both the enclosure and string consist of cellulose-based materials. Cellulose can be obtained from biological sources such as trees, which can be regrown [112]. As such, they can be considered a sustainable source. However, water consumption and land use must still be considered. Farming practices such as excessive expansion into nature reserves, or not replanting farmed trees would cause the acquisition of cellulose to no longer be environmentally and economically sustainable.

The synthesis process of cellulose acetate is a two-step process that uses overstochiometric (excessive) amounts of acetylating agents and concentrated acids, leading to large amounts of waste products that cannot be recovered [113]. However, alternative processes with the use of vinyl acetate can reduce the generation of waste products, leading to an E-factor of 1.92 - or $1.92\,\mathrm{kg}$ of waste for $1\,\mathrm{kg}$ of product [113]. Compared to the typical process, which has an E-factor of 3 to 10, this is a significant improvement.

A requirement for the enclosure is also that it is stable under UV conditions. Fortunately, UV light does not have a significant effect on the decomposition of cellulose acetate [114], and as such this requirement is fulfilled. Finally, its shelf life is important to fulfil requirement REQ-MIS-4. Although it is hard to estimate the shelf life exactly, it is expected that cellulose acetate can be stable for ten years in a dry, controlled environment [97].

The impact of cellulose acetate on the environment in which it is deployed is also important, as the consumption of cellulose acetate when not fully decomposed can be toxic to fauna [115]. It is therefore imperative that the enclosure does not appear as a food source. As such, it should not have a bright colour, and blend in with its environment. The colour of the enclosure is thus chosen to be dark-brown to blend in with the branches or bark.

12.3.2. Electronics

The main components that are neither sustainable nor biodegradable, and sometimes potentially toxic to the environment, are the electronics such as the wiring, PCBs, battery and solar panel. For these components, no commercially available, biodegradable replacements exist.

However, PCBs made out of cellulose derived from banana stems and wheat gluten are currently being developed, and are fully biodegradable while still being resistant to temperatures of up to $100\,°\mathrm{C}$ [116]. Although not currently available, in the upcoming years this can become a viable substitute to increase the percentage of biodegradable mass higher than 56%.

The metal contained in the electronics, such as copper and gold, will not biodegrade and remain in the environment. This is unavoidable for this design, and a cost that must be incurred to fulfil the objective of the mission.

12.4. Risk Analysis

As with any designs, there are a number of risks to consider in the design of this sensor node. In Table 12.6, a risk assessment including its mitigation strategy is given.

Table 12.6: *Risk assessment of sensor nodes.*

Index	Risk Factor	HS	HP	HRI	Mitigation strategy	HS	HP	HRI
1	Node does not detect a fire (false negative)	10	6	60	Variable density depending on risk Good AI training of the sensors Simulation of fire and smoke propagation to predict reliability of sensor network given a sensor density	6	6	36
2	Node parts catch fire	10	4	40	Isolate the fire hazardous parts of the node	6	4	24
3	Node sends false information (false positive)	6	6	36	Require a few minutes of data Isolate the obvious faulty nodes Send a small intervention crew to check on the site	6	4	24
4	Node lands face down	6	6	36	String attachment method ensures that the solar panel always faces upwards	6	4	24
5	Node hits a living being on landing	6	6	36	Low mass of sensor node Sensor node attaches to branches, never reaches the ground Sensor node made as small as possible	2	6	12
6	Water damage to electronics	6	6	36	Water resistant material used in enclosure TEMISH® film used to cover gas sensor opening Gas sensor opening created so no direct waterjet can enter gas sensor opening	2	6	12
7	Weather untangles nodes	6	6	36	String attachment is made redundant, sensor can be supported by one string	6	4	24
8	String deployment failure	6	6	36	Two strings used, one can fail and system is still successful	2	6	12
9	Solar array cannot supply enough power	6	4	24	Solar panel subsystem provides enough power including safety margins Solar irradiance loss due to foliage is accounted for	6	1	6
10	Battery leaks into the forest	6	4	24	Isolate the battery or switch to superconductors	2	1	2
11	Node breaks on landing impact	6	4	24	Attachment to branches	6	1	6
12	Solar panel damaged due to the environment	6	4	24	Add an exterior coating to the solar panel	6	1	6
13	Parts of enclosure are consumed by fauna	6	4	24	Enclosure is coloured brown to blend in with environment and not stand out	6	2	12
14	Battery not charged in time due to harsh conditions	2	4	8	Battery and solar panel should be sized for worst case scenarios	2	1	2
15	Decreased lifespan due to harsh environment	2	4	8	Cellulose acetate is stable and resistant to high temperatures or acids	2	1	2
16	Node gets picked up by animal	6	1	6	Add an accelerometer to know when to discard the node	1	1	1

12.5. Verification and Validation

For the design of the sensor node, estimates were derived from commercially available parts or computer-generated models made in industry-standard software (Autodesk). As such, it can be said with relative certainty that this design is already validated. For safety, a margin of 5% was applied onto all estimates.

In terms of requirements, the design is compliant for all but REQ-SENS-STR-2 until REQ-SENS-STR-5. REQ-SENS-STR-3 and REQ-SENS-STR-4 both cannot be fully verified until tested, as they require specific conditions to be fulfilled that cannot easily be predicted. The design is made with these requirements in mind, but they cannot be fully verified yet.

REQ-SENS-STR-2 and REQ-SENS-STR-5 are not fulfilled. The design does not comply with REQ-SENS-STR-2 as the chosen attachment strategy means that the sensor node will no longer impact the ground, removing the need for the housing to withstand this impact. Instead, the string carries most of the load. REQ-SENS-STR-5 is not fulfilled as the design includes a solar panel and batteries, which are necessary for its operation but potentially harmful to the environment with the current technology available.

13 System Deployment & Reliability

The biggest advantage of EcoSense EMBER is its aerial deployment mechanism. However, this also brings constraints such as the deployment accuracy as the sensor drops to the ground. Thus, a free fall analysis was conducted in Section 13.1. The second driving aspect of EcoSense EMBER is its reliability. The purpose is to develop a sensor network that is able to detect fires. Hence, it needs to be reliable enough that it is actually useful. The placement and mesh strategy is thus developed in Section 13.2. Finally, aspects such as risk and verification & validation are analysed in Section 13.3 and Section 13.4 respectively.

Table 13.1: *Deployment & reliability requirements.*

Req. ID	Requirement	Section	Compl.
REQ-SENS-1	The sensor network shall contain up to 1156 sensor nodes	13.2.8	≈
REQ-SENS-2	The sensor network shall be able to detect $90\,\%$ of the fires smaller than $0.2\,\mathrm{km}^2$	13.2.8	✓
REQ-VEH-CO-15	The vehicle shall deploy the sensor nodes at predetermined locations with an accuracy of ± $25\,\mathrm{m}$	13.1	✓
REQ-SENS-4	The sensor network shall detect $62\,\%$ of the fires in less than $8\,\mathrm{min}$	13.2.8	≈

13.1. Free Fall Analysis

Previously it was established that the sensor node is deployed from the blimp during flight, and free falls to the ground before the strings are deployed at an altitude of approximately $15\,\mathrm{m}$. However, the deployment altitude must first be determined based on the accuracy requirement for the deployment (REQ-VEH-CO-15). Wind can affect the deployment accuracy of the sensor node, and the effect becomes more pronounced the higher the deployment altitude is.

To simulate the effect of wind on deployment altitude, the trajectory of the sensor node is simulated. A block diagram of this simulation is shown below:

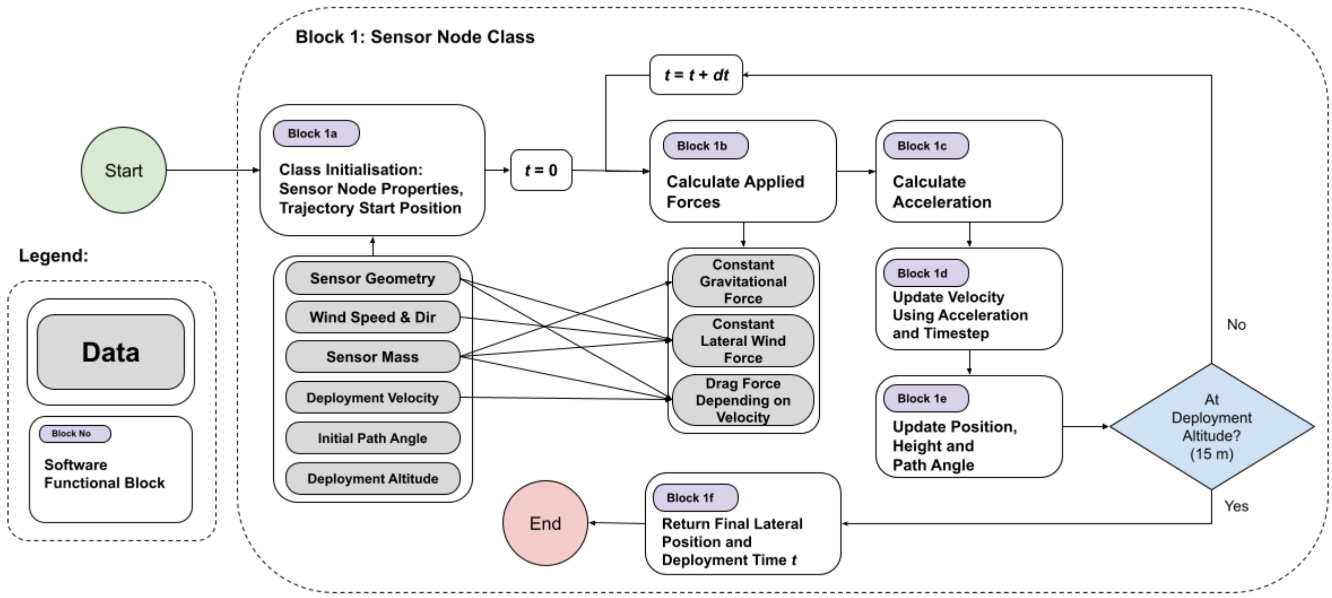

Figure 13.1: *Block diagram of free fall analysis simulation.*

This simulation is repeated for three trajectories, one with no wind, one with maximum wind speed acting opposite the trajectory, and one with maximum wind speed acting with the trajectory. The starting deployment altitude is then tweaked until the difference between these trajectories is equal to the required accuracy given by REQ-VEH-CO-15.

13.1.1. Assumptions

The simulation assumes the forces act upon the sensor node as shown in Figure 13.3. Alongside this free body diagram, the following assumptions are made:

- It is assumed that the maximum wind force in any direction creates the same amount of deviation from the trajectory (so a $20\,\mathrm{km/h}$ wind from the front creates the same deviation as the wind from the side. As such, the trajectory can be simulated in 2D without affecting the result.
- It is assumed that the maximum wind speed is $15\,\mathrm{km/h}$. This is the 80th percentile of wind speed in the mission environment [117]. It shall be included in the operations plan that the vehicle shall not operate when the wind speed is higher than this.
- The effect of gusts is ignored due to their short duration.
- The drag force caused by the wind is assumed to always act on the largest side of the sensor node, which has an area of $65\,\mathrm{mm}$ x $85\,\mathrm{mm}$, regardless of the path angle. It is assumed the drag coefficient of this shape is 1.15 [109]. The wind force is always assumed to act parallel to the ground to have the largest effect on the trajectory.
- The drag force during free-fall is assumed to act on the smallest side of the sensor node, or $65\,\mathrm{mm}$ x $17.5\,\mathrm{mm}$. The drag coefficient of this shape is assumed to be 0.9 [118].
- The terrain the node is deployed on is assumed to be flat.
- Drag force due to free-fall is assumed to be parallel to the velocity vector.
- The sensor node is assumed to generate no lift.
- The starting velocity is assumed to be equal to the velocity of the vehicle during the deployment phase ($55\,\mathrm{km/h}$), and the initial path angle is assumed to be zero.

These assumptions simplify the simulation such that the trajectory can be estimated. It also takes into account the worst-case scenario for wind force, which is that the wind force continuously acts on the largest area parallel to the ground, causing the largest possible deviation from the trajectory.

13.1.2. Results

Plotting the trajectories with the maximum wind speed in both directions creates a plot as follows:

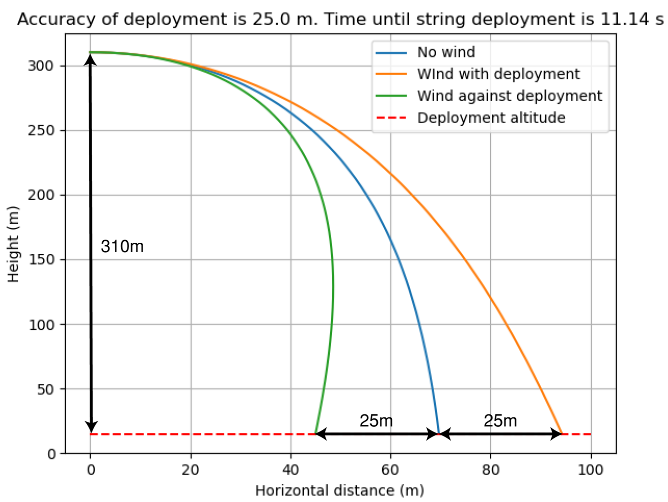

Figure 13.2: *Predicted trajectories of sensor node with maximum expected wind speed in different directions.*

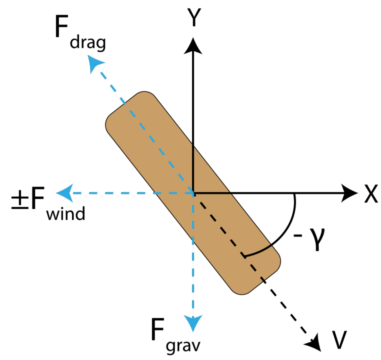

Figure 13.3: *Free body diagram of sensor node in freefall.*

This plot gives an upper bound of the deployment altitude of $310\,\mathrm{m}$. Above this altitude, the deployment accuracy becomes lower than required. From this, the target deployment altitude is selected to be $300\,\mathrm{m}$. The time until string deployment (or the time until an altitude of $15\,\mathrm{m}$) is taken to be the average of the three trajectories. For the deployment path, an altitude of $300\,\mathrm{m}$ will be selected.

13.2. Sensor Placement Strategy

The placement of the sensors is a complex yet important part of the system deployment. The complexity of the sensor placement is mostly due to the reliability requirement (REQ-SENS-1) and its children requirements (REQ-SENS-2 and REQ-SENS-4). In this section, the sensor placement strategy is simulated, verified, and validated using a fire spreading model and reliability simulation.

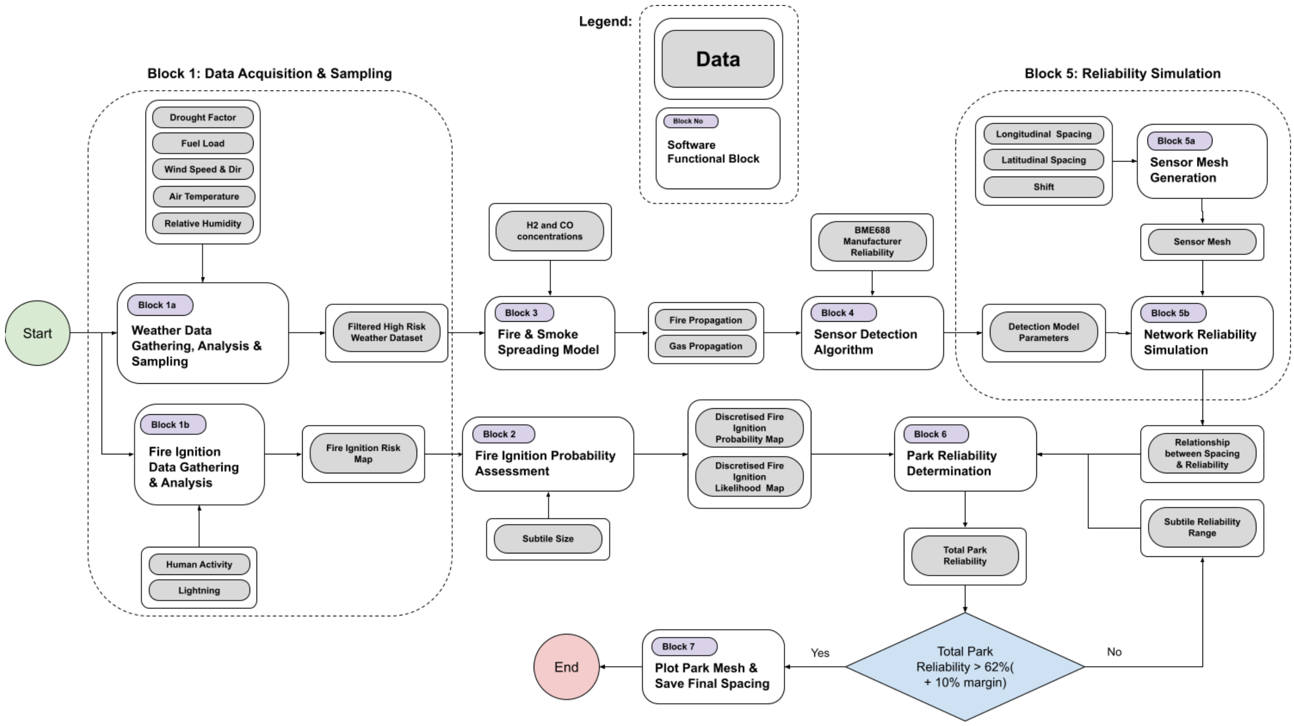

Figure 13.4: *Sensor placement algorithm block diagram.*

13.2.1. Assumptions

A set of assumptions had to be made in order to be able to create such software in a small amount of time. Those are displayed below:

- The Drought Factor used for the fire spreading model is always assumed to be 10 [119]. This assumption was necessary to remove multiple unknowns and variables. It is assumed to be reasonable as this is the worst-case scenario (in other words, the forest is the driest it's ever been).
- The forest type was assumed to be a eucalyptus forest. This is in line with the vegetation analysis performed in Chapter 2 and thus has a negligible impact on the result accuracy.
- It was also assumed that the fire would spread linearly. This, again, is the worst-case assumption as in real life, fire spreads quicker as it grows, leading to exponential growth. For the sake of simplicity, this assumption was needed.
- Weather parameters such as temperature, wind speed, and relative humidity were assumed to have a normal distribution through the law of large numbers. This was a necessary assumption for sampling and was deemed to have a negligible impact on the outcome given samples were subsequently filtered.
- It was assumed that the wind speed below the canopy represents $50\,\%$ of the measured wind speed (above the canopy). According to research, [120], wind speed below the canopy varies between $50\,\%$ and $60\,\%$ of the above-canopy wind speed. Hence, the lower estimate was used to make sure the program doesn't overestimate the propagation.
- It was assumed that the smoke would only propagate in the direction of the wind. This is of course not true in reality, especially below the canopy as the wind can be more whirling there. However, implementing a whirling wind inside the simulation is simply not feasible, and having it propagate in all directions would essentially multiply the computations by 4, leading to a computational time of more than $40\,\mathrm{h}$ for the entire simulation. However, this assumption was deemed acceptable as its effect combined with the lowest wind speed reduction estimate would attenuate its effects greatly.
- A $10\,\%$ margin will be applied to all results that come out of this program. The reason for that is because of the nature of the model and the assumptions made above. Those mean the software cannot be fully trusted regarding the results and thus a safety margin should be applied.

13.2.2. Data Acquisition & Sampling

This section focuses on the data acquisition and sampling needed for analysis. It is separated into two types: weather data and fire ignition data.

Weather Data Gathering

In order to model the spread of fire and smoke within a forest, weather data and forest characteristics must be gathered. The forest characteristics are environmental factors that affect the spread of wildfires such as the drought factor and fuel load of the forest. The drought factor takes values between 0 and 10 and assesses the moisture content of the soil and vegetation. The fuel load assesses the amount of energy that can be supplied by the forest to the wildfire. The fuel load is mainly dependent on the type of vegetation within the forest. Furthermore, weather data is analysed and sampled for weather conditions that have a high risk of starting a wildfire. It is assumed that for high-risk wildfire conditions the drought factor is always maximal, and equal to 10. Furthermore, the fuel load for an Australian eucalyptus forest in NSW heavily depends on the time since the last wildfire occurred. Values range from $7\ \mathrm{t/ha}$ for a year since the last wildfire to $23\ \mathrm{t/ha}$ for >20 years since last fire. A mid-range value was selected: $17\ \mathrm{t/ha}$ which assumes every 6 years a large wildfire burns the eucalyptus forests [121]. According to the Australian Bureau of Meteorology: "The worst conditions occur when deep low-pressure systems near Tasmania bring strong, hot and dry, westerly winds to the coastal districts" [122]. Thus, for a high risk of wildfires, the weather conditions and statistical filter criteria are given in Table 13.3. The statistical criteria are based on a $10\ \%$ confidence interval, meaning "high" and "low" are the $10\ \%$ highest and lowest values from a dataset.

Historical weather data from the Nullo Mountain weather station is gathered from the Australian Bureau of Meteorology [117]. The weather station is located in Wollemi National park at an altitude of $1130\ \mathrm{m}$. This dataset contains the daily temperature, relative humidity, wind speed, and wind direction of the past 412 days (April 2021-May 2022) and can be seen in Figure 13.5. For the temperature, humidity, and wind speed, the distributions are assumed to be normal. Note that for the relative humidity, the 100% humidity values are not taken into account for the distribution since high humidity values do not have a high risk for wildfires as previously stated. Furthermore, for correlation testing purposes, the wind direction is converted from cardinal direction to a binary variable of land- and sea wind which takes values 1 and 0 respectively. The land wind takes cardinal directions: (SW, WSW, W, NWW, NW) and the sea winds take directions: (SE, ESE, E, NEE, NE), the other wind directions are dropped from the dataset. Correlation between the variables is negligible (<0.30 absolute) for all variables except wind direction and humidity. Between wind direction and humidity, the correlation was found to be -0.44 meaning land winds are weakly correlated with lower humidity values. From the distributions given in Figure 13.5, 70,000 samples are independently drawn and filtered for the conditions given in Table 13.3. The filtered high wildfire risk weather conditions are $4.9\ \%$ of all samples, meaning roughly 14 days a year, fire is likely to happen. These filtered weather conditions can be seen in Figure 13.6 and will be the input of the fire spreading model which will be discussed in Subsection 13.2.4.

Table 13.2: *Data sampling parameters.*

Parameter	Average	Standard Deviation
Temperature [C]	15.71	5.22
Wind Speed [km/h]	11.75	5.17
Relative Humidity [%]	71.45	5.17

Table 13.3: *High risk wildfire weather conditions.*

Weather Conditions	Filter criteria
High wind speed	Z score > 1.65
High air temperature	Z score > 1.65
Low humidity	Z score < -1.65
Western (land) winds	225 < dir < 315

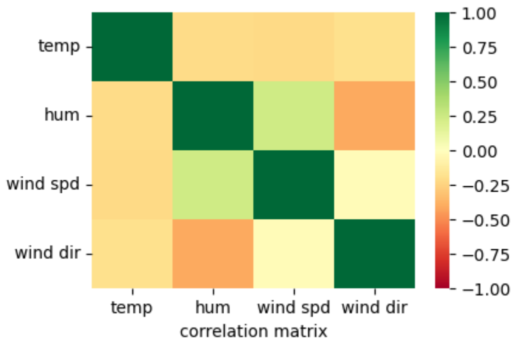

Figure 13.5: *Year round weather conditions in Nullo Mountain (Wollemi National Park).*

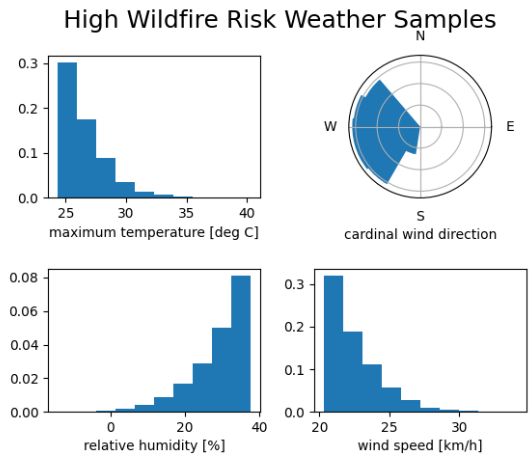

Figure 13.6: *High wildfire risk weather samples (Wollemi National Park).*

Fire Ignition Data

In order to model the fire ignition risk within a forest, ignition data must be gathered and analysed to see what and where the fire ignition sources are.

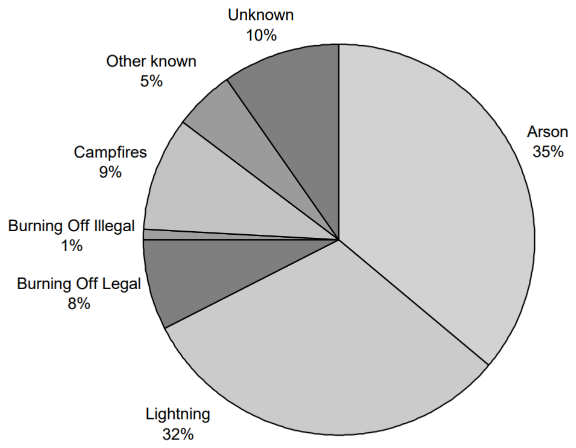

(a) *Blue Mountains national park bush fire ignition sources 1957-2003. [123]*

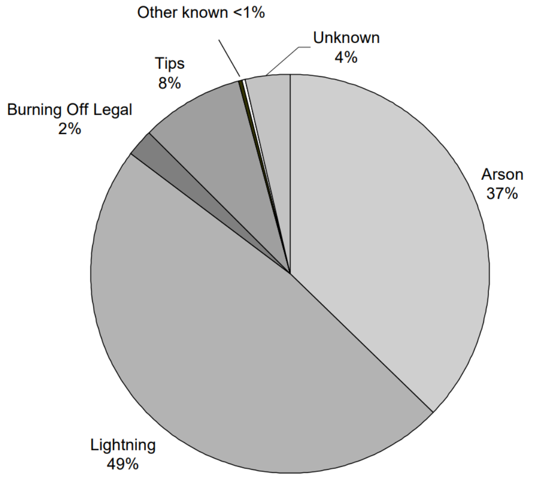

(b) *Blue Mountains national park bush fire ignition sources by area burnt 1957-2003. [123]*

Figure 13.7: *Statistics on the causes of wildfires.*

As can be seen in Figure 13.7a: 35 % suspected arson, 9 % campfires and 1 % illegal burning are all human-caused wildfire ignition sources. Legal burning bushfire ignitions are not in the scope of EcoSense since the local authorities are already aware of the fire and thus can the fires be mitigated much easier. Thus, humans cause at least 45 % of the fires that burn at least 37 % of the total area burnt by wildfires as can be seen in Figure 13.7b. On the other hand, ignition by lightning occurs 32 % of the time, but burns 49 % of the total area burnt by wildfires. As can be seen in Figure 13.8a, suspected arson is mostly located where human activity is present such as near roads or trails. Furthermore, lightning can be assumed to be roughly uniformly spread around Wollemi Park. Knowing this, the same method can be applied to the other parks within the observed area: (Blue Mountains, Wollemi, and Yengo National Parks) and the ignition probability map can be created for the total observed area. In order to do this, human activity such as trails, campsites, and small settlements data are imported from Google Maps as can be seen in Figure 13.8b.

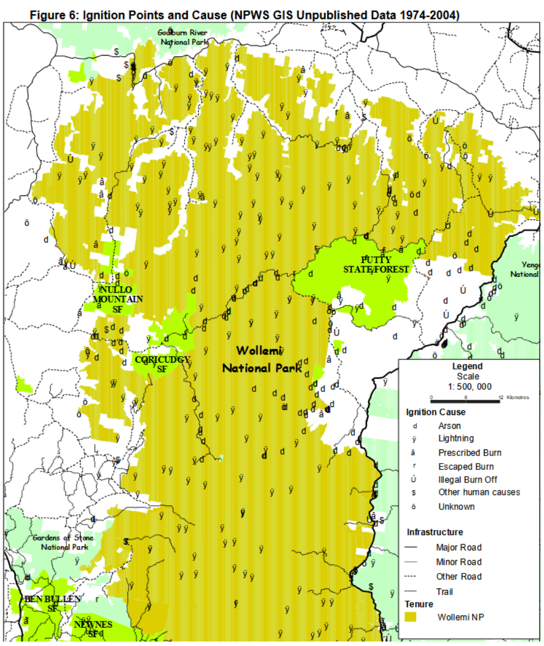

(a) *Fire ignition sources in Wollemi National Park. [124]*

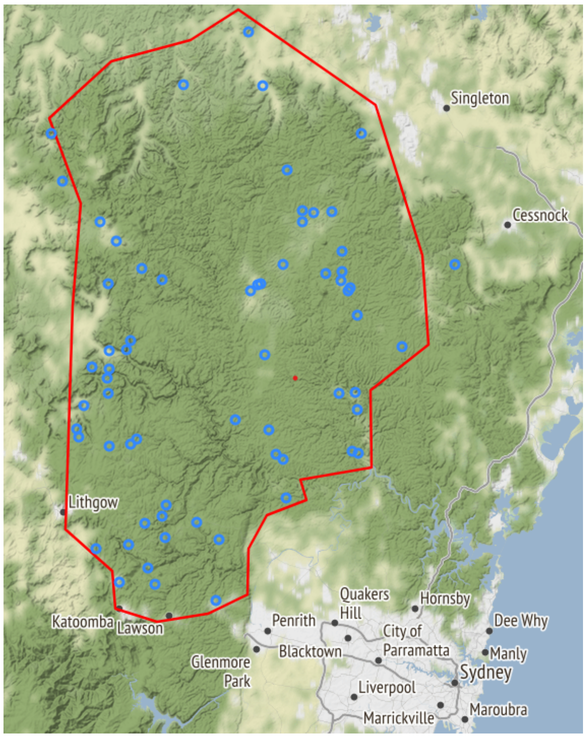

(b) *Human activity (blue dots) within observed area perimeter.*

13.2.3. Fire Ignition Probability Assessment

Using the human activity data from Figure 13.8b, a probability density function/heatmap of the observed area can be constructed as can be seen in Figure 13.10. To make this probability density function as continuous as possible, the observed area must be divided into subtiles. Because the observed area is not a perfect square, some subtiles are located outside the perimeter. In Figure 13.9 the number of subtiles within the park perimeter is plotted against the subtile spacing or width. It was chosen to go for a spacing of $1.5\,\mathrm{km}$ since the computation time effects were minimal while gaining the most continuous probability density function. The probability that a fire will ignite in subtile (i, j) is either random or human-related. From the data ignition data of Figure 13.7a, it is determined that the sum of the random probabilities in the subtiles must equal $47\,\%$ (lightning, other known and unknown). Then the random probability per subtile is simply equal to $\frac{P_{random}}{N}$, with N the number of subtiles within the park from Figure 13.9. The total human ignited fire probability must equal $53\,\%$ from Figure 13.7a, which is equal to $(1-P_{random})$. Furthermore, the human-related fire probability per subtile is estimated using a normalised Gaussian Kernel Density Estimation (KDE). Without going into much detail, this normalised KDE function is a 2D probability density function that is constructed from the human activity data points from Figure 13.8b and assessed at all the subtiles within the park perimeter. The normalised KDE function is written as $\hat{f}(i,j)$ and is dependent on the subtile location (i,j).

$$P_{fire}(i,j) = \frac{P_{random}}{N} + (1-P_{random})\hat{f}(i,j) \tag{13.1}$$

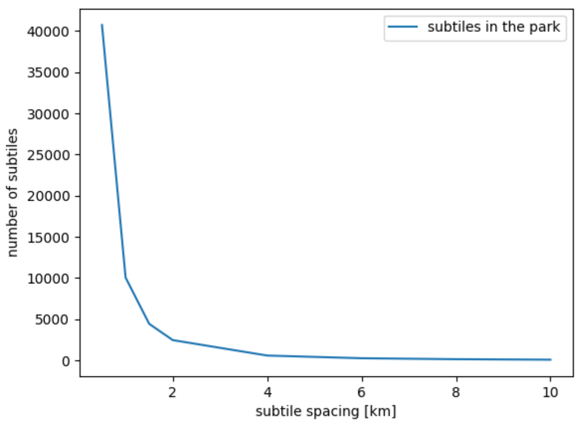

Figure 13.9: *Subtile spacing.*

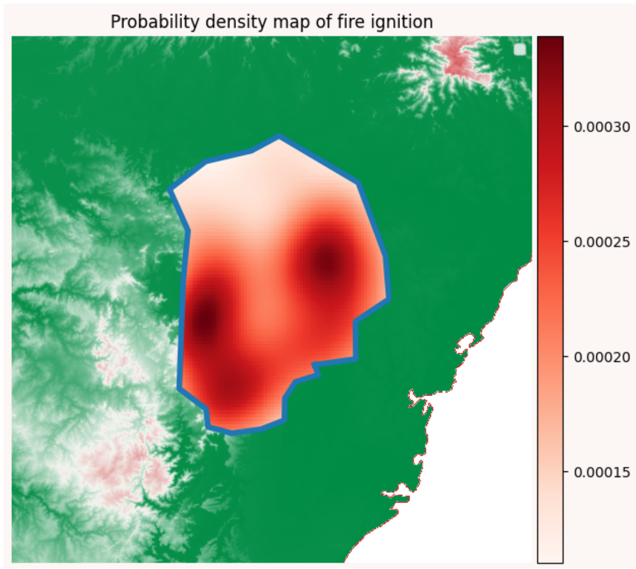

Figure 13.10: *Fire probability map.*

13.2.4. Fire & Smoke Spreading Models

Modelling of wildfire spread is not quite straightforward and is mostly done by empirical relationships. The Australian government in collaboration with the University of Alberta (Canada) has published a paper on the rate of fire spread for different types of Australian vegetation [125]. The block diagram of the fire spread model is given in Figure 13.11 with the corresponding inputs given in Subsection 13.2.2. Furthermore, it is assumed that the soil and vegetation are in the driest conditions which correspond to a drought factor D of 10.

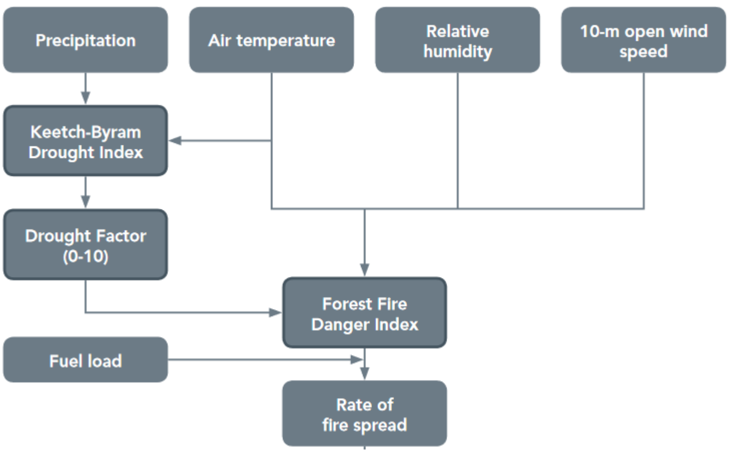

Figure 13.11: *Fire model block diagram. [119]*

For dry eucalyptus forests the Forest Fire Danger Index (FFDI) is given by Equation 13.2 with drought factor D, Moisture content MC and open wind speed $U_{10}[km/h]$.

$$FFDI = 34.81 \cdot e^{0.987 \cdot \ln(D)} \cdot MC^{-2.1} \cdot e^{0.0234 \cdot U_{10}} \tag{13.2}$$

The moisture content is given by equation Equation 13.3 with the relative humidity $RH[\%]$ and air temperature $T[C]$.

$$MC = 5.658 + 0.04651 \cdot RH + 0.0003151 \cdot RH^3 \cdot T^{-1} - 0.184 \cdot T^{0.77} \tag{13.3}$$

Then, the ground rate of spread of the fire $R[km/h]$ is given by Equation 13.4 with the fuel load of the forest $w[t/ha]$.The rate of fire spread was determined for the dataset of high wildfire risk weather conditions and fuel load from Subsection 13.2.2. The results can be seen in Figure 13.12.

$$R = 0.0012 \cdot FFDI \cdot w \tag{13.4}$$

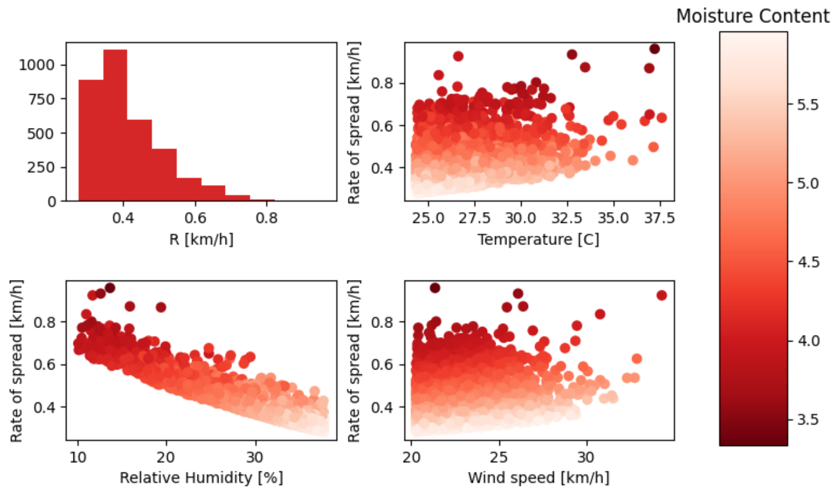

Figure 13.12: *Rate of spread from high wildfire risk dataset.*

Given a fire starts at a certain point at time 0, the burning area will spread in an elliptical shape in the direction of the wind. It is assumed that the centre of the ellipse moves with the constant rate of spread in the direction of the wind. The length to width ratio L_B of the ellipse is dependent on the wind speed $U[m/s]$ and is given by Equation 13.5 [126]. From the centre of the ellipse, the smoke propagation is modelled to travel with the wind in a cone shape. The smoke cone has the same length-to-width ratio as the ellipse, which gets more slender as the wind speed increases. The width of the smoke cone is described by Equation 13.6. To model the concentration of gasses within the smoke cone, the concentration curves are fitted to present a function of time called $c(t)$. The concentration dissipation through space and time is modelled as follows: each time iteration, at the centre of the fire (x0, y0) an initial smoke concentration $c0$ is emitted by the fire [127]. This initial smoke concentration is distributed over space with a normal distribution where the standard deviation is equal to a quarter width of the smoke cone which varies over space. Meaning 95 % of the fire concentration is located within the smoke cone which gets more flattened out over space as can be seen in Figure 13.13.

$$L_B = 1.0 + 10.0[1 - e^{-0.06 \cdot U}] \tag{13.5}$$

$$w(t) = \frac{U \cdot t}{L_B} \tag{13.6}$$

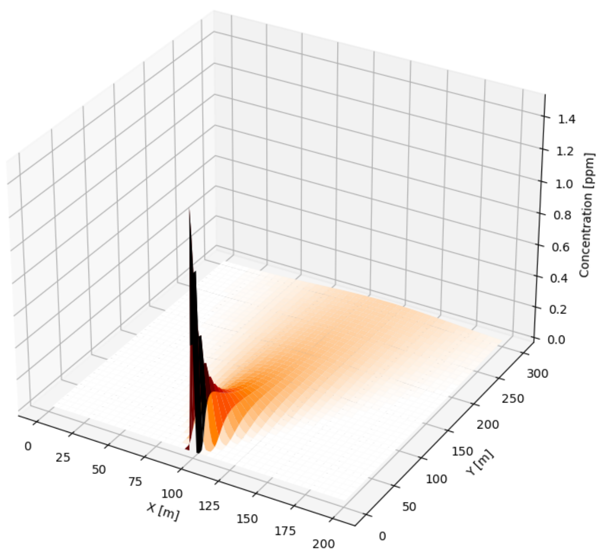

Figure 13.13: *3D dissipation of smoke.*

13.2.5. Sensor Gas Detection Algorithm

This block is the core of the simulation program. It effectively takes care of the simulation part and is iterated multiple times to obtain viable results. This block is split into multiple parts, each of which is explained below. Figure 13.14 shows the three steps of this block.

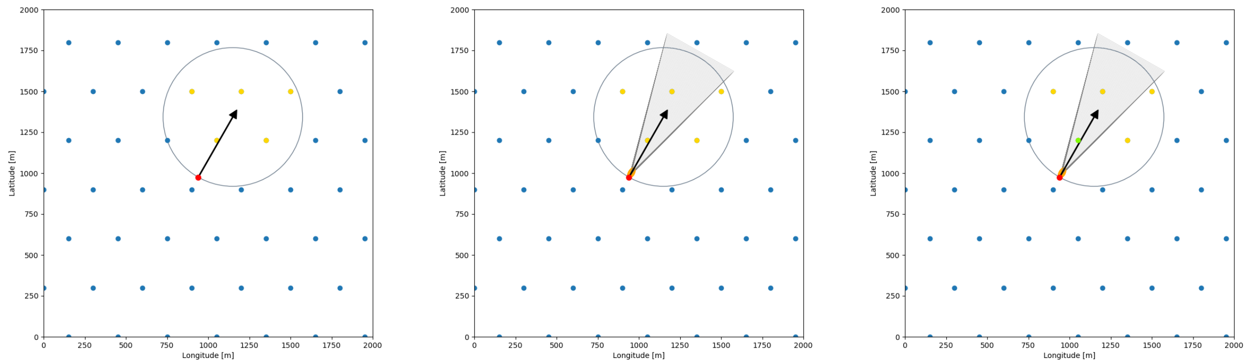

(a) *Fire location & relevant nodes.* **(b)** *Application of fire & smoke propagation models.* **(c)** *Node fire detection.*

Figure 13.14: *Example of a sensor gas detection (wind direction:* $60\,^{\circ}$*, wind speed:* $5.09\,\mathrm{km/h}$*, temperature:* $31.88\,^{\circ}\mathrm{C}$*).*

Fire Location Randomisation & Relevant Nodes Selection

The very first step, given a mesh of nodes (for which the determination method will be explained later), is to determine a random position for the fire, shown as a red dot in Figure 13.14a. This is very simply done using a randomiser function, with proper constraints to make sure the fire's initial ignition point is within the given mesh.

Then, the nodes close to the fire ignition point (within the grey circle) are selected and their coordinates saved. these are shown in gold in Figure 13.14a. These are the sensors for which the gas concentration will be determined. The reason an initial node selection is done is to avoid having to calculate the gas concentration at every sensor location as it would be unnecessarily time-intensive given most would be equal to $0\,\mathrm{ppm}$. The radius is determined based on wind speed and simulation time and points in the wind direction (depicted by a black arrow in Figure 13.14a

Application of Fire & Smoke Propagation Models

Once relevant points have been determined, one can apply the fire & smoke propagation model described in Subsection 13.2.4. This can be done by creating patches (simple mathematical shapes such as grey triangles for smoke and orange ellipses for fire) corresponding to the fire and smoke states at any point in time. Figure 13.14b shows the state of the fire & smoke after 10 minutes. One can note that both of these exactly propagate in the direction of the wind, which is to be expected given our initial assumption.

Gas Concentration at Node Locations

Finally, given the smoke & fire propagation across the relevant nodes, one can determine the gas concentrations as a function of time at those nodes. For that, the coordinates of all the relevant nodes were transformed into the coordinate system of Figure 13.13. From these new coordinates, the gas concentration sensed by every node can be determined.

In order to confirm whether a sensor has detected a fire, one needs to compare the calculated concentration to a threshold. For example, this was set at $50\,\mathrm{ppb}$ in the case of carbon monoxide. This is because the average troposphere CO concentration stagnates around $100\,\mathrm{ppb}$ and can go as low as $50\,\mathrm{ppb}$ in clean, or green, areas [128]. Hence, a $50\,\mathrm{ppb}$ CO concentration due to the fire emissions could represent between a $50\,\%$ and $100\,\%$ jump from average conditions. Such concentrations can be detected by the Bosch BME688 as its threshold is set at $1\,\mathrm{ppb}$ [103]. Implementing manufacturer reliability of $92\,\%$ [103], one can confirm whether a node has detected a fire or not. Furthermore, because this operation is done at every time-step within the $10\,\mathrm{min}$, the detection time can also be determined.

As soon as a fire has been detected, the simulation is stopped to enhance the speed of the program. Sensor node ID (and thus coordinates), as well as detection time, are saved for later analysis. In Figure 13.14c, the node that detected the fire is marked in light green. In that example, the fire was detected in $400\,\mathrm{s}$ which is below the requirement of $10\,\mathrm{min}$.

13.2.6. Reliability Simulation

The next step is to determine the reliability of a mesh when it comes to detecting fires. This takes the shape of an iteration loop, during which the network tries to detect fires in multiple typical wildfire day conditions.

Getting Reliability

In order to find the reliability of a given mesh, one should run the concentration detection algorithm presented in Subsection 13.2.5 multiple times, over a large sample set to determine the reliability of a given mesh (by counting the number of fires detected in less than $10\,\mathrm{min}$). Subsection 13.2.2 show the method behind determining that set. Trial and error were run in order to find the appropriate size of the dataset. It was found that anything under 150 samples per simulation would lead to too many inconsistencies and thus a final set of 200 samples was chosen to perform every simulation. An example of the results of such a sample loop is now presented. Figure 13.15a gives the detection time results of a $300\,\mathrm{m}$ mesh whereas Figure 13.15b shows the size of the fire when it was detected. For such a sensor mesh, $80\,\%$ was the achieved reliability.

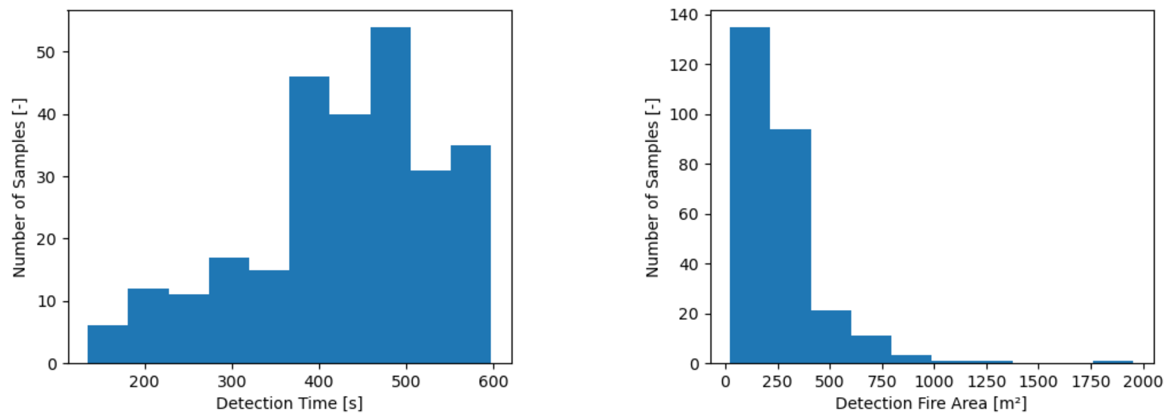

(a) *Detection time (from ignition) distribution of a $300\,\mathrm{m}$ sensor mesh.*

(b) *Fire area at detection distribution of a $300\,\mathrm{m}$ sensor mesh.*

Figure 13.15: *Fire area & detection time distributions of a $300\,\mathrm{m}$ sensor mesh.*

Restricting the Iterables

Now that a link between longitudinal/latitudinal spacing, shift and reliability has been established as was explained above, one should now be interested in finding a mathematical relationship between all these parameters. However, due to the computational heaviness of a single simulation (that takes approximately $1.5\,\mathrm{s}$ to run) one should limit the number of variable parameters to iterate over. This is further aggravated by the nature of the reliability simulation that needs to repeat that operation a few hundred ”typical day with fire” samples per mesh to obtain reliable reliability results. Hence, the variety of meshes needs to be reduced.

In order to do that, a first iteration loop was performed by varying longitudinal/latitudinal spacing and shifting between 3 values each. Spacings could vary between $300\,\mathrm{m}$, $400\,\mathrm{m}$ and $500\,\mathrm{m}$ whereas shift was allowed to vary between $0\,\%$, $25\,\%$ and $50\,\%$. This led to the results shown in Figure 13.16, where the red line shows the $62\,\%$ requirement reliability. One should also note that this result was produced by running 27 iterations (all possible combinations) and then averaging all the reliabilities containing one of the parameters. For example, the $300\,\mathrm{m}$ longitudinal spacing reliability was obtained by averaging the result from all the iterations that had a longitudinal spacing of $300\,\mathrm{m}$, hence one-third of the dataset. All reliabilities hence average a third of the iterations (with the values contained in those thirds varying between parameters and values).

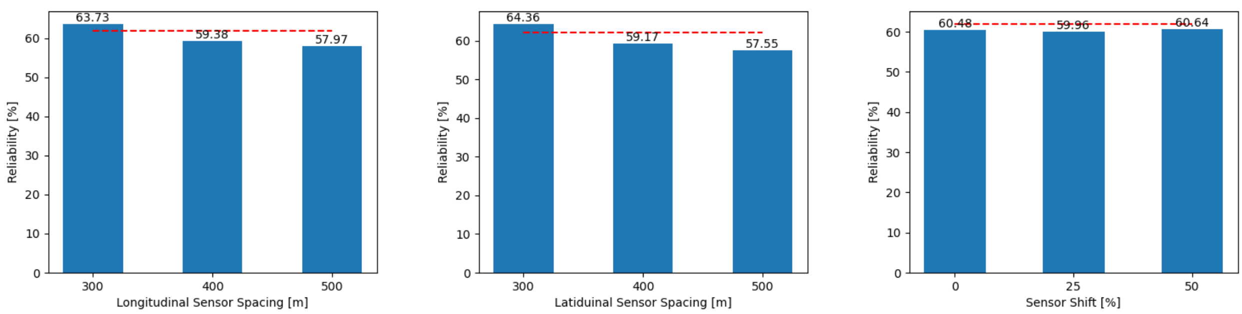

(a) *Reliability against longitudinal spacing.*

(b) *Reliability against latitudinal spacing.*

(c) *Reliability against mesh shift.*

Figure 13.16: *First iteration ran over 200 samples.*

The first obvious result from this first iteration loop is that sensor shift doesn’t matter at all in terms of reliability. As one can see from Figure 13.16c, the reliability stays relatively constant at around $60\,\%$ no matter the shift. This is a very useful result that can already discard sensor-shift from the list of iterables in the final loop. The shift was thus set at a constant 0 % for the remainder of the program for simplicity reasons.

Furthermore, looking at Figure 13.16a and Figure 13.16b, it seems that both longitudinal and latitudinal spacings behave in the same way. This is further confirmed by calculating the correlations between all these datasets. This resulted in the following table:

Table 13.4: *Reliability correlation between longitudinal and latitudinal spacings.*

300 [m]	400 [m]	500 [m]
0.9914	0.9629	0.9322

Such high correlations as seen in Table 13.4 help conclude that making an asymmetrical mesh doesn't affect the final reliability. For that reason, it was decided that the mesh would be simplified from 3 to a single input, namely the spacing (identical in both directions).

Finding the Relationship Between Spacing and Reliability

Now that the reliability simulation only takes a single input (spacing), a second iteration loop can be created in which the reliability is calculated for a given sensor node spacing. This was initially done between 300 m and 550 m over 51 points (to have 50 intervals of 5 m). Figure 13.17 shows the result of such an iteration loop. As shown in Figure 13.17, an R^2 squared value of 0.9814 is determined, showing that this relationship can indeed be used for the final optimisation algorithm.

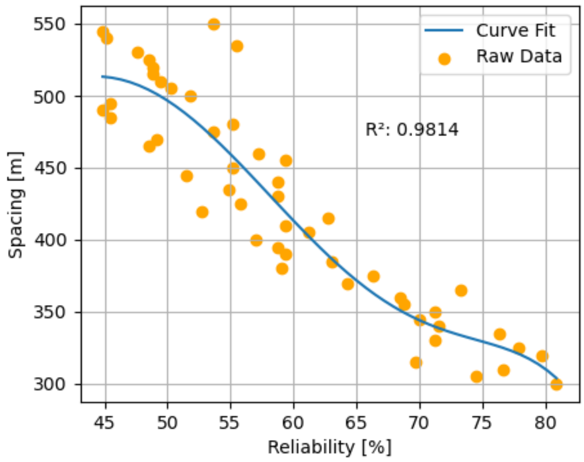

Figure 13.17: *Reliability against spacing relationship.*

13.2.7. Park Sensor Mesh Generation

The very last block of this software is to determine the required reliability in every subtile defined in Subsection 13.2.3. One should understand that the 62 % reliability requirement was set for the entire mission area. In this case, it applies to all three Australian national parks. This means that subtiles could have reliabilities higher or lower than 62 % as long as the reliability across the whole mission area is 62 %. One should also note that according to Subsection 13.2.1, a 10 % margin was set. Hence, one should use the program to get a reliability of at least 68.2 %.

In order to determine the overall sensor network reliability, one should make use of both the subtile reliability and the corresponding fire ignition probability as determined in Subsection 13.2.3. Given the very large amount of subtiles, this will take the form of a dot product between vectors containing the above-mentioned values (essentially getting the weighted average). This means that a subtile where fires are more likely to ignite should have a higher reliability than 68.2 % and inversely. That way, everything will average out to 68.2 %.

Thereafter, the user should select a required reliability range. For example, a range of [50 %-80 %] means that the subtiles with the highest fire ignition risk will require a reliability very close to 80 % and inversely. The way this is done is by using the likelihood index map determined in Subsection 13.2.3. Every subtile will be given a value between 0 and 1. This can then be mapped to a required reliability. Following the example range, a value of 0 would mean the subtile should have a reliability of 50 %. This then goes up linearly until it reaches 80 % for likelihoods of 1.

Using trial and error, one can find the required reliability range for the whole sensor network to have a reliability of 68.2 % (or any other for that matter). This results in an array of required reliabilities where every single value corresponds to a subtile. Hence, using the curve fit relationship developed in Figure 13.17, one can find the required spacing of every subtile that would fulfil the 68.2 % requirement. This essentially creates an optimised variable mesh instead of having to rely on a constant spacing mesh.

13.2.8. Final Results

The final block described in Subsection 13.2.7 was run and trial and error led to a required reliability range of [$53.5\,\%$-$74.5\,\%$]. This led to a final sensor network reliability of $68.44\,\%$, thus passing the product requirement and the $10\,\%$ margin. For such a network, a plot can be made showing how the variable mesh is applied. An example of this, over a $6\,\mathrm{km}$ by $6\,\mathrm{km}$ area, is shown in Figure 13.18b (one can see that some advanced tool will need to be developed in the future to remove clusters and correctly populate the borders of the mesh). On the other hand Figure 13.18a shows the distribution of sensor spacing throughout the subtiles.

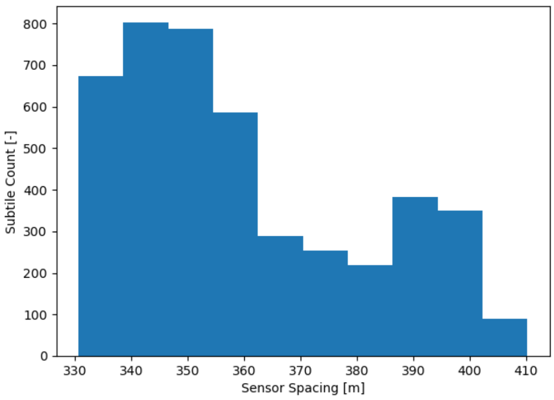

(a) *Mission area sensor spacing distribution.*

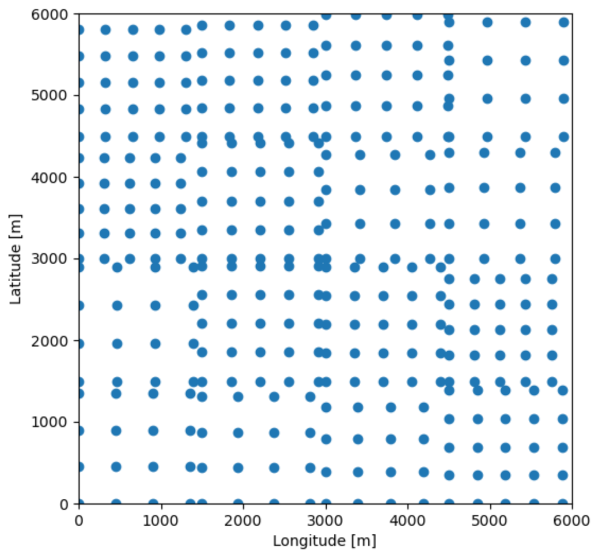

(b) *Part of mission area variable mesh.*

Figure 13.18: *Final results plots.*

Using the variable mesh determined from this program, the total number of sensors for all three national parks amounts to 100517. Using a simple calculation, one can find that using a constant $351\,\mathrm{m}$ spacing (corresponding to the same $68.44\,\%$ reliability within $10\,\mathrm{min}$), one should deploy 110750 sensors. This shows that the variable mesh proposed by the developed program is a considerable improvement as the number of the required sensor is reduced by $9.24\,\%$. One should also note that the curve fitting model outputs ranges from $305\,\mathrm{m}$ to $500\,\mathrm{m}$, hence in the worst-case scenario (most risky), a $10\,\mathrm{km}$ by $10\,\mathrm{km}$ tile would contain 1089 sensor nodes at the maximum.

One can also see from Figure 13.18b that some clusters appear due to the variable spacing mesh. This is something that will need to be tackled in the future as an AI tool recognising and removing them needs to be developed. In the interest of time, this could not be done within 10 weeks and any further research will have to include this aspect. The borders could also raise some eyebrows. This is again something that will need to be developed in the future. One should make sure to add an array of sensors where it is deemed necessary (for example for the subtile located at approximately $5000\,\mathrm{m}$ longitude and $2000\,\mathrm{m}$ latitude).

Finally, REQ-SENS-2 requires the sensors to detect $90\,\%$ of fires that are at most $0.2\,\mathrm{km}^2$, corresponding to a fire of diameter of $505\,\mathrm{m}$. Given the maximum mesh size of $500\,\mathrm{m}$, this would mean that those fires would already be covering at least a sensor, such that the fire could be detected using the temperature sensors. Of course, a better spatial simulation of fire geometries could be proven useful for this requirement and should be developed before releasing the product. However, in the current state of development, the requirement will be assumed to be verified.

13.3. Risk Analysis

Risks can be identified in the deployment procedure and simulations, which are summarised along with their mitigation strategies in the table below. Any risks that are specific to the sensor node, such as the string deployment mechanism, are listed in Table 12.6.

Table 13.5: *Risk assessment of sensor deployment.*

Index	Risk Factor	HS	HP	HRI	Mitigation strategy	HS	HP	HRI
1	Deployment accuracy requirement not being met	6	6	36	Maximum wind speed is set to 15 km/h for operation Maximum deployment altitude set at 310 m	6	2	12
2	Errors in simulation not reflecting real-life performance	6	6	36	V&V performed on all code Margins introduced to estimates Future testing may be implemented to compare simulation to reality	6	4	24

13.4. Verification & Validation

This section deals with the verification & validation of the models described in both Section 13.1 and Section 13.2.

13.4.1. Free Fall Analysis V&V

The simulation used in the free fall analysis was developed by the team, and as such must be verified and validated.

Verification

The simulation class contains 4 functions that modify the class states on each time step. These functions are called *calculate_forces()*, *calculate_acceleration()*, *update_velocities()* and *update_location()*. Each of these functions was unit tested to 7 significant digits.

The coordinate system used in Figure 13.3 was used to ensure that the signs of each force were applied correctly. This is most important with the definition of the path angle as if this is not defined as negative, the simulation does not behave correctly due to the orientation of the coordinate system.

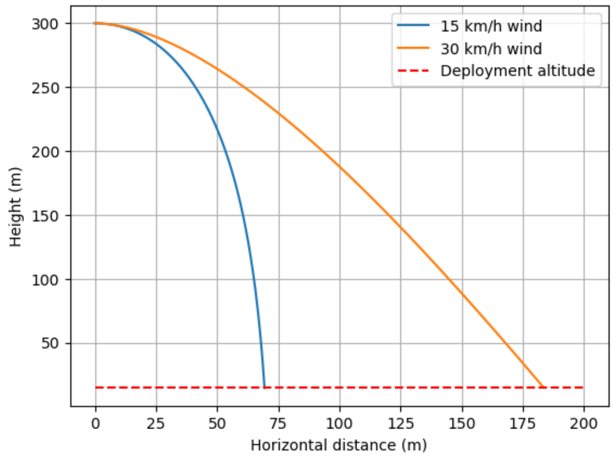

Figure 13.19: *Free fall trajectory with increasing wind speeds in direction of deployment.*

Validation

The simulation was validated by changing the forces acting upon the node during free-fall and seeing whether the trajectory is changed accordingly. For example, increasing the wind speed in the direction of deployment should create a trajectory that travels a longer horizontal distance. This is confirmed by increasing the wind speed as shown in Figure 13.19.

This behaviour is expected and as such validated for the effect of wind on the sensor trajectory. This procedure was repeated for the effect of the gravitational force and drag force that the node experiences, which also behaved as expected.

13.4.2. Sensor Placement Software V&V

The sensor placement software has been entirely developed by the DSE team and thus had to be thoroughly verified and validated to prove its reliability and usefulness in the context of the project at hand.

Verification

Unit tests were the first verification method used. Most mathematical and data handling portions of the program rely on semi-empiric equations and translating/transforming data from one place to another. These are the types of portions that are very easily verifiable by running a unit test and verifying whether the output matches the hand-calculated result. This was done for implementations of the ”Moisture Contents”, ”Forest Fire Danger Index” and ”Rate of Spread”, all of which passed the tests successfully with a minimum accuracy of 7 decimals. Some basic methods such as the calculation of ”Ellipse Geometric Parameters” or the good implementation of a curve fitting model for the gas concentrations were also unit tested by using comparisons to hand calculated results. Although the curve fitting model passed the tests with an accuracy of at least 7 decimals, the ”Ellipse Parameters” method only achieved an accuracy of 2 decimals. This was considered acceptable given the amount of rounding performed in intermediary calculations. The ”Cone Geometric Parameters” function was not verified as it largely shares the same code as the ”Ellipse Geometric Parameters” method. Furthermore, when constructing probability density functions it should be verified that the total sum of the distribution is equal to one.

Given the nature of this program, most of the functions and calculations can be verified visually, using figures or by printing out data frames as was done throughout the sections above. This is the case when calculating the triangle points in the smoke propagation model. This can easily be plotted and thus verified by comparing the visual coordinates to the actual ones (by looking that up while debugging the code). The exact same method is applied for the mesh creation, the fire ignition location randomiser as well as the selection of relevant points. All the above-mentioned functions were successfully verified using visualisation.

The final part of verification are system and subsystem tests. Given the program is a simulation model, with a for loop containing almost all functions in it, the only subsystem that was tested numerically was the "Get Concentration" method (containing curve fitting, transformation, and geometric parameters methods). The rest can be verified when running system tests. The "Get Concentration" function was verified by comparison between the output and a hand-calculated expected value. This test was successfully passed with an accuracy of at least 7 decimals. The final system test was conducted visually. This is because the simulation model lends itself perfectly to this type of verification. By running the program multiple times and by printing both results and visuals of the simulation throughout the iterations, one could check that the whole program was indeed working as expected.

It is estimated that the large majority of the code has been verified this way as the only omissions that were made are the redundant methods and extreme values testing. The latter was ignored as the input data was filtered for the sole purpose of removing such values. Hence, the program is not built to work with extreme temperature or concentration measures. This is a known feature/flaw of the program but was necessary given the time required to build such a program. Finally, a full system test could be performed by running the simulation multiple times, printing corresponding wind speeds, directions, temperatures, and rates of spread, or by plotting the relevant points and detection points in different colours, or by creating gas emission animations.

Validation

In order to check if the sensor placement is valid for the intended use, one should check whether the mathematical model that has been used is indeed usable for such simulations. The mathematical model that was used [119] was derived from Australian Eucalypt forests, exactly corresponding to that of the three NSW national parks in which the mission is expected to be launched. This effectively validates the entire program for this specific type of forest. However, this also means that, even though this program is usable for other missions, the fire spreading model should be modified and adapted to the case at hand. A look at research and wild measurements [129] [130] help validate the calculated fire rates of spread, which lie within the measured ranges, used as intermediates to the final simulations.

14

Network & Relay Nodes

In order for the customer to receive crucial information regarding the forest and potential wildfires, a capable and efficient network is to be designed. This network comprises the sensor nodes themselves, relay nodes and a ground station. For the sensor and relay nodes to be able to communicate together, a communication link budget needs to be developed, this is done in Section 14.1. Then, one should construct a suitable and redundant network infrastructure as is done in Section 14.2. To connect the sensor nodes to the end user, some relay nodes are designed preliminarily in Section 14.3. Finally, the important aspects of risk, sustainability and verification & validation are performed in Section 14.4, Section 14.5 and Section 14.6 respectively.

Table 14.1: *Network & relay nodes Requirements.*

Req. ID	Requirement	Section	Compl.
REQ-SENS-COM-1	The sensor network shall be capable of communicating with the ground station	14.2	✓
REQ-SENS-COM-2	The sensor network shall transmit scientific data (temperature, humidity, concentration)	14.2	✓
REQ-SENS-COM-3	The sensor network shall be able to receive telecommands	14.1	✓
REQ-SENS-COM-4	The sensor node shall communicate to corresponding its corresponding relay	14.2	✓
REQ-SENS-COM-5	The sensor network shall have an uptime of 99.999 % throughout its mission.	20.2	✓
REQ-SENS-COM-6	The sensor network shall operate on the LoRa protocol	14.1	✓
REQ-SENS-COM-9	The communications software shall allow for operation without all deployed nodes	14.2	✓
REQ-SENS-COM-10	The communications software shall be capable of detecting damaged nodes	14.2	✓

14.1. Communications Link Budget

For applications such as sensor networks, or more generally the Internet of Things (IoT), LoRaWAN, more commonly known as LoRa, is a suitable protocol. It is extremely low powered and supports ranges of up to $800\,\mathrm{km}$, thanks to a modular spreading factor technology. LoRa uses specific frequency ranges and the link budget has to incorporate this (this ranges from $137\,\mathrm{MHz}$ to $1020\,\mathrm{MHz}$ worldwide). For long range applications, a spreading factor of 12 should be used. The communications link can now be sized and budgeted for the current sensor network design.

In order to determine the link budget margin (LM) for both sensor-relay and relay-relay transmission, one can make use of the general formula shown in Equation 14.1:

$$LM = P_{TX} + G_{TX} - L_{TX} - L_{\text{path}} + G_{RX} - L_{RX} - S \tag{14.1}$$

- P_{TX}: Transmitter power output: $20\,\mathrm{dBm}$ from Chapter 12
- G_{TX} & G_{RX}: Transmitter & Receiver antenna gain: $3\,\mathrm{dBi}$ from Chapter 12
- L_{TX} & L_{RX}: Transmitter & Receiver losses, assumed: $1\,\mathrm{dBm}$ due to short cables and plastic enclosure
- L_{path}: Path loss in forests
- S: Sensitivity of the Receiver

It was assumed that no atmospheric or rain losses are encountered for any of the links given the low frequencies [131]. One of two unknowns in Equation 14.1 is L_{path}, corresponding to the path loss. Given the sensor network (both relays and sensor nodes) are placed in the forest (and thus have trees surrounding them). Hence, an appropriate path loss estimation method needs to be used. For that, Equation 14.2 [132] will be used.

$$L_{\text{path}} = 0.48 f^{0.43} d^{0.13} + 40\log_{10}(d) - 20\log_{10}(h_T) - 20\log_{10}(h_R) \tag{14.2}$$

- f: Transmitting frequency (assumed at $1020\,\mathrm{MHz}$ for the worst case scenario)
- d: Distance between the receiver and the transmitter (covered by trees), will be optimised for each link.
- h_T & h_R: Transmitter & Receiver placement height. A higher placement means ground effects are impeding less on the communications link. Sensor nodes are assumed to be placed at a height of $1\,\mathrm{m}$ whereas relays are assumed to be placed at $30\,\mathrm{m}$ height.

That estimation method was empirically determined from rain forest experiments and measurements, which are renowned to be the worst possible forests for electromagnetic waves. Hence, it was concluded that Equation 14.2 models the worst case scenario.

A second unknown in Equation 14.1 is the sensitivity. This is a hardware based parameter that is mainly dependent on the bandwidth of the transmission. Equation 14.3 [133] shows the relation given in the handbook of the SX1278 LoRa module:

$$S = -174 + 10 \cdot \log_{10}(B) + NF + SNR_{\text{limit}} \tag{14.3}$$

- B: Bandwidth of the transmission in Hz
- NF: Noise Figure of the SX1278 transmitter: $6\,\mathrm{dB}$ [133]
- SNR_{limit}: Minimum Signal to Noise Ratio of the SX1278: $-20\,\mathrm{dB}$ [111]

Given all of this, one can determine the link margin using Equation 14.1. The maximum range can then be determined by using a very simple solver and setting the link margin equal to $3\,\mathrm{dB}$. The latter value being a common safety margin that allows the Signal power to be 2 times higher than the noise power.

Node-Relay Link Budget

The very first step in determining the communications link budget is to find how much data needs to be sent and at what rate. A typical packet structure is shown in Figure 14.1. The data that needs to be transferred is called ”payload” and is transmitted using a ”nominal bitrate”

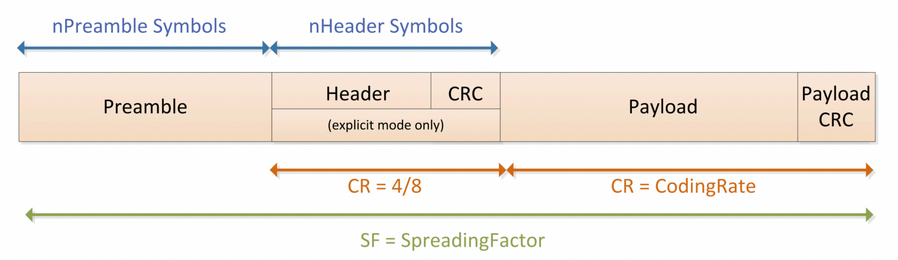

Figure 14.1: *A Typical LoRa Packet Structure [111]*

The bitrate will be sized based on the bi-daily status checks. This is because the only other use of the link is the case where a fire has been detected. However, because of the time of transmission and low amount of data that needs to be transmitted in the case of a fire (only Yes/No, gas concentrations and sensor node ID), the required bitrate will be significantly lower than the one for the status check. For the latter, every sensor node will be required to send the following:

- Node ID: integer
- $12\,\mathrm{h}$ hourly measurements history (temperature, humidity, CO and Gas concentrations): 2 decimal point floats
- Indicators (Fire Detected?, Node Disturbed): 0 or 1

The hourly measurements are used by the relay nodes to identify high-risk areas. The indicators indicate whether a fire is detected - if this is ’yes’ during a status check, the node is not working correctly as a fire alert should occur independently - and whether the accelerometer has picked up a large disturbance in the movement of the sensor. This movement may indicate an animal has moved the sensor, or it has fallen from the foliage. If this happens, the recorded position of the sensor is no longer valid.

By creating a dummy CSV file, one can estimate that such a payload will weigh $3200\,\mathrm{b}$. One should now look at the densest possible $10\,\mathrm{km}$ by $10\,\mathrm{km}$ grid which should contain 1089 sensors. This means that twice a day, $3.48\,\mathrm{Mb}$ need to be sent out by the sensors. Assuming a transmission time of $1\,\mathrm{min}$ from Chapter 12, one can determine that a nominal bitrate of $58.08\,\mathrm{kbps}$ is required. Assuming the standard spreading factor of 4/5, one can use the performance table of the SX1278 to determine the required bandwidth.

Bandwidth (kHz)	Spreading Factor	Coding rate	Nominal Rb (bps)
7.8	12	4/5	18
10.4	12	4/5	24
15.6	12	4/5	37
20.8	12	4/5	49
31.2	12	4/5	73
41.7	12	4/5	98
62.5	12	4/5	146
125	12	4/5	293
250	12	4/5	586
500	12	4/5	1172

Figure 14.2: *LoRa Required Bandwidth Given Bitrate [111]*

One can clearly see that the required bitrate is too high to fall in any of those categories. Furthermore, sending all the data at once could mean some could interfere with each other, leading to corrupt data, which is unwanted. Hence, what could be done is to send all the data over $12\,\mathrm{h}$. This means that the last transmitting node will be sending $12\,\mathrm{h}$ old data to the relay station. This is considered acceptable as this only means a constant shift will be introduced. Given a transmission time of $1\,\mathrm{min}$ during $12\,\mathrm{h}$, 720 sensors can be sending data to a single relay station. This means that transmission time can be decreased to $30\,\mathrm{sec}$ such that all sensor nodes can transmit their data to the relay node within an hour.

Thanks to this design, the bitrate can be decreased $106.67\,\mathrm{bps}$, which, according to Figure 14.2, means a bandwidth of $62.5\,\mathrm{kHz}$ is sufficient, from which a sensitivity of $-140.04\,\mathrm{dB}$ can be determined. Using a solver on the combination of Equation 14.1 and Equation 14.2, one can find that the maximum range for the Sensor Node - Relay Communications Link is $8.42\,\mathrm{km}$. It is assumed the enclosure does not hinder the performance of the antenna, as it is made out of a cellulose-based plastic [134]. The final communications link can be visualised in Figure 14.3b.

Relay-Relay Link Budget

Determining the communications link budget for the relay - relay transmissions largely follows the same steps as the sensor node - relay one. The same L_{forest} model will be used as even though the relays will be placed above the canopy, the large variations in canopy height mean that there could very much be trees between two relays. One now needs to determine the required bitrate of that transmission link.

The relay network will take the form of a distributed network. This is because the range of the relay nodes will not be enough to reach the ground station, that can be placed at a maximum of $100\,\mathrm{km}$. In the case of a decentralised network, the failure of that station would mean the failure of the entire product. Hence, having a distributed network results in multiple paths that connect back to the ground station.

As was done previously, the link will be sized for status checks as those send out significantly more data than the fire alerts (which only send out temperature, CO and Gas readings as well as the node ID of the sensor that detected the fire). The following status data has to be transferred between relays to the ground station twice a day for a duration of $5\,\mathrm{min}$ following the design in Section 14.3:

- Relay ID
- The 3 maximum temperatures over the last $12\,\mathrm{h}$ and the corresponding node IDs
- The 3 maximum CO and Gas concentration readings over the last $12\,\mathrm{h}$ and the corresponding node IDs
- The 3 minimum humidity readings over the last $12\,\mathrm{h}$ and the corresponding node IDs
- The nodes that have sensed a positional disturbance (the sequence of IDs of such nodes)

As was done previously, one can estimate the size of such data which is estimated to be $35.672\,\mathrm{kb}$. Through the distributed nature of the design, it is expected that 35 relays will be connected together at the same time (because of redundancies and assuming that all adjacent tiles communicate between each other, assuming two rows of communications). If the sensor nodes are transmitting each $30\,\mathrm{s}$ during the $12\,\mathrm{h}$, this leaves $175.5\,\mathrm{min}$ of transmission between relays. At 35 relays, this leaves $5\,\mathrm{min}$ of transmission per relay. Hence, the bitrate required for the Relay - Relay link is $118.9\,\mathrm{bps}$. From Figure 14.2, a bandwidth of $62.5\,\mathrm{kHz}$ is required, leading to a sensitivity of $-140.04\,\mathrm{dB}$ and a final maximum range of $23.84\,\mathrm{km}$. This can be visualised in Figure 14.3a.

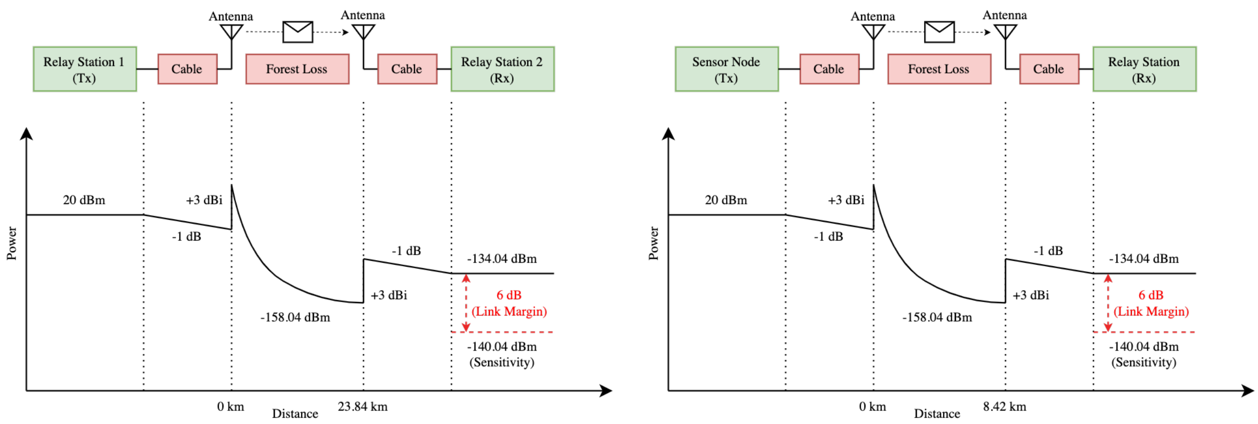

(a) *Relay - Relay communications link*

(b) *Sensor node - Relay communications link*

Figure 14.3: *Communications link budgets.*

14.2. Network Infrastructure

The sensor network consists of two types of nodes: relay nodes and sensor nodes. The sensor nodes and their design are previously described in Chapter 12, and monitor for fires. The relay nodes act as the communication link between these nodes and the ground station. The relays act as a distributed network, with the relay nodes being able to communicate to one another. This allows a series of relay nodes to carry signals from the sensor nodes to the ground station.

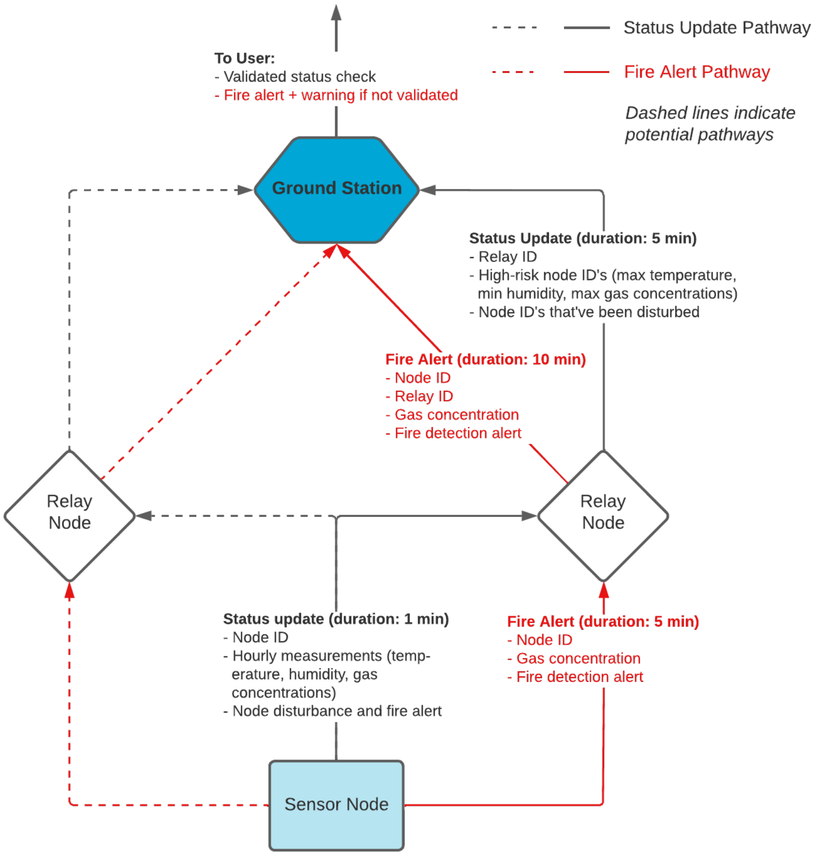

Figure 14.4: *Overview of network infrastructure and communication pathways in the sensor network.*

The network carries two types of transmissions, a regular status check to confirm the functioning of each sensor and relay, and a fire alert which triggers in case a fire is detected. The status check can also be used to identify areas of the park that are at risk of starting a fire, which can be indicated by high temperature or low humidity readings. An overview of the network infrastructure is given in Figure 14.4.

All previously sized link budgets in Section 14.1 are based on the communication pathways described in Figure 14.4. The system is designed for the worst-case scenario, which is a high-risk area of $10\,\mathrm{km}$ x $10\,\mathrm{km}$ located $100\,\mathrm{km}$ away from the ground station. As described in Section 13.2, for a high risk area the minimum spacing is $305\,\mathrm{m}$. This leads to an upper limit of 1089 sensor nodes per $100\,\mathrm{km}^2$ tile. Given the effective range of the sensor nodes being $8.42\,\mathrm{km}$, this means 2 relay nodes per tile are required to receive the transmission of all sensor nodes within the tile while still being redundant.

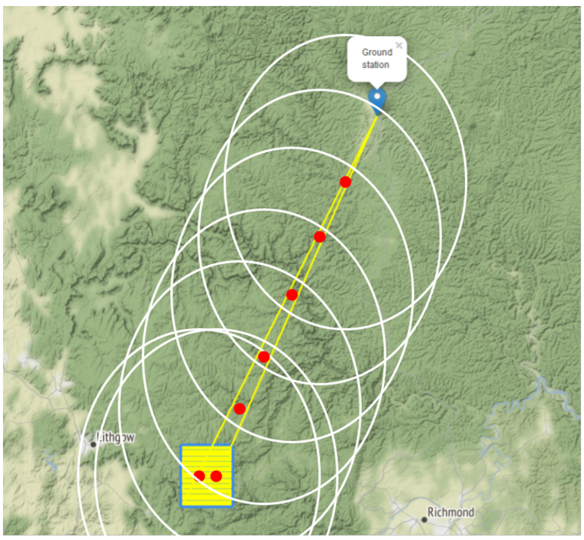

Figure 14.5: *Relays needed in the case of a $100\,\mathrm{km}^2$ tile located $100\,\mathrm{km}$ from the ground station.*

In the case that these relay nodes within the $100\,\mathrm{km}^2$ tile are out of the range of the ground station, a corridor of relay nodes must be created. Each of these relays has a range of $23.84\,\mathrm{km}$, which leads to a corridor of five relays being deployed to the ground station. Again, this corridor needs to be redundant. This can be seen in Figure 14.5.

Finally, one should note that this corridor is only needed if there are no other tiles between the detection area and ground station. In the case of a larger mission (with multiple tiles), the relays located inside the tiles will create a bridge to the ground station.

14.3. Relay Node Design

The design of the relay nodes is based upon that of the sensor node, but is mounted in the canopy. This increases the solar panel and communication system performance significantly, as shown in Section 14.1. The main differences between the relay and sensor node are summarised below:

- No Bosch BME688 sensor or accelerometer and a Raspberry Pi Pico is used as microcontroller.
- When idle the relay constantly receives transmissions as in case of a fire, the relay has to be ready to transmit.
- Larger battery ($3.7\,\mathrm{V}$, $750\,\mathrm{mAh}$) to account for constant receiving of transmissions, even during night.
- Solar panel area is identical to sensor node, as increased power consumption is compensated with increased solar irradiance in the canopy [135].
- Antenna and communications module is identical, as additional height in canopy increases the effective range of the relay.
- String diameter increased to $1.5\,\mathrm{mm}$ to compensate for additional mass of relay node.
- Four strings are deployed instead of two, creating additional attachment points in the canopy. Strings are still redundant, where one string is rated to withstand the impact of deployment with the same method as in Subsection 12.2.2.
- Enclosure doubled in height, dimensions being $65\,\mathrm{mm}$ x $85\,\mathrm{mm}$ x $35\,\mathrm{mm}$. Allows for additional string storage and a larger battery. The width and length remaining constant means the deployment system does not have to be adjusted. The mass of the enclosure is assumed to be twice that of the sensor enclosure.

The mass, power and cost estimations of the relay node with these changes is found below. The margin taken for the final estimation is 10% instead of 5%, as the design is less developed compared to that of the sensor node. If masses are not based on the sensor node, they are derived from commercially available parts such as the Raspberry Pi Pico. [136].

Table 14.2: *Mass estimation of relay node, with values based on commercial parts or sensor node prototype from Subsection 12.1.2. [137] [136]*

Component	Contribution (g)
Raspberry Pi Pico	5.00
SX1278 + Antenna	5.00
Battery	15.0
Solar Array	17.0
Spring	4.00
String Anchors	1.32
String	5.00
Steel Plate	2.70
Enclosure	87.0
Subtotal	142
Total (+10% margin)	156

Table 14.3: *Cost estimation of relay node, with values based on commercial parts or sensor node prototype from Subsection 12.1.2. [138] [137]*

Component	Contribution (€)
Raspberry Pi Pico	3.71
SX1278 + Antenna	8.00
Battery	4.19
Solar Array	17.0
Spring	2.00
String Anchors	1.35
String	4.00
Steel Plate	0.10
Enclosure	3.92
Subtotal	29.12
Total (+10% margin)	32.03

Table 14.4: *Power consumption of sensor node, with values based on commercial parts or the sensor design from Subsection 12.1.2. [136]*

Component	Contribution (mW)	
	Transmitting	*Receiving*
Raspberry Pi Pico	45.60	45.60
SX1278 + Antenna	396.0	39.60
Subtotal	411.6	85.20
Total (+10% margin)	485.8	93.72

Assuming ten minutes of transmission in case of a fire alert, and ten minutes of transmission dedicated to a bidaily status check, this gives an average power consumption of $0.20\,\mathrm{W}$. Given an solar irradiance of $472.2\,\mathrm{W/m^2}$ in the canopy, and an efficiency of 20% for poly-crystalline solar panels, this allows a solar panel of $3850\,\mathrm{mm^2}$ to produce $0.36\,\mathrm{W}$ [135] [139]. This is enough to charge both the battery for the night, as well as provide power during operation in the day. At night, an average of $\mathrm{mW}100.7$ is needed for operation. Given the night lasts at most 14 hours, this requires the battery to have a capacity of $1.41\,\mathrm{Wh}$. Given that the battery chosen has a capacity of $2.78\,\mathrm{Wh}$, this additional capacity is enough to compensate for degradation over time of the battery during its lifetime [107].

14.3.1. Relay Node Deployment Mechanism

The relay nodes will use the same deployment mechanism as the sensor nodes as was explained in Subsection 12.2.2. As explained in Section 14.3, 4 strings will be used to improve the positioning of the relays. The strings are sized such that a single one could still carry the relay completely. The strings of the relay deploy directly after deployment.

14.4. Risk Analysis

As was done for the sensor node design, a number of risks need to be assessed and mitigated. Given the large resemblance between the sensor node and relay designs, most of the risks are going to be common, and can be found in Section 12.4. Hence, only the specific network and communications risks will be detailed in Table 14.5.

Table 14.5: *Risk assessment of relay nodes.*

Index	Risk Factor	HS	HP	HRI	Mitigation strategy	HS	HP	HRI
1	Relay parts catch fire	10	4	40	Isolate the fire hazardous parts of the node	6	4	24
2	Relay sends false information (false positive)	6	6	36	Require a few minutes of data Isolate the obvious faulty nodes Make use of a distributed network Send a small intervention crew to check on the site	6	4	24
3	Relay lands face down	6	6	36	String attachment method ensures that the solar panel always faces upwards	6	4	24
4	Relay hits a living being on landing	6	6	36	Low mass of sensor node Relay attaches to branches, never reaches the ground Relay node made as small as possible	2	6	12
5	Water damage to electronics	6	6	36	Water resistant material used in enclosure Enclose is sealed from the environment	2	6	12
6	Weather untangles nodes	6	6	36	String attachment is made redundant, sensor can be supported by one string	6	4	24
7	String deployment failure	6	6	36	Two strings used, one can fail and system is still successful	2	6	12
8	Relay not able to decrypt data from the communication links	6	6	36	Include a $6\,\mathrm{dB}$ link margin to ensure it is easy to dissociate data from noise	6	2	12
9	Corrupt transmissions	6	6	36	Make use of a distributed network to cross validated and verify the data Send the data back to the ground station to run additional checks	6	2	12
10	Solar array cannot supply enough power	6	4	24	Solar panel subsystem provides enough power including safety margins Solar irradiance loss due to foliage is accounted for	6	1	6
11	Data transmitted on the same frequency leads to interference between signals	6	4	24	Make use of a transmitting schedule such that no signal is sent at the same time	6	1	6
12	Battery leaks into the forest	6	4	24	Isolate the battery or switch to superconductors	2	1	2
13	Solar panel damaged due to the environment	6	4	24	Add an exterior coating to the solar panel	6	1	6
14	Parts of enclosure are consumed by fauna	6	4	24	Enclosure is coloured brown to blend in with environment and not stand out	6	2	12
15	Relay attachment traps in animals	6	2	12	Use strings instead of nets	6	1	6
16	Battery not charged in time due to harsh conditions	2	4	8	Battery and solar panel should be sized for worst case scenarios	2	1	2
17	Decreased lifespan due to harsh environment	2	4	8	Cellulose acetate is stable and resistant to high temperatures or acids	2	1	2

14.5. Sustainability Analysis

Given the relay node design is largely similar to the sensor node design, all sustainability aspects developed in Section 12.3 are redundant. One characteristic not developed in the sensor sustainability analysis is the network architecture. LoRa is a high efficiency network protocol that allows the transmission of little data over extreme ranges using very little amounts of power. Compared to regular RF, Satellite, Wi-Fi or Bluetooth, the chosen network architecture is far more sustainable both in terms of energy and required infrastructure.

14.6. Verification & Validation

While performing the communications link budget for both the Node - Relay and Relay - Relay transmission links, a forest path loss model has been used. This has to be verified, and appropriate measures need to be taken in the case that the model is not completely suitable to this application.

The model [132] was developed in a Singaporean rain forest and thus constitutes the worst case scenario for fire endangered forests that are usually less humid (less atmospheric loss) and less dense. Hence, one could already make the case that this model overestimate the path loss.

However, this model claims to have been verified and validated for VHF bands (up to $300\,\mathrm{MHz}$) and is only accurate for ranges up to $5\,\mathrm{km}$. For UHF bands (around $1000\,\mathrm{MHz}$), the model is only accurate up to $1.2\,\mathrm{km}$. Anything beyond these ranges leads to an underestimation of the path loss. Furthermore, the model decreases in accuracy as the receiver and transmitter approach the top of the canopy. This however, leads to an overestimation of the loss as ground and branch effects are not as applicable.

From these considerations, it looks like the model should not be used in the first place. However, due to the lack of other forest path loss models, it was used to determine the path loss. In order to mitigate the effects of the underestimation due to model inaccuracy, an extra $3\,\mathrm{dB}$ was added to the link margin for both transmission links. This means that the range was maximised for a total link margin of $6\,\mathrm{dB}$. However, if a new, more accurate, model were to be developed, that should be used to come up with a better estimate. Furthermore, experiments should be conducted in the future to validate the estimations.

15
Production Plan

To design the EcoSense EMBER properly, manufacturing needs to be considered. Thinking about how the system is sequentially build up is useful and requires a different engineering approach which might clear up problems encountered in design, or create new ones. The manufacturing plan described in this chapter entails the construction of the envelope, the sensor nodes and the gondola in Sections 15.3, 15.3, 15.2 respectively.

15.1. Manufacturing of the Envelope

Manufacturing of the envelope starts off by cutting out the sheet patterns required for the envelope from the purchased textile laminate. Lengthwise, the sheet is limited to allow for manual joining of the sheets. Therefore, the envelope will be split in 5 separate cross-sections, namely 2 ends and three sections at the center, see Figure 15.1. The circular cross-sections are located at the centre of the blimp, and the cones are the front and rear. Concerning the width of the envelope sheets, the width of an envelope sheet is limited to $1.2\mathrm{m}$ as the machines used in production have such a width, but they may be even narrower to avoid any wrinkling.

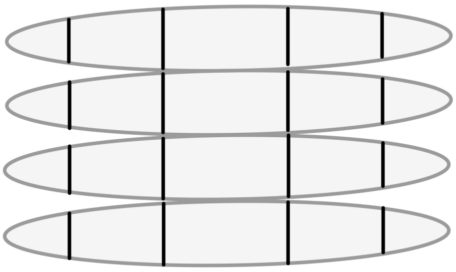

Figure 15.1: *Cutting pattern of the envelope.*

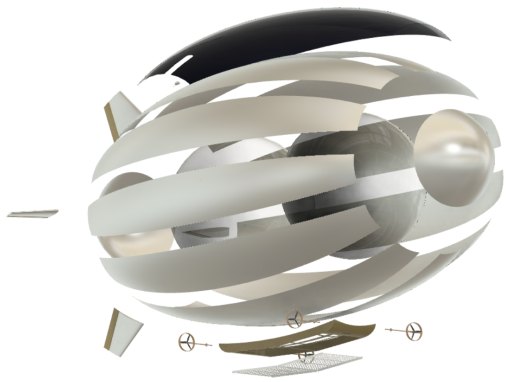

Figure 15.2: *Exploded view of the airship.*

In order to assemble the envelope manually, sheets have to be joined in a simple manner. A lap joint is selected, as it is the easiest to manufacture. Each connection consist of an overlap of sheets bonded together by an adhesive. To not interfere with the heat sealable adhesive used to laminate the fabric, a cold, flexible and strong adhesive needs to be selected. The adhesive opted for in all the joints is a cross-linking polyurethane, which fulfils the aforementioned criteria.

Assembly of the envelope goes as follows. First, the three centred sections are assembled separately from the end sections. This three unclosed cross-sections and 2 ends. Then, the three cross-sections are connected to form one. After this step, the circular cross-section is closed. Finally, the cone-elements are joined and connected to seal the envelope.

As an intermediate step in the assembly of the envelope, after cutting the sheets and before the assembly of the envelope, the required valves are installed in the sheets. In total, four valves are installed. Three are installed at the bottom, of which two belong to the ballonet system and one to fill and deflate the envelope with hydrogen. An extra one is installed at the end cone of the envelope as a venting mechanism to actively control the buoyancy of the airship. Each valve is connected to the envelope similarly as a bicycle tire's valve, see Figure 15.3. The valve has an inner plastic circular patch which is joined to the envelope by an adhesive. An extra layer of Tedlar film will be placed around the valve and attached via an adhesive. This is done to reinforce and seal the valve.

To control the attitude of the airship, fins need to be installed. This control system is made of an inflatable structure with the same material as the envelope. In order for the control surfaces to fulfil their function, extra support is required to prevent the fin from fluttering. To avoid this phenomenon from occurring, cables are attached on both sides of the control surface, connecting it to the envelope. The connection between the cable and the surface is improved by adding an extra patch to limit peak stresses in the sheet material. The patches are bonded to the surface via an adhesive.

After the circular cross-section is joined, the solar panels can be installed. The solar panels are attached by bonding with an adhesive. At the same time, the antenna is connected in front of the top fin. Simultaneously, the

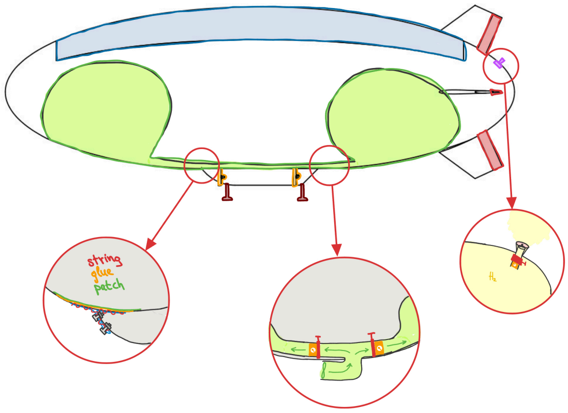

Figure 15.3: *Blimp overview.*

production of the gondola needs to be produced.

15.2. Manufacturing of the Gondola

The gondola will be manufactured from Bcomp [1] material, AmpliTex. The material is a composite with reinforcing flax fibres. The gondola design will be separated into two parts: The lower part of the gondola (the hull) and the upper part (the deck). The hull, which will house the deployment system as shown in Figure 4.3, will be made out of one Bcomp sheet with vacuum infusion. The sheet will bend and fold to create structural strength with its shape where needed. Moreover, the gondola will have four supports for the engine mount that will also be made with vacuum infusion.

The deck of the gondola will be made with vacuum infusion in the shape of the envelope. The two parts will be connected with L-profiles along its longitudinal axis.

The deployment structure will be constructed of flat plates connected with L-profiles to prevent shearing deflection of the structure. The inner plates will have holes that will give space to hollow tubes, which will accommodate the electromagnet holders. The plates and hollow tubes will be made from Bcomp material with vacuum infusion and roll wrapping respectively. As for the electromagnet holder, injection moulding will be used.

Part of the gondola structure is the engine housing. It can be seen in Figure 6.26. This part is made out of a rod that is attached to a servo housing. An outer duct will be present around the propeller for aerodynamic purposes. The rod will be made out of Bcomp material with roll wrapping and connect to a vacuum infused servo housing. The propeller duct will be 3D printed made out of PLA or PHA since it is a part that could be replaced regularly.

Lastly, four landing legs will be attached to the gondola that will be made out of roll wrapped tubes. Next, the manufacturing of the sensor nodes will be discussed.

15.3. Manufacturing of the Sensor Nodes

As the enclosure of the sensor needs to be manufactured in large batches, up to 1000 per mission, the manufacturing method must be scalable. Cellulose acetate can be injection moulded, which allows for manufacturing of large quantities at a relatively low price per unit, apart from the start-up costs. This is preferable over additive manufacturing or machining as it is more scalable and wastes less material, in addition to being less power intensive.

This manufacturing method was taken into consideration when designing the enclosure. Draft angles were included on all walls, allowing for the part to be extracted more easily from the mould. The walls were also kept at uniform thickness to avoid warping of the part during cooling. The geometry of the part was also designed to be injection moulded as three separate sections shown in Figure 15.4, and to be joined together afterwards.

This allows for overhangs and holes to be created that would typically be impossible with injection moulding. Sharp edges are also avoided, with fillets being introduced wherever possible to create rounded edges that are simpler to produce with injection moulding.

The internal electronics, purchased off the shelf, must be assembled by hand into each enclosure. Once done, the top

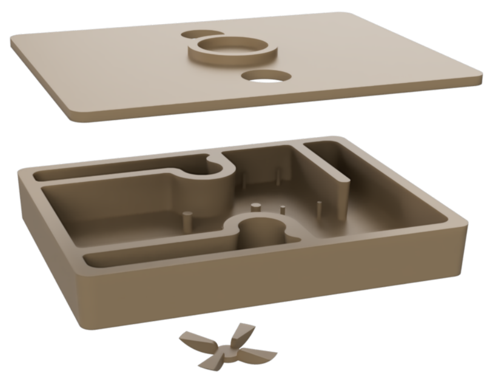

Figure 15.4: *Separated view of manufacturable parts within the sensor node enclosure.*

cover shown in Figure 15.4 can be joined to the rest of the enclosure, and the solar panels can be attached. Once the string anchors are latched into place, and the sensor node is ready to be attached to the vehicle.

16
Logistics

The purpose of this chapter is to present the logistical side of the EcoSense EMBER mission. The logistical aspect of the mission has a strong impact on the assembly of the vehicle and directly translates into the operations phase described in Chapter 17 and transportation methods are important for the life cycle assessment in Chapter 19. The logistics start with an overview of the locations and transport routes involved with EcoSense EMBER in Section 16.1 and Subsection 16.1.1. Then, a risk assessment and sustainability analysis is performed in Sections 16.2 and 16.3 respectively.

Table 16.1: *Logistics Requirements.*

Req. ID	Requirement	Section	Compl.
REQ-LOG-1	Only "Green Hydrogen" shall be produced by electrolysis exclusively from renewable power sources	16.1.2	✓
REQ-LOG-2	Hydrogen shall be produced and delivered to the ground station as a service	16.1.2	✓
REQ-LOG-3	Quality verification testing shall be done, resulting in a minimum of 99.99% purity	16.1.2	✓
REQ-LOG-4	Hydrogen shall be produced, transported, and operated following the ME-093 Strategic Work Plan	16.1.2	✓
REQ-MIS-16	The EcoSense product storage shall have dimensions that fit within a Ford Ranger with towing car : (1.8x1.5x1) meter car (4.8x2.1x2.2) meter towing car	16.1.1	✓

16.1. Logistics Locations

The three main locations from which logistics need to be performed are explained in this section. In Subsection 16.1.1 the locations are elaborated more on:

- **NSW RFS HQ**: The HQ of the New South Wales Rural Fire Service is located in downtown Sydney. From here, the operations and management of the NSW RFS are performed. It is a central location where all the interactions with the NSW RFS happen.
- **EcoSense HQ**: EcoSense will need an office where the operations can be planned, managed and the product can be stored manufactured. This office is strategically located near the NSW RFS HQ, Sydney Airport, train station and harbour. Due to the large space and garage accessibility, the manufacturing and storage of the EcoSense EMBER will happen on the ground floor. On the top floor the planning and operations will be carried out.
- **Ground Station**: The ground station should be strategically located in the global area of interested which can reach the entire area within $100\,\mathrm{km}$. Furthermore, the ground station should be as flat as possible while also being spacious enough to fit the launch operations ($80\,\mathrm{m} \times 200\,\mathrm{m}$). Therefore, the location of Putty, NSW was chosen. A large grass field is located near the first exit of the state road.

(a) *NSW RFS, 4 Murray Rose Ave, Sydney*

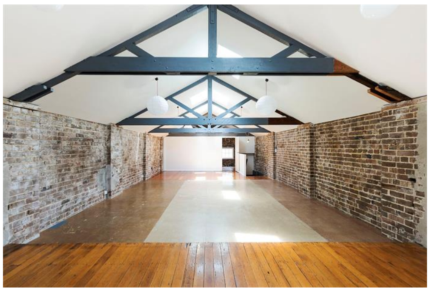

(b) *EcoSense HQ, Alexandria, Sydney*

(c) *Ground station, Putty NSW*

Figure 16.1: *Logistical locations*

16.1.1. Product Assembly and Transportation

All the parts necessary for manufacturing are ordered and are transported to the EcoSense HQ either via a plane, ship or train. The EcoSense HQ is strategically located in between these logistical distribution points as can be seen in Figure 16.3a. When all the parts are shipped to the EcoSense HQ, the pre-assembly and production can be started as described by Chapter 15. The pre-assembled product needs to be made ready for transportation in the following sub-parts: The folded blimp envelope, the gondola with sensor deployment system, sensors, relays and tools. These sub-parts will be transported to the ground station in a $6\,\mathrm{m}$ container which is towed by a Ford Ranger. An overview of the assembly in the container of the sub-parts can be seen in Figure 16.2. The folded blimp envelope was estimated to have dimensions of $3\,\mathrm{m}$ length, $2\,\mathrm{m}$ width and $0.50\,\mathrm{m}$ height. The gondola has estimated dimensions of $4.5\,\mathrm{m}$ length, $1.5\,\mathrm{m}$ width and $0.4\,\mathrm{m}$ height. The gondola is mounted on the ceiling of the container using struts and straps. Lastly, the sensors and equipment is transported in a $2\,\mathrm{m}$ length $\times 1\,\mathrm{m}$ width $\times 1\,\mathrm{m}$ height box. Furthermore, the envelope and box are mounted with struts and straps. Miscellaneous items are located in the back of the Ford Ranger pick-up.

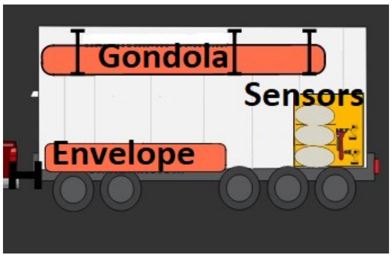

Figure 16.2: *Transportation*

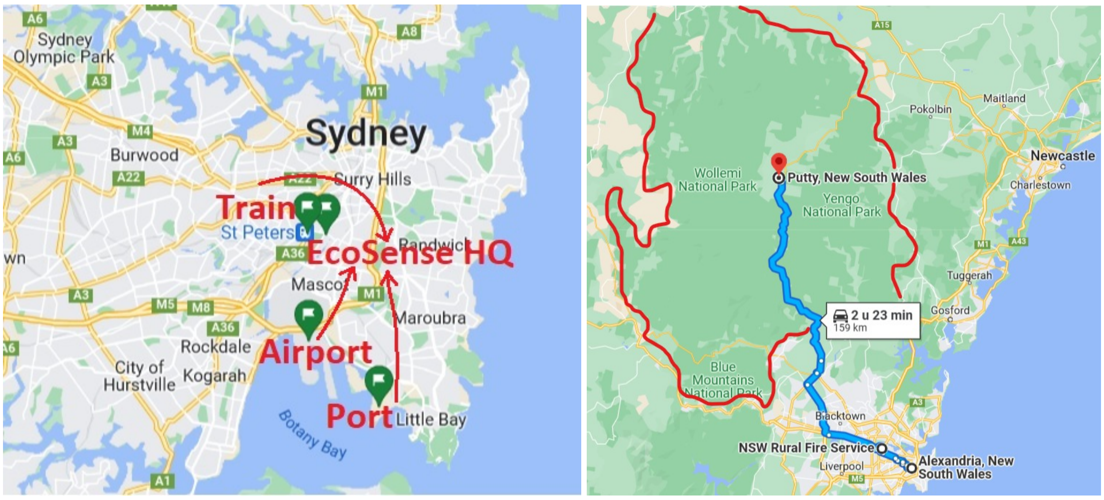

(a) *Assembly logistics*

(b) *Route to ground station via NSW RFS*

Figure 16.3: *Logistics of the product (Source: Google Maps)*

16.1.2. Hydrogen Logistics

An important part of the mission logistics is the journey of the hydrogen to be used as the lifting gas of the vehicle. Hydrogen is the most abundant element in the universe, it is essential for life, and is present in almost all living things. However, on Earth, pure hydrogen is very scarce, instead it mainly exists combined with oxygen in the form of water. This subsection describes the journey depicted in figure 16.4 in detail.

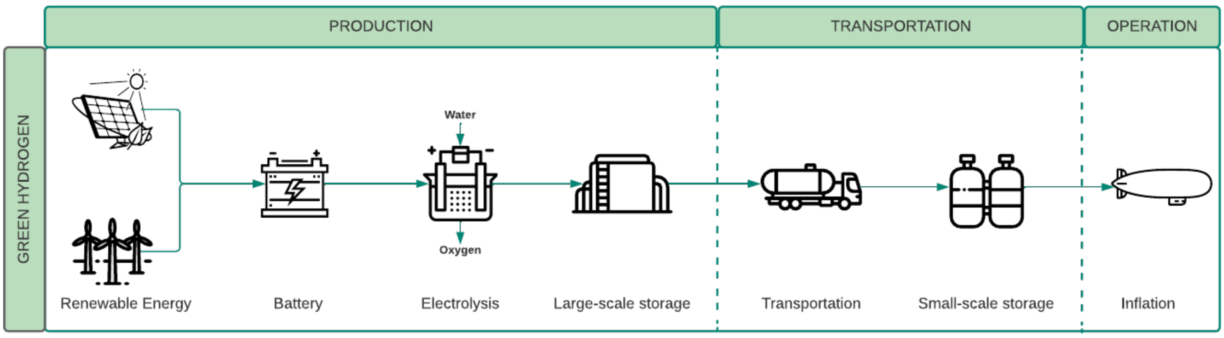

Figure 16.4: *Life cycle of hydrogen throughout the mission.*

Production of hydrogen

Green hydrogen is produced by the electrolysis of water. This process directly emits only oxygen as a by-product of the reaction $2H_2O \longrightarrow 2H_2 + O_2$. However, electrolysis is an energy intensive process. Therefore, the only way to truly produce emission-free hydrogen is exclusively through the use of renewable energy. In March 2020, the New South Wales Government released its Net Zero Plan Stage 1: 2020-2030. The Net Zero Plan includes an action to support commercialisation of green hydrogen as an emerging technology for emissions reduction.

Under the Net Zero Plan umbrella, Government funding support of AUD$750 million, equivalent to €500 million is announced. Funding for the program focuses on three key areas:

- AUD$380 million to support existing industries to re-tool with low emissions alternatives
- AUD$175 million to set up low carbon industries such as green hydrogen
- AUD$195 million to research and develop new clean technologies

To conclude, green hydrogen is widely available in the New South Wales area, and its availability will rapidly increase in the following years. Therefore, transportation of other countries by cargo ship can be replaced with more efficient, already built pipeline infrastructures.

Transportation of hydrogen
Now that the fact that green hydrogen is produced locally in the New South Wales region is known, the transportation from the production facility to the mission ground base is to be dealt with next. As stated in the driving requirements described in Table 16.1, hydrogen shall be produced and delivered to the ground station as a service. Coregas is a company based in NSW that operates Australia's largest merchant hydrogen plant in Port Kembla, NSW. Commencing in the second half of 2022, Coregas will be operating between Port Kembla and Sydney averaging $400\,\mathrm{km/day}$, exclusively using Hyzon Hymax 450 prime movers. In other words, the hydrogen needed for the EcoSense EMBER mission, will be transported with Australia's first net-zero emissions heavy road transport infrastructure. Coregas offers delivery of a $99.999\,\%$ purity 12-pack of G-sized (Ø $204\,\mathrm{mm}$ ×$780\,\mathrm{mm}$ high) pressurized tanks at $200\,\mathrm{bar}$, filled with a total of $1775.5\,\mathrm{kg}$ of H_2. Enough for the entire EMBER mission in a single delivery. Transportation regulation and driver certifications are managed by the delivery company. For Australia these are derived from the ME-903 Strategic Work Plan and ISO/TC 197 industry standards. Furthermore, all Coregas cylinders can be tracked by their mobile app, which forms an integral part of quality assurance, cylinder tracking and easy re-ordering if necessary. This means that cryogenic tanks are not necessary for this amount of lifting gas.

On-site storage
After the lifting gas is delivered to the ground station, the tanks must be stored in a responsible and easy-to-access way. For safety reasons, which are further elaborated in the risk assessment in Section 16.2, the tanks containing pressurized hydrogen must be stored at least $200\,\mathrm{m}$ from the operation station, trees, and possible camping sites in an open-air environment protected from direct sunlight. For this, a gazebo can be used. The IKEA HIMMELSÖ is a cheap, accessible and sustainable version of this product made from 100% polyester from which minimum 90% is recycled. Furthermore, potentially leaking hydrogen can travel through the polyester of the roof, avoiding hydrogen gas build-up. A second tent will be included that operators can use for extra shade.

Figure 16.5: *Hydrogen tanks placed inside the gazebo.*

16.2. Risk Assessment

Understanding Hydrogen
Hydrogen is no more or less dangerous than other flammable materials. In fact, some of hydrogen's differences actually provide safety benefits compared with petrol or other fuels. However, all flammable materials should be handled responsively, since hydrogen is flammable and can behave dangerously under specific conditions. Nonetheless, hydrogen can be handled safely with the right guidelines and understanding of its behaviour.

Comparison with Other Flammable Materials
Hydrogen is lighter than air and diffuses rapidly, when released, it dilutes quickly into a non-flammable concentration. Hydrogen rises two times faster than helium and six times faster than natural gas at a speed of almost 20 m/s. Therefore, unless a roof, a poorly ventilated room, or some other structure contains the rising gas, the laws of physics prevent hydrogen from lingering near a leak (or near people using hydrogen-filled equipment). Industry takes these properties into account when designing pressurized storage vessels. The designs help hydrogen escape up and away from the user in case of an unexpected release. The tanks to be used for the mission are equipped with safety mechanisms such as the check valve, the shut-off valve and the thermally-activated pressure relief device (TPRD), as defined by the previously mentioned ISO/TC 197 Australian industry standards [140]. Hydrogen is odorless, colorless, and tasteless, so human senses cannot detect a leak. However, given hydrogen's tendency to rise quickly, a hydrogen leak indoors would briefly collect on the ceiling and eventually move toward the corners. For that and other reasons, the hydrogen tanks must not be contained in an enclosed room.

Explosion
An explosion cannot occur in a tank or any contained location that contains only hydrogen. An oxidizer such as oxygen must be present in a concentration of at least 10% pure oxygen or 41% air. Hydrogen can be explosive at concentrations of 18.3% to 59%. Although this range is wide, it is important to remember that petrol can present a greater danger than hydrogen because the potential for explosion occurs with petrol at much lower concentrations: 1.1% to 3.3%. Furthermore, there is very little likelihood that hydrogen will explode in open air due to its tendency to rise quickly. This is the opposite of what we find for heavier gases such as propane or petrol fumes, which hover near the ground, creating a greater danger for explosion [141].

Table 16.2: *Logistics risk assessment*

Index	Risk factor	HS	HP	HRI	Mitigation strategy	HS	HP	HRI
				Detailed logistics risk assessment				
29	Unavailability of filling material.	6	6	36	Use supplier with redundancy in production	6	4	24
x	Transport can't reach the destination.	6	4	24	Locate ground station accessible by road. Have a 4x4 vehicle available.	2	1	2
x	Components don't arrive on time.	6	6	36	Order components well in advance.	2	6	12
x	Components don't fit properly during assembly.	6	6	36	Clear assembly check in the manufacturing plan	6	4	24
x	Too much pressure in the tanks due to heating.	10	6	60	Use tanks equipped with a TPRD. Avoid tanks being exposed to direct sunlight.	6	4	24
x	Gazebo flies away due to heavy winds.	2	4	8	Remove fabric from the frame of the gazebo in windy conditions.	2	1	2

16.3. Sustainability

As explained in the LCA in chapter 19, transportation and logistics have a large contribution to sustainability of the mission. The EcoSense HQ is located on purpose near the big distribution centres of Sydney, therefore minimizing the transportation distance. Furthermore, because of environmental reasons, EcoSense promotes and prefers the shipment of parts by train then ship and lastly by plane if really necessary.

The environmental impact of the logistical concepts discussed in this chapter was already identified in the LCA. Environmental sustainability in logistics include local production of components allowing for transport by road, the use of green hydrogen-powered trucks by Coregas, and the rental of hydrogen tanks to be reused later.

From a social sustainability point of view, the work of operators is made much more simple as the hydrogen is delivered, managed and maintained as a service by Coregas. Moreover, a second gazebo with curtains is included in the transportation to give the operators protection against the sun.

Economically, the logistics of the mission are made sustainable by the use of temporary infrastructure, by focusing on production facilities near HQ and only one single transport needed to deliver the lifting gas, and one to recover the tanks.

17 Operations

The operations chapter focuses on the operational procedures that occur when deploying and using the EcoSense EMBER system. To give a more personal feel for the operations, each procedure is described as seen from a persona given in Table 17.2 and Figure 17.1. In the first 4 sections, the operations of the product deployment and usage are assessed and described. Then lastly, the risks and sustainability aspects of the product are assessed and described in the last two sections. An overview of the operational requirements is given in Table 17.1

Table 17.1: *Operations requirements*

Req. ID	Requirement	Section	Compl.
REQ-VEH-CO-14	The vehicle shall deploy the sensors from an altitude of less than 500 metres above ground.	17.1	≈
REQ-VEH-CO-16	Launch shall not leave non-degradable waste in the environment.	17.2	✓
REQ-VEH-CO-17	Launch infrastructure shall support the loaded vehicle mass.	17.2	✓
REQ-VEH-CO-18	During launch, a zone of 80x200 m2 from the infrastructure shall be clear of obstacles or operators.	17.2	×
REQ-SENS-COM-7	The ground station shall perform data validation.	17.2	✓
REQ-SENS-COM-8	The ground station shall be able to perform data correction.	17.2	✓

(a) *NSW RFS left to right (Mark, Beth, Roger, Michael, Judy).* **(b)** *EcoSense team left to right (Sita, Maria, Steve).* **(c)** *Externally hired employees left to right (Brian, Derek).* **(d)** *Homeowner in Yengo Park (Markus).*

Figure 17.1: *Operations personas.*

Table 17.2: *Personas involved with the EcoSense EMBER system, note that all personas are fictional except Rob Rogers.*

Name	Role	Description
Rob Rogers	EcoSense Customer	As commissioner, mr.Rogers is the chief of the NSW RFS which includes responsibilities on operations, regional management and community safety.
Mark, Beth, Judy and Margret	Volunteers at the NSW Rural Fire Service	With over 70000 volunteers, the NSW RFS is the largest volunteer fire service. The volunteers will help out the EcoSense team with operations.
Maria	Manager at EcoSense	As manager, Maria is responsible for the sales, communication, planning and managing the departments within EcoSense.
Sita	Operations Engineer at EcoSense	As operations engineer, Sita is responsible for mission assessment and deployment.
Steve	Technician at EcoSense	As technician, Steve is responsible for the assembly and hardware of the EcoSense EMBER product.
Brian	Drone Pilot Freelancer	As a freelance drone pilot, Brian is hired by EcoSense whenever missions are planned.
Derek	Software Engineer Freelancer	As freelance software engineer, Derek is hired periodically by EcoSense whenever software maintenance needs to be performed.
Markus	Proud homeowner in Higher MacDonald, NSW	The small town of Higher MacDonald, NSW is located in the centre of Yengo National Park which has was devastated by the Bushfires of 2019/2020.

17.1. Mission Planning

Given the need of the NSW RFS for an early fire detection system in a global area of interest, the commissioner's office of Rob Rogers will be in contact with the EcoSense manager Maria for a possible business proposition. Given the global area of interest, Maria will inform the operations engineer Sita to start the initial mission planning phase.

Initial Mission Analysis

In the initial mission analysis phase, the operations engineer starts by dividing the global area of interest up into tiles of $100\,\mathrm{km}^2$. The sensor placement mesh is determined using the fire ignition risk as described by Section 13.2.

The division of the global area of interest into tiles of $100\,\mathrm{km}^2$ is given in Figure 17.2. The customer can always negotiate with the manager which tiles can be dropped due to redundancy or other reasons. Given the payload capacity of 550 sensors. Therefore, almost all tiles of $100\,\mathrm{km}^2$ need to be populated by performing 2 flights. The estimated costs and days of deployment per $100\,\mathrm{km}^2$ tile is given in Table 17.3. A fully detailed cost breakdown is given in Chapter 20.

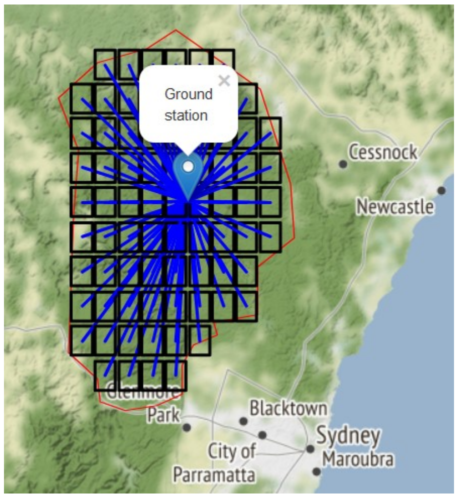

Figure 17.2: *Division of global area into tiles of* $100\,\mathrm{km}^2$

Mission Proposition

The results of the initial mission assessment are summarized and are presented by the manager and operations engineer to the commissioner's office. This presentation should show clearly how many missions need to be performed to cover the entire global area of interest, how much time this will take and how much this will cost, such as can be seen in Table 17.3 Depending on the budget and time constraint of the customer, the customer may choose to deploy multiple products at the same time. This will decrease the deployment time but increase the cost.

The conclusion from the initial mission assessment should be:

1. The total number of products which will be deployed
2. The tiles of the global area of interest which are selected for deployment

Amount of products	Amount of flights per product	Costs per 100km2	Deployment days per 100km2
1	185	$ 157,000.00	2
2	93	$ 314,000.00	1
3	62	$ 471,000.00	1

Table 17.3: *Costs and Deployment days*

Mission Set-Up

For demonstration purposes, the next sections assume that one product will be chosen which will perform a mission for one tile. A total deployment time frame of three days is planned with one product to deploy. To determine the operations plan for a multi-tile and -product operation, the current operations can be scaled/repeated accordingly. Using this, the case-mission for the operations is the deployment of sensors in the lower left tile in Figure 17.2. This tile was chosen since it the furthest away from the ground station and has the most change in terrain elevation. The elevation terrain and sensor deployment area can be seen in the lower left of Figure 17.3.

The operations engineer Sita will first check the amount and locations of the sensors within the $100\,\mathrm{km}^2$ tile. It should be checked that all the sensors within the selected tile are placed correctly. Note that sensors placed above infrastructure, private premises or water bodies are not desired, and these sensors should be removed from the mesh. Given the selected tile, the total amount of sensors is 1028. Therefore, two flights are needed. The $100\,\mathrm{km}^2$ tile is divided up into two deployment area's each containing 514 sensors.

For the flight planning, the flight plan consists of the route from the ground station towards the deployment area. When arrived at the deployment area, the sensor dropping route is initiated. In order to deploy the sensors as effectively as possible while minimizing energy loss due to climbing and descending, the sensors are divided into three altitude levels in which the deployment vehicle will perform three step-climbs. For each altitude level, the route is optimized using a heuristic local-search algorithm [142]. It was chosen to use a local search algorithm because it is computationally fast and did not differ that much with solutions from more sophisticated algorithms such as two-opt or simulated annealing. The algorithm will minimize the distance travelled between the sensors and altitude shift. This will allow the deployment vehicle to fly at a constant altitude within an altitude level, therefore minimizing the climb and descend during flight. The analysis of the flight path for the first deployment area can be seen in Figure 17.3. The operations engineer should check that the ground clearance of the sensors should stay between the bounds of [$50\,\mathrm{m}$ - $315\,\mathrm{m}$]. Therefore, REQ-VEH-CO-14 is complied with. The requirement changed from $500\,\mathrm{m}$ to $315\,\mathrm{m}$ as described by the sensor fall analysis Section 13.1. The absolute yaw rates remain between $0.8\,\mathrm{rad/s}$, which is controllable as described by Chapter 10. Furthermore, the absolute pitch rates remain within $0.09\,\mathrm{rad/s}$ which is also controllable. Lastly, it is analysed that when flying at $55\,\mathrm{km/h}$ the total mission time is $6.3\,\mathrm{hrs}$ and $310\,\mathrm{km}$ distance travelled, which remains within the vehicle constrains.

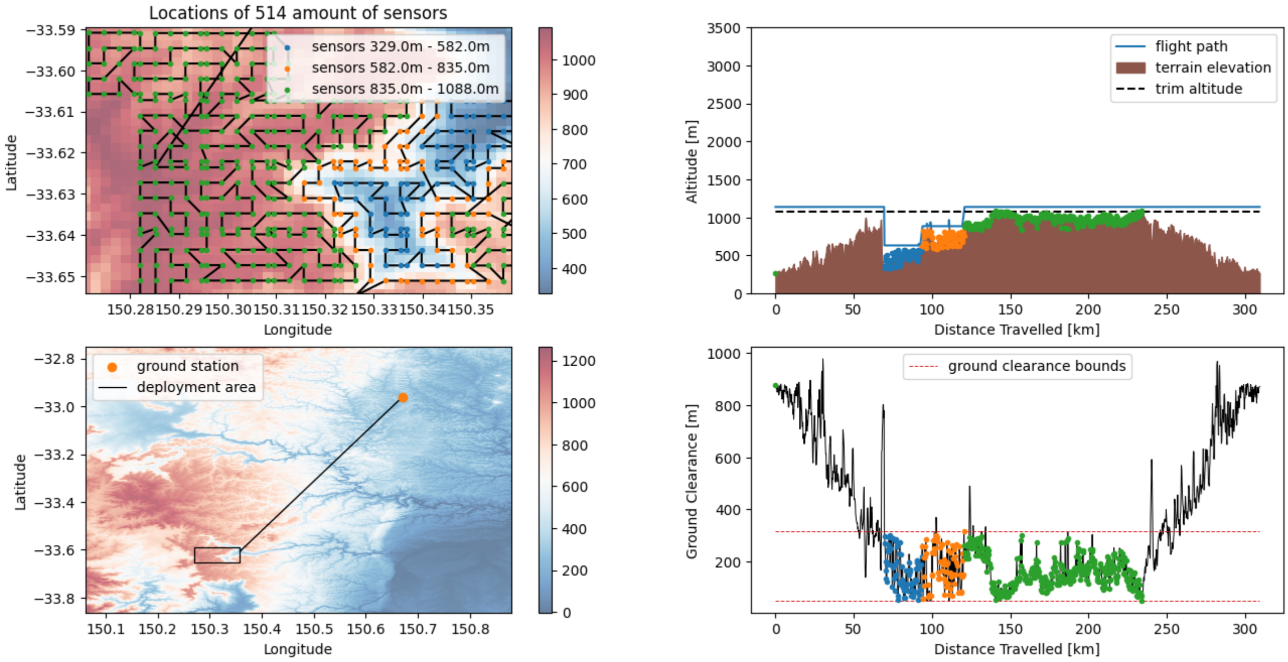

Figure 17.3: *Flight Path Analysis*

Furthermore, the manager Maria will discuss with the commissioner's office for a feasible date of deployment. Note that due to solar intensity, the window of opportunity is between October-March. If the time of deployment is known, it is Maria's responsibility to schedule all on-site required employees, rent necessary equipment such as the Ford Ranger with container and two RVs. Furthermore, the manager should stock up on supplies and request and file the permit needed for the mission that is obligatory to fly over national parks in NSW [143]. The Ford Ranger was selected since it is a common car in Australia which can tow $3400\,\mathrm{kg}$, the 20ft container is assumed to be $2300\,\mathrm{kg}$. Therefore, the total vehicle mass of $143.4\,\mathrm{kg}$ can be transported by the Ford Ranger and REQ-VEH-CO-17 is complied with. The RV's are rented in which the crew can spend the night and not travel back and forth to the ground station during the two-day launch phase.

(a) *Initial mission analysis.*

(b) *Mission proposition.*

(c) *Mission set-up.*

Figure 17.4: *Mission planning.*

17.2. Deployment of System

From Chapter 4, flight is only possible between 09:00-16:00, therefore take-off and landing are scheduled at 09:00 and 16:00 respectively.

Day0: 12:00: Transportation
On the day before launch, the product will be transported and pre-assembled at the ground station. The transportation from the EcoSense HQ to the ground station starts by the technician Steve performing installation checks on the hardware that will be transported on the main vehicle. Furthermore, the manager is responsible to rent two RVs which should be equipped with food and drinks for the crew for a total of three days. Furthermore, the NSW RFS volunteers can choose to be picked up at the NSW RFS HQ, or arrange their own transportation to the ground station as long as they are on time.

Day0, 15:00, Pre-Assembly
When arriving at the ground station, the container of the main vehicle which contains the hardware of the product should be unpacked by all the crew present. The volunteer's main job is to help with carrying and supporting wherever is necessary. When the product is unpacked, Steve the technician will start by assembling the product with help from the volunteers. The operations engineer Sita will set up the flight and sensor deployment systems.

Day1, 07:00, Pre-Launch
The technician who is licensed to handle hydrogen systems, will start by inflating the deployment vehicle with hydrogen and strapping it to the ground. The inflation procedure will approximately take $1\ \mathrm{hr}$. The operations engineer shall plan and forecast weather conditions and continue to monitor them closely. After the deployment vehicle is inflated, final pre-launch checks are performed.

- Pressure of the hydrogen is within $490\ \mathrm{MPa}$-$510\ \mathrm{MPa}$.
- The flight controls, communications and deployment mechanism respond correctly.
- Solar intensity and power generation should be $2\ \mathrm{kW}$ or higher.
- The current and forecast wind speed remain below $15\ \mathrm{km/h}$.
- No heavy rain or wildfires are located on the flight path.

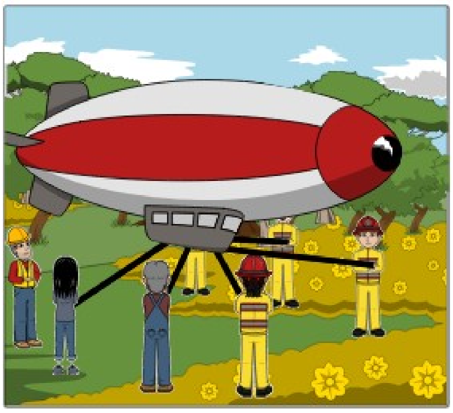

Figure 17.5: *Deployment vehicle launch*

Day1, 09:00, Launch and Cruise flight
The supports of the deployment vehicle are removed, and the deployment vehicle is supported by a rope connection which is held by the bare hands of the technician, operations engineer and the four volunteers Figure 17.5. The requirement of REQ-VEH-CO-18 is not complied with. When trimmed for $1000\ \mathrm{m}$, the deployment vehicle will exert a force of $100\ \mathrm{N}$ upward at launch. Therefore, the load per person will be approximately $16\ \mathrm{N}$ to hold the blimp down. Using ropes, a minimum safe distance of $3\ \mathrm{m}$ can be held from the deployment vehicle. The deployment vehicle must be rotated into the direction of the wind, which will minimize the amount of side force experienced by the wind. When take-off is performed by the drone pilot, the rope connections are disconnected from the deployment vehicle and the blimp will increase altitude to trim altitude. When the trim altitude is reached, the deployment vehicle accelerates to cruise speed of $55\ \mathrm{km/h}$ and heads for the deployment area on autopilot.

Day1, 10:30, Sensor Deployment
When the deployment vehicle reaches the selected area, the operations engineer initiates the route in which the sensors need to be deployed. The drone pilot will ensure the deployment vehicle will follow this route and intervene the autopilot if necessary. The operations engineer will ensure the deployment mechanism deploys correctly at the right locations.

Day1, 14:30, Returning to Ground Station
After the last sensor has been dropped, the deployment vehicle returns to the ground station at cruise speed. When $2\ \mathrm{km}$ removed from the ground station, the deployment vehicle starts descending and dropping speed to landing speed. When hovering at $5\ \mathrm{m}$ above ground, the operations engineer, technician and four volunteers will fasten the deployment vehicle with ropes. The crew will pull the deployment vehicle to the ground. The drone pilot will idle the power setting such that the ground crew is not in danger of the fans. When the blimp is finally secured to the ground, the hydrogen lifting gas of the deployment vehicle is partly recycled and vented. Using empty hydrogen storage tanks, part of the hydrogen can be recycled and stored under low pressure $20\ \mathrm{bar}$. This will safely recycle $20\ \%$ of the hydrogen.

Day1, 16:45, Storage
When the deployment vehicle is deflated, the technician and volunteers will dis-assemble and store the deployment vehicle and sensor deployment system in the container at the ground station. The operations engineer will take care of the flight and sensor systems and other highly valuable systems which will be also stored in the

container. When the storage of the product is done, the technician will lock the container and the whole crew will relax and do some nice evening activities including an Australian BBQ.

Day2, 07:00, Deploy Remaining Sensors

On the next day, the remaining sensors in the $100\,\mathrm{km}^2$ are placed. The previous steps up and to the landing are repeated for the remaining sensors.

Day2, 16:45, Storage and Returning to Sydney

When the deployment vehicle is deflated, the recycled and remaining hydrogen is picked up by the transportation company. The deployment vehicle should be dis-assembled and made ready for transport in the container. The remaining sensors and tools should also be stored in the container and made ready for transport. The volunteers will make sure that the ground station is left nice and tidy and no rubbish is left behind, thus complying with the requirement REQ-VEH-CO-16. The volunteers will either ride back with the RV or with their own transport. When the volunteers are dropped off at the NSW RFS HQ and the crew has arrived at the EcoSense HQ, the hardware is stored in the EcoSense workplace and the rented items Ford Ranger, RV and container are returned. The technician will perform maintenance on the deployment vehicle as described in Chapter 18.

Day2, 20:00, Sensor Data Verification and Validation

The operations engineer performs unit test checks on the sensors dropped and sees if the data uploaded to the server is correct using weather data available. From Figure 14.4, the data sent twice a day from the sensors is: maximum temperature, minimum humidity, CO and H_2 concentrations. When the system is filtered for any malfunctioning sensors, a dashboard is developed which will supply the customer NSW RFS with interactive fire risk monitoring software which will be discussed in the Section 17.3.

17.3. Product Usage

The operations engineer together with the freelance software engineer will create a dashboard which will supply the NSW RFS with interactive fire risk software. The software supplies the NSW RFS with two main insights: Wildfire prevention and Wildfire detection. Using the temperature and humidity data, the sensors can create a heatmap of wildfire risk. The risk of wildfires starting is high when temperatures are high and humidity is low. Using this information, the NSW RFS can patrol high risk areas more often, and close them down to the public if necessary to mitigate human caused wildfires. Furthermore, when the CO and H_2 data will peak in the sensors, a signal is sent to the relay which will sent a warning to the database. The NSW RFS will receive a warning on the dashboard from which the wildfire detection sequence is started Figure 17.6a. The NSW RFS will send a helicopter to search the area in which the sensor detected a spike in concentration and will look for wildfires using visual inspection and heat detection cameras. If a wildfire is found, the helicopter will alert the NSW RFS HQ and deploy some fire retardant as an initial fire extinguishing method and send fire fighting reinforcements to the wildfire location Figure 17.6b. The software engineer performs weekly maintenance on the database and dashboard such that no bugs prevent a fire from being detected. Furthermore, the NSW RFS may choose to publish the wildfire risk map to the internet from which local residents check the wildfire risk of their local area. Furthermore, in case a wildfire is detected, local residents can get an alert on their cellphones from the NSW RFS with the magnitude and location of the wildfire. This will make sure the residents of rural fire-prone areas can be evacuated on time in case a fire starts nearby Figure 17.6c.

(a) *Fire detected, alert residents and send helicopter.* **(b)** *Fire verified, reinforcements sent.* **(c)** *Nearby residents can be evacuated early.*

Figure 17.6: *Product usage.*

17.4. Risk Assessment

Table 17.4 shows an overview of the operational risks and their mitigation's. The method of HRI used here is explained in Section 5.3.

Table 17.4: *Operations risk.*

Index	Risk Factor	HS	HP	HRI	Mitigation strategy	HS	HP	HRI
1	Dashboard not working.	10	6	60	Hire freelance software engineer to perform software maintenance.	6	2	12
2	Blimp drifts off during launch.	10	6	60	During launch, let ground crew secure the blimp with ropes until blimp is stable.	6	3	18
3	Unexpected weather conditions.	10	6	60	Perform weather forecast checks and not launch if conditions are unfeasible. Otherwise, return back to ground station if weather conditions are getting worse and dangerous.	4	3	12
4	Collision in flight	10	6	60	During flight planning, add anti-collision with terrain and check for ground clearance during the whole flight. For collisions with animals, mitigate by cruising as high as possible to prevent collisions with birds.	6	3	18
5	Rebound during landing.	8	6	48	Throttle down during landing such that ground crew can secure blimp by ropes and connect it to ground.	5	3	15
6	Drone pilot missing.	10	4	40	Contact other drone pilots on short notice.	7	4	28
7	Transportation vehicle malfunction.	8	4	32	See if NSW RFS has back-up vehicles available.	5	3	15
8	Volunteers missing.	6	6	30	1 volunteer is redundant, meaning 3 works fine Otherwise, check if NSW RFS has additional volunteers.	2	5	10
9	Hydrogen explosion during handling.	9	3	27	Keep hydrogen cooled in shade, only handle hydrogen if licensed.	6	2	12
10	Item breaks while on transport.	6	4	24	Proper installment by technician, brittle items such as sensor must be wrapped in protective materials for transport.	2	3	6
11	Rentals not available.	2	10	20	EcoSense HQ is located near the Sydney Airport, Try other car rentals otherwise use NSW RFS transport vehicles.	2	3	6
12	Parts getting stolen.	2	1	2	Store and lock the container with valuable parts over night.	1	1	1

17.5. Sustainability

Transportation

During the transportation, EcoSense focuses on sustainability by car-pooling as much as possible. Although currently there are no suitable non-fossil transportation vehicles available on the market, EcoSense plans to rent the electric Ford Ranger which come to market in 2023. The electric Ford Ranger will have enough range and towing capacity and will save approximately $95\,\mathrm{kg}$ of CO_2e per $100\,\mathrm{km}^2$ of area.

Flight Planning

By using smart algorithms which minimize the change in altitude of the flight path, energy is saved. By performing this constant altitude flight path, the fans will not have to spool up and down as much, therefore limiting the noise pollution in the area.

Storage

When returned to the ground station, $10\,\%$ of the hydrogen can be recycled and stored safely in low pressure tanks without having to bring more highly advanced equipment and employees. EcoSense plans to increase the percentage of recyclable hydrogen in the future by hiring more employees which will handle the hydrogen extraction and storage of the blimp. This recycled energy use can be put to use somewhere such as transportation or heating.

Social Sustainability

By letting local residents such as Markus access the wildfire risk map dashboard, the residents in rural fire prone area's will feel a lot safer and can protect their homes and loved ones more effectively against rapidly spreading wildfires.

18

Reliability, Availability, Maintainability & Safety

The Reliability, Availability, Maintainability & Safety, or RAMS analysis consists of analysing the above-mentioned characteristics of the finalised product design. Sections made for each component, namely maintainability, reliability, availability and safety in Section 18.1, Section 18.2, Section 18.3 and Section 18.4, respectively.

18.1. Maintainability

Given the remote nature of the detection location, only the blimp is maintained (explanations regarding actions taken if a sensor fails are given in Section 18.2).

The blimp will be inflated before flight. In the meanwhile, the launching team looks out for any defects such as holes, tears, leaks, UV or water damage. Bigger and more extensive checks will need to be made at the end of each mission, such that the team has enough time to order a new blimp (or do maintenance) in case of defects. Subsection 5.2.7 contains a more detailed overview of the maintenance procedures of the envelope of the vehicle.

In order to estimate the time and money needed for such maintenance operations, a more in depth analysis should be done and one should get in contact with maintenance companies. In the interest of time and lack of finalised detailed blimp design, this was left out and a very rough estimate was made: $25\,\%$ of the cost of the blimp will be required every year to maintain the blimp in operational conditions.

18.2. Reliability

The reliability of the EcoSense EMBER product, or the probability that the mission is fulfilled properly, can be assessed by determining the reliability of every system the product is composed of. The biggest part of the reliability of EcoSense EMBER is determined by the sensor network part (both hardware and software). This is because the sensors are sent out to a remote location, and left untouched for $5\,\mathrm{yrs}$ (during which everything should work as intended) whereas the deployment blimp is only used once, to deploy the sensors.

The sensor network, from Subsection 13.2.8, is currently designed such that it can detect $62\,\%$ of the fires in less than $10\,\mathrm{min}$ and $90\,\%$ of fires larger than $0.2\,\mathrm{km}^2$ (although it is believed that this number is severely underestimated and will have to be verified experimentally). This reliability measure is very high, as it outperforms any current fire detection method. Given the sensors are deployed in a remote location, they are maintenance-free and them failing would lead to a decrease in the overall reliability of the network. However, if a sensor fails, a new analysis can be run to determine the new reliability of the network (one should also remember that a $10\,\%$ margin was established to cover program simplifications and sensors failing). It is then up to the customer to decide whether that reliability is too low and if a new mission should be sent, further improving the sensor networks' reliability.

On the other hand, the deployment vehicle also has a deployment reliability. Solar incidence angle was taken into account when sizing the battery and power system such that the blimp would still be able to operate at the desired speed even with the worst possible incidence. Furthermore, although headwind was not explicitly taken into account when designing the blimp, the over-sizing of both the solar panels and batteries means the blimp is expected to be able to fly during the large majority of Australia summer days. A delay in departure could pose a reliability problem too. This was implicitly taken care of by assuming the blimp could fly between 9am and 4pm only. However, given the slight over-design of the solar panels and batteries, it is possible for the blimp to fly a few tens of minutes outside this range and thus recover lost time due to delays.

18.3. Availability

Availability, defined as the probability that the product is available at any time, is of prime importance for EcoSense EMBER given it has to provide a reliable fire detection service. The sensor network availability only consists of the server uptime, as all the other subsystems fall under reliability and are developed in Section 18.2. For this, a high performance server was chosen [144] which have uptimes of at least $99.999\,\%$.

On the blimp side, there are some limitations regarding the conditions during which it can fly. From Section 13.1, the blimp is not allowed to deploy if wind speeds exceed $15\,\mathrm{km/h}$. According to yearly wind readings at Nullo

Mountain [117], this is only the case in approximately 15 % of the days, meaning the blimp could fly 85 % of the month according to those limitations. Some other assumptions were made in Chapter 6 such as cloud coverage and average solar radiation. Again, due to the over sizing of the solar panels, it was concluded that the blimp could fly on any reasonably sunny day, the key here being ”reasonably”. Of course, it goes without saying that the blimp should not fly during storms or rainy days, as not enough power could be harvested. However, the use of a solar radiation meter should be made, as explained in Section 17.2, in order to verify whether the blimp can fly. Due to lack of historical measurement, it is currently not possible to quantify the availability of the blimp due to solar radiation.

18.4. Safety

When talking about hydrogen blimps flying over a high fire risk forest, an obvious safety red flag is raised. Most safety concerns regarding hydrogen are described and mitigated in their corresponding risk assessment sections. Safety risks regarding hydrogen storage are developed in Section 16.2 and those concerned with the buoyancy mechanisms were described in Section 9.8.

One aspect that is very important when talking about large masses of inflammable particles is the energy stored in the reservoir/envelope. An assessment is required, given some could think that a hydrogen blimp would essentially constitute a flying bomb (given recent Zeppelin history). Multiple countries currently make use of general aviation aircraft such as the Cessna 172 to detect fires from the skies. Such an aircraft can carry 43 gal, or 163 L [145], corresponding to 156 kg of kerosene. At a fuel energy density of 43.1 MJ/kg [146], this amounts to a total of 6.725 TJ of energy carried by a Cessna 172 while looking out for fires. On the other hand, the EcoSense EMBER blimp carries 1.5 TJ of energy.

Thanks to this comparison, one can see that not only the blimp is carrying close to 78 % less energy in case of an issue, but it is also only operated during deployment of the sensor network. On the other hand, the Cessna is continuously looking out for fire, leading to a higher overall risk. Additionally, the electronics bay in the gondola includes a fire suppression system including 4 kg of ABC powder.

19
Life-Cycle Assessment

Sustainability is a crucial part of the EcoSense design methodology. The EcoSense system is built to help save the environment and therefore, the impact of its manufacturing, use, and end-of-life needs to be minimised in order not to diminish the positive impacts it aims to achieve. To do this, a life-cycle analysis will be performed with the intent to evaluate the impact of the system, its components, and its phases of life. With this information, not only will the impact be quantifiable, but key areas for improvement will be identified and shall be improved upon before the system goes into production. The assessment will be elaborated on for the singular components of the mission, being the airship deployment vehicle in Section 19.2 and the sensors it deploys in Section 19.3. Following this, their relative impact on the entire mission will be discussed in Section 19.4. However, first, the general overview of the LCA will be provided in Section 19.1 below.

19.1. General Overview

First, the goal of the studies is explained in Subsection 19.1.1, followed by the scope of the studies discussed in Subsection 19.1.2. Next, the resources used and to be used in the studies are elaborated on in Subsection 19.1.3 and, finally, some general assumptions are mentioned in Subsection 19.1.4.

19.1.1. Goal

The goal of the life-cycle assessment studies, and the assessment of the impact of the mission in general, will be discussed in this section. Initially, with some preliminary investigations performed as part of this paper, one of the main goals is to identify the areas which require a proper LCA as well as the level of detail this LCA should go into. Throughout the whole process of impact assessment, the main goal is to inform the team about areas where design changes make the biggest impact on environmental sustainability, to maximise the efficient allocation of resources. Finally, the goal of the LCA will be to quantify the impact caused by each of the subsystems involved in the EcoSense mission, as well as the mission in total.

19.1.2. Scope

The scope determines which parts of the mission will be considered in the analysis, what phases of their life shall be considered, and how deeply all of this shall be done. It would be possible to spend months analysing the exact environmental impact of the EcoSense system, however, there is an opportunity cost to doing this, as the resources dedicated to this analysis could have instead been used to, for example, improve the design to lower the impact based on a simpler LCA study. This being a preliminary design report, the scope of the LCA will be limited, however, recommendations will be made along with some preparatory tasks for more detailed LCA studies in the further stages of the project.

The parts of the system examined shall include the airship deployment vehicle and the sensors being deployed, along with their operations. There is one more thing being deployed during the mission, and that is the relay station. However, only about 0.7 percent of the devices deployed are relay stations and the relay station is at least 80 percent the same as the sensor, with the only difference being fewer electronics. Therefore, it will be assumed in the analysis that these relays have the same impact as the sensors. The impact of this assumption should be less than 0.14%, given the similarity and the deployment density of the relays. Furthermore, this small difference would only impact the assessment positively, so by making this assumption, the analysis is assuming the worst case. Furthermore, the resources spent in the development phase of the mission will not be considered. Although there is some impact caused by the prototypes and samples produced during the development and for testing, it is expected these impacts are negligible in comparison to the other mission components.

To further evaluate the required relative depth of exploration for each of the components, let us look at the mission and make some assumptions about the impact of each component. The mission, described in detail in Chapter 16, entails a vehicle deploying an average of 841 sensors over an $100\,\mathrm{km}^2$ area. This average mission would have to be conducted in two flights. The sensors will then be left in the deployment area to report throughout their functional lifespan. After this, their casings biodegrade while the electronics remain in the deployment area. The deployment vehicle, on the other hand, shall be reused for further missions. In total, over its lifespan, the vehicle is expected to deploy 1,100,000 sensors. Rounding the weight of these sensors to $80\,\mathrm{g}$, this results in a total of $88000\,\mathrm{kg}$ of sensors being deployed by a single deployment vehicle, which itself weighs below $150\,\mathrm{kg}$, or over 585 times less than the mass of sensors it deploys. Considering that there is at least somewhat of a relation between the mass of a product and its environmental impact, and considering that the sensor and the airship are not that different in the grand scheme of things, both containing off the shelf electronic components and parts that require industrial manufacturing methods and more, it is reasonable to say that the impact of the sensor is significantly more important than that of the deployment vehicle. This calls for the LCA of the sensor to be more detailed than that of the airship. However, the airship shall not be forgotten in the analysis, as several of these airship systems are expected to be produced. This means that although the impact of the airship is small in relation to the sensors, it can still add up to a significant overall impact. Furthermore, the assumption based on the mass fraction presented above needs to be verified and validated, and one way of doing this is by performing the LCA of the deployment vehicle.

The airship LCA shall therefore be made, at least to a screening degree of detail in further research. Within the scope of this paper, preparatory steps for this will be taken, mapping all the flows and processes needed to complete the life-cycle of the airship, from cradle to grave, with the use phase elaborated even further. This will be further discussed in the section dedicated to the airship, Section 19.2. For the sensors, a detailed LCA shall be conducted at a later stage of the development, since a small change will quickly accumulate with the number of sensors to be produced. Within the scope of this research, a screening LCA of the sensor shall be conducted, shown in Section 19.3. Finally, the impact of the mission will be estimated solely based on the impact of the sensors within the scope of this report. When an LCA of the deployment vehicle becomes available, this shall be incorporated too.

19.1.3. Resources

The LCA studies shall be performed in the OpenLCA software, one of the industry-standard LCA software, which is also open source. The main source of the data will be the EcoInvent database, supplemented by other available databases. In further parts of the developments, more attempts shall be made to acquire data directly from manufacturers. Gaps in the data may be filled by using equivalent materials, however, this shall be limited and replaced by data sourced from literature or manufacturers in further development. The impact shall be modelled using ReCiPe impact assessment methods.

19.1.4. Assumptions

The assumptions will be more concretely discussed in the respective relevant sections, however, one general assumption can be discussed already. For the purposes of all the assessments within this report, all the electronics will be considered the same, and equivalent to a populated phone motherboard of the same mass, or similar. This is done since electronics themselves are immensely complex systems, and analysing them in any more detail would require an excessive amount of resources. Attempts at locating the impacts for the exact parts used proved to be futile, however, more specific equivalents from literature, or from manufacturer-provided data shall be located at least for the electronics in the sensor in further development efforts, since these will likely be the parts with the biggest impact in the sensor.

19.2. Airship LCA

The airship is the biggest single component of the EcoSense mission, but, as discussed, it is most likely not the part with the biggest effect on the impact of the EcoSense mission. Still, an LCA shall be performed as part of future development efforts past the scope of this paper, to achieve the aforementioned goal of improving the design and decreasing its impact, though small in comparison to the sensor. Furthermore, the impact assessment is necessary to prove the assumed notion that the impact of the sensors is of a much higher magnitude. Within the scope of this paper, preparatory measures and some first investigations will be performed, per life-cycle phase. The functional unit of the eventual LCA shall be a unit of the blimp. First, a preliminary breakdown of all the flows and processes used in the manufacturing, use, and end-of-life phases is provided below in Figure 19.1.

19.2.1. Manufacturing Phase

The first considered phase of the airship LCA is the manufacturing phase. Since the airship is a complicated system, using at times quite exotic materials, it is expected that this phase will take up a significant fraction of the resources required to perform the airship LCA. Therefore, this is the phase covered with the most detail in the breakdown seen in Figure 19.1, to provide a head-start for this undertaking. The lower boundary was placed at part level if it was clear the data for this part could be located from literature or the available databases. Otherwise, the lower boundary was put on some, usually pre-processed, materials. Further, some assumptions, simplifications, and substitutions will be discussed.

The transport is one area where simplifications are expected to be made. For one, for most components, transport to the assembly destination is included. Some parts may need transport in between different stages of manufacturing, but this is deemed outside the scope of the study. Furthermore, transport shall not be accounted for at all for materials such as fasteners, solder, adhesive PU film, PLA filament, wiring or steel wire, since it is expected that these will be sourced locally, at relatively low masses and additionally, their origins may not be known. The impact of their transport is therefore also deemed past the scope of this study unless it is found that a significant mass of these materials is required in the assembly, in which case this decision shall be reconsidered.

In relation to the soldering, it is expected that small soldering jobs, requiring minute amounts of solder and soldering, will be required throughout the assembly of the system. These are also deemed outside the scope of

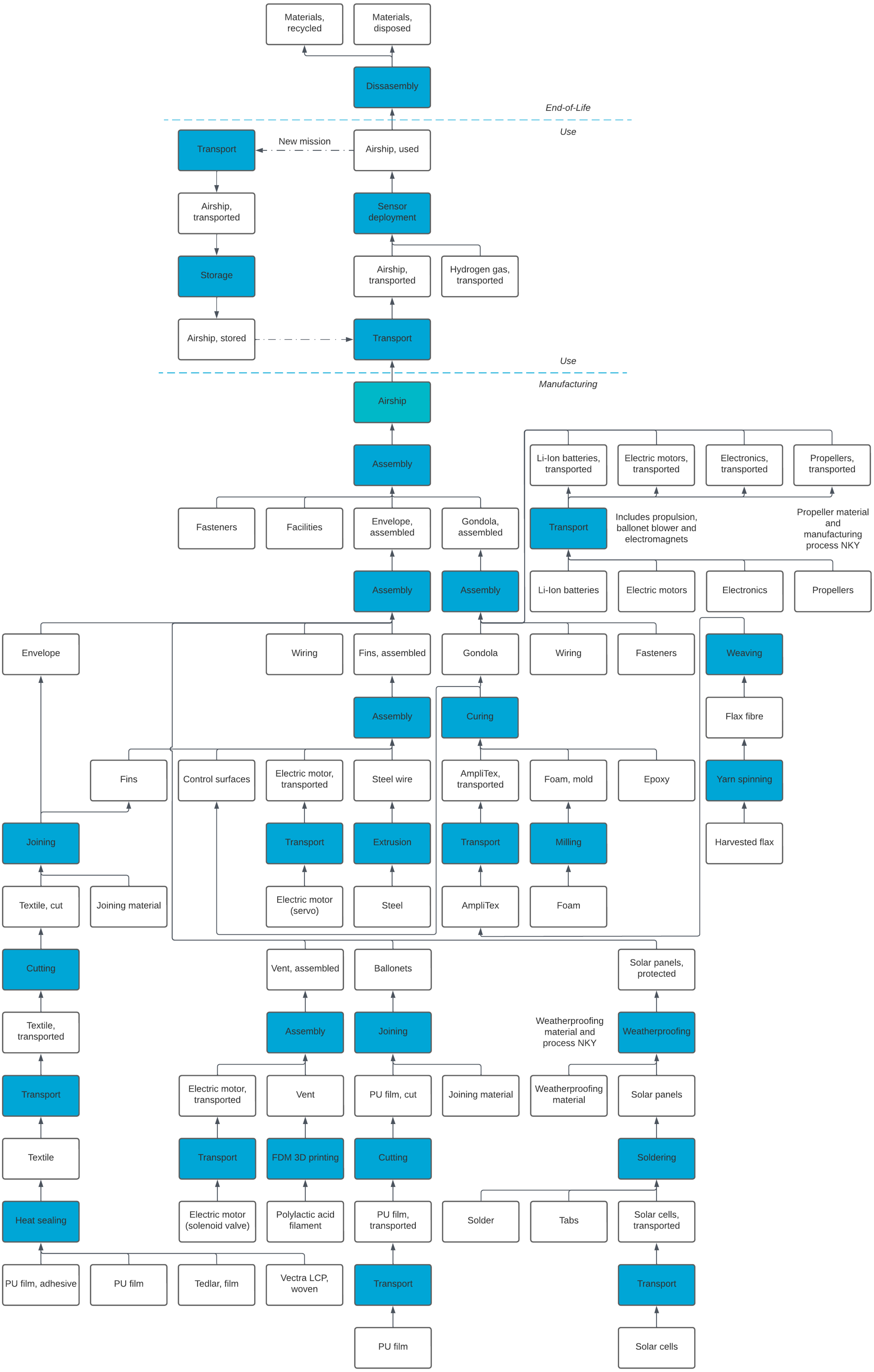

Figure 19.1: *Breakdown of the airship life-cycle*

the study. For processes where a lot of soldering is required, such as the creation of the solar panels, where hundreds of connections will be made, the soldering is still considered.

There are some processes that are already identified but not yet known. These include the weatherproofing process and material and the propeller production process and material, both of which are included in the breakdown in Figure 19.1 with the note that they are not known yet (NKY).

While the handling of the electronics was already explained in Subsection 19.1.4, some electronic components were deemed too different from the proposed substitute. Namely, these include the electric motors, servos, blower for buoyancy control, solenoid valves, and electromagnets. For these components, a separate substitute will be selected from the database, as exact flows for them are also not available. Given that all of these components work on the same principle of magnets, coils, and induction, they will all be assumed to be equivalent to an electric motor of the same mass. This assumption should hold, since from a material composition and manufacturing process perspective, these components should be very similar.

Furthermore, all the assembly processes are performed in the EcoSense facility. Therefore, all of them could actually be summed into one process, but they are kept separate for better readability. Therefore, these processes will not add any impact and will simply aggregate parts into meaningful sub-assemblies. To consider the impact of operating the assembly facilities, a separate flow shall be created, and added to the final assembly process as an additional input. The impact for this facilities flow, as well as the storage process, will be sourced from literature, for an industrial building in the target or equivalent area, with the required space, being operated for the required time to assemble or store the blimp respectively.

19.2.2. Use Phase

The blimp might not require any fuel for its flight, since it is powered purely by solar energy, it requires hydrogen due to the way the buoyancy control system works, described in Chapter 9, as well as requiring to be fully deflated every night, i.e. after each flight, to ensure safe storage. It is expected that the blimp will be used to distribute a total of 1,100,000 sensors. With the carrying capacity of $45\,\mathrm{kg}$, distributing this many sensors will require at least 1,956 flights. Since the airship needs to be fully deflated after each flight, each flight consumes a total of $145.57\,\mathrm{m}^3$ or about $12.2\,\mathrm{kg}$[147] of hydrogen gas at NTP, which is vented to the atmosphere during deflation. In total then, during the lifespan of a single airship, up to $284734.92\,\mathrm{m}^3$ or about $23847\,\mathrm{kg}$ of hydrogen gas will be used, about enough to fill 9.5 Olympic pools with [148]. This is once again vastly eclipsing the mass of the blimp itself and although these masses are not of comparable products, it is clear that this aspect of the blimp needs to be examined closely. While the release of the hydrogen into the atmosphere has no impact in itself [149], the production and transport of the hydrogen gas do have an impact and will be investigated in a separate section in Section 19.5 below. From this study, it was found that using the best hydrogen generation source, being wind energy, about $970\,\mathrm{g}$ of CO_2 equivalent emissions are produced per kilogram of hydrogen gas used. This means that during the lifespan of the blimp, up to $23132\,\mathrm{kg}$ of CO_2 equivalent emissions will be released just due to the use of hydrogen lifting gas. This is equivalent to about five years of operation of an average gas-powered car [150]. From this, it is already clear that the use of hydrogen will be a major contributor to the overall impact of the airship deployment vehicle.

Further activities which shall be included in the use phase assessment of the vehicle include its transport between launch sites and the impact of its storage, as seen in Figure 19.1. What is not seen in the use phase diagram, is the maintenance of the airship. This will also have an impact, as new parts will likely need to be produced, however, it is expected that this impact will be relatively negligible in comparison to the manufacturing of the blimp itself. Therefore, it was decided it shall not be included in the study.

19.2.3. End-of-Life Phase

The last phase in the life cycle of the airship is its end of life. This phase may have significant impacts, however, it is the phase that requires the deepest knowledge of the detailed design of the vehicle. This is because, in this preliminary design stage, it is not yet known exactly what parts of which materials will be able to be recycled, and which will need to be simply disposed of. Efforts are, however, being made, to ensure that the mixing of materials is minimised with recyclable materials used where possible. This is to ensure the maintainability and recyclability of the airship. Since this is the case, the end-of-life phase still requires the most work in the breakdown in Figure 19.1 as well as in the eventual LCA itself.

19.2.4. Recommendations

Even though the LCA has not been performed yet, some findings can already be presented, which align with the goal of the study expressed in Subsection 19.1.1 and decreasing the impact of the blimp. By examining the use phase, it was clearly found that the hydrogen use of the airship will constitute a significant part of the impact of the vehicle. Therefore, strategies should already be made to start decreasing this impact. A relatively easy one, affecting only the operations of the blimp, would be to compress the circa two-thirds of hydrogen, which still remain in the blimp at the end of the flight, back to a storage canister to be reused, instead of venting it to the atmosphere. If this could be done effectively, it could reduce the hydrogen use by up to two-thirds. Furthermore, since the impact of the use of hydrogen is somewhat higher than initially thought, the buoyancy control system could be reconsidered to use an option that does not involve the venting of hydrogen. Combining these two measures, the emission of hydrogen could be almost completely eliminated.

Furthermore, it is clear that due diligence needs to be put on the ability to disassemble the blimp, to ensure a sustainable end of life. Research will also need to be made to identify all the materials used in the blimp which could be recycled, and all the processes by which this can be done. In addition to ensuring a higher recyclability, it will also allow the team to estimate the costs associated with a sustainable end of life, and include this in the budget for the mission.

19.3. Sensor LCA

While the majority of this report is dedicated to the design of the airship deployment vehicle, in the life-cycle assessment it is expected that the effect of the sensors on the impact of the mission will be far greater than that of the vehicle, due to the sheer number of sensors to be deployed. This makes the careful assessment of the life-cycle of the sensors even more pertinent.

19.3.1. Manufacturing Phase

The manufacturing phase of the sensor nodes plays an essential role in its LCA, as manufacturing will be done in large batches. For the scope of this phase of the LCA, several substitutions with ecological equivalent materials and processes are done according to the data available in the EcoInvent database. The manufacturing of the sensor nodes is analysed as follows: Firstly, as discussed in the manufacturing plan in Chapter 15, the top and bottom parts of the enclosure will be manufactured from cellulose acetate using injection moulding. This material is substituted with PLA. This material behaves differently in terms of biodegradability but can be produced the same way. Concerning the inside of the sensor node, the lyocell string is analysed with a substitution of cotton wire manufactured by spinning, weaving, and finishing raw cotton. The steel plate where the deployment magnet is attached and the anchor hook is considered to be laser-cut from a steel sheet, and the spring mechanism is assumed to be extruded from a thin steel rod. For the scope of this assessment, electronics will be considered as a whole, taken from the EcoInvent database. Said components are then fitted into the sensor node enclosing and glued together forming the final product which is then transported to the customer.

Transportation of products is also included in the assessment, all components are assumed to ship by cargo boat from Shanghai, the main export hub for all of these products except for the raw cotton which is widely produced in the NSW area, which will be transported by truck from Port Kembla, around 100 km away from the EcoSense HQ.

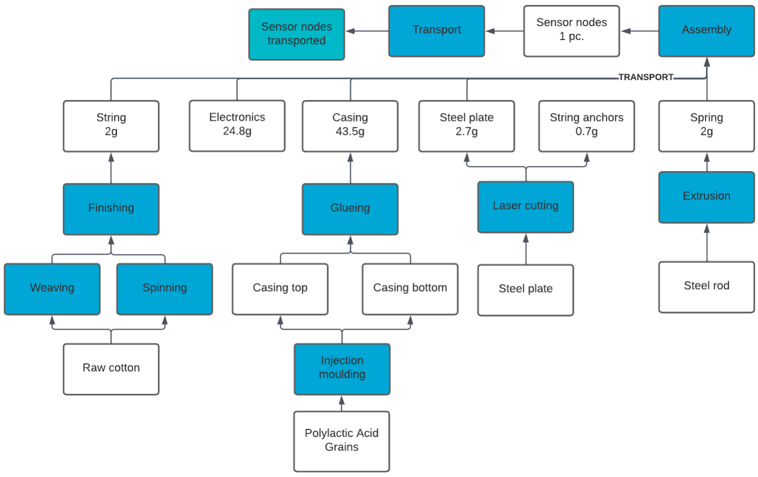

Figure 19.2: *Flow chart of sensor node LCA for the manufacturing phase of a single product.*

For the scope of this design, only CO_2 equivalency is analysed. Yet, in the post-DSE phase, a full LCA will be performed using the exact same method as described throughout the chapter. The CO_2 equivalent emissions for the manufacturing phase are computed per $100km^2$ coverage, which translates to a total of 846 sensors. From table 19.1 and figure 19.3, the main CO_2 equivalent emissions come from manufacturing of the casing. Manufacturing of the string is negligible, and electronics will be analysed in depth in further stages.

Table 19.1: *CO_2 equivalent emissions for the manufacturing phase of the sensor node per $100km^2$ coverage.*

Process	CO_2e emissions [g CO_2e]	Component	CO_2e emissions [g CO_2e]
Shipping	7967.0	String	8.9
		Electronincs	2680.9
		Casing	4702.3
		Steel components	583.7
Manufacturing	85083.9	Casing	66241.8
		Steel components	18842.1

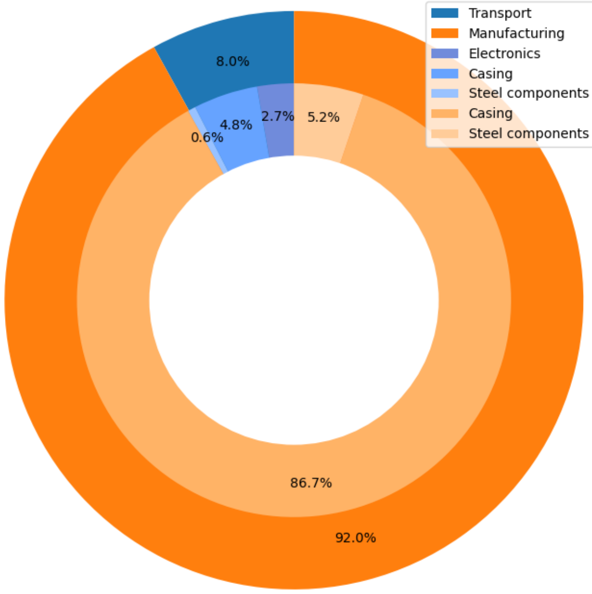

Figure 19.3: *Outer: process CO_2 e emissions. Inner: component CO_2 e emissions.*

19.3.2. Use Phase

The main difference between the assessment of the airship and a sensor, is the impact of the use phase of the sensor. The use phase of the sensor involves very little impact on the surrounding world. No further resources are spent in the operation of the sensor, except for sunlight. There is an impact caused by the operation of the ground and cloud infrastructure required to collect and analyse the data collected from the sensor, however, per sensor, it is expected that this impact will be negligibly small, and it is thus omitted from the analysis. This aspect of the mission, along with the deployment of the sensor by the airship, which one could argue shall be included in the use phase of the sensor, will be covered separately as described in Section 19.4, since this makes the evaluation simpler.

19.3.3. End-of-Life Phase

Concerning the end of life (EOL) of the sensor, the case of the sensor is an unusual one for a life-cycle analysis. The casing, which makes up the majority of the mass of the sensor, will biodegrade freely in nature. The electronic components, however, will be left in nature too, and it is not expected for these sensor remains to be collected. Therefore, no disposal method is determined for these components. For the purpose of this LCA plan, it will be assumed that these components will be disposed of in a rubbish heap, but the impact of this assumption and possible ways to better model the end of life of the sensor shall be considered more deeply in further stages of the development of the EcoSense project.

19.4. Mission LCA

With both the impacts of the airship and the sensor established, it will be possible to estimate their relative contribution to the overall impact of the mission. To do this, the path from the singular components to the LCA of the mission will be described in this section.

First, a functional unit for this LCA shall be established. A unit that makes sense is the sensor coverage of $100\,\mathrm{km}^2$ of area, as this was also the unit worked with in many parts of the design and analysis. This unit shall then include the impact of the sensors which must be used, an appropriate fraction of the blimp manufacturing, use, and EOL phases, and the infrastructure needed to support this sensor network during its lifetime. For the sensors, while up to 1089 sensors may be deployed on a $100\,\mathrm{km}^2$ square, the average number is estimated to be 841 sensors. An additional average of about 2 relay stations need to be used as well, which are considered equivalent to the sensors in this analysis, resulting in a sum of 843 sensors. With the number of sensors to be deployed by the blimp over its lifetime, 0.076 percent of the overall impact of the life of the airship needs to be accounted for in covering this $100\,\mathrm{km}^2$ area.

Additionally, the infrastructure required to manage the collected data from the sensors needs to be considered. For every mission, a high-performance (due to the high up-time requirements) server needs to be run for the duration of the sensor's lifespan, which is five years. The pilot mission in New South Wales will contain 76 tiles of the $100\,\mathrm{km}^2$ size, and it is assumed that this is an average mission. Taking all of this into account, to account for the sensor infrastructure, the impact of 1/76th of a high-performance server running for five years must be considered per functional unit of $100\,\mathrm{km}^2$ covered. The server can be further sized using the estimated data collected from the sensors, once the exact way of data handling, storage, and compression is known. The impact of this server shall be estimated from literature, running on a power mix relevant to the area of the mission.

Together, this shall enable the estimation of the impact of the entire mission, and once again, allow the team to identify the critical areas for improvement, reflecting the goals described in Subsection 19.1.1.

19.5. Hydrogen Production LCA

The objectives of this study are to conduct a comprehensive LCA for conventional production methods of green hydrogen by including all the major steps for photovoltaic electrolysis and wind electrolysis, comparing the energy consumption, and CO_2 equivalent emissions to examine the impact on the environment [151]. The system boundaries for the hydrogen production LCA study cover the following major processes: Infrastructure for fuel production, feedstock production and transport, fuel production and distribution, vehicle body and fuel cell production, vehicle use, vehicle disposal, and recycling.

The results of the life cycle assessment on both green hydrogen processes are shown in table 19.2 and graphically represented in figures 19.4 and 19.5 for wind and photovoltaic electrolysis respectively. From this analysis, the conclusion can be drawn that most energy goes into the manufacturing and maintaining of wind turbines and solar panels. To put this in perspective, according to the life cycle analysis done by Cetinkaya et al. [151], the total CO_2 equivalent emissions of grey and brown hydrogen are over 11000 g CO_2/kg H_2.

Table 19.2: *LCA of two different green hydrogen processes [151].*

Wind power plant energy equivalents and carbon dioxide equivalent emissions.			Photovoltaic power plant energy equivalents and carbon dioxide equivalent emissions.		
Processes	**Energy equivalent [kJ/kg H_2]**	**CO2 equivalent emissions [g CO_2e/kg H_2]**	**Processes**	**Energy equivalent [kJ/kg H_2]**	**CO_2 equivalent emissions [g CO_2e/kg H_2]**
Manufacturing and operation of turbines	6606.60	757.00	Materials and manufacturing of PV modules	25550.48	1519.53
Electrolysis	436.80	43.00	Transportation	602.53	461.36
Hydrogen compression and storage	2875.60	170.00	Inverters	830.91	110.93
			Wiring	602.41	60.24
			Installation	2679.68	37.18
			Operation and maintenance	2285.00	161.20
			Decommissioning and disposal	893.23	61.70
Total	*9919.00*	*970.00*	*Total*	*33444.24*	*2412.13*

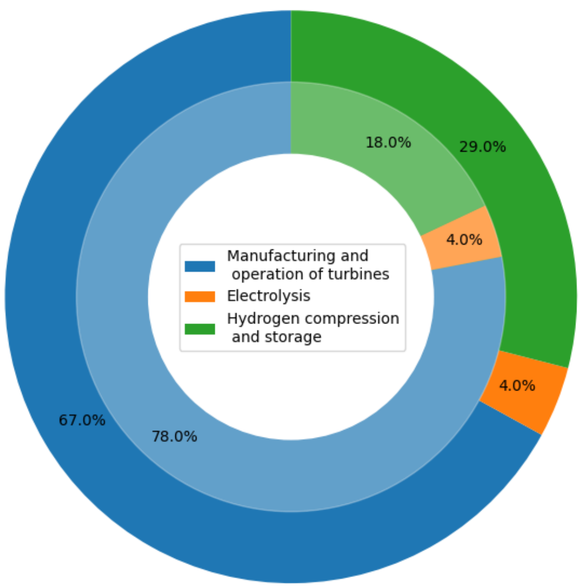

Figure 19.4: *Outer: Energy equivalent, Inner: CO_2 equivalent for wind electrolysis*

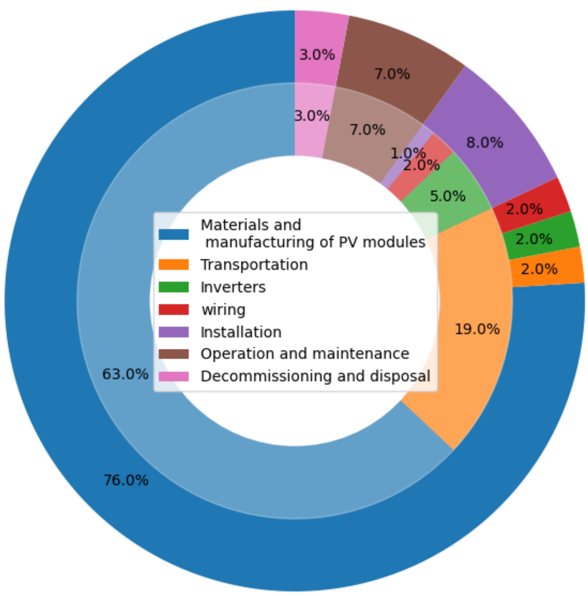

Figure 19.5: *Outer: Energy equivalent, Inner: CO_2 equivalent for photovoltaic electrolysis*

20

Market Analysis

The Market Analysis is one of the most important parts of the development of a product, as no matter how well-designed it is, a product that does not fit a clear market segment will not be successful. Hence, it is important to understand what market segment EcoSense EMBER will be aiming at. This takes the form of an opportunity cost estimation in Section 20.1. Then, the total cost breakdown of the product needs to be established, which is done in Section 20.2. Once those values are known, a business model is drawn up in Section 20.3 and the product's characteristics are compared to competitors and available market solutions in Section 20.4.

Table 20.1: *Market Requirements.*

Req. ID	Requirement	Section	Compl.
REQ-CG-9	The EcoSense system shall cost less than EUR $450\ /\mathrm{yr}/\mathrm{km}^2$ to operate	20.2	✓

20.1. Forest Fire Loss Estimation in Australia

An important step in assessing the current market conditions and the potential share the EcoSense EMBER could achieve, one should look at the losses incurred by bushfires in Australia - as that is the intended initial market, as will be further explained in Section 20.3.

In the years from 2011 to 2016 $41\ \%$ of the Australian forested area burned at least once. In total, an area equivalent to $79\ \%$ of the Australian forested area was burned during that period, accounting for some forests having burnt more than once [152]. This amounts to $106\ \mathrm{Mha}$ (or more than 25 times the size of the Netherlands) of burnt forests in $5\ \mathrm{yrs}$. Given a $5\ \mathrm{yrs}$ mission length and the future underestimation of this number due to climate change [153], this estimate was deemed conservative and applicable to this calculation.

The next step is to determine how much a typical forest fire costs to governments and inhabitants of the affected regions. According to research performed by the Australian National University following the disastrous 2019-2020 bushfires in Australia, forest fires between 2009 and 2019 have cost on average EUR $1\mathrm{b}$ per year [154]. According to the research, this estimate is deemed conservative as it bases the results on the insured costs, when undisclosed costs have very often been a lot higher. Based on an empirically developed cost model [154], Australian forest fires between 2020 and 2049 are estimated to have a reported cost of EUR $0.8\mathrm{b}$ per year, whereas the undisclosed costs could reach more than EUR $1.4\mathrm{b}$ per year. This confirms the conservative nature of the EUR $1\mathrm{b}$ estimate of past years, which will be used for consistency reasons with the burnt area. IQ Firewatch [10], estimates that around EUR $500.000\ /\mathrm{km}^2$ could be saved using ultra-early detection of forest fire. Given the lack of proof for that number, it wasn't used, although it comforts the underestimation that was done here.

Using both of the above-mentioned estimates, one could estimate the costs of forest fires to be at EUR $4700\ /\mathrm{km}^2$. Given a reliability of $62\ \%$ achieved by the EcoSense EMBER product, one can estimate that the EcoSense EMBER sensor network could help prevent around EUR $2900\ /\mathrm{km}^2$ per fire cycle. Although early detection of the fires won't prevent $100\ \%$ of the forest fire economic burden, this is assumed given the conservativeness of previous estimates. This is again a conservative estimate given this reliability applies to fires detected under $10\ \mathrm{min}$, when $90\ \%$ of fires under $0.2\ \mathrm{km}^2$ will be detected, but fires this size could already lead to large losses and costs. For a tile of $100\ \mathrm{km}^2$ and given a mission length of $5\ \mathrm{yrs}$ (a typical Australian fire cycle length of $3\ \mathrm{yrs}$ [155], adding $2\ \mathrm{yrs}$ for the impact of the sensor network), this leads to an estimate of EUR $290\ \mathrm{k}$ that could be saved using EcoSense EMBER (or EUR $580\ \mathrm{yr}/\mathrm{km}^2$).

20.2. Product Cost Estimation

Now that an opportunity cost has been established for Australian forest fires, one should determine the cost of the actual product, to position it competitively in the market while generating value for both its users and creators. This will be split into multiple components being the sensor network in Table 20.2, the vehicle in Table 20.3, the deployment costs in Table 20.4, the recurring costs in Table 20.5 and the miscellaneous costs in Table 20.6. Throughout this section, a "typical mission" is defined as a mission $100\ \mathrm{km}$ away from the ground station, with the densest possible sensor network (being 1089 sensors and 7 relays) deployed in two trips, that will last for $5\ \mathrm{yrs}$. It is also assumed that the deployment vehicle will have a lifespan of 1000 cycles (or 500 missions).

Table 20.2: *Sensor Network Cost Estimation*

Component	Contribution (EUR)	Reasoning
Sensor Hardware	49,549.5	1089 Sensors @ EUR 45.5 each
Relay Hardware	224.21	7 Relays @ EUR 32.03 each
Sensor Manufacturing	2,950	Injection Moulding Estimation [156]
Relay Manufacturing	196	Injection Moulding Estimation [156]
Ground Station	550	Not designed yet, price was taken from competitor [157]
Total (EUR)	53,470	

Table 20.3: *Deployment Vehicle Cost Estimation*

Component	Contribution (EUR)	Reasoning
Solar Panels	6,000	Shown in Table 4.7
Hydrogen	100	Shown in Table 4.7
Electronics	7,500	Shown in Table 4.7
Engines	600	Shown in Table 4.7
Envelope	5,000	Shown in Table 4.7
Deployment System	7,000	Shown in Table 4.7
Fins	700	Shown in Table 4.7
Gondola	5,000	Shown in Table 4.7
Ballonets	500	Shown in Table 4.7
Battery	800	Shown in Table 4.7
Manufacturing	10,000	Assumed 5 mechanics working for 40 hrs over a week [158]
Total - One Blimp (EUR)	43,200	
Total - One Mission (EUR)	87	

Table 20.4: *Deployment Operations Cost Estimation*

Component	Contribution (EUR)	Reasoning
Certified Drone Pilot	5,400	3 days for 10 hours @ EUR 180/h [159]
Airport Technician	1,200	3 days for 10 hours @ EUR 40/h
National Park Flying Permit	4,000	2 day commercial flying permit [160]
Motorhomes	2,500	Two 3-bed motorhomes rented for 2 nights
Life Expenses	800	Living expenses for the crew
Ford Ranger Rental & Fuel	1,500	Rented for 3 days
Total (EUR)	15,400	

Table 20.5: *Recurring Costs Estimation*

Component	Contribution (EUR)	Explanation
Software Engineer	31,250	Based on an EUR 50k yearly salary & estimating a single engineer allocates 1 h per day to a mission (1 engineer = 8 missions)
Server Costs	20,000	One high performance server per mission [144]
Maintenance	500	Explained in Chapter 18
Total (EUR)	51,750	

Table 20.6: *Miscellaneous Costs Estimation*

Component	Contribution (EUR)	Reasoning
Hydrogen Delivery	40	Worst case cost for $10\,\mathrm{kg}$ of H_2 [161]
Freight Shipping	33.75	From Manufacturing Locations to Warehouse (See Below)
Energy Costs	60	(See Below)
Office Rental	3,750	Section 16.1
Team Salaries	31,250	Assuming 5 team members at the Minimum Australian Salary of EUR $2500\,/\mathrm{month}$
Total (EUR)	35,134	

Given their ambiguity, estimates in Table 20.6 are explained in more detail:

- **Freight Shipping:** From Chapter 16, it is assumed that all manufacturing will be done in Australia. As such, given an EUR $3\,/\mathrm{ton}/\mathrm{km}$ rail freight cost in Australia in 2015 [162], and a maximum trip of $4500\,\mathrm{km}$ (railroad between Sydney and Perth), this leads to a freight cost of EUR $135\,/\mathrm{ton}$. At a total package estimate of $250\,\mathrm{kg}$, this leads to a total mission freight cost of EUR 33.75.
- **Energy Costs:** This estimate was done thanks to a total energy consumption estimate of $500\,\mathrm{kWh}$. This results, at EUR $0.12\,/\mathrm{kWh}$ [163], in an energy cost of EUR 60 per mission.

Taking all those costs into account leads to a total mission estimate of EUR $156\mathrm{k}$. An overview of the different components and their share in the final cost can be found in Figure 20.1.

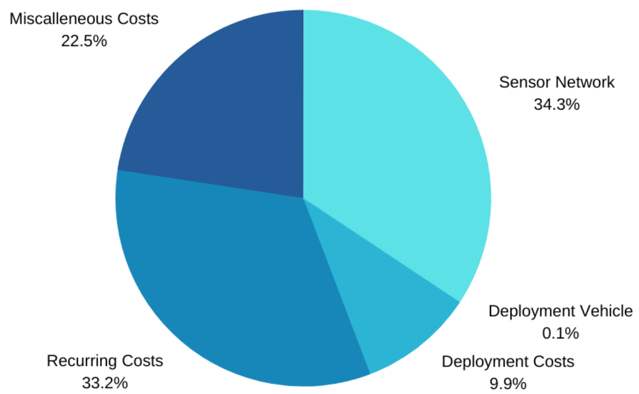

Figure 20.1: *EcoSense EMBER Mission Cost.*

However, the EcoSense EMBER design is not fully developed at this phase, and extra R&D costs will have to be incurred in order to finalise the design. Testing, certifications and potential hiccups should also be taken into account during both the design and testing phases. Hence, it is estimated that the work done in this report will have to be performed for at least an extra $2\,\mathrm{yrs}$. This would add another EUR $2\,\mathrm{M}$ R&D costs before pushing the product to the market, at the current junior aerospace engineer salary of EUR $100\,\mathrm{k}/\mathrm{yr}$.

20.3. Business Model

Given the results of both Section 20.2 and Section 20.1, it becomes apparent that there is a possibility EcoSense EMBER becomes considerably profitable. This is because the fire prevention market is not yet developed, despite the increasing occurrence and severity of wildfires brought on by climate change. The business model, as was briefly mentioned in Section 20.2, will that of a one-time purchase, covering the provision of the entire service. The customer (in this case Rob Rogers) will be buying a specified amount of coverage area in a given location and the EcoSense team will take charge of the manufacturing, shipping and deployment for a one-off fee. This is chosen over a subscription model, as it could be the case that the sensor network could operate more than $5\,\mathrm{yrs}$ without failing or burning down in a fire. However, given some materials are biodegradable, a very high retention and renewal rate is to be expected.

Looking at REQ-CG-9, the EcoSense EMBER could be sold at EUR $450\,/\mathrm{km}^2/\mathrm{yr}$, or EUR $225\,\mathrm{k}$ per mission. With a product cost of EUR $156\,\mathrm{k}$ and an opportunity cost of EUR $290\,\mathrm{k}$, this would end up being both competitive (as will be seen in more detail in Section 20.4) and profitable for the Australian firefighters. One should also keep in mind this is the worst case product cost and conservative opportunity cost. For the EcoSense team, this leads to a $7.7\,\%$ profit margin, assuming a $25\,\%$ corporate tax for startups in Australia. The exact sale price of the service has to be determined by means of an extensive market analysis and customer surveys. One should also note that the cost that was estimated in Section 20.2 is a worst-case scenario. In the case of a larger contract (consisting of more than one tile), relay corridors won't be necessary and one-off or large costs will be smoothed out over the multiple flights, leading to a bigger margin.

Assuming the equivalent of two missions can be launched every month (most likely in the form of a single contract consisting of multiple $100\,\mathrm{km}^2$ tiles), EcoSense EMBER is expected to generate around EUR $52\,\mathrm{k}$ of profit every year, allowing it to develop and improve the product itself. It was also decided amongst the team that $25\,\%$ of all profits would be donated to local NGOs centred around wildlife protection and firefighter associations. As for any startup and new business idea, the goal is to first launch the product in New South Wales only, before then launching throughout Australia and eventually, given the product is profitable enough and the number of clients keeps on growing, worldwide. It is hoped that at least $30\,\%$ of New South Wales endangered remote forests will be protected within the first five years of operations.

One should also note that at each expansion phase, the product will have to be adapted to its intended environment. Finally, it is also important to understand that the EcoSense EMBER deployment system is fully adaptable as long as sensors are redesigned. One could for example design forest monitoring sensors to monitor a forest's health on top of detecting fires - a lot more options are available, given the high adaptability of such a deployment and sensor system.

20.4. Market Competitiveness

EcoSense EMBER serves a very specific and unique market segment, mainly the one of remote ultra-early fire detection. As of today, solutions for the current fire detection problems are shown in Table 20.7, an updated overview of the market competition done during the first quarter of the DSE [2]. The update was done thanks to a Dryad customer pitch [157], leading to a more accurate EUR $450\,\mathrm{km}^2/\mathrm{yr}$ cost for environmental sensors (also resulting in REQ-CG-9).

Table 20.7: *Overview of market solution analysis [2].*

Detection Method	Environmental Sensors	Radiation Sensors	Aircraft Inspection	Satellites	EcoSense EMBER
Cost [EUR/km2/yr]	450	12	7.2	46-115	450
Detection Time [min]	4	10	480	31	10
Fire Size [km2]	0.2	0.004	0.005	0.2	0.002
Accuracy [%]	92	95	93	62	62-90
Applicability	medium-high	low	medium-high	medium	high
Sustainability	medium-high	high	low	medium	high

From Table 20.7, EcoSense EMBER does not outperform its competitors if it is assessed one aspect at a time. However, all aspects should be taken into account. In fact, EcoSense EMBER is certainly more expensive than radiation sensors, satellites or aircraft inspections. However, its sustainability, passivity, detection time and detection time are great advantages that have to be taken into account when looking at overall competitiveness. With this in mind, EcoSense EMBER is as expensive as the current environmental sensors, while achieving far better applicability and automation when it comes to deployment. It is also more precise and faster than both satellite and aircraft sensors, its main competitor for large scale areas. As such, EcoSense EMBER takes the best of all worlds as it keeps high precision and timing while being usable in large scale remote locations.

21

Beyond the DSE

A lot of research, design, testing and experiments have to be conducted before reaching a commercial product. In this chapter, the steps needed to be taken after the DSE are planned ahead. Section 21.1 shows an overview of the project design & development logic diagram, presenting the steps, whereas Section 21.2 shows the timeline of these steps in a Gantt chart.

21.1. Project Design & Development Logic

The project design & development logic is shown in the diagram below Figure 21.1, expressed in the steps needed to be taken after the DSE. It starts off with the results obtained during the DSE, and ends with the sale and "end-of-life" of the product. Having an estimated outlook of future steps could prove useful if the design were to be worked on further.

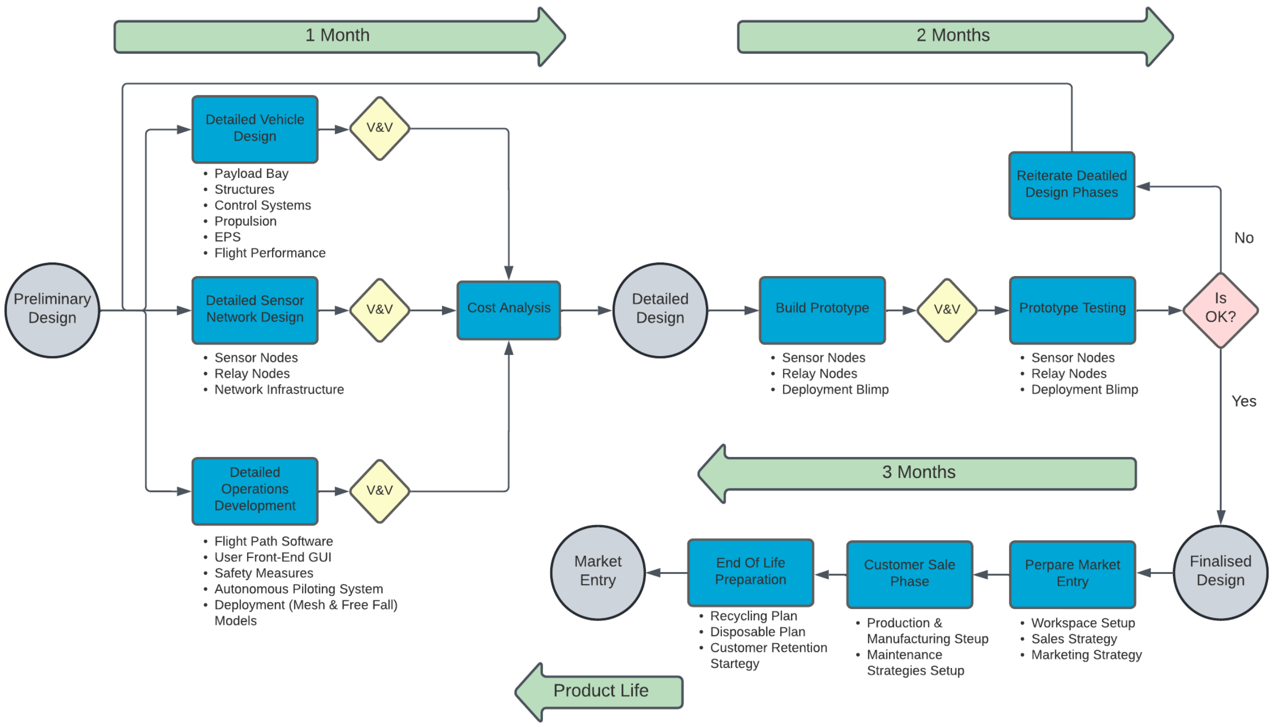

Figure 21.1: *EcoSense EMBER project design & development logic.*

21.2. Post-DSE Gantt Chart

Following the project design & development logic diagram developed in Section 21.1, one can take the same blocks and functions to be performed and lay them out over a timeline in a Gantt chart presented in Figure A.1.

22 Conclusion & Recommendations

With the ever-increasing rate of forest fires, EcoSense EMBER fills the void in early fire detection in hard-to-reach fire-prone areas. Large satellites have low accuracy, and monitoring airplanes have limited operational time and long fire detection time. These fire detection systems are not optimal for the job and need to be improved. EcoSense Ember consists of a sensor network deployed by an airship. Once the sensor network is operational, fire can be detected before actual flames arise, reducing the time to detect a fire and thus the impact of bushfires. The initial mission area is set to be in the national parks located North-west of Sydney.

The airship is $14\,\mathrm{m}$ long and $4.5\,\mathrm{m}$ wide, with a volume of $146\,\mathrm{m}^3$ of hydrogen as a lifting gas. A total of 550 sensors can be carried, weighing approximately $45\,\mathrm{kg}$. Each operational day, the vehicle can travel $350\,\mathrm{km}$ at a speed of $50\,\mathrm{km/h}$ such that the vehicle flies for 5 hours. The vehicle is propelled by 4 propellers, which require $2.2\,\mathrm{kW}$ of power. To power up the whole vehicle, $35\,\mathrm{m}^2$ of solar panels are installed on the envelope. The vehicle comes at a price per unit of EUR 33,200.

In order to be transported, the vehicle structure needs to be designed. For the airship, the most important structures are the gondola, the envelope, and its connection. The gondola contains all the systems required to operate the airship and the payload deployment mechanism with the sensors. The structure of the gondola consists of an aerodynamic outer shell, to which a roster is fixed. All the sensors are connected to the vehicle by permanent electromagnets. On the gondola, the four propellers are attached. The propellers are designed such that both forward and upward thrust can be delivered, and a duct is installed around each propeller for safety reasons. The envelope is composed of a three-layer fabric called Uretek-3216LV, which has been applied in other airships. The envelope and gondola are bonded to each other via an adhesive.

The vehicle is controlled via fins that are installed at the back of the envelope. A four-fin configuration is opted for to have control in the six axes. Each fin is made up of an inflatable fabric with a rigid, movable control surface. For the control surface to work properly, strings are attached on both sides to prevent flutter. To control the altitude of the vehicle, a combination of venting and ballonets is used. The ballonets maintain the pressure on the envelope when hydrogen is vented to decrease lift and go down.

The sensor network operates for five years after the vehicle has deployed it. Sensor nodes contain gas sensors that measure carbon monoxide and hydrogen gas levels, an elevated presence of which can indicate a starting forest fire. Once detected, the sensor nodes send an alert via relay nodes to the ground station, where local firefighters are alerted. This early response allows preventative measures to be taken to stop the fire before it becomes too large, reducing the potential damage and destruction.

Although EcoSense EMBER focuses specifically on forest fires, the deployment vehicle is modular enough to deploy any type of sensor that the user may desire. From detecting oil spills in the Niger Delta, or dropping aid packages in humanitarian scenarios, the platform may be adapted to extend its usefulness to a variety of other applications.

EcoSense EMBER positions itself into a specific niche, creating a solution for early forest fire detection that compensates for the areas in which existing solutions lack. With rising global temperatures, the prevalence and intensity of wildfires are predicted to increase significantly, increasing the demand for a solution that can help mitigate the effects. EcoSense EMBER is an unfortunate consequence of these rising temperatures but may protect these vulnerable environments in the years to come.

Bibliography

[1] Bcomp. Products: AmpliTex.

[2] M.Xausa, J.van der Saag, H.Hennecken, C.Aristodemou, L.Naets, V.Morizon, S.Cajagi, T.Potocnik L.Uptmoor, and S. van den Abeele. Aerial Deployment of an Autonomous Remote Sensing Network: Baseline Report. 2(1), 2022.

[3] Nicholas Biddle, Colleen Bryant,Matthew Gray, Dinith Marasinghe. Measuring the Economic Impact of Early Bushfire Detection. March 2020.

[4] M.Xausa, J.van der Saag, H.Hennecken, C.Aristodemou, L.Naets, V.Morizon, S.Cajagi, T.Potocnik L.Uptmoor, and S. van den Abeele. Aerial Deployment of an Autonomous Remote Sensing Network: Midterm Report. 3(1), 2022.

[5] Aster Ferguson. Record Budget Investment to Support Emergency Services. Media Release, June 2021.

[6] Kate Hammill and Liz Tasker. Vegetation (formations and classes) of the Greater Blue Mountain World Heritage Area, 2010.

[7] NSW Department of Planning and Environment. Be Aware, Bird Breeding Season is Here. Media Release, September 2016.

[8] Patricia To, Ejemai Eboreime, and Vincent I. O. Agyapong. The Impact of Wildfires on Mental Health: A Scoping Review. *Behavioral Sciences*, 11(9), 2021. ISSN 2076-328X. doi: 10.3390/bs11090126.

[9] Sharon Bernstein. Refugees in their own country as wildfire destroys california towns. October 2020.

[10] IQ Firewatch. Early detection of wildfires to protect the environment.

[11] National Interagency Fire Center. Federal firefighting costs (suppression only), September 2017.

[12] EPA. Research Shows Health Impacts and Economic Costs of Wildland Fires, September 2017.

[13] USDA. Climate Change Likely to Alter Post-Fire Forest Restoration Patterns, June 2021.

[14] Bo Zheng, Philippe Ciais, Frederic Chevallier, Emilio Chuvieco, Yang Chen, and Hui Yang. Increasing forest fire emissions despite the decline in global burned area. *Science Advances*, 7(39):eabh2646, 2021. doi: 10.1126/sciadv.abh2646.

[15] Greg Doudrich, Guillaume Corriveau, Denis Walch, Kahina Oudjehani, and Franck Dervault. Defining environmental indicators at detail design stage as part of an ecodesign strategy. *SAE International Journal of Aerospace*, 6:727–735, 07 2013. doi: 10.4271/2013-01-2276.

[16] Philip V. Hunt. *Advanced Airship Technologies and Design Approaches*. The American Institute of Aeronautics and Astronautics, 2015. ISBN 978-1-62410-351-3.

[17] L.M. Nicolai and G. Carichner. *Fundamentals of Aircraft and Airship Design*. Number v. 2 in AIAA education series. American Institute of Aeronautics and Astronautics, 2010. ISBN 9781600868986.

[18] Yasin Uslu and Sakir Bal. Numerical prediction of wave drag of 2-d and 3-d bodies under or on a free surface. *Env. Sci*, 32:177–188, 01 2008.

[19] Craig Freudenrich. How blimps work.

[20] Kamal Kumar Biswa Ranjan. A brief review of technology and materials for aerostat application. *Asian textile*, 8(1): 1–14, 2018.

[21] Dupont. Adhesive and lamination guide. Technical report, Delaware, 2018.

[22] Honglian Zhai and Anthony Euler. Material challenges for lighter-than-air systems in high altitude applications. *AIAA*, 1(5):1–12, 2005.

[23] Taibai Shi Bing Zhao Chengjun Goa, Wujun Chen and Jianhui Hu. Investigations of the mechanical behavior of naturally weathered envelopes based on a long-term service airship. *ASCE*, 34(1):1–10, 2021.

[24] A.P. Mouritz and B.N. Cox. A mechanistic approach to the properties of stitched laminates. *Composites Part A: Applied Science and Manufacturing*, 31(1):1–27, 2000. ISSN 1359-835X. doi: https://doi.org/10.1016/S1359-835X(99)00056-1.

[25] M. Banea and L.F.M. Silva. Mechanical characterization of flexible adhesives. *Journal of Adhesion - J ADHES*, 85: 261–285, 05 2009.

[26] Manuela Battipede, P. Gili, Paolo Maggiore, and Marco Lando. Risk assessment and failure analysis for an innovative remotely-piloted airship. 09 2006. ISBN 978-1-62410-043-7. doi: 10.2514/6.2006-7716.

[27] Ansys. Granta edupac.

[28] Alexander Mijatovic. Trans-atlantic solar blimp, 11 2021.

[29] Ubs hong kong open golf airship solutions, 5 2016.

[30] Ana Lara-Nuñez, José Guerrero, and Areli Rizo-Aguilar. Effect of anthropogenic noise on the echolocation pulses of the bats molossus sinaloae and mormoops megalophylla. 13:235–243, 06 2022.

[31] Andrei et al. Evulet. Adaptive vertical take-off and landing propulsion system, U.S. Patent 20200324890 16/680479.

[32] C. Jordi, Silvain Michel, and Erich Fink. Fish-like propulsion of an airship with planar membrane dielectric elastomer actuators. *Bioinspiration biomimetics*, 5:026007, 06 2010. doi: 10.1088/1748-3182/5/2/026007.

[33] José Páscoa, Antonio Dumas, and Michele Trancossi. A novel look at the performance of the cyclorotor propulsion system for air vehicles. volume 1, pages 455–462, 11 2012. doi: 10.1115/IMECE2012-85544.

[34] Daniel Valdenegro, Austin Capunay, Daniel Gonzalez, Luis Rodolfo Garcia Carrillo, and Pablo Rangel. Improving safety: Design and development of a bladeless thruster for autonomous multicopters. pages 158–167, 06 2018. doi: 10.1109/ICUAS.2018.8453474.

[35] Aparna Ravi, Arun Dsouza, Sunil Kumar, and G Tejaswini. Development of bladeless thruster for an uav application. 2020.

[36] Sivaraman S, Saravana V, and Rajalakshmi S. An overview of bladeless drone. *IJIREEICE*, 9, 10 2021. doi: 10.17148/IJIREEICE.2021.91015.

[37] Silvain Michel, Michele Bernasconi, Alexander Bormann, Martin Zobel, and Erich Fink. Feasability studies for a bionic blimp with a fish-like propulsion systems. 09 2007. ISBN 978-1-62410-014-7. doi: 10.2514/6.2007-7703.

[38] Rijksluchtvaardienst. Transport Airship Requirements.

[39] TYTO Robotics. https://database.tytorobotics.com/tests.

[40] Moble Benedict, J. Mullins, Vikram Hrishikeshavan, and Inderjit Chopra. Development of a quad cycloidal-rotor unmanned aerial vehicle. 61, 04 2016. doi: 10.4050/JAHS.61.022005.

[41] Yuhang Wu, Yan ting Ai, Wang Ze, Tian Jing, Xiang Song, and Yingtao Chen. A novel aerodynamic noise reduction method based on improving spanwise blade shape for electric propeller aircraft. *International Journal of Aerospace Engineering*, 2019:1–10, 2019.

[42] M. Boschma, J.; McNabb. Cycloidal propulsion for uav vtol applications. 1998.

[43] T-motor. V505 KV260.

[44] Alex Morgan Stoll. Design of quiet uav propellers. Master's thesis, Stanford University, Department of Aeronautics and Astronautics, 2012.

[45] Ole Bergmann, Falk Götten, Carsten Braun, and Frank Janser. Comparison and evaluation of blade element methods against rans simulations and test data. 09 2020.

[46] Ole Bergmann, Falk Götten, Carsten Braun, and Frank Janser. Comparison and evaluation of blade element methods against rans simulations and test data. 09 2020.

[47] Jose Ignacio de Alvear Cardenas, Francesco Avallone, Yvonne Eggers, Joost Ellerbroek, Flip Hoorn, Laura Ferrer, Edzer Oosterhof, Roelof Stikker, Lorenzo Terenzi, Eirini Tsiangou, Rano Veder, Lars Velthausz, and Max van der Waals. Silentium: Silent delivery drone dse 2018, 07 2018.

[48] Sema Yilmaz, D. Erdem, and M. Kavsaoğlu. Performance of a ducted propeller designed for uav applications at zero angle of attack flight: An experimental study. *Aerospace Science and Technology*, 45, 06 2015. doi: 10.1016/j.ast.2015.06.005.

[49] Yi Li, Koichi Yonezawa, and Hao Liu. Effect of ducted multi-propeller configuration on aerodynamic performance in quadrotor drone. *Drones*, 5(3), 2021. ISSN 2504-446X. doi: 10.3390/drones5030101.

[50] Omron. Servo Selection. URL https://www.ia.omron.com/data_pdf/guide/14/servo_selection_tg_e_1_1_3-13%28further_info%29.pdf.

[51] Kristiina Oksman. High quality flax fibre composites manufactured by the resin transfer moulding process. *Journal of Reinforced Plastics and Composites*, 20(7):621–627, 2001. doi: 10.1177/073168401772678634.

[52] Chapter 10 - wind turbines. In S.L. Dixon and C.A. Hall, editors, *Fluid Mechanics and Thermodynamics of Turbomachinery (Seventh Edition)*, pages 419–485. Butterworth-Heinemann, Boston, seventh edition edition, 2014.

[53] Auterion. Skynode Auterion.

[54] Honeywell. Honeywell UAV SATCOM.

[55] UBlox. ZED-F9P module.

[56] HiTEC. HS-5805MG Mega, Metal Gear, Giant Scale Servo.

[57] KENDRION. Industrial line - PEM1213A.

[58] Juried Engineering. GL5516 LDR Resistor Light-Dependent Photoresistor Optoresistor 5516.

[59] SANYODENKI PRODUCTS. Counter Rotating Fan San Ace 40 9CRA0412P4K03.

[60] RS PRO. RS PRO Solenoid Valve, 2 port (s), NC, 24 V DC.

[61] T-MOTOR. V505 KV260, .

[62] T-MOTOR. FLAME 80A, .

[63] EURO-GAS. H2-7HYE.

[64] Reichelt. MPX 2200DP.

[65] Farnell. Tmp36gt9z.

[66] BOSCH. Air mass meter BOSCH 0281002980.

[67] NKON. Sony / Murata US18650VTC6.

[68] TINYTRONICS. LM2596 3A.

[69] BLUEPOWERSHOP. Victron SmartSolar MPPT 250/70-TR.

[70] SunPower. Maxeon gen iii solar cells.

[71] SANJAY VASHISHTHA. Differentiate between the dni, dhi and ghi?, 2012.

[72] EcoSmart. Ghi to poa, 2022.

[73] Eric Weisstein. Ellipsoid, 2022.

[74] Sighard F. Hoerner. *Fluid-Dynamic drag*. Hoerner Fluid Dynamics, 1965.

[75] AC Gawale and Rajkumar S Pant. Design, fabrication and flight testing of remotely controlled airship. In *Proceedings of National Conference on LTA Technologies, Aerial Delivery R&D Establishment, Agra, India*, 2002.

[76] J.S. Carlton. Chapter 12 - resistance and propulsion. In J.S. Carlton, editor, *Marine Propellers and Propulsion (Fourth Edition)*, pages 313–365. Butterworth-Heinemann, fourth edition edition, 2019. ISBN 978-0-08-100366-4. doi: 10.1016/B978-0-08-100366-4.00012-2.

[77] Airfoil Tools. Naca 0008.

[78] Sanyo Denki. San Ace 40 9CRA type.

[79] RS Pro. Sol Series.

[80] Kenneth L Cashdollar, Isaac A. Zlochower, Gregory M Green, Richard A Thomas, and Martin Hertzberg. Flammability of methane, propane, and hydrogen gases. *Journal of Loss Prevention in the Process Industries*, 13(3):327–340, 2000. ISSN 0950-4230. doi: https://doi.org/10.1016/S0950-4230(99)00037-6.

[81] P Fullick. *Physics Heinemann Advanced Science*. 01 1994. ISBN 9780435570781.

[82] R. C. Hibbeler, P. Schiavone, and G. Emmert. *Engineering Mechanics*. Pearson Education Limited, 14th edition edition, March 2016.

[83] *Catalogue | Holding Magnets of the Industrial Line*. Kendrion, August-Fischbach-Straße 1, Donaueschingen, . Accesed on: 02-06-2022.

[84] Alibaba. 12V DC JSP-1010K 0.5kgs small holding electromagnet, opposite electromagnet permanent electromagnet, . Accessed on: 03/06/2022.

[85] *Technical Definitions | Electromagnets Actuators*. Kendrion, August-Fischbach-Straße 1, Donaueschingen, . Accesed on: 02-06-2022.

[86] Raymearst. 550 Nylon Mil-Spec Type III Paracord - 10 metre. Accessed on: 03/06/2022.

[87] Stepper Online. PLE Series Planetary Gearbox Gear Ratio 100:1 Backlash 20 arc-min for Nema 17 Stepper Motor. Accessed on: 03/06/2022.

[88] Paracord Planet. INTL Orange 550 Type III MIL-C-5040 Paracord. Accessed on: 03/06/2022.

[89] Online Aluminium. Geperst Rondstaf 7075 T6. Accessed on: 06/06/2022.

[90] All About the Density of PLA. *All3DP*.

[91] Fruugo. 5RPM Low Speed 2.5G. CM DC 12V Motor High Torque Turbo Worm 370 Geared Motor. Accessed on: 13/06/2022.

[92] Alibaba. 12v dc jsp-1010k 0.5kgs small holding electromagnet, opposite electromagnet permanent electromagnet electric linear actuator 200mm 150mm 12v / 24v dc motor stroke linear motor controller 100/200/300/500 / 750/800/900/1100 / 1300 / 1500n, . Accessed on: 13/06/2022.

[93] RubberMatter24. Rubber Plate - NBR - Thickness 1mm - Width 140 cm - Roll of 10 m. Accessed on: 13/06/2022.

[94] Air filtration: Advantages of PTFE materials. *Cleanroom Technologies*, 2019.

[95] Yutaka Tokiwa, Buenaventurada P. Calabia, Charles U. Ugwu, and Seiichi Aiba. Biodegradability of plastics. 10(9):3722–3742. ISSN 1422-0067. doi: 10.3390/ijms10093722.

[96] Dirk Hölter and Philippe Lapersonne. New aspects of cellulose acetate biodegradation.

[97] Daicel Corporation. Biodegradability of cellulose acetate.

[98] Charles M. Buchanan, Robert M. Gardner, and Ronald J. Komarek. Aerobic biodegradation of cellulose acetate.

Journal of Applied Polymer Science, 47(10):1709–1719, 1993. doi: 10.1002/app.1993.070471001.

[99] Udaya Dampage, Lumini Bandaranayake, Ridma Wanasinghe, Kishanga Kottahachchi, and Bathiya Jayasanka. Forest fire detection system using wireless sensor networks and machine learning. 2022. doi: 10.1038/s41598-021-03882-9.

[100] Amazon. Thin Film Solar Panel. Accessed on: 13-06-2022.

[101] Richard K. Johnson. Wetlaid cellulose fiber-thermoplastic hybrid composites - effects of lyocell and steam exploded wood fiber blends. 2004.

[102] Made-In-China. Lowest Price CAS 9004-35-7 Cellulose Acetate. Accessed on: 09-06-2022.

[103] Bosch Sensortec. Gas Sensor BME688 Datasheet.

[104] Vikram Iyer, Maruchi Kim, Shirley Xue, Anran Wang, and Shyamnath Gollakota. *Airdropping Sensor Networks from Drones and Insects*. Association for Computing Machinery, New York, NY, USA, 2020. ISBN 9781450370851.

[105] R. Gunasagarana, L.M. Kamarudina, E. Kanagaraja, A. Zakariaa, and A.Y.M. Shakaff. Internet of things: Solar power under forest canopy. *IEEE Student Conference on Research and Development (SCOReD)*, 2016. doi: 10.1109/SCORED.2016.7810056.

[106] Crisis24 Experts. Australian Bushfire Summer Forecast – 2021-2022, December 2021.

[107] T. Guena and P. Leblanc. How depth of discharge affects the cycle life of lithium-metal-polymer batteries. 09 2006. doi: 10.1109/INTLEC.2006.251641.

[108] Dangerous Prototypes. Free-fall sensing for drop-force modeling using a Kionix MEMS tri-axis accelerometer.

[109] ESDU 7101. *Fluid forces, pressures and moments on rectangular blocks*. ESDU International, 1978. ISBN 9781862463721.

[110] The Spring Store. PC010-312-4000-SST-0380-C-N-IN. Accessed on: 01-06-2022.

[111] Semtech. SX1276/77/78/79. Accessed on: 16-05-2022.

[112] Mónica Sánchez-Gutiérrez, Eduardo Espinosa Víctor, Isabel Bascón-Villegas, Fernando Pérez-Rodríguez, Elena Carrasco, and Alejandro Rodríguez. Production of cellulose nanofibers from olive tree harvest—a residue with wide applications. *Agronomy*, 10:696, 05 2020. doi: 10.3390/agronomy10050696.

[113] Jonas Wolfs and Michael A. R. Meier. A more sustainable synthesis approach for cellulose acetate using the dbu/co2 switchable solvent system. *Green Chem.*, 23:4410–4420, 2021. doi: 10.1039/D1GC01508G.

[114] T. S. Lawton and H. K. Nason. Effect of ultraviolet light on cellulose acetate and nitrate. *Industrial & Engineering Chemistry*, 36(12):1128–1130, 1944. doi: 10.1021/ie50420a011.

[115] W.C. Thomas, L.F. McGrath, K.A. Baarson, C.S. Auletta, I.W. Daly, and R.F. McConnell. Subchronic oral toxicity of cellulose acetate in rats. *Food and Chemical Toxicology*, 29(7):453–458, 1991. ISSN 0278-6915. doi: https://doi.org/10.1016/0278-6915(91)90090-T.

[116] Vijay Kumar Guna, Geethapriya Murugesan, Bhuvaneswari Hulikal Basavarajaiah, Manikandan Ilangovan, Sharon Olivera, Venkatesh Krishna, and Narendra Reddy. Plant-based completely biodegradable printed circuit boards. *IEEE Transactions on Electron Devices*, 63(12): 4893–4898, 2016. doi: 10.1109/TED.2016.2619983.

[117] Australian Government. Nullo Mountain, NSW - daily weather observations. Accessed: 2022-6-2.

[118] Alberto Zasso, Aly Mousaad Aly, Lorenzo Rosa, and Gisella Tomasini. Wind induced dynamics of a prismatic slender building with 1:3 rectangular section. 07 2008.

[119] Miguel G Cruz, James S. Gould, Lachie Mccaw, and Martin Edward Alexander. *A guide to rate of fire spread models for Australian vegetation*. Australasian Fire and Emergency Service Authorities Council Ltd and Commonwealth Scientific and Industrial Research Organisation, 2015. ISBN 978-0-9872065-4-1.

[120] Przemysław Sypkaa and Rafał Starzak. Simplified, empirical model of wind speed profile under canopy of istebna spruce stand in mountain valley. *Agricultural and Forest Meteorology*, 171-172:220–233, 04 2013. doi: 10.1016/j.agrformet.2012.11.003.

[121] Jan Gilroy and Cuong Tran. A new fuel load model for eucalypt forests in southeast queensland. 06 2006.

[122] F A Powell. Bushfire weather. *Weatherwise*, 36(3):126–131, 1983.

[123] NSW National Parks and Wildlife Service. Blue Mountains National Park Fire Management Strategy, May 2004.

[124] NSW National Parks and Wildlife Service. Fire Management Strategy Wollemi National Park, March 2006.

[125] Miguel Cruz, James Gould, Martin Alexander, Lachie Mccaw, and Stuart Matthews. *A guide to rate of fire spread models for Australian vegetation*. 01 2015. ISBN 978-0-9872065-4-1.

[126] Fang Li, X. Zeng, and Samuel Levis. A process-based fire parameterization of intermediate complexity in a dynamic global vegetation model. *Biogeosciences*, 9, 07 2012. doi: 10.5194/bg-9-2761-2012.

[127] M.A. Jackson and I. Robins. Gas sensing for fire detection: Measurements of co, co2, h2, o2, and smoke density in european standard fire tests. *Fire Safety Journal*, 22(2):181–205, 1994. ISSN 0379-7112. doi: https://doi.org/10.1016/0379-7112(94)90072-8.

[128] Center for Science Education. Carbon monoxide.

[129] Miguel G. Cruz, Martin E. Alexander, and Musa Kilinc. Wildfire rates of spread in grasslands under critical burning conditions. *Fire*, 5(2), 2022. ISSN 2571-6255. doi: 10.3390/fire5020055.

[130] Mark Finney. Calculation of fire spread rates across random landscapes. *International Journal of Wildland Fire - INT J WILDLAND FIRE*, 12, 01 2003. doi: 10.1071/WF03010.

[131] Geo Sat Tech. Atmospheric attenuation. Accessed on: 08-06-2022.

[132] Yu Song Meng, Yee Hui Lee, and Boon Ng. Empirical near ground path loss modeling in a forest at vhf and uhf bands. *Antennas and Propagation, IEEE Transactions on*, 57:1461 – 1468, 06 2009. doi: 10.1109/TAP.2009.2016703.

[133] SemTech. An1200.22 lora™ - modulation basics. Accessed on: 08-06-2022.

[134] Martina Poggiani, Federico Alimenti, Paolo Mezzanotte, Marco Virili, Chiara Mariotti, Giulia Orecchini, and Luca Roselli. 24-ghz patch antenna array on cellulose-based materials for green wireless internet applications. *IET Science, Measurement & Technology*, 8(6):342–349, 2014. doi: 10.1049/iet-smt.2013.0279.

[135] S.L. Wade, C.M. Barry, and M.D Nelson. Renewable energy map of new south wales: solar resource fact sheet. 2016.

[136] Xuyun Zeng. Everything about the Raspberry Pi Pico, February 2022.

[137] LiPol Battery. 503337 Lithium Polymer Battery. Accessed on: 08-06-2022.

[138] RS. Raspberry Pi Pico - Reel of 480. Accessed on: 16-05-2022.

[139] Catherine Lane. Types of solar panels: which one is the best choice?

[140] W. Buttner, C. Rivkin, R. Burgess, K. Hartmann, I. Bloomfield, M. Bubar, M. Post, L. Boon-Brett, E. Weidner, and P. Moretto. Hydrogen monitoring requirements in the global technical regulation on hydrogen and fuel cell vehicles. *In-*

ternational Journal of Hydrogen Energy, 42(11):7664–7671, 2017. ISSN 0360-3199. doi: 10.1016/j.ijhydene.2016.06.053. Special issue on The 6th International Conference on Hydrogen Safety (ICHS 2015), 19-21 October 2015, Yokohama, Japan.

[141] Lessons Learned from a Hydrogen Explosion. *POWER Magazine*, 2009.

[142] Fillipe Goulart. Local_search.py at master · fillipe-gsm/python-tsp.

[143] NSW National Parks Service. Drones in Parks.

[144] Server Mania. How much does a server cost for app hosting? Accessed on: 10-06-2022.

[145] Cessna. *Cessna SkyHawk Pilot's Operating Handbook*. Cessna, 1978.

[146] Kalam Azad, Sayed Uddin, and Muhammad Alam. Experimental study of di diesel engine performance using biodiesel blends with kerosene. *International Journal of Energy and Environment*, 4:265–278, 01 2013.

[147] H2Tools. Basic Hydrogen Properties.

[148] FINA Facilities Rules, Part IX. Technical report, FINA, 2017.

[149] D.G. Derwent. Hydrogen for heating: Atmospheric impacts. 11 2018.

[150] Office of Transportation and Air Quality. Greenhouse gas emissions from a typical passenger vehicle. Technical report, United States Environmental Protection Agency, 03 2018.

[151] E. Cetinkaya, I. Dincer, and G.F. Naterer. Life cycle assessment of various hydrogen production methods. *International Journal of Hydrogen Energy*, 37(3):2071–2080, 2012. ISSN 0360-3199. doi: doi.org/10.1016/j.ijhydene.2011.10.064.

[152] Water Australian Government, Department of Agriculture and Environment. Stocktake of fire in australia's forests, 2011 to 2016. Accessed on: 11-06-2022.

[153] Josep G. Canadell, C. P. Meyer, Garry D. Cook, Andrew Dowdy, Peter R. Briggs, Jürgen Knauer, Acacia Pepler, and Vanessa Haverd. Multi-decadal increase of forest burned area in australia is linked to climate change. *Nature Communications*, 12(6921), 2021. doi: 10.1038/s41467-021-27225-4.

[154] Nicholas Biddle, Colleen Bryant, Matthew Gray, and Dinith Marasinghe. Measuring the economic impact of early bushfire detection. *ANU Centre for Social Research and Methods*, 2020.

[155] Trevor H. Booth and Beth Riordan. Csiro submission 09/355. Technical report, Climate Adaptation National Research Flagship, 2009.

[156] CustomPart.net. Injetion Moulding Cost Estimator. Accessed on: 10-06-2022.

[157] Dryad. Ultra-Early Detection of Wildfires. 09 2021. URL https://www.businessjoensuu.fi/files/carsten_brinkschulte_dryad.pdf. Accessed on: 10-06-2022.

[158] Epic Flight Academy. How Much is an Aircraft Mechanic Salary?

[159] DroneU. Drone Pilot Salary: How Much Do Drone Pilots Make in 2022? Accessed on: 10-06-2022.

[160] Forty Four Degrees. Drones and Filming in Australian Parks. Accessed on: 10-06-2022.

[161] European Commission. Assessment of hydrogen delivery options. Technical report, European Union, 2021.

[162] Bureau of Infrastructure and Regional Development. Freight Rates in Australia. Technical report, Australian Government, 2017.

A

[163]

Gantt Chart

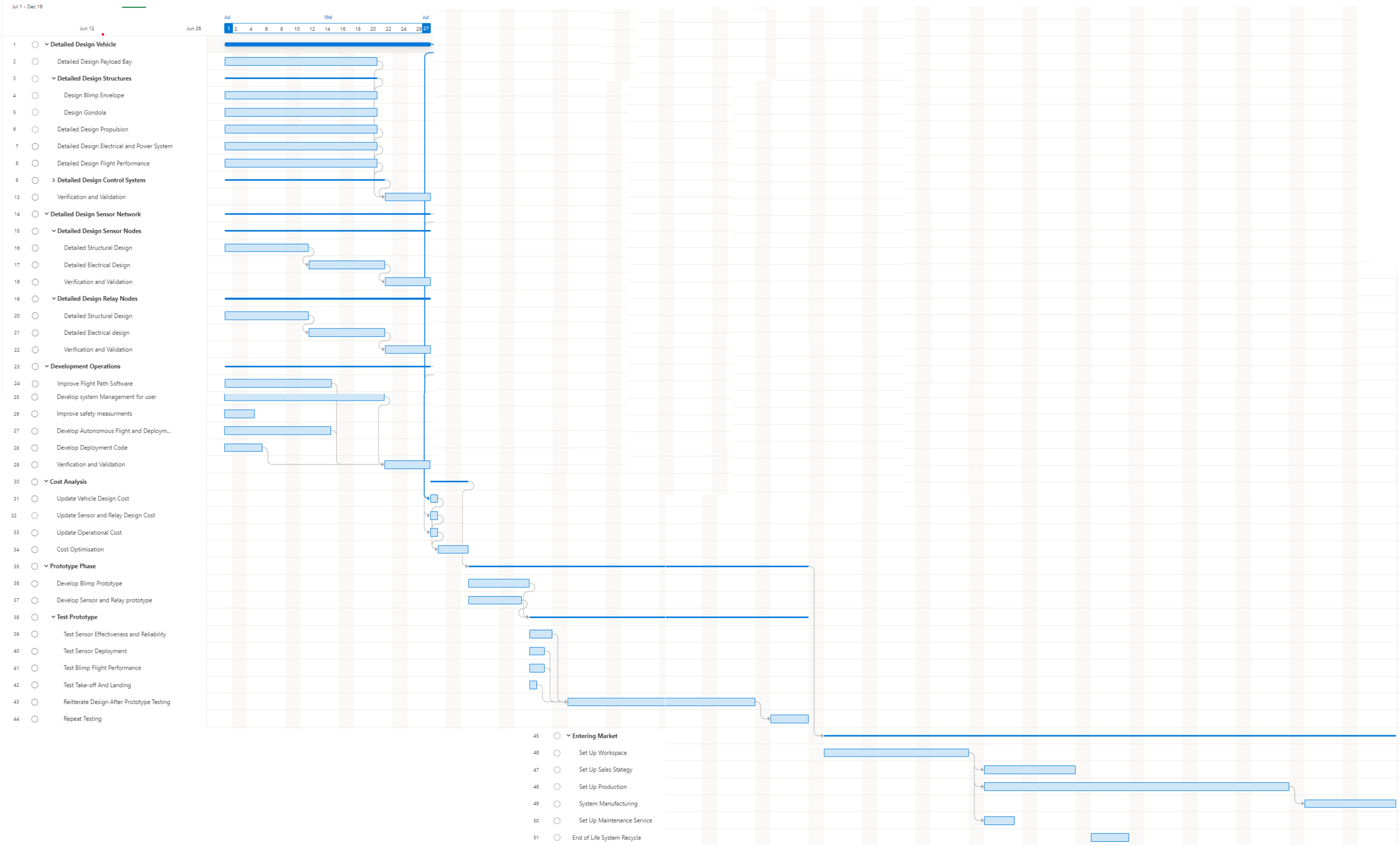

Figure A.1: *Gantt Chart of Phase three.*

B

Functional Flow Diagrams

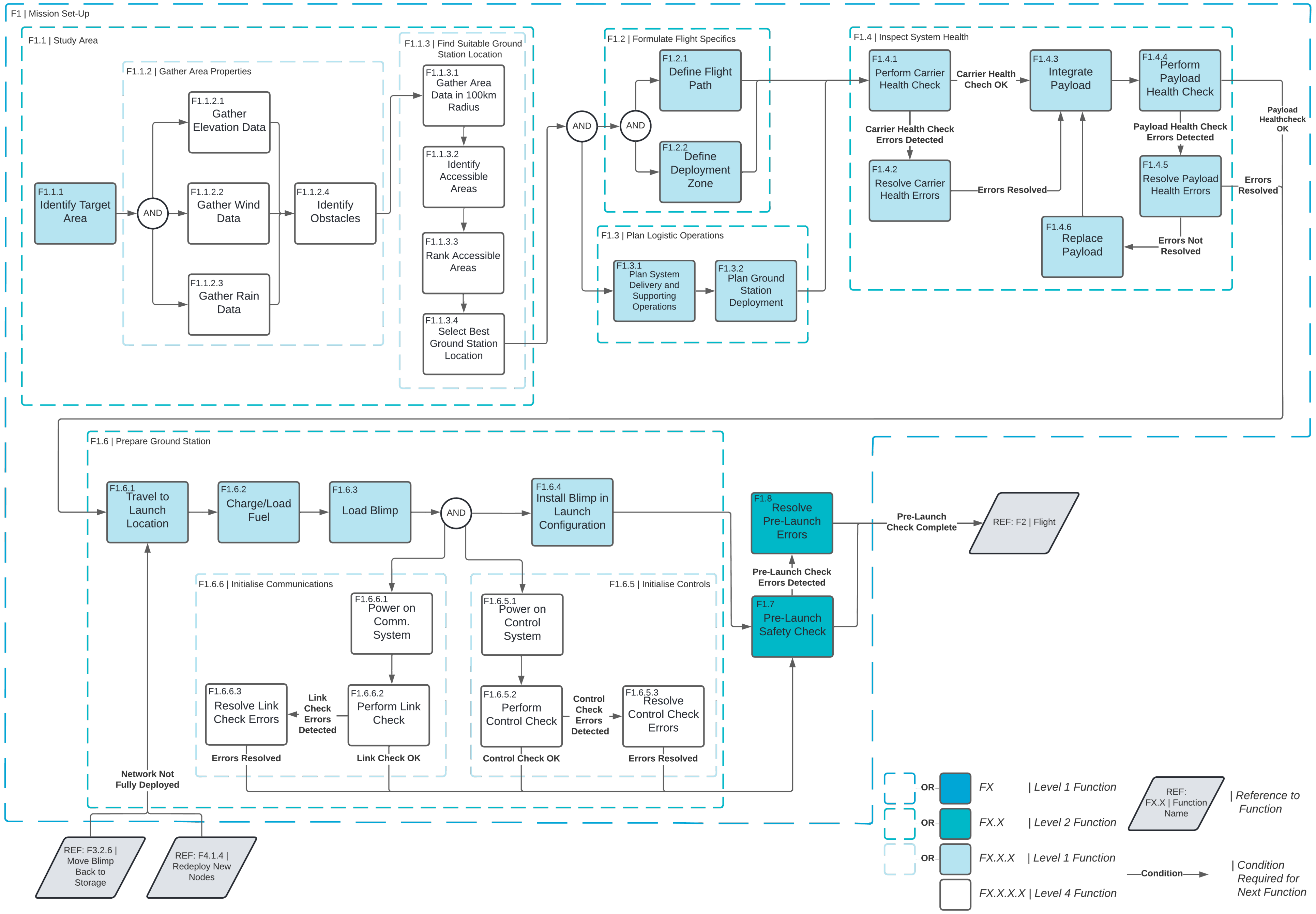

Figure B.1: *Functional Flow Diagram of F1 up to level four.*

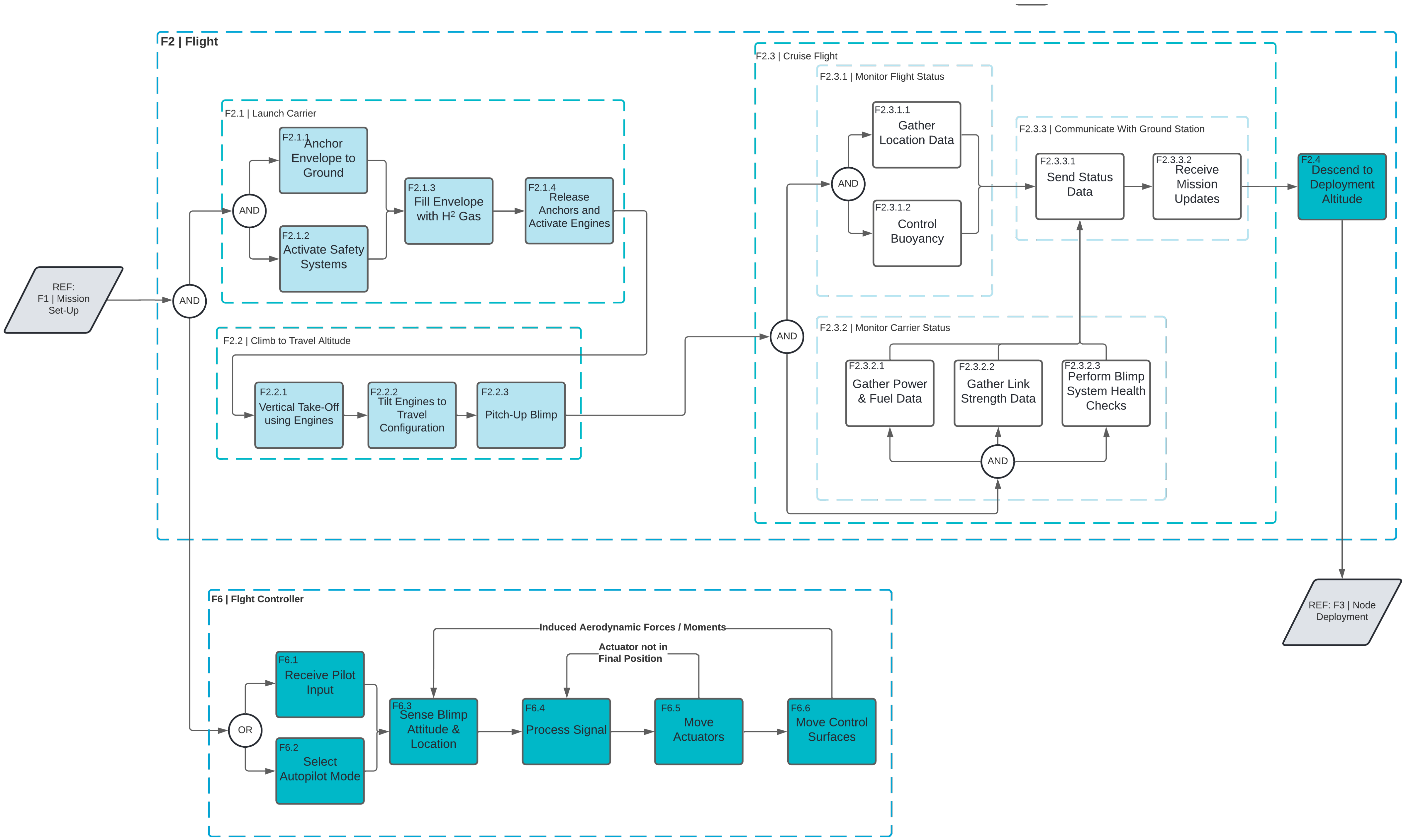

Figure B.2: *Functional Flow Diagram of F2 and F6 up to level four.*

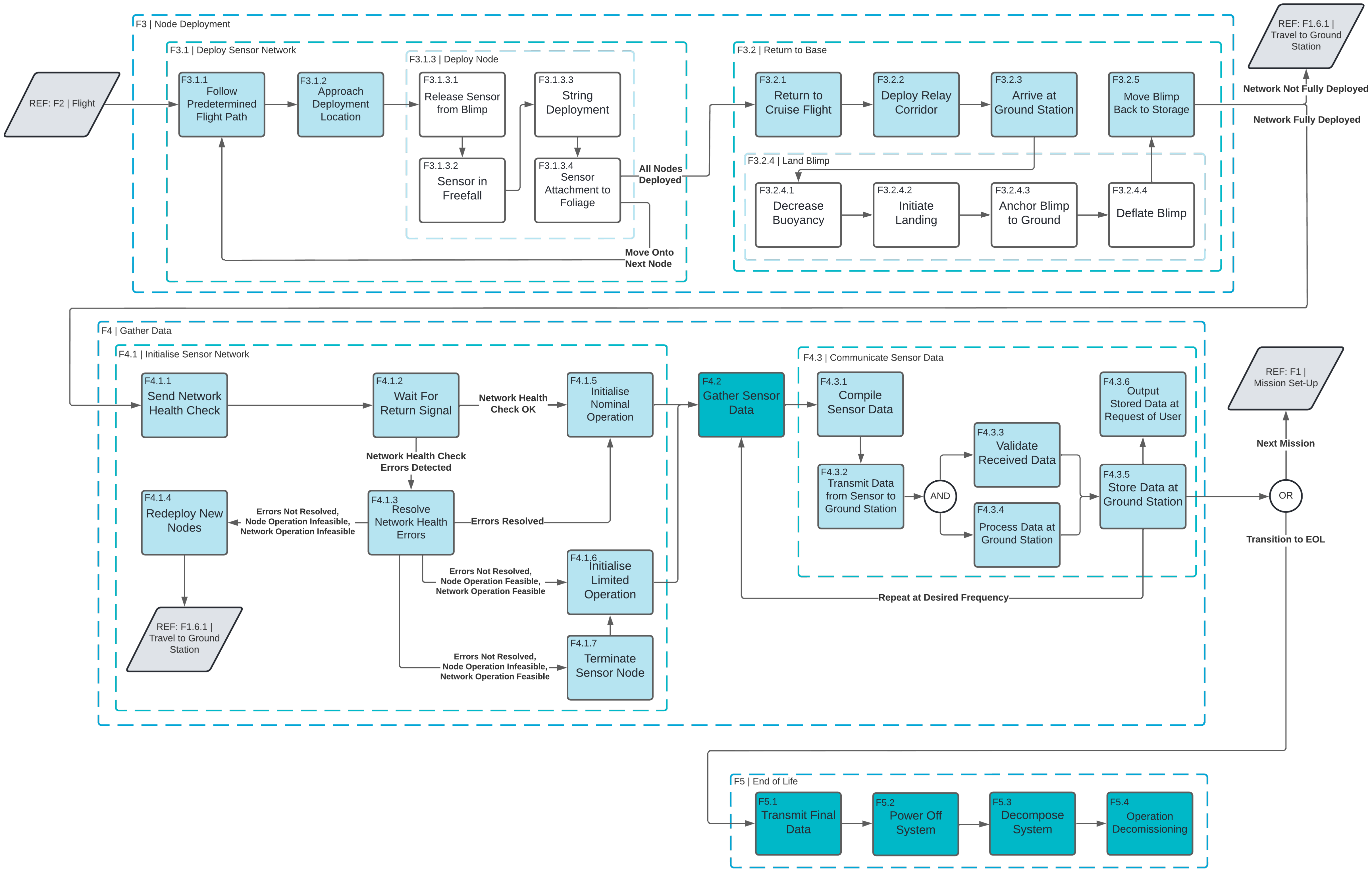

Figure B.3: *Functional Flow Diagram of F3, F4 and F5 up to level four.*

C

Functional Breakdown Diagram

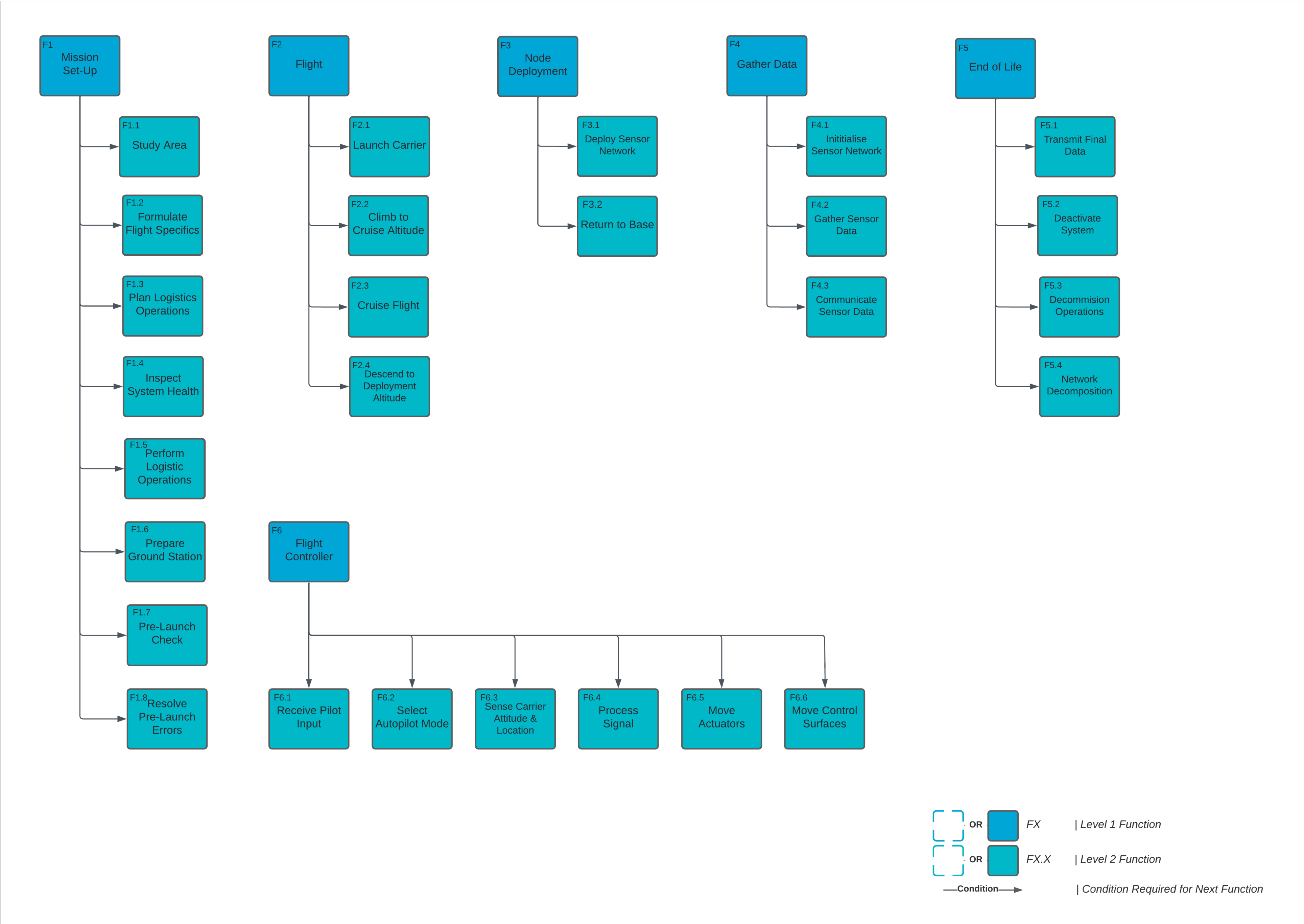

Figure C.1: *Functional Breakdown Diagram of EcoSense EMBER up to level 2.*

D

State-Space Derivation

D.1. Longitudinal Dynamics

The equations of motion for the longitudinal dynamics were found to be:

$$\Sigma F_z: \quad L_e + L_h - F - F_{atm} = m\ddot{z} \tag{D.1}$$

$$\Sigma M_y^{cb}: \quad F x_{hinge} + L_e x_{ac} - L_h x_{fin} - M_{damp} - M_{pend} = I_{yy}^{cb}\ddot{\theta} \tag{D.2}$$

The next step is to further define the acting forces as functions of potential state variables. The lift coefficients are assumed to be proportional to angle of attack, as the bodies are almost symmetric and angles of attack are generally small.

$$\frac{1}{2}\rho V^2 S C_{L_{\alpha_e}}\alpha + \frac{1}{2}\rho V^2 S\left(\frac{V_h}{V}\right)^2 C_{L_{\alpha_h}}\alpha - \frac{1}{2}\rho V^2 S\left(\frac{V_h}{V}\right)^2 C_{F_{\delta_e}}\delta_e - c_{atm}\dot{z} - k_{atm}z = m\ddot{z} \tag{D.3}$$

$$\frac{1}{2}\rho V^2 S\left(\frac{V_h}{V}\right)^2 C_{F_{\delta_e}} x_{hinge}\delta_e + \frac{1}{2}\rho V^2 S C_{L_{\alpha_e}} x_{ac}\alpha - \frac{1}{2}\rho V^2 S\left(\frac{V_h}{V}\right)^2 C_{L_{\alpha_h}} x_{fin}\alpha - \frac{1}{2}\rho V^2 S l C_{M_q}\dot{\theta} - W z_{cg}\theta = I_{yy}^{cb}\ddot{\theta} \tag{D.4}$$

Now, the force equation can be normalised by $\frac{1}{2}\rho V^2 S$ and the moment equation by $\frac{1}{2}\rho V^2 S l$, where l is the length of the envelope. Tail coefficients are already given with respect to the overall reference area. However, the velocity reduction at the tail due to skin friction still needs to be taken into account. Those parameters are taken from the cruise condition, which the dynamics are superimposed on.

$$-C_{F_{\delta e}}\delta_e + \left(C_{L_{\alpha_e}} + C_{L_{\alpha_h}}\right)\alpha - C_m\ddot{z} - C_c\dot{z} - C_k z = 0 \tag{D.5}$$

$$\left(\frac{V_h}{V}\right)^2 C_{F_{\delta e}}\frac{x_{hinge}}{l}\delta_e + \left(C_{L_{\alpha_e}}\frac{x_{ac}}{l} - \left(\frac{V_h}{V}\right)^2 C_{L_{\alpha_h}}\frac{x_{fin}}{l}\right)\alpha - K_{yy}\ddot{\theta} - C_{m_q}\dot{\theta} - C_W\frac{z_{cg}}{l}\theta = 0 \tag{D.6}$$

Assuming only small deviations from the cruise condition, namely in V and ρ, it becomes apparent that this is a linear, time-invariant system of differential equations with variables α, z and θ. In order to represent this in state-space, the equations need to be rewritten as first-order differential equations, defining the rate of climb $RC = \dot{z}$ and pitch rate $q = \dot{\theta}$. Furthermore, since there are three prospective state-variables, one more equation is needed, defining how the angle of attack behaves:

$$\alpha = \theta - \gamma, \tag{D.7}$$

where γ is the flight path angle, defined for small angles by $\gamma V = RC$. In fact, for flight path planning, the flight path or climb angle is a more convenient measure than the rate of climb and is therefore used in the equations of motion instead. Since for state-space, the rate of changes need to be defined, Equation D.7 is differentiated to complete the system, leaving us with the following equations:

$$\dot{\alpha} - q + \dot{\gamma} = 0 \tag{D.8}$$

$$-\left(\frac{V_h}{V}\right)^2 C_{F_{\delta e}}\delta_e + \left(C_{L_{\alpha_e}} + \left(\frac{V_h}{V}\right)^2 C_{L_{\alpha_h}}\right)\alpha - C_m V\dot{\gamma} - C_c V\gamma - C_k z = 0 \tag{D.9}$$

$$\dot{z} - \gamma V = 0 \tag{D.10}$$

$$\left(\frac{V_h}{V}\right)^2 C_{F_{\delta e}}\frac{x_{hinge}}{l}\delta_e + \left(C_{L_{\alpha_e}}\frac{x_{ac}}{l} - \left(\frac{V_h}{V}\right)^2 C_{L_{\alpha_h}}\frac{x_{fin}}{l}\right)\alpha - K_{yy}\dot{q} - C_{m_q}q - C_W\frac{z_{cg}}{l}\theta = 0 \tag{D.11}$$

$$\dot{\theta} - q = 0 \tag{D.12}$$

This system can be rewritten in matrix form as follows:

$$
\begin{bmatrix}
0 & 0 & 0 & 0 & -1 \\
C_{L_{\alpha_e}}+\left(\frac{V_h}{V}\right)^2 C_{L_{\alpha_h}} & -C_k & -C_c V & 0 & 0 \\
0 & 0 & -V & 0 & 0 \\
C_{L_{\alpha_e}}\frac{x_{ac}}{l}-C_{L_{\alpha_h}}\left(\frac{V_h}{V}\right)^2\frac{x_{fin}}{l} & 0 & 0 & -C_W\frac{z_{cg}}{l} & -C_{m_q} \\
0 & 0 & 0 & 0 & -1
\end{bmatrix}
\begin{bmatrix} \alpha \\ z \\ \gamma \\ \theta \\ q \end{bmatrix}
+
\begin{bmatrix}
1 & 0 & 1 & 0 & 0 \\
0 & 0 & -C_m V & 0 & 0 \\
0 & 1 & 0 & 0 & 0 \\
0 & 0 & 0 & 0 & -K_{yy} \\
0 & 0 & 0 & 1 & 0
\end{bmatrix}
\begin{bmatrix} \dot{\alpha} \\ \dot{z} \\ \dot{\gamma} \\ \dot{\theta} \\ \dot{q} \end{bmatrix}
+
\begin{bmatrix}
0 \\
-C_{F_{\delta e}}\left(\frac{V_h}{V}\right)^2 \\
0 \\
C_{F_{\delta e}}\left(\frac{V_h}{V}\right)^2\frac{x_{hinge}}{l} \\
0
\end{bmatrix}
\delta_e = \vec{0}
\tag{D.13}
$$

Defining the state vector $\vec{x} = [\ \alpha \quad z \quad \gamma \quad \theta \quad q\ ]^T$, and the input vector $\vec{u} = U$, this can be written more compactly as:

$$C_1\dot{\vec{x}} + C_2\vec{x} + C_3\vec{u} = \vec{0} \tag{D.14}$$

Finally, comparing to the state equation

$$\dot{\vec{x}} = A\vec{x} + B\vec{u}, \tag{D.15}$$

we have

$$A = C_1^{-1}C_2 \tag{D.16}$$

$$B = C_1^{-1}C_3 \tag{D.17}$$

D.2. Lateral Dynamics

The derivation for the lateral dynamics works the same way as the one for longitudinal dynamics, so it will be presented a bit shorter. Starting again with the equations of motion:

$$\Sigma F_y: \quad F + Y_r - Y_e - Y_v = m\ddot{y} + mV\dot{\psi} \tag{D.18}$$

$$\Sigma M_z^{cb}: \quad F x_{hinge} + Y_e x_{ac} - Y_v x_{fin} - N_{damp} = I_{zz}^{cb}\ddot{\psi} \tag{D.19}$$

Similar to the previous section, aerodynamic forces are written in terms of the prospective state variables and normalised.

$$\left(\frac{V_h}{V}\right)^2 C_{F_\delta}\delta - \left(C_{Y_{\beta e}} + \left(\frac{V_h}{V}\right)^2 C_{Y_{\beta v}}\right)\beta + (C_{Yr} - \mu V)\dot{\psi} - C_m\ddot{y} = 0 \tag{D.20}$$

$$\left(\frac{V_h}{V}\right)^2 C_{F_\delta}\frac{x_{hinge}}{l}\delta + \left(C_{Y_{\beta e}}\frac{x_{ac}}{l} - \left(\frac{V_h}{V}\right)^2 C_{Y_{\beta v}}\frac{x_{fin}}{l}\right)\beta - C_{N_r}\dot{\psi} - K_z z\ddot{\psi} = 0 \tag{D.21}$$

Prospective states are sideslip angle β and turn rate $\dot{\psi} = r$, so the equations are rewritten as a system of first order linear differential equations. Moreover, a relation between both is required to eliminate the y in the system. This variable is not interesting, as the coordinate frame constantly rotates and only the heading is to be controlled. For this, typically the following equation is used [17].

$$\dot{\beta} = \frac{\ddot{y}}{V} \tag{D.22}$$

Having eliminated the y and rewritten the equations as a system of first order differential equations, the result in matrix form looks as follows:

$$
\begin{bmatrix}
\left(C_{Y_{\beta e}}\frac{x_{ac}}{l} - \left(\frac{V_v}{V}\right)^2 C_{Y_{\beta v}}\frac{x_{fin}}{l}\right) & -C_{N_r} \\
-\left(C_{Y_{\beta e}} + C_{Y_{\beta v}}\left(\frac{V_v}{V}\right)^2\right) & C_{Y_r} - \mu V
\end{bmatrix}
\begin{bmatrix} \beta \\ r \end{bmatrix}
+
\begin{bmatrix}
0 & -K_{zz} \\
-\mu V & 0
\end{bmatrix}
\begin{bmatrix} \dot{\beta} \\ \dot{r} \end{bmatrix}
+
\begin{bmatrix}
C_{F_\delta}\left(\frac{V_v}{V}\right)^2\frac{x_{hinge}}{l} \\
C_{F_\delta}\left(\frac{V_v}{V}\right)^2
\end{bmatrix}
\delta = \vec{0}
\tag{D.23}
$$

Applying the steps of the previous section, the state and input matrix can be obtained.

D.3. Stability and Control Derivatives

Table D.1 shows the stability and control derivatives used in the state-space model, based on the final design and the cruise parameters given in the head of the table. Values are defined according to the equations shown earlier and might differ from conventions used in other models, so they are only valid within the model derived in this chapter.

Table D.1: *Stability and control derivatives as well as other coefficients and characteristics used for the model.*

V	=	13.922 $\mathrm{m/s}$	V_h/V	=	0.75
ρ	=	1.058 $\mathrm{kg/m^3}$	S	=	27.695 $\mathrm{m^2}$
x_{ac}	=	1.766 m	x_{fin}	=	5.433 m
x_{hinge}	=	5.988 m	z_{cg}	=	1.420 m
l	=	13.581 m	μ	=	0.051
C_k	=	0.0005	C_c	=	0.0019
$C_{L_{\alpha_e}}$	=	0.6667	$C_{L_{\alpha_h}}$	=	0.3636
C_{m_q}	=	0.0828	K_{yy}	=	0.0289
C_{F_δ}	=	0.3273			
$C_{Y_{\beta_e}}$	=	0.6667	$C_{Y_{\beta_v}}$	=	0.3636
C_{N_r}	=	0.0211	C_{Y_r}	=	0.0512
C_{F_δ}	=	0.3273	K_{zz}	=	0.0183

E
Detailed Vehicle Mass Breakdown

Table E.1: *Detailed mass breakdown of final vehicle design.*

VEHICLE MASS BREAKDOWN			
Structures			
Component	**Unit Weight**	**Quantity**	**Set Weight**
Envelope	30.3 kg	1	30.30 kg
Gondola Shell	16.3 kg	1	16.30 kg
Envelope Connection Grid	5.4 kg	1	5.40 kg
Total Structures Mass			**52.00 kg**
Electronics			
Component	**Unit Weight**	**Quantity**	**Set Weight**
Flight Controller	188.0 g	1	188 g
Satcom Module	994.0 g	1	994 g
Pressure Sensor	50.0 g	2	100 g
Temperature Sensor	0.2 g	10	2 g
GPS Module	5.0 g	1	5 g
Electronic Speed Controller	109.0 g	4	436 g
Hydrogen Sensor	40.0 g	1	40 g
Battery Cell	46.6 g	108	5033 g
DC Stepdown Converter	20.0 g	2	40 g
Solar Charge Controller	3.0 g	1	3 g
Solar Array	1330.0 g	1	1330 g
Fire Suppression System	6000.0 g	1	6000 g
Total Electronics Mass			**14.17 kg**
Deployment System			
Component	**Unit Weight**	**Quantity**	**Set Weight**
Side Plates	537.8 g	4	2151 g
Transverse Ribs	108.5 g	8	868 g
Rods	15.0 g	24	360 g
Magnet Holder	3.0 g	552	1656 g
Electromagnet	10.0 g	552	5520 g
Photoresistor	0.3 g	552	138 g
Total Deployment System Mass			**10.69 kg**

Buoyancy Control System			
Component	**Unit Weight**	**Quantity**	**Set Weight**
Ballonet	2275.0 g	2	4550 g
Ballonet Valve	235.0 g	2	470 g
Hydrogen Sensor	40.0 g	2	80 g
Blower	80.0 g	1	80 g
Massflow Sensor	450.0 g	3	1350 g
Venting Valve	235.0 g	1	235 g
Total Buoyancy Control System Mass			**6.77 kg**
Propulsion System			
Component	**Unit Weight**	**Quantity**	**Set Weight**
Servo Motor	197.0 g	4	788 g
Enclosure	153.4 g	4	614 g
Bearing	10.0 g	4	40 g
Motor	255.0 g	4	1020 g
Propeller	129.0 g	4	516 g
Duct	284.9 g	4	1140 g
Rod	166.8 g	4	667 g
Fasteners	46.4 g	4	186 g
Total Propulsion System Mass			**4.97 kg**
Empennage			
Component	**Unit Weight**	**Quantity**	**Set Weight**
Stabilising Fin	1274.0 g	4	5096 g
Rudder	319.0 g	2	638 g
Elevator	319.0 g	2	638 g
Servo Motor	136.0 g	4	544 g
Total Empennage Mass			**6.92 kg**
Operational Empty Mass			**95.52 kg**
Payload Mass			**45.00 kg**
Maximum Take-Off Mass			**140.52 kg**